Determination of TMD parton densities from HERA data and application to pp processes

Dissertation

zur Erlangung des Doktorgrades

an der Fakultät für Mathematik, Informatik und Naturwissenschaften

Fachbereich Physik

der Universität Hamburg

vorgelegt von

Aleksandra Lelek

Hamburg

2018

Gutachter der Dissertation:	Prof. Dr. Brian Foster PD Dr. Hannes Jung
Gutachter der Disputation:	PD Dr. Markus Diehl Prof. Dr. Brian Foster Prof. Dr. Johannes Haller PD Dr. Hannes Jung Prof. Dr. Sven-Olaf Moch
Datum der Disputation:	26. April 2018
Vorsitzender Fach-Promotionsausschusses Physik:	Prof. Dr. Wolfgang Hansen
Leiter des Fachbereichs Physik:	Prof. Dr. Michael Potthoff
Dekan der Fakultät MIN:	Prof. Dr. Heinrich Graener

Eidesstattliche Versicherung

Hiermit versichere ich an Eides statt, die vorliegende Dissertationsschrift selbst verfasst und keine anderen als die angegebenen Hilfsmittel und Quellen benutzt zu haben.

Die eingereichte schriftliche Fassung entspricht der auf dem elektronischen Speichermedium.

Die Dissertation wurde in der vorgelegten oder einer ähnlichen Form nicht schon einmal in einem früheren Promotionsverfahren angenommen oder als ungenügend beurteilt.

Declaration on oath

I hereby declare, on oath, that I have written the present dissertation on my own and have not used other than the acknowledged resources and aids.

The submitted written version corresponds to the version on the electronic storage medium.

I hereby declare that I have not previously applied or pursued for a doctorate (Ph.D. studies).

Hamburg, den 27 März 2018

Abstract

The topic of this thesis is a new approach to solve the DGLAP evolution equation to obtain not only the collinear Parton Distribution Functions (PDFs) but also the Transverse Momentum Dependent (TMD) PDFs (TMDs). The DGLAP equation is solved with the Parton Branching (PB) method, which allows a determination of kinematic variables at every branching and a construction of the TMDs in a large range in longitudinal momentum fraction x and evolution scale μ^2.
The new method is validated against the semi-analytical solutions for the usual integrated parton distribution functions. Moreover, the PB method enables to study details of the parton evolution in a way which is not possible in standard methods. The PB method is applied to perform a fit to HERA H1 and ZEUS combined F_2 data using the `xFitter` package. The newly obtained TMDs are used for predictions of the Z boson $p_\perp$ spectrum and a comparison with a measurement from LHC is performed.
This thesis is a part of a broader approach to obtain predictions for many QCD observables where the hard process and higher order corrections follow the same TMDs. The method to solve evolution equations is a first step towards a consistent treatment of parton densities and the simulation of higher order corrections used in the predictions for high energy collisions of particles.

Zusammenfassung

Das Thema dieser Arbeit ist die Lösung der DGLAP - Evolutionsgleichung um kollineare Partondichterverteilungen (PDFs), wie auch Transverse Momentum Dependent (TMD) PDFs (TMDs) zu bestimmen. Die DGLAP-Gleichung wird mit der Parton Branching (PB) -Methode gelöst, eine Methode, die eine Bestimmung von kinematischen Variablen in jedem Schritt ermöglicht und die die Bestimmung der Partondichteverteilungen in einem großen Bereich des longitudinalen Impulsbruchteils x und Entwiklungsskala μ^2 erlaubt. Die neue Methode wird mit semi-analytischen Lösungen der DGLAP Gelichung validiert. Die PB-Methode ermöglicht es, Details der Partondichte-Evolution in einer Weise zu studieren, die in den Standardlösungen nicht möglich ist. Die PB-Methode wird angewendet, um die Startverteilungen mit Hilfes der kombinierten HERA H1 und ZEUS Messungen der Protonstrukturfuntkion zu bestimmen. Diese TMDs werden für Vorhersagen des Trnasversalimpulsspektrums des Z Boson bei LHC und einem Vergleich mit Messungen verwendet.
Die vorliegende Arbeit These ist ein Teil eines groesseren Projektes um Vorhersagen für Messungen zu erhalten, wobei der partonische Prozess wie auch höhere Ordnung Korrketuren mit den gleichen TMDs bestimmt werden. Die Methode zur Lösung der Evolutionsgleichungen ist ein erster Schritt in Richtung einer konsistenten Behandlung von Parton-Dichten und der Simulation von höheren Ordnung Korrekturen bei hochenergetischen Teilchenkollisionen.

O wiele rzeczy za dużo by zmieścić w tak małym pudełku
Lawrence Weiner

To Marek, Aśka and Dionizy. I love you!

Table of Contents

1 Introduction

1.1 Preface

The Standard Model (SM) is the theory of Particle Physics which explains the structure of matter in the Universe describing the elementary particles and the electroweak and strong interactions between them. It arose in the second half of the XX century and it was formulated in the current version in the mid 1970s.

Elementary particles are divided into fermions (quarks and leptons) and bosons. Mathematically, the SM is based on the *Quantum Field Theory* (QFT) which allows one to write the *Langrangian density* (called very often *Langrangian*) to describe the kinematics and dynamics of the theory. The SM is a gauge invariant theory- its Lagrangian is invariant under the local $SU(3) \times SU(2)_L \times U(1)_Y$ symmetry. The group symmetry of colour is $SU(3)$, $SU(2)_L$ is the approximate isospin symmetry (exact, if u and d had the same masses) and $U(1)_Y$ is the baryon number conservation symmetry. The SM can be divided into the sectors: Quantum Chromodynamics (QCD) sector, electroweak sector, which incorporates Quantum Electrodynamics (QED) and weak interaction, Higgs sector and Yukawa sector. Each of these sectors has its own Lagrangian.
This thesis is focused on the QCD part of the SM that is the theory which predicts that hadrons are built from quarks and gluons and *glue* together via the strong interaction. The key ingredients of the QCD are the colour confinement and the asymptotic freedom, the consequences of the running of the QCD coupling α_s, which is decreasing with the scale. QCD is a perturbation theory - any dimensionless observable can be written as an expansion in terms of α_s.

The SM is an extremely successful theory. An enormous amount of measurements turned out to be consistent with its theoretical predictions. Nevertheless, it is already known that the theory is not complete. There are phenomena, like baryon asymmetry, neutrino masses or galactic velocity distribution, which cannot be explained within the SM. A great effort focuses on finding hints of a theory which could describe physics beyond the Standard Model (BSM). To find them, the SM must be well understood. That is why it is so important to perform precision measurements: every inconsistency can be a clue of how to construct the BSM theory and which of the existing ones can be preserved and which should be abandoned.

A powerful tool to predict the cross sections is the QCD collinear factorization theorem. It allows one to separate the processes at different scales and factorize them into the perturbatively calculable parton level cross sections dependent on the process and the universal parton distribution functions (PDFs) - pieces which contain non-perturbative information on the hadron structure and which, extracted once

in a given experiment, can be used to obtain predictions in another one. The evolution of the PDFs is described by the QCD evolution equations. However, there are observables where the collinear approximation cannot give the satisfactory results and where also the transverse degrees of freedom have to be taken into account to achieve predictive power. This is where the Transverse Momentum Dependent (TMD) factorization theorems enter the game.

Several approaches to the TMD factorization theorem exist and many methods were proposed to obtain TMD PDFs. The differences between them, such as the formalism used, the TMD concept or the physical application, make the effort of comparing them very complicated. Most of these methods have limited kinematic regions in which they can be used. A recipe, which could describe the data in the broad range of the phase space, is on the wish list of particle physicists.

In this thesis a new approach to the Dokshitzer-Gribov-Lipatov-Altarelli-Parisi (DGLAP) evolution equation is proposed. We show, that by solving it with the Parton Branching (PB) method one can construct TMD PDFs. These TMD PDF sets can be used in a wide kinematic range. To demonstrate the fact, that this method works, we apply the obtained TMD PDFs to LHC measurements.

The thesis is organised as follows.

In **Chapter 1** we introduce the basic concepts of QCD: asymptotic freedom and colour confinement.

Chapter 2 explains the origin of DGLAP- the central equation for this thesis. We begin with the Parton Model to explain the Deep Inelastic Scattering and we show how, by including the QCD corrections, one can explain the Bjorken scaling violation. We introduce the concept of Parton Distribution Functions (PDFs) and factorization theorem.

In **Chapter 3** we move forward to the Parton Branching method and discuss the aspects of DGLAP necessary to interpret the equation in terms of a parton branching process. We show how the association of the kinematic variables with the evolution scale leads to a certain ordering conditions. We present the idea of the Sudakov form factor which allows for a probabilistic interpretation of the evolution equation and enables the solution using Monte Carlo methods.

In **Chapter 4** the Balitsky-Fadin-Kuraev-Lipatov (BFKL) and the Catani-Ciafaloni-Fiorani-Marchesini (CCFM) evolution equations are discussed. These equations introduce the $k_\perp$ dependence to the PDF.

Chapter 5 presents two approaches to the TMD factorization theorem: the high energy ($k_\perp$) and the Collins-Soper-Sterman (CSS) factorization. Examples of the existing TMD parametrizations are quoted and shortly compared. The areas, where the TMDs can be applied, are reviewed and examples of TMD applications are given.

In **Chapter 6** we begin the discussion of the Parton Branching (PB) method. We motivate the introduction of the new method to obtain TMDs and explain the details of the solution. The way how to obtain the $k_\perp$ dependence by solving DGLAP is described.

In **Chapter 7** we validate the PB method by comparing the obtained collinear PDFs with the results from another evolution package, QCDNUM.

In **Chapter 8** we present the results for the collinear PDFs and TMDs we obtained using the PB method. We study the effects of different ordering conditions on collinear PDFs and TMD densities.

In **Chapter 9** we perform a fit of the integrated TMDs obtained with the PB method to HERA F_2 data. We apply the resulting TMDs to the LHC measuerements of the Z boson $p_\perp$ spectrum to illustrate that the method works.

In **Chapter 10** we summarize the results presented in this thesis and give conclusions.

1.2 | Colour confinement and asymptotic freedom in QCD

Before we start the actual introduction to the topic, in this section we would like to briefly introduce the QCD running coupling, asymptotic freedom and colour confinement, the basic concepts of QCD. We follow the argumentation from [1].

Let us assume we have a dimensionless observable R dependent on a single energy scale Q^2, bigger than all the other scales in the process. In a renormalizable quantum field theory R can be expanded in the powers of the coupling α_s. During such a procedure a scale μ, at which the ultraviolet divergences are removed, is introduced. The observable R is dimensionless so it can depend only on a ratio Q^2/μ^2. However, the scale μ is an arbitrary parameter and the observable R should not depend on that. This is guaranteed mathematically by an equation

$$\mu^2 \frac{\mathrm{d}}{\mathrm{d}\mu^2} R\left(\frac{Q^2}{\mu^2}, \alpha_s\right) \equiv \left(\mu^2 \frac{\partial}{\partial \mu^2} + \mu^2 \frac{\partial \alpha_s}{\partial \mu^2} \frac{\partial}{\partial \alpha_s}\right) R = 0 \,. \tag{1.1}$$

One can define

$$\beta(\alpha_s) = \mu^2 \frac{\partial \alpha_s}{\partial \mu^2} \tag{1.2}$$

where α_s is the fixed bare coupling, and

$$t = \ln\left(\frac{Q^2}{\mu^2}\right) \tag{1.3}$$

to rewrite eq. (1.1)

$$\left(-\frac{\partial}{\partial t} + \beta(\alpha_s) \frac{\partial}{\partial \alpha_s}\right) R(\mathrm{e}^t, \alpha_s) = 0 \,. \tag{1.4}$$

The solution of this equation is obtained by defining *the running coupling* $\alpha_s\left(Q^2\right)$

$$t = \int_{\alpha_s}^{\alpha_s\left(Q^2\right)} \mathrm{d}x \, \frac{1}{\beta(x)} \tag{1.5}$$

with $\alpha_s(\mu^2) \equiv \alpha_s$. From that one can see that $R(1, \alpha_s(Q^2))$ is a solution of eq. (1.4).

Differentiation of eq. (1.5) gives the renormalization group equation for the coupling α_s:

$$Q^2 \frac{\partial \alpha_s\left(Q^2\right)}{\partial Q^2} = \beta\left(\alpha_s\left(Q^2\right)\right) \,. \tag{1.6}$$

The function β has a perturbative expansion

$$\beta\left(\alpha_s\left(Q^2\right)\right) = -b_1 \alpha_s^2\left(Q^2\right)\left(1 + b_2 \alpha_s\left(Q^2\right) + b_3 \alpha_s^2\left(Q^2\right) + ...\right) \tag{1.7}$$

whose coefficients were obtained at the 1-loop level in [2–4], 2-loop in [5–7], 3-loop [8, 9] and 4-loop in [10] by calculating corrections to the bare QCD vertices. The Feynman diagrams contributing to the β function at the 1-loop level are shown in fig. 1.1 and the 1-loop coefficient is given by

$$b_1 = \frac{33 - 2n_f}{12\pi} \tag{1.8}$$

where n_f is the number of active flavours. There are different ways of treating the number of flavours in the calculations. One of the most popular ones is the *Variable-Flavour-Number Scheme* (VFNS) where the light quarks are assumed to be massless and the heavy quarks are not active at the scales below their masses. Once the mass threshold of the heavy quark is reached, the number of flavours changes. In the *Zero-Mass* VFNS (ZM-VFNS), after reaching the mass threshold, one still neglects the mass of the heavy quark in the calculation of the short-distance cross sections.

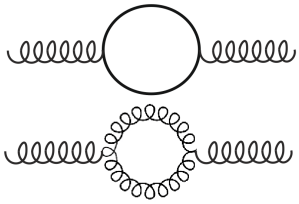

Figure 1.1: The Feynman diagrams contributing to the β function at the 1-loop level.

The coefficients b_i for $i \geq 3$ [1] depend on the *renormalization scheme* - the way of absorbing the infinities arising in the perturbative calculation of the Feynman diagrams beyond the tree level. The counterterms to cancel the divergences are introduced using a set of renormalization conditions fixed by the renormalization scheme. The frequently used renormalization schemes are Minimal Subtraction (MS) [11] and Modified Minimal Subtraction ($\overline{\text{MS}}$) [12] scheme.

From eq. (1.6) and (1.7) at the 1-loop accuracy one obtains the relation between $\alpha_s\left(\mu^2\right)$ and $\alpha_s\left(Q^2\right)$ (both in the perturbative region)

$$\alpha_s\left(Q^2\right) = \frac{\alpha_s\left(\mu^2\right)}{1 + \alpha_s\left(\mu^2\right) b_1 t} \,. \tag{1.9}$$

For large $t \to \infty$ the strong coupling decreases $\alpha_s\left(Q^2\right) \to 0$ if $b_1 > 0$ which is true for $n_f \leq 16$. This feature of QCD is called *asymptotic freedom*. At the higher scales, at small distances, the coupling is small and the quarks and gluons can be treated as the free particles. The approach to the asymptotic behaviour is slow, the coupling decreases as an inverse power of $\ln Q^2$. On the other hand, at smaller scales, i.e. large distances, the coupling is very strong and the quarks and gluons are *confined* inside the hadrons and this is the reason why they are not observed as the free particles. The behaviour of α_s is opposite to the QED coupling α which increases with scale.

The solution of eq. (1.4) can be written in terms of the series expansion

$$R\left(1, \alpha_s\left(Q^2\right)\right) = R_1 \alpha_s\left(\mu^2\right)\left(1 - \alpha_s\left(\mu^2\right) b_1 t + \alpha_s^2\left(\mu^2\right) b_1^2 t^2 + ...\right) \,. \tag{1.10}$$

From that one can see that by using the running coupling, the logarithms of Q^2/μ^2 are resummed order by order. By cutting the series at pieces $\sim \alpha_s$ one obtains the *leading order* (LO) approximation, by cutting the series at the pieces $\sim \alpha_s^2$ one obtains the next-to-leading order (NLO) approximation etc.

The solution for the running coupling can be also written in terms of a parameter Λ in the following way

$$\ln \frac{Q^2}{\Lambda^2} = -\int_{\alpha_s(Q^2)}^{\infty} \mathrm{d}x \frac{1}{\beta(x)} \tag{1.11}$$

and from that at LO one obtains

$$\alpha_s\left(Q^2\right) = \frac{1}{b \ln\left(\frac{Q^2}{\Lambda^2}\right)} \,. \tag{1.12}$$

The parameter Λ corresponds to a scale at which the running coupling diverges and gives the order of magnitude of a scale at which α_s becomes strong. The precise definition of Λ depends on the renormalization scheme and its value is approximately 200 MeV. It means that at the scale $Q \simeq 1$ GeV α_s becomes strong and the perturbation theory breaks down.

Λ depends also on the number of active flavours. Some conditions are imposed on Λ to guarantee the continuity of α_s: definitions for different flavour numbers at the scales $\mu = m$ where m are the masses of heavy quarks, have to be matched.

QCD tells us how the running coupling changes with the scale but its actual value has to be measured experimentally. Different measurements can be compared when α_s is given at the same reference scale, very often chosen to be the mass of the Z boson M_Z. Measured at the scale Q, it can be evolved to the mass of the Z boson using the renormalization group equation truncated at a given order. An example of some of the α_s measurements performed in the hadron collisions is shown in fig. 1.2 [13].

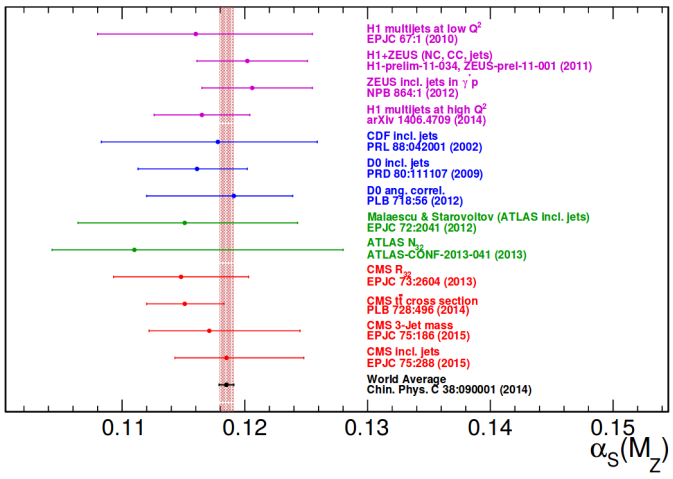

Figure 1.2: An overview of some of the α_s measurements made in hadron collisions [13] and the world-average value [14].

2 | Deep Inelastic Scattering, Parton Distribution Functions and QCD Evolution Equations

This chapter gives a short overview on the Parton Model, Deep Inelastic Scattering (DIS), Parton Distribution Functions (PDFs), collinear factorization theorem and QCD evolution equations - the basics of this thesis. We review how the Parton Model can explain the Bjorken scaling and how the QCD corrections justify the Bjorken scaling violation and lead to the DGLAP evolution equation. We discuss the importance of the PDFs and collinear factorization theorem. We summarize different solutions of the DGLAP evolution equation and mark where our method enters the stage. Extensive literature (e.g. [1, 15–20]) covers these topics in detail, here only the most important results are summarized.

2.1 | Parton Model and Deep Inelastic Scattering

The Parton Model was introduced before QCD achieved a status of the theory of strong interactions. It was formulated at the end of 1960s ([21–25]) using the basic idea that the interactions of hadrons can be described as the interactions of partons, the point-like constituents of hadrons. In the simple Parton Model, very often called *naive* in the literature, partons inside one hadron do not interact with each other, which is a good approximation in processes with high transverse momentum transfer. An improved version of the Parton Model including QCD corrections is still widely used nowadays and partons are understood to be quarks and gluons.

The Parton Model was used to explain Deep Inelastic Scattering (DIS) [26] where a lepton l scatters on the proton P through the exchange of a virtual photon γ^*, Z or W^+/W^- boson with four - momentum q

$$l + P \to l' + ... \, . \tag{2.1}$$

The momentum transfer q^2 must be large enough to eject the quark from the proton. The final state consist then of the outgoing lepton l' and other produced particles with a large total invariant mass. The proton normally does not survive the scattering, that is why the process is called *inelastic*. DIS is very often compared to a microscope - thanks to the high transverse momentum of the virtual photon one can go *deeply* inside the proton and probe its structure at distances much smaller than its size. The photon - proton interaction time is much shorter than the time needed by partons to interact with each other, which is why the structure of the proton stays the same during the probing time and the Parton Model can be used to describe the DIS.

In this section we focus on DIS of an electron on a proton through the exchange of a virtual photon, as shown in fig. 2.1. We do not consider any electroweak effects coming from Z or W^+/W^- exchange.

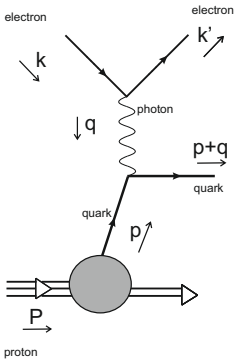

Figure 2.1: DIS Feynman diagram.

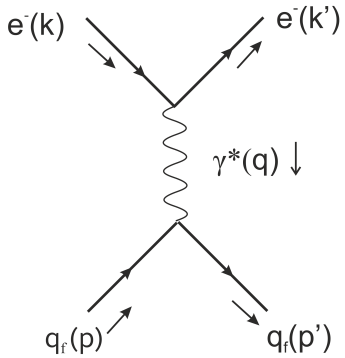

Figure 2.2: The LO Feynman diagram contributing to DIS process.

To calculate the DIS inclusive cross section, we will consider the underlying process of an electron-quark scattering which at LO can be calculated within perturbative QED. An electron e^- with a four-momentum k interacts with a quark q_f (being a point-like constituent of a proton with the four-momentum P) with a four-momentum p through the exchange of a virtual photon γ^* with a four-momentum $q = k - k'$ which is transferred from the electron to the quark. The outgoing particles are an electron with four momentum k' and a quark of the same flavour as the incoming one with the four-momentum $p' = p + q$. The LO diagram contributing to the DIS is shown in fig. 2.2.
It is assumed that the quark and proton are collinear, the quark carries a fraction ξ of the proton momentum $p = \xi P$. The DIS cross section is given by the cross section of the electron-quark scattering, multiplied by a probability density $f_f(\xi)$ that a proton contains a quark of a flavour f with momentum fraction ξ, integrated over all possible ξ and summed over all possible quark flavours f [16]

$$\sigma\left(e^-(k) + \text{proton}(P) \to e^-(k') + X\right) = \int_0^1 \mathrm{d}\xi \sum_f f_f(\xi)\sigma\left(e^-(k) + q_f(\xi P) \to e^-(k') + q_f(p')\right). \quad (2.2)$$

The functions $f_f(\xi)$, called *parton distribution functions* (PDFs) or *collinear* PDFs, cannot be computed from the rules of perturbative QCD since they contain also non-perturbative information on hadron structure and they must be extracted from experiments.

The LO differential cross section for electron-quark scattering is given by the formula [16]

$$\frac{\mathrm{d}\sigma}{\mathrm{d}\hat{t}}\left(e^- q_f \to e^- q_f\right) = \frac{2\pi\alpha^2 Q_f^2}{\hat{s}^2}\left(\frac{\hat{s}^2 + \hat{u}^2}{\hat{t}^2}\right) \quad (2.3)$$

where Q_f is electric charge of a quark in units of e , α is the QED coupling and $\hat{s}, \hat{u}, \hat{t}$ are the Mandelstam variables for two body scattering at the parton level. In DIS, the Mandelstam variables are given by

$$\begin{aligned} \hat{s} &= (p+k)^2 = 2p\cdot k = 2\xi P\cdot k = \xi s \\ \hat{t} &= q^2 \equiv -Q^2 \end{aligned} \quad (2.4)$$

where $\hat{s}$ is the center of mass energy of the electron-quark system, $s = (P+k)^2$ is the center of mass energy of the electron-proton system, the masses of proton, quark and electron are set to zero $P^2 = p^2 = k^2 = 0$

and the relation for Mandalstam variables is $\hat{s}+\hat{t}+\hat{u}=0$. The variable Q^2 is called the *virtuality* of the photon. Moreover, the following variables are defined in the literature to describe DIS

$$\begin{aligned} x &= \frac{Q^2}{2P\cdot q}, \\ y &= \frac{P\cdot q}{P\cdot k} \end{aligned} \tag{2.5}$$

where x is the so-called *Bjorken* x and y is a dimensionless variable equal to the fraction of electron's energy transferred to the proton in the proton's rest frame. The following relation holds for Q, x, y and s: $Q^2 = xys$. Using the above defined variables, the differential cross section for DIS, eq. (2.2), can be rewritten

$$\frac{\mathrm{d}\sigma}{\mathrm{d}\xi \mathrm{d}Q^2} = \sum_f f_f(\xi) Q_f^2 \frac{2\pi\alpha^2}{Q^4}\left(1+(1-y)^2\right) \ . \tag{2.6}$$

The outgoing quark is on mass-shell $p'^2 = 0$ so the following relation holds

$$p'^2 = (p+q)^2 = p^2 + q^2 + 2p\cdot q = -Q^2 + \frac{Q^2\xi}{x} = Q^2(\xi/x - 1) = 0 \ . \tag{2.7}$$

Thus $\xi = x$ and Bjorken x is the longitudinal fraction of the proton's momentum carried by the parton. In the calculation above the definition of Bjorken x with the substitution $P = p/\xi$ was used.

The DIS cross section for the electron proton scattering can be parametrized in the following way [1]

$$\frac{\mathrm{d}^2\sigma}{\mathrm{d}x\mathrm{d}Q^2} = \frac{4\pi\alpha^2}{Q^4}\left(\frac{1+(1-y)^2}{2}\frac{F_2\left(x,Q^2\right)}{x} + \frac{(1-y)}{x}\left(F_2\left(x,Q^2\right) - 2xF_1\left(x,Q^2\right)\right)\right) \tag{2.8}$$

where the mass of the proton is neglected and Q^2 is much lower than the mass of the Z boson $Q^2 \ll M_Z^2$. The formula is a consequence of electromagnetic current conservation and symmetry arguments [15]. The functions F_1 and F_2 parametrize the interaction of the virtual photon with the proton, i.e. the whole QCD physics in DIS. This parametrization agrees with eq. (2.6) after identifying

$$F_2\left(x,Q^2\right) = \sum_f x f_f(x) Q_f^2 \tag{2.9}$$

and

$$F_2\left(x,Q^2\right) = 2xF_1\left(x,Q^2\right) \ . \tag{2.10}$$

The functions F_1 and F_2 are the so-called *structure functions*. Eq. (2.10) is called *Callan - Gross* relation and it is a consequence of the fact that the spin of the quarks is 1/2 [27]. The relation is true for massless quarks, without intrinsic transverse momenta. When QCD corrections are taken into account, it is violated.
By dividing eq. (2.8) by a factor $\frac{2\pi\alpha^2}{xQ^4}\left(1+(1-y)^2\right)$ one obtains the formula for the *reduced cross section* σ_r, which is equal to F_2 at low Q^2 and not very large y [28]. At LO this function is independent of Q^2. This feature is called *Bjorken scaling*. The reduced cross section is shown in fig. 2.3 as a function of Q^2 for different values of x . The figure shows that the Bjorken scaling, being deduced from the Parton Model, is a very good approximation at large (but not very large) x and not very large Q^2. This is the region explored by the first DIS measurements at Stanford Linear Accelerator Center (SLAC) [29, 30].
For smaller x and very large x one can clearly see the violation of Bjorken scaling which comes from higher order contributions to DIS. This issue is the subject of the next section.

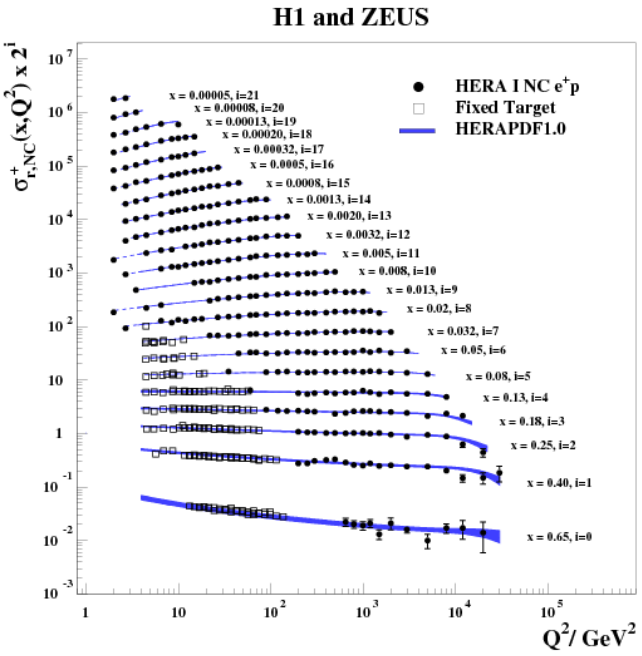

Figure 2.3: The HERA measurement of neutral current e^+p reduced cross section σ_r vs Q^2 for different values of x. Figure from [28].

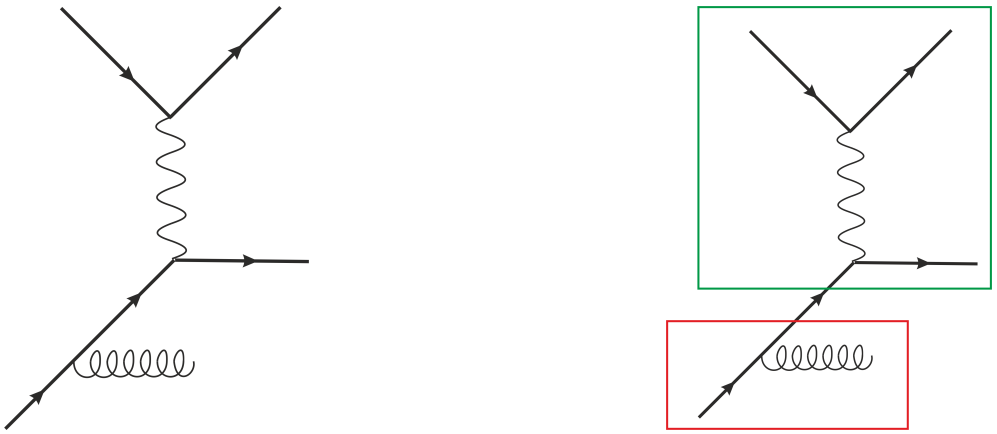

(a) Quark emits a gluon before entering the hard interaction.

(b) The cross section factorizes into a two pieces marked with the colour frames.

Figure 2.4: One of the higher order contributions to DIS.

2.2 | Introduction to the DGLAP evolution equation

The LO DIS cross section from eq. (2.8), discussed in the previous section, is proportional to the second power of the QED coupling α^2. Now we would like to concentrate on the QCD corrections. One example of the QCD corrections to DIS comes from the diagram shown in fig. 2.4a where a quark, being a proton's constituent, emits a gluon before the interaction with the virtual photon. Such a diagram gives the contribution proportional to the QCD running coupling α_s.

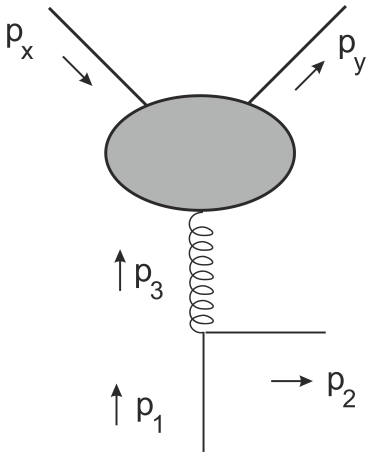

(a) General process in which a quark splits into a quark and gluon. Gluon continues the evolution and enters the hard process.

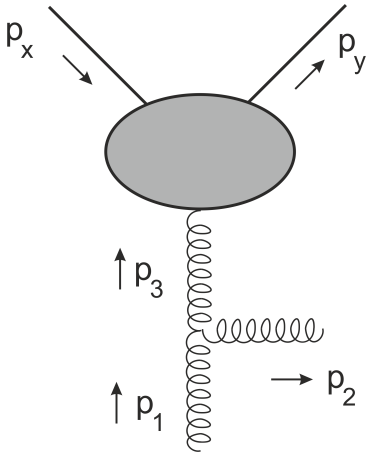

(b) General process in which a gluon emits a gluon before entering the hard process.

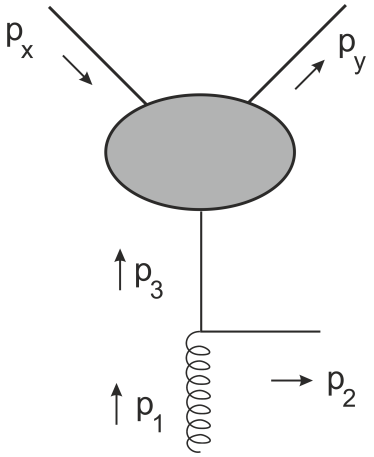

(c) General process in which a gluon splits into a quark pair. One of the quarks continues the evolution and enters the hard process.

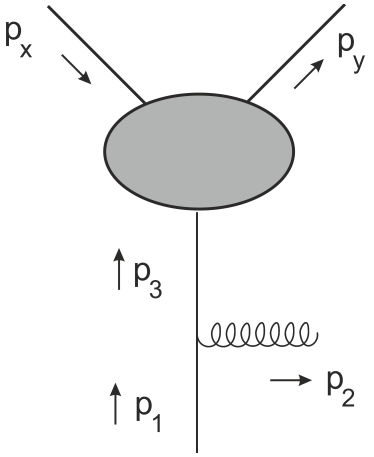

(d) General process in which a quark emits a gluon before entering the hard process.

Figure 2.5: General processes in which a parton splits before entering the hard interaction.

2.2.1 | QCD corrections: factorization of the process

The cross section for DIS including also the gluon radiation can be factorized in the collinear limit (when it is assumed that the angle between beam axis and emitted gluon is small) into two parts calculated separately, as shown in the fig. 2.4b [1, 17]. The part marked with the green frame is the LO electron-quark scattering for which the matrix element was given in the previous section. The part marked with the red frame corresponds to the splitting of an initial quark into a gluon and a quark.

One can imagine a more general process, in which the parton 1 (being the proton constituent) splits before the interaction into the particles 2 and 3. The particle 3 enters the interaction with another initial particle X. Y is the final state of the interaction. The processes to be considered here are shown in fig. 2.5, where the interaction with large momentum transfer is denoted with the gray circle and it is not necessarily DIS.

The formula to compute the cross sections from fig. 2.5 is given by [16]

$$\begin{aligned}\sigma_{1+X\to 2+Y} &= \frac{N_s}{2\sqrt{\lambda((p_X+p_1)^2,m_1,m_X)}}\int |\mathrm{ME}_{1+X\to 2+Y}|^2(2\pi)^4\delta^{(4)}(p_1+P_X-p_2-p_Y)\times \\ &\times \prod_{j=2,Y}\frac{1}{(2\pi)^3}\frac{\mathrm{d}^3p_j}{2|\overrightarrow{p}_j|}\end{aligned} \tag{2.11}$$

where N_s is a symmetry factor when the final state consists of identical particles, $\lambda(x,y,z)=x^2+y^2+z^2-2(xy+xz+yz)$, $m_1=m_X=0$ are the masses of the initial particles (quark and electron in fig. 2.4a), and the momenta are explained in figures. The four-momenta of the particles 1 and X do not have a transverse component and are given by

$$\begin{aligned}p_1 &= (p,0,0,p)\,, \\ p_X &= (E_X,0,0,-E_X)\,.\end{aligned} \tag{2.12}$$

With this choice $\sqrt{\lambda((p_X+p_1)^2,0,0)}=4pE_X$.
In the collinear limit the matrix element factorizes in the following way [1, 16, 17]

$$|\mathrm{ME}_{1+X\to 2+Y}|^2 = |\mathrm{ME}_{3+X\to Y}|^2|\mathrm{ME}_{1\to 2+3^*}|^2\mathcal{P}_3^2 \tag{2.13}$$

where $\mathrm{ME}_{3+X\to Y}$ is a matrix element for the interaction of the particles 3 and X producing the final state Y, $\mathcal{P}_3$ is the propagator of the particle 3 which can be a gluon or a quark and $\mathrm{ME}_{1\to 2+3^*}$ is the matrix element for the splitting of the particle 1 into the particles 2 and 3. It is important to notice that in this approximation, when $\mathrm{ME}_{3+X\to Y}$ is calculated, the incoming particle 3 is taken to be on-shell, but during the calculation of $\mathrm{ME}_{1\to 2+3^*}$ it is assumed that particle 3 is slightly off-shell.

The cross section $\sigma_{3+X\to Y}$ is given by

$$\sigma_{3+X\to Y} = \frac{N_s}{2\sqrt{\lambda((p_X+p_3)^2,0,0)}}\int |\mathrm{ME}_{3+X\to Y}|^2(2\pi)^4\delta^{(4)}(p_3+p_X-p_Y)\prod_{j=Y}\frac{1}{(2\pi)^3}\frac{\mathrm{d}^3p_j}{|\overrightarrow{p}_j|}\,. \tag{2.14}$$

Assuming that $m_3=m_X=0$ and ignoring the transverse component of p_3 (which is a good approximation because p_3 is only slightly off-shell and is important only in the propagator [16], see also Sec. (A.2) and eq. (2.17) where the full expressions for 4-momenta are given) we obtain $\sqrt{\lambda((p_X+p_3)^2,m_3,m_X)}=4zpE_X$. With that, eq. (2.11) can be evaluated in the following way

$$\sigma_{1+X\to 2+Y} = \int \sigma_{3+X\to Y}|\mathrm{ME}_{1\to 2+3^*}|^2 z\mathcal{P}_3^2\frac{1}{(2\pi)^3}\frac{\mathrm{d}^3p_2}{2|\overrightarrow{p}_2|}\,. \tag{2.15}$$

In Appendix (A.2) the matrix element for $|\mathrm{ME}_{1\to 2+3^*}|^2$, in the case when the particle 3 is a slightly off-shell gluon with momentum fraction z, is calculated. Here just the final expression (eq. (A.26)) is quoted

$$|\mathrm{ME}_{1\to 2+3^*}|^2 = 8\pi\alpha_s C_F\frac{p_\perp^2}{z^2}\left(\frac{1+(1-z)^2}{1-z}\right) \tag{2.16}$$

where $C_F=T_F\frac{N^2-1}{N}$, N being the number of SU(N) generators, $N=3$ in SU(3) and $T_F=\frac{1}{2}$. The quark and gluon four-momenta are

$$\begin{aligned}p_2 &= ((1-z)p,-p_\perp,(1-z)p-\frac{p_\perp^2}{2(1-z)p}), \\ p_3 &= (zp,p_\perp,zp+\frac{p_\perp^2}{2(1-z)p})\end{aligned} \tag{2.17}$$

with the convention $p^\mu = (p^0, \overrightarrow{p}) = (p^0, p_\perp, p^3)$. The gluon propagator is

$$\mathcal{P}_3^2 = \left(\frac{1}{p_3^2}\right)^2 = \frac{(1-z)^2}{p_\perp^4} \,. \tag{2.18}$$

Combining eq. (2.15)-(2.18) and using $\mathrm{d}^3 p_2 = \pi p \mathrm{d}p_\perp^2 \mathrm{d}z$ the cross section formula for the process shown in fig. 2.5a is obtained:

$$\sigma_{1+X\to 2+Y} = \frac{\alpha_s}{2\pi} C_F \int \sigma_{3+X\to Y} \frac{\mathrm{d}p_\perp^2}{p_\perp^2} \mathrm{d}z \frac{1+(1-z)^2}{z} \,. \tag{2.19}$$

The integral over $p_\perp^2$ runs from 0 up to some maximum scale μ^2, called *factorization scale* (which cannot be larger then s). One can clearly see that this integral is divergent and some cut off on the initial scale μ_0^2 (which is $\mathcal{O}(\Lambda)$) must be introduced. From that one gets the final result for the cross section in fig. 2.5a

$$\sigma_{1+X\to 2+Y} = \frac{\alpha_s}{2\pi} C_F \int \sigma_{3+X\to Y} \mathrm{d}z \ln\left(\frac{\mu^2}{\mu_0^2}\right) \frac{1+(1-z)^2}{z} \,. \tag{2.20}$$

This allows an interpretation that the cross section $\sigma_{1+X\to 2+Y}$ of the process depicted in fig. (2.5a) is equal to the cross section $\sigma_{3+X\to Y}$ times the probability that the initial quark will split into a gluon and a quark. Analogous interpretations hold for all processes in fig. 2.5.

2.2.2 | Evolution and LO splitting functions

One can imagine that the splitting processes from fig. 2.5 take place continuously and before a parton enters the hard interaction many splittings happen. This cascade of splittings is called *initial state radiation* and it is sketched in fig. 2.6.

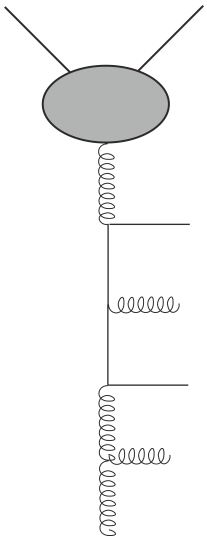

Figure 2.6: The splittings inside the proton take place continuously.

It is interesting to look at the transverse momenta of the partons propagating in the cascade in fig. 2.6. For this purpose let us assume we have two branchings, as shown on the left hand side of fig. 2.7. In the collinear approximation one can factorize the matrix element for this process in an analogous way as in fig. 2.4b, dividing the process from fig. 2.7 into a matrix element from fig. 2.5d and the matrix element for the gluon emission. To do so one assumes that the particle which undergoes the splitting is

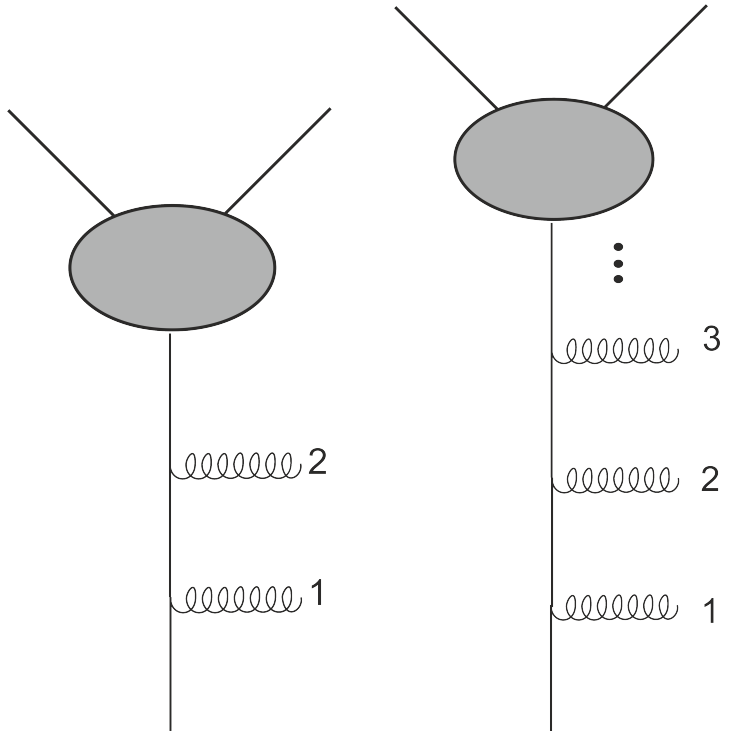

Figure 2.7: The event with two branchings and with many branchings.

on mass-shell compared to the produced particles and the angle of the emission of the produced particle with respect to the beam line is small. If $p_{2\perp}^2 \gg p_{1\perp}^2$ the virtuality of the quark between the particles 1 and 2 is very small compared to the virtuality of the quark which enters the interaction and it can be ignored while computing the emission of the particle 2. The integral over the transverse momenta gives then the factor

$$\left(\frac{\alpha_s}{2\pi}\right)^2 \int_{\mu_0^2}^{\mu^2} \frac{\mathrm{d}p_{2\perp}^2}{p_{2\perp}^2} \int_{\mu_0^2}^{p_{2\perp}^2} \frac{\mathrm{d}p_{1\perp}^2}{p_{1\perp}^2} = \left(\frac{\alpha_s}{2\pi}\right)^2 \frac{1}{2} \ln^2\left(\frac{\mu^2}{\mu_0^2}\right) \tag{2.21}$$

where the α_s^2 term is multiplied by a logarithm which can be large when the difference between the scales μ_0^2 and μ^2 is large. In the opposite case, when $p_{1\perp}^2 \gg p_{2\perp}^2$ or when $p_{2\perp}^2 \approx p_{1\perp}^2$ one can not assume that the particle which undergoes the splitting, is on the mass-shell compared to the produced particles when calculating the next emission, and the collinear approximation is broken. Moreover, even if we still use the same formalism to compute the cross section, we find that if the emission of the particle 1 involved larger transverse momenta than the emission of the particle 2, the emission of the particle 2 does not change much the cross section. The contribution coming from it can be neglected so that there is at least one power of the large logarithm $\ln\left(\frac{\mu^2}{\mu_0^2}\right)$ less at a given order of α_s. That is why in this approximation the main contribution comes from partons *strongly ordered* in transverse momenta for which $p_{2\perp}^2 \gg p_{1\perp}^2$. This result can be generalised to the case with n emissions (fig. 2.7 right). If the momenta are ordered in the following way

$$p_{1\perp}^2 \ll p_{2\perp}^2 \ll p_{3\perp}^2 \ll ... \tag{2.22}$$

then the contribution from these emissions is proportional to

$$\left(\frac{\alpha_s}{2\pi}\right)^n \frac{1}{n!} \ln^n\left(\frac{\mu^2}{\mu_0^2}\right) \ . \tag{2.23}$$

The interaction is called *hard interaction* because the particle, which enters the interaction, has higher

transverse momentum than all the previous particles in the cascade.

From the discussion above the following interpretation arises: it is known from the Rayleigh criterion in optics that one can distinguish two points which are separated by a distance r when the following relation holds

$$r = A\lambda \,, \tag{2.24}$$

where λ is the wavelength with which one wants to probe the object and A is a constant describing the properties of the apparatus used for the observation (for example for a microscope it involves the diameter of the lens and focal length of the objective). To distinguish the emitted and propagating partons in the cascade, it is necessary to resolve transverse distances between them. To resolve partons with a transverse momentum smaller than some $p_\perp$, one needs a probe with a wavelength of the order of $1/p_\perp$. It means that by using a probe with smaller wavelength one can resolve more partons at smaller distances inside a proton than with a probe with bigger wavelength. That is the reason why DIS is very often compared to a microscope: it serves to probe, using the virtual photon (or another exchanged particle), the structure of the proton. The photon's virtuality can be considered as the resolution scale of the process: a photon with virtuality Q^2 can probe distances inside the proton of order $1/Q$ and it can resolve particles with virtualities of the same order. Partons which are emitted with a $p_\perp$ smaller than a certain value given by a resolution scale, are *non-resolvable*. This feature is illustrated in fig. 2.8 [15].

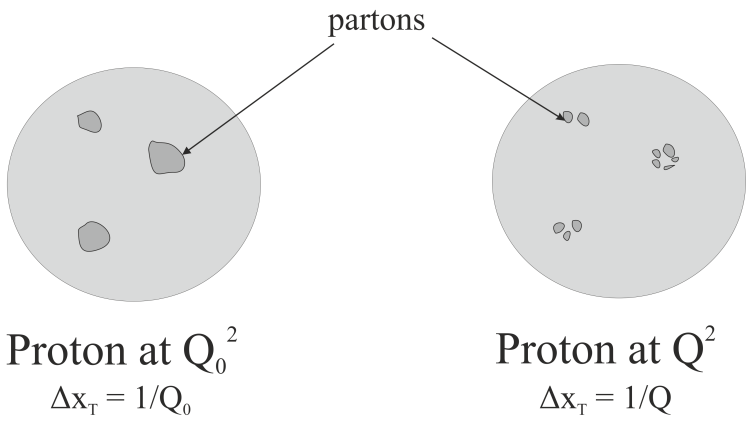

Figure 2.8: Virtual photon with a higher virtuality Q^2 can resolve more partons inside the proton than a photon with lower virtuality Q_0^2.

One can ask then the question what happens with the parton distribution when the scale μ^2 changes by a small amount from μ^2 to $\mu^2 + \Delta\mu^2$. The probability that the quark of a flavour i carrying a momentum fraction x' at scale μ^2 will split into a gluon at the scale $\mu^2 + \Delta\mu^2$ with momentum fraction x is then given by

$$\int_0^1 \mathrm{d}x' \int_0^1 \mathrm{d}z \frac{\alpha_s}{2\pi} C_F \frac{\Delta\mu^2}{\mu^2} \frac{1+(1-z)^2}{z} f_{q_i}(x', \mu^2) \delta(x - zx') \Theta(x' - x) \tag{2.25}$$

where $f_{q_i}(x', \mu^2)$ is the probability to find inside a proton at a scale μ^2 a quark of flavour i with energy fraction $x' > x$, where x is the momentum fraction of the considered final gluon at the scale $\mu^2 + \Delta\mu^2$. The delta function $\delta(x - zx')$ is the energy-momentum conservation condition, z is the splitting variable and $\Theta(x' - x)$ is the Heaviside step function to guarantee that the parent parton has higher momentum

fraction than the daughter one. It can also happen that inside the proton there is a gluon at the scale μ^2 and it will not split up at a scale $\mu^2 + \Delta\mu^2$. The probability to find a gluon with the proton's momentum fraction x at scale $\mu^2 + \Delta\mu^2$ is then given by

$$f_g(x, \mu^2 + \Delta\mu^2) = f_g(x, \mu^2) + \int_0^1 \mathrm{d}x' \int_0^1 \mathrm{d}z \frac{\alpha_s}{2\pi} C_F \sum_i \frac{\Delta\mu^2}{\mu^2} \frac{1 + (1-z)^2}{z} f_{q_i}(x', \mu^2) \delta(x - zx') \Theta(x' - x) \tag{2.26}$$

and it can be rewritten in a form of an integro-differential equation

$$\frac{\mathrm{d}f_g(x, \mu^2)}{\mathrm{d}\mu^2} = \int_0^1 \mathrm{d}x' \int_0^1 \mathrm{d}z \frac{\alpha_s}{2\pi} C_F \sum_i \frac{1}{\mu^2} \frac{1 + (1-z)^2}{z} f_{q_i}(x', \mu^2) \delta(x - zx') \Theta(x' - x). \tag{2.27}$$

The piece $\frac{\alpha_s}{2\pi} C_F \frac{1+(1-z)^2}{z}$ is called a *real* part of a leading order (LO) quark - gluon *splitting function* because it describes the splitting

$$P^R_{gq}(z, \mu^2) = \frac{\alpha_s}{2\pi} C_F \frac{1 + (1-z)^2}{z} \tag{2.28}$$

and it has a probabilistic interpretation that a quark at the scale μ^2 will undergo the splitting into a gluon with a momentum fraction z of the parent quark. It is the same for all quark flavours so $P_{gq_i} \equiv P_{gq}$.

The splitting function $P^R_{gq}(z, \mu^2)$ is divergent when $z \to 0$. This corresponds to the situation when the gluon entering the hard interaction has an energy $\to 0$. On the other hand, to be able to use perturbative QCD in the calculation, some minimum scale of the hard process $\hat{s}$ has to be assumed. To be able to study such a process with a gluon at very low x, the energy of the incoming beams must be very large. The formalism, which is being described in this section, leading to the DGLAP equation (see later in this section), is not a good description in the limit of $s \to \infty$ or equivalently $x \to 0$. There must be some small cut off on the value of z protecting against situation when $s \to \infty$. Nevertheless, there are other formalisms (like BFKL equation [31–34]), which are more appropriate in the region of small x.

Up to now only the splitting of a quark into a gluon was considered. But as one can see from fig. 2.5, it is also possible that a gluon splits into gluon pair and this process contributes to the gluon distribution.

The real part of the LO gluon-gluon splitting function, the one visualised in fig. 2.5b, is given by the formula

$$P^R_{gg}(z, \mu^2) = \frac{\alpha_s}{2\pi} 2C_A \left(\frac{1-z}{z} + \frac{1}{1-z} + z(1-z) - 1 \right) \tag{2.29}$$

where $C_A = N_C = 3$ is the number of colours. This equation is divergent when $z \to 0$ and $z \to 1$. The first divergency was already discussed in the case of P^R_{gq}. The second divergency corresponds to the case, when the energy of the emitted gluon (particle 2 in fig. 2.5b) is very small. It is also the case when the transverse momentum of the gluon 2 is very small. Such gluons with $p_2^\mu \to 0$ are called *soft gluons*. One needs to find a way to regularize this singularity. Additionally, in the case of gluon splitting into a gluon there are also virtual corrections, shown in fig. 2.9a, which must be included. Such virtual contributions affect the region of $z = 1$ because they do not change the momentum fraction. They can be computed from the diagrams or from unitarity arguments (for more details see e.g. [1, 15]). The full expression for the gluon-gluon splitting function is given by

$$P_{gg}(z, \mu^2) = \frac{\alpha_s}{2\pi} 2C_A \left(\frac{1}{(1-z)_+} + \frac{1-z}{z} + z(1-z) - 1 \right) + \left(\frac{11}{6} C_A - \frac{2}{3} T_R n_f \right) \delta(1-z) \tag{2.30}$$

where $T_R = \frac{1}{2}$, n_f is the number of active flavours. The *plus prescription* is defined in the following way for any test function φ

$$\int_0^1 \frac{1}{(1-z)_+} \varphi(z)\, dz = \int_0^1 \frac{1}{1-z} [\varphi(z) - \varphi(1)]\, dz\ . \tag{2.31}$$

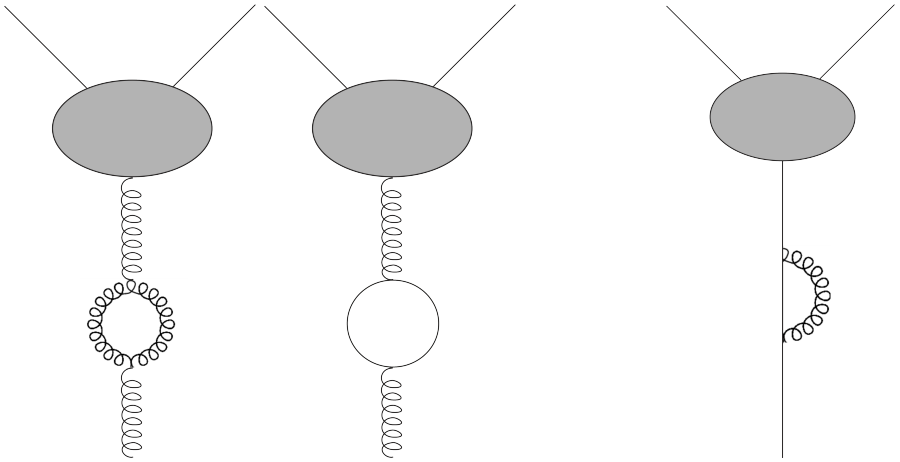

(a) Virtual contributions to the LO gluon distribution function.

(b) Virtual contributions to the LO quark distribution function.

Figure 2.9: LO virtual contributions to the DIS process.

It is important to mention that in the cross section calculations the divergences from soft and collinear (when the angle of the emission goes to zero) emissions and virtual corrections cancel exactly via Bloch, Nordsieck [35] and Konoshita, Lee, Nauenberg [36, 37] theorems for suitable defined inclusive quantities. For exclusive quantities the cancellation is not exact. The contribution, which is not cancelled, can be potentially large and it needs to be additionally resummed to obtain proper cross section prediction.

With this result, the full equation for a gluon distribution function can be written as

$$\frac{\mathrm{d}f_g(x,\mu^2)}{\mathrm{d}\mu^2} = \int_0^1 \mathrm{d}x' \int_0^1 \mathrm{d}z \frac{1}{\mu^2} \left(\sum_i P_{gq}(z,\mu^2) f_{q_i}(x',\mu^2) + P_{gg}(z,\mu^2) f_g(x',\mu^2) \right) \delta(x - zx') \Theta(x' - x) \tag{2.32}$$

where, to make the notation consistent, the following relation was used

$$P^R_{gq}(z,\mu^2) = P_{gq}(z,\mu^2) \tag{2.33}$$

because there are no virtual corrections to be accounted for at LO for the splitting of a quark into a gluon.

Now we can discuss the quark distribution corresponding to fig. 2.5c and fig. 2.5d. The LO real part of the splitting function of a gluon into a quark (shown in fig. 2.5c) is given by

$$P^R_{qg}(z,\mu^2) = \frac{\alpha_s}{2\pi} T_R \left(z^2 + (1-z)^2 \right) \ . \tag{2.34}$$

This expression is not divergent and there are no virtual contributions at LO so $P^R_{qg}(z,\mu^2) = P_{qg}(z,\mu^2)$.

The case of quark-quark splitting is similar to gluon-gluon case. The real part of the LO quark-quark splitting function (fig. 2.5d) is given by

$$P^R_{qq}(z,\mu^2) = \frac{\alpha_s}{2\pi} C_F \left(\frac{1+z^2}{1-z} \right) \ . \tag{2.35}$$

This expression is divergent when $z \to 1$ which corresponds again to the emission of a soft gluon. Similarly, as in the gluon-gluon splitting case, there are also virtual corrections shown in fig. 2.9b, which

have to be taken into account. The full P_{qq} splitting function is then

$$P_{qq}(z,\mu^2) = \frac{\alpha_s}{2\pi} C_F \left(\frac{1+z^2}{(1-z)_+} + \frac{3}{2}\delta(1-z) \right) . \tag{2.36}$$

Fig. 2.5d and fig. 2.9b show that at LO a quark can split only into a quark of the same flavour.

It is worth to draw the diagrams contributing to the LO splitting functions as the amplitudes squared as shown in fig. 2.10 for quark - quark splitting. One can notice that these diagrams contain 1 loop. That is why the LO splitting functions are very often called 1-*loop* splitting functions.

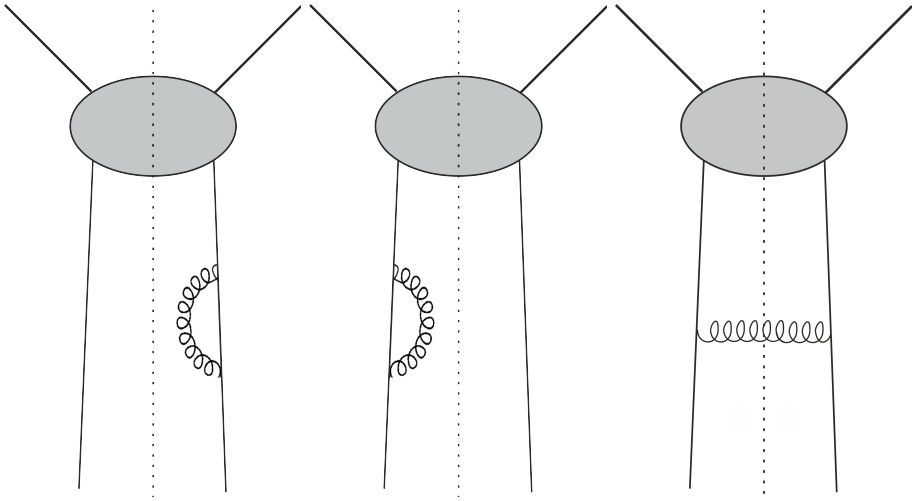

Figure 2.10: The amplitude squared diagrams contributing to quark - quark splitting function at LO.

The evolution equation for a quark density can be written now in an analogous form as eq. (2.32)

$$\frac{\mathrm{d}f_q(x,\mu^2)}{\mathrm{d}\mu^2} = \int_0^1 \mathrm{d}x' \int_0^1 \mathrm{d}z \frac{1}{\mu^2} \left(P_{qg}(z,\mu^2) f_g(x',\mu^2) + P_{qq}(z,\mu^2) f_q(x',\mu^2) \right) \delta(x - zx') \Theta(x'-x) . \tag{2.37}$$

Both eq. (2.32) and eq. (2.37) can be put together in a compact form

$$\frac{\mathrm{d}f_i(x,\mu^2)}{\mathrm{d}\ln\mu^2} = \sum_j \int_x^1 \frac{\mathrm{d}z}{z} P_{ij}(\mu^2,z) f_j(x/z,\mu^2) , \tag{2.38}$$

where i,j denote quarks and antiquarks flavours (we have n_f quark flavours which can depend on the evolution scale so $n_f \equiv n_f(\mu^2)$) or gluons. This is the famous *Dokshitzer-Gribov-Lipatov-Altarelli-Parisi (DGLAP) evolution equation* [38–41] which describes the *evolution* of parton distribution functions $f_i(x,\mu^2)$ with the scale μ^2. The initial distributions cannot be calculated using the perturbative QCD but they have to be determined from the measurements, for example in the DIS experiments by measuring the cross section at a given value of Q^2. The predictions for inclusive reduced cross section σ_r vs x for a given Q^2 compared to the data coming from H1 and ZEUS are shown in fig. 2.11 [42]. The DGLAP equation explains the Bjorken scaling violation observation. If the initial distribution $f_i(x,\mu_0^2)$ is known then one can obtain the distribution at another scale $f_i(x,\mu^2)$ using the DGLAP equation, as illustrated in fig. 2.12.

Very often, instead of parton distributions, momentum-weighted parton distribution functions are used $\widetilde{f}_a$,

$$\widetilde{f}_a(x,\mu^2) \equiv x f_a(x,\mu^2) \ , \tag{2.39}$$

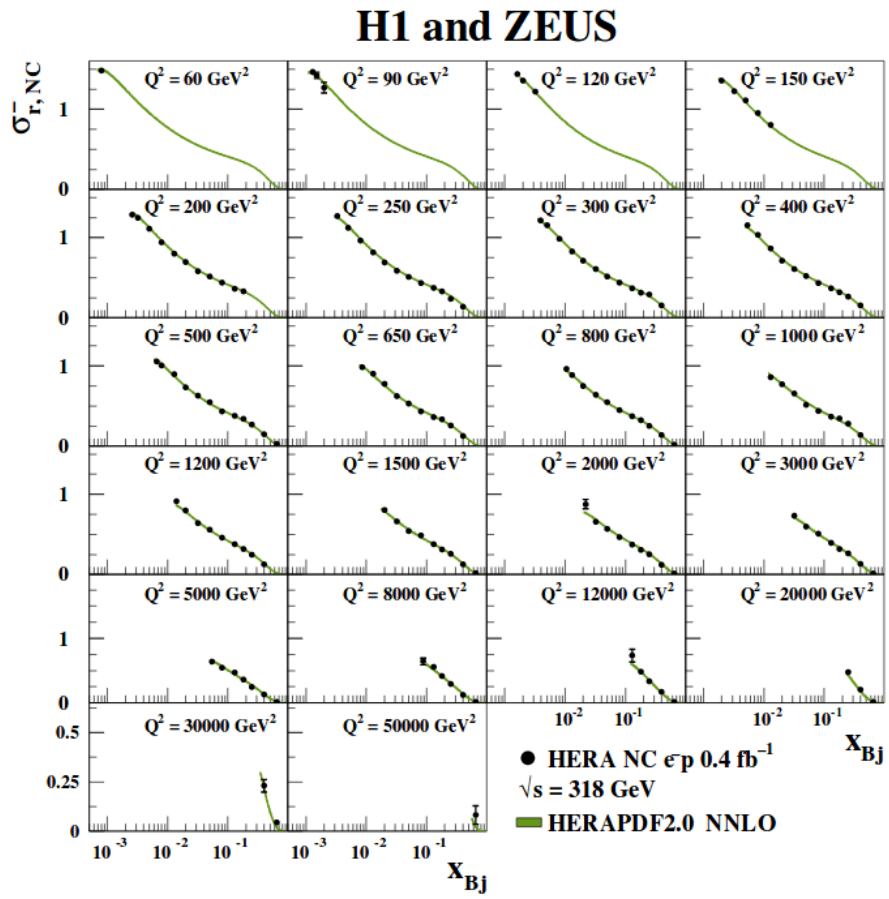

Figure 2.11: The combined HERA data for the inclusive reduced cross sections vs x for different values of Q^2 measured at $\sqrt{s} = 318$ GeV compared to the predictions from HERAPDF2.0 NNLO [42].

for which the evolution equation has the form

$$\frac{d\,\widetilde{f}_a(x,\mu^2)}{d\ln\mu^2} = \sum_b \int_x^1 dz\; P_{ab}(\mu^2, z)\; \widetilde{f}_b(x/z, \mu^2)\;\; . \tag{2.40}$$

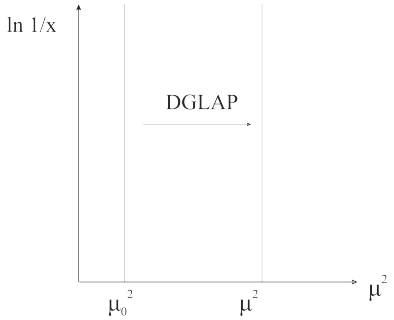

Figure 2.12: The DGLAP evolution equation evolves the parton distribution functions in μ^2.

Up to now we said nothing about the running coupling. It is a feature of QCD that α_s depends on the *renormalization scale*. The easiest choice is to set μ^2, which is the only scale in the processes discussed up to now, as the scale in α_s:

$$\alpha_s \equiv \alpha_s(\mu^2)\;. \tag{2.41}$$

2.2.3 | Sum rules in DGLAP

In Sec. (2.2.2) in eq. (2.36) we presented the formula for the P_{qq} splitting function which includes the real splittings and virtual corrections. The virtual corrections can be computed from the diagrams using the Feynman rules, but there is a trick with which the answer can be obtained much faster [40]. It uses the *quark number conservation rule* (i.e. baryon number conservation). Let us define the net (non-singlet) number of quarks and antiquarks of a given flavour i as

$$f(x,\mu^2)^{\mathrm{NS}}_{q_i} = f_{q_i}(x,\mu^2) - f_{\overline{q}_i}(x,\mu^2)\,. \tag{2.42}$$

Such distribution evolves only according to P_{qq} splitting function. It is because the splitting of P_{qg} contributes equally to the quark and antiquark distribution. Let us concentrate for a moment on the P_{qq} piece of eq. (2.37). We can rewrite it in a following way

$$f_{q_i}\left(x,\mu^2\right)+\Delta f_{q_i}\left(x,\mu^2\right) = \int_0^1 \mathrm{d}x' \int_0^1 \mathrm{d}z \left(\delta(1-z)+\ln\left(\frac{\mu^2}{\mu_0^2}\right) P_{qq}\left(z,\mu^2\right)\right) f_{q_i}\left(x',\mu^2\right)\delta(x-zx')\Theta(x'-x) \tag{2.43}$$

where $\Delta f_{q_i}\left(x,\mu^2\right) = f_{q_i}\left(x,\mu^2\right) - f_{q_i}\left(x,\mu_0^2\right)$. The piece $\mathcal{P}_{qq} = \delta(1-z)+\ln\left(\frac{\mu^2}{\mu_0^2}\right) P_{qq}\left(z,\mu^2\right)$ can be interpreted as a probability density to find inside a quark another quark with a fraction z of the momentum of the mother quark. The piece with $\delta(1-z)$ corresponds to the situation when the quark distribution does not change and it includes the virtual corrections. The probability density $\mathcal{P}_{qq}$ integrated over z has to give 1. Thus the integral over the quark-quark splitting function should give 0 [1, 17]

$$\int_0^1 \mathrm{d}z P_{qq}(z,\mu^2) = 0\,. \tag{2.44}$$

The straightforward way of taking into account eq. (2.44) in eq. (2.35) is to replace

$$\frac{\alpha_s}{2\pi} C_F \left(\frac{1+z^2}{1-z}\right) \to \frac{\alpha_s}{2\pi} C_F \left(\frac{1+z^2}{1-z}\right)_+\,. \tag{2.45}$$

Using eq. (2.44), eq. (2.45) it can be rewritten in a form of eq. (2.36).

Let us also discuss briefly one of the rules satisfied by the parton densities, which is especially important in this thesis: the *momentum sum rule for the splitting functions*. To begin with, we notice that the sum over momentum fractions of all partons inside proton should be equal to 1

$$\int_0^1 \mathrm{d}x\, x \sum_i\, f_i(x,\mu^2) = 1\,. \tag{2.46}$$

Integrating eq. (2.38) between μ_0^2 and μ^2 gives

$$f_i(x,\mu^2) = f_i(x,\mu_0^2) + \int_{\mu_0^2}^{\mu^2} \mathrm{d}\ln\mu_1^2 \sum_j \int_x^1 \frac{\mathrm{d}z}{z} P_{ij}(\mu_1^2,z) f_j\left(\frac{x}{z},\mu_1^2\right). \tag{2.47}$$

This can be inserted into eq. (2.46)

$$\int_0^1 \mathrm{d}x x \sum_i\, f_i(x,\mu^2) = \int_0^1 \mathrm{d}x x \sum_i \left[f_i(x,\mu_0^2) + \int_{\mu_0^2}^{\mu^2} \mathrm{d}\ln\mu_1^2 \sum_j \int_x^1 \frac{\mathrm{d}z}{z} P_{ij}(\mu_1^2,z) f_j\left(\frac{x}{z},\mu_1^2\right)\right] = 1\,. \tag{2.48}$$

The momentum sum rule is fulfilled at every scale, also at μ_0^2 which results in $\int_0^1 \mathrm{d}x x \sum_i\, f_i(x,\mu_0^2) = 1$. It means that the second part of the eq. (2.48) must be equal to 0. With the change of the integration variable from x to $a = \frac{x}{z}$ one obtains

$$\sum_i \int_{\mu_0^2}^{\mu^2} \mathrm{d}\ln\mu_1^2 \sum_j \int_0^1 \mathrm{d}x \int_x^1 \mathrm{d}z P_{ij}(\mu_1^2,z) \frac{x}{z} f_j\left(\frac{x}{z},\mu_1^2\right)$$

$$
\begin{aligned}
&= \sum_i \int_{\mu_0^2}^{\mu^2} \mathrm{d}\ln\mu_1^2 \sum_j \int_0^1 \mathrm{d}z \int_0^z \mathrm{d}x P_{ij}(\mu_1^2, z) \frac{x}{z} f_j\left(\frac{x}{z}, \mu_1^2\right) \\
&= \sum_i \int_{\mu_0^2}^{\mu^2} \mathrm{d}\ln\mu_1^2 \sum_j \int_0^1 \mathrm{d}z z P_{ij}(\mu_1^2, z) \int_0^1 \mathrm{d}a a f_j\left(a, \mu_1^2\right) \\
&= 0.
\end{aligned} \tag{2.49}
$$

This equality must be always true so

$$
\sum_i \int_0^1 \mathrm{d}z\ z P_{ij}(\mu^2, z) = 0 \tag{2.50}
$$

This is the *momentum sum rule for the splitting functions* and it expresses the conservation of the momenta in the splittings of quarks and gluon [1].

2.2.4 | DGLAP evolution and NLO splitting functions

At NLO there are more diagrams, which need to be taken into account. In addition to the LO diagrams introduced in Sec. (2.2.2) also diagrams proportional to α_s^2 are considered.
It is interesting to mention that to obtain a complete set of splitting functions, 18 1-loop Feynman diagrams were computed at LO, 350 2-loop diagrams at NLO and 9607 3-loops diagrams at NNLO [43].

DGLAP equation with LO splitting functions sums the contributions coming from the strongly ordered emissions discussed in Sec. (2.2.2). An event with n emissions gives the factor

$$
\sim \left(\frac{\alpha_s}{2\pi}\right)^n \ln^n\left(\frac{\mu^2}{\mu_0^2}\right) . \tag{2.51}
$$

This is the *leading logarithm* approximation (LL) where the power of the logarithm is the same as the power of α_s. DGLAP with LO splitting functions sums such terms up to all orders in α_s. The NLO splitting functions sum contributions, where one of the emissions is not strongly ordered so terms like

$$
\sim \left(\frac{\alpha_s}{2\pi}\right)^n \ln^{n-1}\left(\frac{\mu^2}{\mu_0^2}\right) . \tag{2.52}
$$

Respectively, this is called *next-to-leading logarithm* (NLL) approximation [44].

In fig. 2.13 some of the diagrams for the squared amplitudes contributing to the NLO quark-quark splitting functions are shown. These diagrams contain 2 loops so the NLO splitting functions are very often called 2-*loop* splitting functions. From these diagrams one can see that at NLO a quark can split into or a quark or antiquark of either the same or different flavour. The formulas for the NLO splitting functions calculated in the $\overline{\mathrm{MS}}$ scheme are given in [45–47] and in Appendix (A.1).

In is important to note that, except the increased amount of diagrams and, as a consequence, the increased complexity of the computation, the concept of the splitting functions remains simple and their structure is the same as at LO. These issues will be discussed in detail in the next subsection.

2.2.5 | Structure of the DGLAP splitting functions

In this subsection the DGLAP splitting functions are discussed in more detail. Their structure is one of the essential points in solving the DGLAP equation.

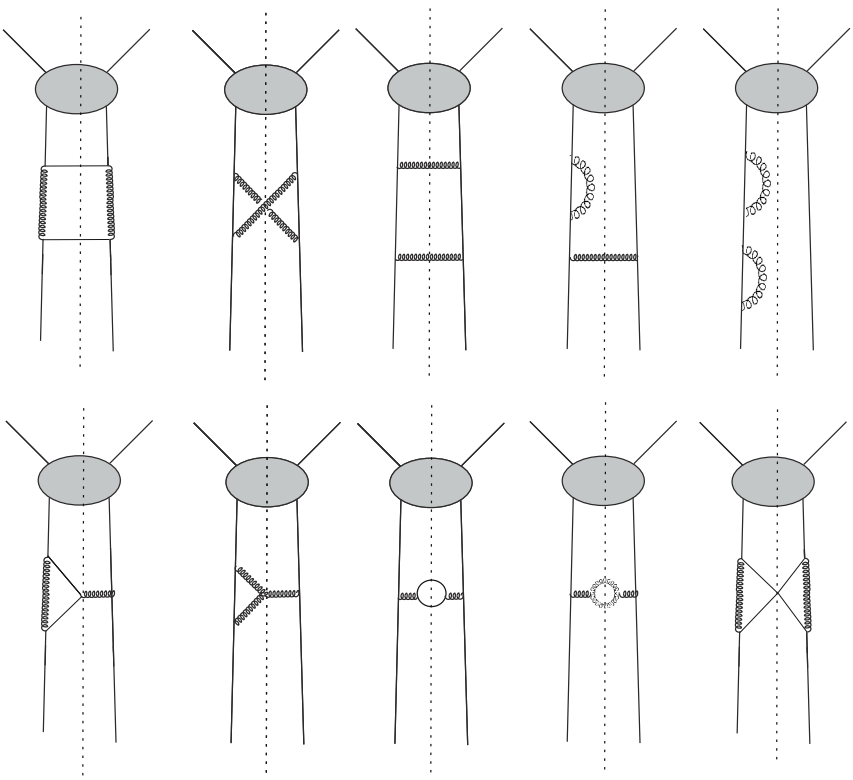

Figure 2.13: Schematic representation of some of the NLO splitting diagrams. The diagrams contain 2 loops.

The DGLAP splitting functions $P_{ab}(z,\mu^2)$ depend on two variables: the splitting variable z and the evolution scale μ. The dependence on μ enters the splitting function via the running coupling $\alpha_s(\mu^2)$ and the number of flavours $n_f \equiv n_f(\mu^2)$.

The splitting functions have a perturbative series expansion

$$P_{ab}\left(z,\mu^2\right) = \sum_{n=1}^{\infty}\left(\frac{\alpha_s(\mu^2)}{2\pi}\right)^n P_{ab}^{(n-1)}\left(z,\mu^2\right). \tag{2.53}$$

SU(n_f) symmetry leads to the following relations for the splitting functions at any order in α_s

$$P_{q_iq_j} = P_{\overline{q}_i\overline{q}_j}\,, \tag{2.54}$$

$$P_{q_i\overline{q}_j} = P_{\overline{q}_iq_j}\,, \tag{2.55}$$

$$P_{q_ig} = P_{\overline{q}_ig} \equiv P_{qg}\,, \tag{2.56}$$

$$P_{gq_i} = P_{g\overline{q}_i} \equiv P_{gq}\,. \tag{2.57}$$

The splitting functions are flavour independent since the strong interaction is flavour independent.

At LO the series expansion in eq.(2.53) is truncated after the first term

$$P_{qg}\left(z,\mu^2\right) = \frac{\alpha_s(\mu^2)}{2\pi}P_{qg}^{(0)}\left(z,\mu^2\right), \tag{2.58}$$

$$P_{gq}\left(z,\mu^2\right) = \frac{\alpha_s(\mu^2)}{2\pi}P_{gq}^{(0)}\left(z,\mu^2\right), \tag{2.59}$$

$$P_{gg}\left(z,\mu^2\right) = \frac{\alpha_s(\mu^2)}{2\pi}P_{gg}^{(0)}\left(z,\mu^2\right), \tag{2.60}$$

$$P_{q_i q_j}\left(z,\mu^2\right) = \frac{\alpha_s(\mu^2)}{2\pi} P^{(0)}_{q_i q_j}\left(z,\mu^2\right) \equiv \frac{\alpha_s(\mu^2)}{2\pi}\delta_{ij} P^{(0)}_{qq}\left(z,\mu^2\right) \tag{2.61}$$

so

$$P^{(0)}_{q_i q_j}\left(z,\mu^2\right) \equiv \delta_{ij} P^{(0)}_{qq}\left(z,\mu^2\right) \tag{2.62}$$

and

$$P^{(0)}_{\overline{q}_i q_j}\left(z,\mu^2\right) = 0\,. \tag{2.63}$$

This means that at LO a quark can split and continue the evolution only as a gluon or as a quark of the same flavour.

At NLO, the splitting functions are the following

$$P_{qg}\left(z,\mu^2\right) = \frac{\alpha_s(\mu^2)}{2\pi} P^{(0)}_{qg}\left(z,\mu^2\right) + \left(\frac{\alpha_s(\mu^2)}{2\pi}\right)^2 P^{(1)}_{qg}\left(z,\mu^2\right)\,, \tag{2.64}$$

$$P_{gq}\left(z,\mu^2\right) = \frac{\alpha_s(\mu^2)}{2\pi} P^{(0)}_{gq}\left(z,\mu^2\right) + \left(\frac{\alpha_s(\mu^2)}{2\pi}\right)^2 P^{(1)}_{gq}\left(z,\mu^2\right)\,, \tag{2.65}$$

$$P_{gg}\left(z,\mu^2\right) = \frac{\alpha_s(\mu^2)}{2\pi} P^{(0)}_{gg}\left(z,\mu^2\right) + \left(\frac{\alpha_s(\mu^2)}{2\pi}\right)^2 P^{(1)}_{gg}\left(z,\mu^2\right)\,. \tag{2.66}$$

In this case the splitting functions for quarks are more complicated than at LO because a quark can continue the evolution not only as a gluon or quark of the same flavour but also as a quark/antiquark of different flavour or antiquark of the same flavour. The NLO splitting functions for a quark splitting into a given quark/antiquark are given by

$$P_{q_j q_j}\left(z,\mu^2\right) = \frac{\alpha_s(\mu^2)}{2\pi} P^{(0)}_{q_j q_j}\left(z,\mu^2\right) + \left(\frac{\alpha_s(\mu^2)}{2\pi}\right)^2 P^{(1)}_{q_j q_j}\left(z,\mu^2\right)\,, \tag{2.67}$$

$$P_{q_{i\neq j} q_j}\left(z,\mu^2\right) = \left(\frac{\alpha_s(\mu^2)}{2\pi}\right)^2 P^{(1)}_{q_{i\neq j} q_j}\left(z,\mu^2\right)\,, \tag{2.68}$$

$$P_{\overline{q}_j q_j}\left(z,\mu^2\right) = \left(\frac{\alpha_s(\mu^2)}{2\pi}\right)^2 P^{(1)}_{\overline{q}_j q_j}\left(z,\mu^2\right)\,, \tag{2.69}$$

$$P_{\overline{q}_{i\neq j} q_j}\left(z,\mu^2\right) = \left(\frac{\alpha_s(\mu^2)}{2\pi}\right)^2 P^{(1)}_{\overline{q}_{i\neq j} q_j}\left(z,\mu^2\right)\,. \tag{2.70}$$

At NLO

$$P_{q_{i\neq j} q_j}\left(z,\mu^2\right) = P_{\overline{q}_{i\neq j} q_j}\left(z,\mu^2\right)\,. \tag{2.71}$$

The splitting functions can be also decomposed as follows

$$P_{ab}\left(z,\mu^2\right) = D_{ab}\left(\mu^2\right)\delta(1-z) + K_{ab}\left(\mu^2\right)\frac{1}{(1-z)_+} + R_{ab}\left(z,\mu^2\right), \tag{2.72}$$

where D_{ab} and K_{ab} are diagonal in flavour,

$$D_{ab}\left(\mu^2\right) = \delta_{ab} d_a\left(\mu^2\right),\;\; K_{ab}\left(\mu^2\right) = \delta_{ab} k_a\left(\mu^2\right) \tag{2.73}$$

(there is no summation over repeated indices) and the function R_{ab} does not contain any power divergences when $z \to 1$ (no terms $\sim (1-z)^{-n}$ for $n = 1, 2, ...$) but it can contain logarithmic divergences (terms $\sim \ln^n(1-z)$, $n = 1, 2$). These can be, however, integrated to give a finite result (see the NLO splitting functions given in Appendix (A.1)). The functions D_{ab} and K_{ab}, or equivalently d_a and k_a, and the functions R_{ab} in eq. (2.72) have the following expansions

$$d_a\left(\mu^2\right) = \sum_{n=1}^{\infty}\left(\frac{\alpha_s(\mu^2)}{2\pi}\right)^n d_a^{(n-1)}\left(\mu^2\right),\;\; k_a\left(\mu^2\right) = \sum_{n=1}^{\infty}\left(\frac{\alpha_s(\mu^2)}{2\pi}\right)^n k_a^{(n-1)}\left(\mu^2\right), \tag{2.74}$$

$$R_{ab}\left(z,\mu^2\right)=\sum_{n=1}^{\infty}\left(\frac{\alpha_s(\mu^2)}{2\pi}\right)^n R_{ab}^{(n-1)}\left(z,\mu^2\right)\ .$$

At LO, d_a, k_a and R_{ab} have the form

$$d_q^{(0)}=\frac{3}{2}\,C_F\quad,\quad d_g^{(0)}\left(\mu^2\right)=\frac{11}{6}\,C_A-\frac{2}{3}\,T_R\,n_f\ , \tag{2.75}$$

$$k_q^{(0)}=2\ C_F\ ,\ \ k_g^{(0)}=2\ C_A\ , \tag{2.76}$$

$$\begin{aligned}
R_{gg}^{(0)}(z) &= 2\,C_A\left[\frac{1-z}{z}+z(1-z)-1\right]\ ,\\
R_{gq}^{(0)}(z) &= C_F\,\frac{1+(1-z)^2}{z}\ ,\\
R_{qg}^{(0)}(z) &= T_R\left[z^2+(1-z)^2\right]\ ,\\
R_{q_iq_j}^{(0)}(z) &= -C_F\,(1+z)\,\delta_{ij}\ ,\quad R_{q_i\bar{q}_j}^{(0)}(z)=0\ ,
\end{aligned} \tag{2.77}$$

where $n_f\equiv n_f(\mu^2)$ and the $SU(N_c)$ color factors (with $N_c=3$ the number of colors) are given by

$$C_A=N_c\quad,\quad C_F=\frac{N_c^2-1}{2\,N_c}\quad,\quad \mathrm{Tr}\left(T^AT^B\right)=\delta^{AB}\,T_R=\frac{1}{2}\,\delta^{AB} \tag{2.78}$$

and T^A, T^B are the Gell-Mann matrices (SU(3) generators).
The formulas of the splitting functions at NLO are given in Appendix (A.1).

2.3 | Features of DGLAP

In the previous sections we discussed general features of the DGLAP equation. Now we would like to concentrate more on two aspects, which are important for the parton branching method.

2.3.1 | Momentum sum rule

In this section we discuss a reformulation of the evolution equation (eq. (2.40)) using the momentum sum rule introduced in Sec. (2.2.3) in order to treat the virtual corrections.

To begin with, let us insert eq. (2.72) into the evolution equation (eq. (2.40))

$$\begin{aligned}
\frac{d\ \widetilde{f}_a(x,\mu^2)}{d\ln\mu^2} &= \sum_b\int_0^1 dz\ P_{ab}(\mu^2,z)\widetilde{f}_b(x/z,\mu^2)\Theta(z-x)\\
&= \sum_b\int_0^1 dz\left(K_{ab}(\mu^2)\frac{1}{(1-z)}+R_{ab}(\mu^2,z)\right)\widetilde{f}_b(x/z,\mu^2)\Theta(z-x)\\
&\quad -\sum_b\int_0^1 dz\ \ \left(K_{ab}(\mu^2)\frac{1}{(1-z)}\right)\widetilde{f}_b(x,\mu^2)\Theta(1-x)\\
&\quad +\sum_b\int_0^1 dz\ D_{ab}(\mu^2)\delta(z-1)\widetilde{f}_b(x/z,\mu^2)\Theta(z-x)\\
&= \sum_b\int_x^1 dz\ \left(K_{ab}(\mu^2)\frac{1}{(1-z)}+R_{ab}(\mu^2,z)\right)\widetilde{f}_b(x/z,\mu^2)\\
&\quad -\sum_b\int_0^1 dz\ \left(K_{ab}(\mu^2)\frac{1}{(1-z)}-D_{ab}\delta(1-z)\right)\widetilde{f}_b(x,\mu^2)\\
&= \sum_b\int_x^1 \mathrm{dz}\ \left(K_{ab}\left(\mu^2\right)\frac{1}{1-z}+R_{ab}\left(\mu^2,z\right)\right)\widetilde{f}_b\left(\frac{x}{z},\mu^2\right)
\end{aligned}$$

$$-\widetilde{f}_a\left(x,\mu^2\right)\int_0^1 \mathrm{dz}\; P_a^V\left(\mu^2,z\right) \tag{2.79}$$

where the $P_a^V\left(\mu^2,z\right) = k_a\left(\mu^2\right)1/(1-z) - d_a\left(\mu^2\right)\delta(1-z)$ contains the virtual corrections.

At this stage one can notice two possible difficulties for a numerical solution: the presence of virtual pieces with the $\delta(1-z)$ function and the fact that all the integrals after the second equality sign in eq. (2.79) are separately divergent. This divergence is treated formally correctly when the divergent pieces are under one integral written with a plus prescription. Once the decomposition from eq. (2.31) is written with two separate integrals, they are not properly defined anymore. However, if one wants to obtain a numerical solution of the evolution equation it is better to not use the plus prescription and take this singularities into account in another way.

First, we concentrate on the presence of the delta function. In Sec. (2.2.3) the momentum sum rule was introduced in eq. (2.50). Let us insert it into the DGLAP evolution equation. We do this by subtracting the momentum sum rule inside eq. (2.79)

$$\begin{aligned}
\frac{d\widetilde{f}_a(x,\mu^2)}{d\ln\mu^2} &= \sum_b\int_x^1 \mathrm{dz}\;\left(K_{ab}\left(\mu^2\right)\frac{1}{1-z}+R_{ab}\left(\mu^2,z\right)\right)\widetilde{f}_b\left(\frac{x}{z},\mu^2\right)\\
&\quad -\widetilde{f}_a\left(x,\mu^2\right)\int_0^1 \mathrm{dz}\; P_a^V\left(\mu^2,z\right) - \widetilde{f}_a\left(x,\mu^2\right)\sum_c\int_0^1 \mathrm{dz}\; zP_{ca}\left(\mu^2,z\right)\\
&= \sum_b\int_x^1 \mathrm{dz}\;\left(K_{ab}\left(\mu^2\right)\frac{1}{1-z}+R_{ab}\left(\mu^2,z\right)\right)\widetilde{f}_b\left(\frac{x}{z},\mu^2\right)\\
&\quad -\widetilde{f}_a\left(x,\mu^2\right)\int_0^1 \mathrm{dz}\; P_a^V\left(\mu^2,z\right)\\
&\quad -\widetilde{f}_a(x,\mu^2)\sum_c\int_0^1 \mathrm{dz}\; z\left[K_{ca}\left(\mu^2\right)\frac{1}{(1-z)_+}+D_{ca}\left(\mu^2\right)\delta(1-z)+R_{ca}\left(\mu^2,z\right)\right]\\
&= \sum_b\int_x^1 \mathrm{dz}\;\left(K_{ab}\left(\mu^2\right)\frac{1}{1-z}+R_{ab}\left(\mu^2,z\right)\right)\widetilde{f}_b\left(\frac{x}{z},\mu^2\right)\\
&\quad -\widetilde{f}_a\left(x,\mu^2\right)\int_0^1 \mathrm{dz}\; P_a^V\left(\mu^2,z\right)\\
&\quad -\widetilde{f}_a(x,\mu^2)\sum_c\int_0^1 \mathrm{dz}\; z\left[K_{ca}\left(\mu^2\right)\frac{1}{1-z}+R_{ca}\left(\mu^2,z\right)\right]\\
&\quad -\widetilde{f}_a(x,\mu^2)\sum_c\underbrace{\int_0^1 \mathrm{dz}\; z\left[D_{ca}\left(\mu^2\right)\delta(1-z)\right]}_{\int_0^1 \mathrm{dz}\;\left[D_{ca}(\mu^2)\delta(1-z)\right]}+\widetilde{f}_a(x,\mu^2)\sum_c\int_0^1 \mathrm{dz}\;\left[K_{ca}\left(\mu^2\right)\frac{1}{1-z}\right]\\
&= \sum_b\int_x^1 \mathrm{dz}\;\left(K_{ab}\left(\mu^2\right)\frac{1}{1-z}+R_{ab}\left(\mu^2,z\right)\right)\widetilde{f}_b\left(\frac{x}{z},\mu^2\right)\\
&\quad -\widetilde{f}_a\left(x,\mu^2\right)\int_0^1 \mathrm{dz}\; P_a^V\left(\mu^2,z\right)\\
&\quad -\widetilde{f}_a(x,\mu^2)\sum_c\int_0^1 \mathrm{dz}\; z\left[K_{ca}\left(\mu^2\right)\frac{1}{1-z}+R_{ca}\left(\mu^2,z\right)\right]\\
&\quad +\widetilde{f}_a(x,\mu^2)\int_0^1 \mathrm{dz}\;\underbrace{\left[k_a\left(\mu^2\right)\frac{1}{1-z}-d_a\left(\mu^2\right)\delta(1-z)\right]}_{P_a^V(\mu^2,z)}\\
&= \sum_b\int_x^1 \mathrm{dz}\;\left(K_{ab}\left(\mu^2\right)\frac{1}{1-z}+R_{ab}\left(\mu^2,z\right)\right)\widetilde{f}_b\left(\frac{x}{z},\mu^2\right)
\end{aligned}$$

$$-\widetilde{f}_a\left(x,\mu^2\right)\sum_c\int_0^1 \mathrm{dz}\; z\left(K_{ca}\left(\mu^2\right)\frac{1}{1-z}+R_{ca}\left(\mu^2,z\right)\right)\;. \tag{2.80}$$

By using the momentum sum rule, the P^V part of the splitting functions was replaced by the real part of the splitting function. One sould note that the virtual corrections are still included in eq.(2.80), just written in a different way.

2.3.2 | Endpoint $z \to 1$ contributions to the evolution

Now we will discuss the second possible difficulty for a numerical solution of eq. (2.79) mentioned in Sec. (2.3.1), i.e. the limit of $z \to 1$. In eq. (2.80) one can still notice the problem that the integrals are divergent for $z \to 1$ when they are written separately (without using the plus prescription).

As discussed in Sec. (2.2.2), partons emitted with the transverse momentum smaller than a certain value cannot be resolved. Using energy-momentum conservation it can be reformulated into the condition that partons with z larger than some value z_M are *non-resolvable*. This corresponds to the limit of $z \to 1$ of eq. (2.40) where the soft gluons are emitted. These singularities are cured by the plus prescription where the divergencies cancel between real emissions and virtual corrections. However as already mentioned, if one does not want to use the plus prescription, these singularities must be taken into account in some other way.

Let us analyse the $z \to 1$ contribution to the evolution equation eq. (2.80). To begin with it is useful to split the integration region in two subregions $z < z_M$ and $z > z_M$, where $z_M > x$ is a parameter with a value near 1, $z_M = 1-\varepsilon$, $\varepsilon \ll 1$. The parameter z_M can be understood as a separation between resolvable and non-resolvable branchings, branchings with $z > z_M$ cannot be resolved. We rewrite the evolution equation eq. (2.80) as

$$\begin{aligned}
\frac{d\widetilde{f}_a(x,\mu^2)}{d\ln\mu^2} \;=\; & \sum_b\int_x^{z_M}\mathrm{dz}\;\left(K_{ab}\left(\mu^2\right)\frac{1}{1-z}+R_{ab}\left(\mu^2,z\right)\right)\widetilde{f}_b\left(\frac{x}{z},\mu^2\right)+\\
& -\widetilde{f}_a\left(x,\mu^2\right)\sum_c\int_0^{z_M}\mathrm{dz}\;z\left(K_{ca}\left(\mu^2\right)\frac{1}{1-z}+R_{ca}\left(\mu^2,z\right)\right)\\
& +\sum_b\int_{z_M}^1\mathrm{dz}\;\left(K_{ab}\left(\mu^2\right)\frac{1}{1-z}+R_{ab}\left(\mu^2,z\right)\right)\widetilde{f}_b\left(\frac{x}{z},\mu^2\right)+\\
& -\widetilde{f}_a\left(x,\mu^2\right)\sum_c\int_{z_M}^1\mathrm{dz}\;z\left(K_{ca}\left(\mu^2\right)\frac{1}{1-z}+R_{ca}\left(\mu^2,z\right)\right)\;.
\end{aligned} \tag{2.81}$$

We can use $z = 1+(z-1)$, eq. (2.73) and the Taylor expansion of the parton density $\widetilde{f}_b(x/z,\mu^2) = \widetilde{f}_b(x,\mu^2)+x(1-z)\widetilde{f}'_b(x,\mu^2)+\mathcal{O}(1-z)^2$ to analyse the region $z > z_M$ of eq. (2.81)

$$\begin{aligned}
& \sum_b\int_{z_M}^1\mathrm{dz}\;\left(K_{ab}\left(\mu^2\right)\frac{1}{1-z}+R_{ab}\left(\mu^2,z\right)\right)\widetilde{f}_b\left(\frac{x}{z},\mu^2\right)+\\
& -\widetilde{f}_a\left(x,\mu^2\right)\sum_c\int_{z_M}^1\mathrm{dz}\;z\left(K_{ca}\left(\mu^2\right)\frac{1}{1-z}+R_{ca}\left(\mu^2,z\right)\right)=\\
=\;& \sum_b\int_{z_M}^1\mathrm{dz}\;\left(K_{ab}\left(\mu^2\right)\frac{1}{1-z}+R_{ab}\left(\mu^2,z\right)\right)\left[\widetilde{f}_b(x,\mu^2)+x(1-z)\widetilde{f}'_b(x,\mu^2)+\mathcal{O}(1-z)^2\right]+\\
& -\widetilde{f}_a\left(x,\mu^2\right)\sum_c\int_{z_M}^1\mathrm{dz}\;(1+(z-1))\left(K_{ca}\left(\mu^2\right)\frac{1}{1-z}+R_{ca}\left(\mu^2,z\right)\right)=\\
=\;& \int_{z_M}^1\mathrm{dz}\;k_a\left(\mu^2\right)\frac{1}{1-z}\left[\widetilde{f}_a(x,\mu^2)+x(1-z)\widetilde{f}'_a(x,\mu^2)+\mathcal{O}(1-z)^2\right]+
\end{aligned}$$

$$-\widetilde{f}_a\left(x,\mu^2\right)\int_{z_M}^1 \mathrm{dz}\; k_a\left(\mu^2\right)\frac{1}{1-z} - \widetilde{f}_a\left(x,\mu^2\right)\int_{z_M}^1 \mathrm{dz}(z-1)\; k_a\frac{1}{1-z} + \mathcal{O}(1-z_M) =$$
$$= \quad \mathcal{O}(1-z_M)\,. \tag{2.82}$$

Above we have used that the integration over the pieces containing R_{ab} for $z > z_M$ gives at most terms of order $\mathcal{O}(1-z_M)$.

Therefore one can rewrite eq. (2.80) up to $\mathcal{O}(1-z_M)$ as

$$\begin{aligned}\frac{d\widetilde{f}_a(x,\mu^2)}{d\ln\mu^2} &= \sum_b \int_x^{z_M} \mathrm{dz}\;\left(K_{ab}\left(\mu^2\right)\frac{1}{1-z} + R_{ab}\left(\mu^2,z\right)\right)\widetilde{f}_b\left(\frac{x}{z},\mu^2\right) + \\ &- \widetilde{f}_a\left(x,\mu^2\right)\sum_c \int_0^{z_M} \mathrm{dz}\; z\left(K_{ca}\left(\mu^2\right)\frac{1}{1-z} + R_{ca}\left(\mu^2,z\right)\right)\,. \end{aligned}\tag{2.83}$$

It is thus convenient to define the kernels in the bracket as the real-emission branching probabilities $P^R_{ab}\left(\alpha_s(\mu^2),z\right)$,

$$P^R_{ab}\left(\mu^2,z\right) = K_{ab}\left(\mu^2\right)\;\frac{1}{1-z} + R_{ab}\left(\mu^2,z\right) \tag{2.84}$$

and rewrite eq. (2.83) as

$$\begin{aligned}\frac{d\widetilde{f}_a(x,\mu^2)}{d\ln\mu^2} &= \sum_b \int_x^{z_M} \mathrm{dz}\; P^R_{ab}\left(\mu^2,z\right)\widetilde{f}_b\left(\frac{x}{z},\mu^2\right) + \\ &- \widetilde{f}_a\left(x,\mu^2\right)\sum_c \int_0^{z_M} \mathrm{dz}\; zP^R_{ca}\left(\mu^2,z\right)\,. \end{aligned}\tag{2.85}$$

One can notice that the same cut off z_M was introduced in both pieces on the right hand side of the evolution equation eq.(2.80). If the cut off was different in these two pieces then the cancellation between the pieces of order $\mathcal{O}(1)$ would not be exact.

The practical choice of the form of the z_M parameter will be discussed in Sec. (3.1.3) where the issue of resolvable branching is further investigated.

2.4 | Solutions of DGLAP and PDFs measurements

Before we move to the PB method to solve DGLAP and to construct TMDs, in the last section of this chapter we would like to describe the landscape of the existing DGLAP solutions and introduce the mother of the TMD factorization - the collinear factorization theorem.

2.4.1 | Methods to solve the DGLAP equation

The DGLAP evolution equation eq. (2.38) is an integro-differential equation and it does not have an analytical solution in the x-space. Nevertheless, there are many other methods to solve DGLAP available. This section gives a short overview of these methods. Further references can be found in [48–51].

Mellin transform In the first method the DGLAP evolution is solved in the Mellin space. The DGLAP equations can be formulated in the Mellin space by taking the Mellin transform of the parton distributions [1] (so called *moments*)

$$f_a(j,\mu^2) = \int_0^1 \mathrm{d}x x^{j-1} f_a(x,\mu^2)\,. \tag{2.86}$$

The *anomalous dimension* is defined in the following way

$$\gamma_{ab}(j,\mu^2) = \int_0^1 \mathrm{d}x x^{j-1} P_{ab}(x,\mu^2) \ . \tag{2.87}$$

With these definitions, the DGLAP equation eq. (2.38) can be written in a form

$$\mu^2 \frac{\mathrm{d}f_a(j,\mu^2)}{\mathrm{d}\mu^2} = \sum_b \gamma_{ab}(j,\mu^2) f_b(j,\mu^2) \tag{2.88}$$

which is now a simple product whereas eq. (2.38) is a convolution. An analytical solution of this equation can be obtained but the inverse Mellin transform cannot be done analytically and a numerical procedure is required to obtain the distributions in the x-space. Many results were obtained with this method (see e.g. [52–54]). Its accuracy is good, but it is CPU time consuming. Moreover, the results are model dependent [48, 50]. The reason for that is that the limit of $x \to 0$ corresponds to infinite energy. Because of that every moment has an uncertainty which is reduced by model dependent assumptions. One way of dealing with this problem is to use *truncated Mellin moments* instead of full moments [48, 55, 56]. The method works well for $j \geq 2$.

Laguerre polynomials The method based on the Laguerre polynomials expansion solves the DGLAP evolution directly in the x-space. This method was proposed by Furmanski and Petronzio [57]. It reduces the DGLAP integro-differential equation into a set of ordinary differential equations. An evolution function is introduced, expanded in terms of the Laguerre polynomials, then the integro-differential equation becomes a simple differential equation rewritten in terms of some recursion relation and at the end of the evolution the parton distribution is calculated via summation of the Laguerre coefficients expansion [49]. This method is very efficient for $x > 10^{-3}$ [50], however, it has some accuracy problems in the small x limit since the Laguerre polynomials go to infinity for $x \to 0$ [49].

Brute force The DGLAP equation can be also solved directly in the x-space with so called *brute force* method [58–61]. The idea is very simple: the space in x and μ^2 is divided into a small steps, the differential is calculated then in the following way

$$\frac{\mathrm{d}f(\mu^2)}{\mathrm{d}\mu^2} = \frac{f(\mu^2_{m+1}) - f(\,u^2_m)}{\mu^2_{m+1} - \mu^2_m} \tag{2.89}$$

and the integral is calculated as

$$\int \mathrm{d}x f(x) = \sum_m (x_{m+1} - x_m) f(x_m) \ . \tag{2.90}$$

The evolution is then solved step by step and, if the space in x and μ^2 is divided into many small intervals, the accuracy of this method can be high but it is CPU time consuming.

Polynomial spline The next numerical method to solve DGLAP is the polynomial spline interpolation used by QCDNUM [62]. The function to be interpolated is divided into n intervals and it is parametrized in each interval by the polynomial of order k. Continuity conditions are imposed on the function at each of the grid points and its derivatives, usually on all but the highest derivative. This gives us $n + k - 1$

free parameters. The function $f(x)$, which one wants to interpolate in this method, is sampled at $n+1$ points $x_0 < x_1 < ... < x_n$ and it is rewritten as a linear combination of *B-splines* Y_i

$$f(x) = \sum_i A_i Y_i(x) \ . \tag{2.91}$$

In the DGLAP case the function to be evaluated is the derivative of the parton density (or more strictly speaking in QCDNUM it is the derivative of the *momentum weighted* parton density $\widetilde{f}(x,\mu^2) = xf(x,\mu^2)$). The right hand side of the DGLAP equation eq. (2.40) is rewritten as a linear combination of B-spline coefficients and weight functions.

In QCDNUM there are two interpolation schemes, a linear and a quadratic one. The accuracy increases with the number of grid points but it also causes an increase of CPU time, nevertheless the QCDNUM method is very fast. Both interpolation schemes were compared with another evolution package and per mill level agreement was obtained between these two packages at small and medium x. At higher x the accuracy is $\sim 2-3\%$ but it can even reach $< 1\%$ for $x < 0.9$ depending on technical details [62].

Parton Branching The DGLAP equation can be also solved with a *parton branching* (PB) method [63–66]. Applying the PB method the splitting variables z and scales μ^2, at which the branchings happen, are generated according to the appropriate distributions. With this method the whole chain in the evolution is generated, with the information about all partons and their momenta. Moreover, the kinematics of every single splitting process can be treated exactly and this makes this method attractive comparing to semi-analytical solutions of the evolution equations. The uncertainty of this method is easy to estimate by the statistical uncertainty of the Monte Carlo sample used. The parton branching allows also to construct MC Parton Shower programs - key ingredient of nowadays experimental analyses of high energy collisions. The parton branching method is the main topic of this thesis and will be discussed in details later on.

2.4.2 | Collinear factorization theorem

In Sec. (2.1) the DIS cross section in eq. (2.2) was written as a convolution of the partonic cross section and parton distribution function. This formalism can be generalized. The cross sections for other QCD processes with a large momentum transfer can be written in an analogous way, using the parton level cross sections, computable in perturbative QCD, and the parton distribution functions which incorporate all the non-perturbative physics and collinear singularities. This is the content of the *QCD collinear factorization theorem* [67, 68] which is proven for sufficiently inclusive observables in the final state of the scattering of colorless hadrons, i.e. besides DIS and diffractive DIS, also for the Drell-Yan (DY) process and single particle inclusive spectra [67]. The factorization theorem is the basis of many QCD calculations, e.g. Monte Carlo generators are based on it. The theorem is also assumed to be valid for processes for which it is not strictly proven.

As an example, let us consider the DY cross section. The LO differential cross section σ for a collision of two protons with the four-momenta P_1, P_2 is shown in fig. 2.14. A partonic differential cross section $\hat{\sigma}$ of a quark - antiquark collision, which carry the fractions ξ_1 and ξ_2 of the protons momenta, is multiplied by the probabilities to find inside the protons the partons with these momentum fractions. Then it is integrated over all possible momentum fractions carried by the quarks and summed over all possible

quark flavours i, j to give the DY differential cross section [67]

$$\frac{\mathrm{d}\sigma}{\mathrm{d}Q^2\mathrm{d}y} \sim \sum_{i,j} \int_{x_1}^{1} \mathrm{d}\xi_1 \int_{x_2}^{1} \mathrm{d}\xi_2 f_{i/1}(\xi_1, \mu)\hat{\sigma}_{ij}\left(\frac{x_1}{\xi_1}, \frac{x_2}{\xi_2}, Q, \frac{\mu}{Q}, \alpha_s(\mu)\right) f_{j/2}(\xi_2, \mu) \,. \tag{2.92}$$

In eq. (2.92) Q is the lepton pair invariant mass, μ is the renormalization scale, $x_1 = e^y\sqrt{\frac{Q^2}{s}}$, $x_2 = e^{-y}\sqrt{\frac{Q^2}{s}}$, $y = \frac{1}{2}\ln\left(\frac{q\cdot P_1}{q\cdot P_2}\right)$ is the rapidity of the lepton pair.

The essential point of the factorization theorem is that the parton distribution functions are universal for a given hadron - if they are measured in one process, let us say DIS, they can be used in a calculation for another process involving the same hadrons, for example proton-proton collisions.

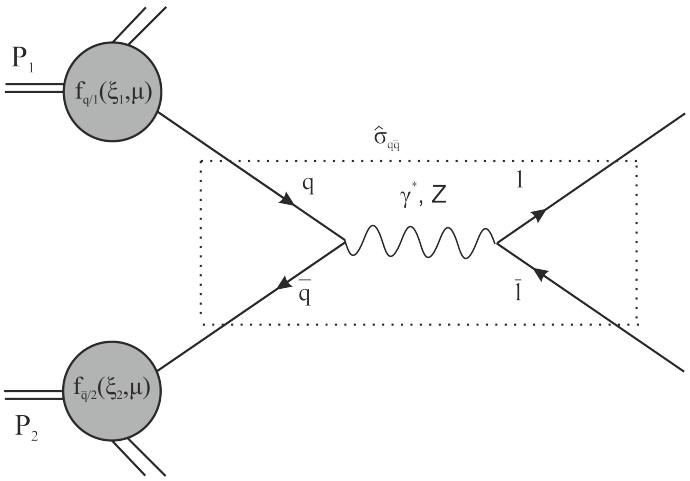

Figure 2.14: Illustration of the QCD Factorization Theorem for the LO DY. The dotted frame represents the partonic cross section $\hat{\sigma}$.

The short and long distance physics can be divided between PDFs and partonic cross sections in a different way, defined by the *factorization scheme*. The same scheme has to be used for both the parton density and the partonic cross section to obtain consistent results. Frequently used schemes are the $\overline{\mathrm{MS}}$ [12] and in earlier days also the DIS scheme [69].

2.4.3 | PDFs measurements

There are many measurements from which PDFs can be extracted. The kinematic range in x and Q^2 covered by these experiments is presented in fig. 2.15. This section gives a short overview of some of them.

The basic process, in which PDFs are measured, is DIS. The measurements of the DIS process were performed in fixed target experiments (e.g. Bologna-CERN-Dubna-Munich-Saclay (BCDMS) and NMC experiments at CERN, E665 experiment at Fermilab, SLAC National Accelerator Laboratory) and collider experiments (HERA at DESY), for overview see e.g. [70].

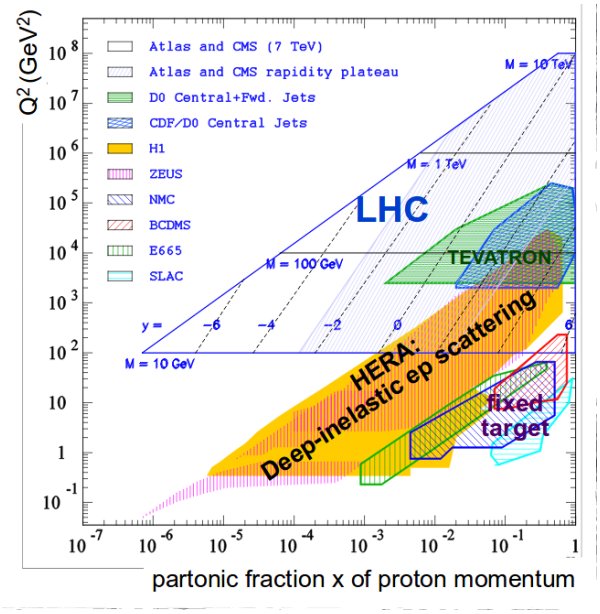

Figure 2.15: The phase space in x and Q^2 covered by different PDFs measurements [71].

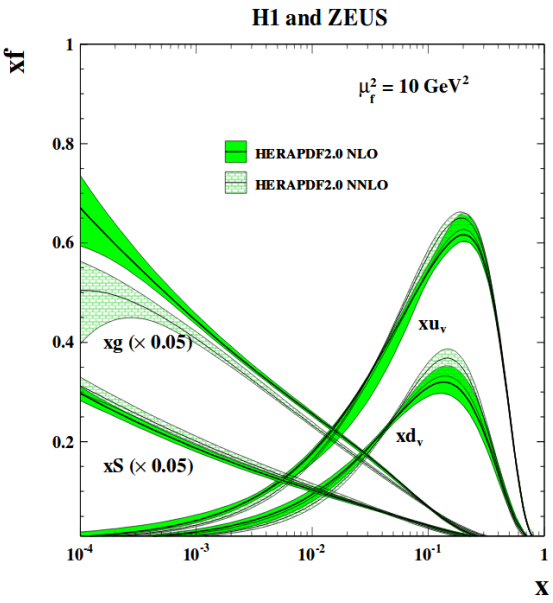

Figure 2.16: The parton distribution functions from HERAPDF2.0 at NLO and NNLO [42].

There are two DIS processes from which PDFs are extracted: neutral current (NC) in which a lepton scatters on a proton through the exchange of a virtual photon or a Z boson, and charged current (CC) where a lepton scatters on a proton through the exchange of a W^+ or a W^- boson. NC scattering allows to measure the valance quark distributions and the gluon distribution which enter the evolution of a quark through the DGLAP equations (which is the consequence of the Bjorken scaling violation). The quark flavour separation is possible in the CC exchange.

The cornerstone DIS collider experiment took place at HERA electron(positron)-proton accelerator [42] at DESY. There were two phases at HERA: HERA I in 1992-2000 and HERA II in 2002-2007 during which the two experiments, H1 and ZEUS, collected a total integrated luminosity of approximately $\approx 0.5\text{fb}^{-1}$ each. From 1994 the electron beam energy in HERA was $E_e \simeq 27.5$ GeV and for most of the time the proton beam energy was $E_p = 920$ GeV which gives the center of mass energy of $\sqrt{s} \simeq 320$ GeV. HERA NC measurements covered the range of $0.045 \leq Q^2 \leq 50000$ GeV^2 and $6 \cdot 10^{-7} \leq x \leq 0.65$ and the CC experiments covered the range $200 \leq Q^2 \leq 50000$ GeV^2 and $1.3 \cdot 10^{-2} \leq x \leq 0.4$. The predictions of inclusive reduced cross section σ_r vs x for a given Q^2 compared to the data coming from H1 and ZEUS are shown in fig. 2.11. The x and Q^2 dependence of the reduced cross section was used to determine the sets of parton distributions. The parton distribution functions from HERAPDF2.0 at NLO and NNLO are shown in fig. 2.16 [42].

Another group of important measurements of PDFs are the measurements performed in proton-antiproton collisions ($p\bar{p}$) at the Tevatron at Fermilab and proton-proton (pp) collisions at the Large Hadron Collider (LHC) at CERN.

In a Drell-Yan process, shown in fig. 2.17a, the quarks and gluon PDFs can be measured. The W and Z bosons are sensitive to different combinations of quark flavours and flavour separation is indirectly possible. The example of the impact of DY ATLAS data on $x\overline{u}$-sea quark PDF is shown in fig. 2.17b.

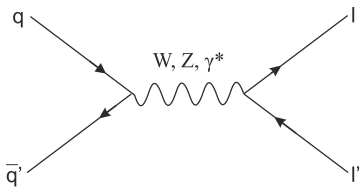

(a)

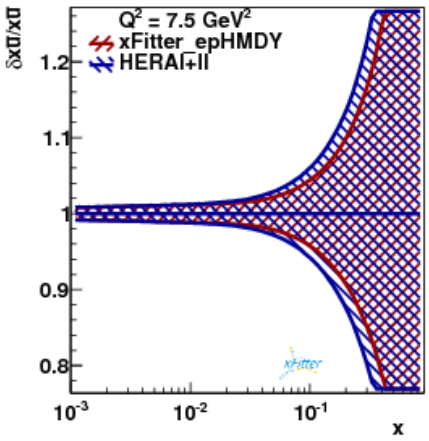

(b)

Figure 2.17: DY process from which quark PDFs can be constructed and the impact of the ATLAS 8 TeV DY data on the $x\overline{u}$-sea quark PDF [72].

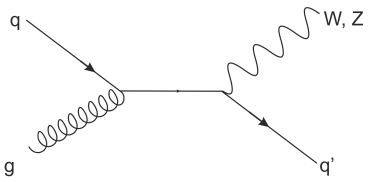

Figure 2.18: Vector boson + jet production.

In vector boson + jet production shown in fig. 2.18 the flavour of the quarks can be accessed directly if the final state is explicitly tagged.

One of the processes which can be used to constrain the u and d valence quark parton densities or sea antiquark densities, is the annihilation process of valence quark from one proton and sea antiquark from another proton in which a W^+ or a W^- is produced ($u\overline{d} \to W^+$, $d\overline{u} \to W^-$), shown in fig. 2.19a. Since there are more u valence quarks inside proton than d quarks, W^+ are produced more often than W^-. This asymmetry was measured at the LHC in ATLAS, CMS and LHCb (e.g. [73–77]) and in D0 and CDF experiments at the Tevatron [78–80] providing better constraints on the quark PDFs. The comparison of the PDF constraint with and without CMS W data is shown in fig. 2.19b [77] and the improvement is visible.

The strange quark PDF is constrained mainly from the NOMAD DIS experiment with neutrino scattering shown in fig. 2.20a [81], but also the LHC experiments produce constraints by studying $W + c$ production, as shown in fig. 2.20b [73]. The processes initiated by d or $\overline{d}$ quarks are Cabibbo suppressed.

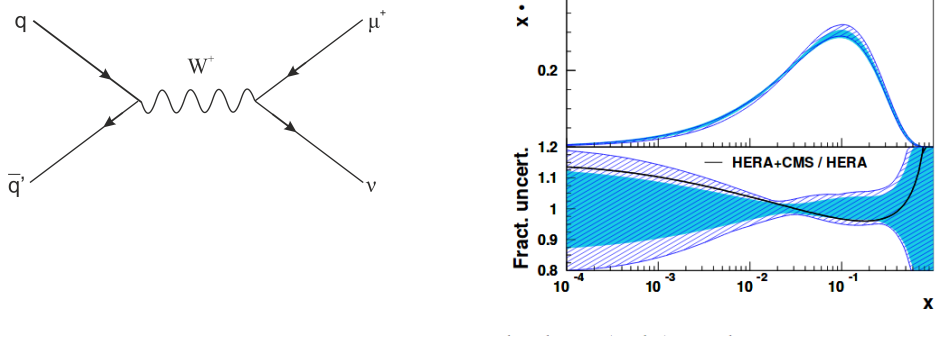

(a) (b)

Figure 2.19: Process contributing to the W^+/W^- asymmetry measurement to constraint the quark PDFs and the comparison of the d valance quark PDF with and without CMS data [77].

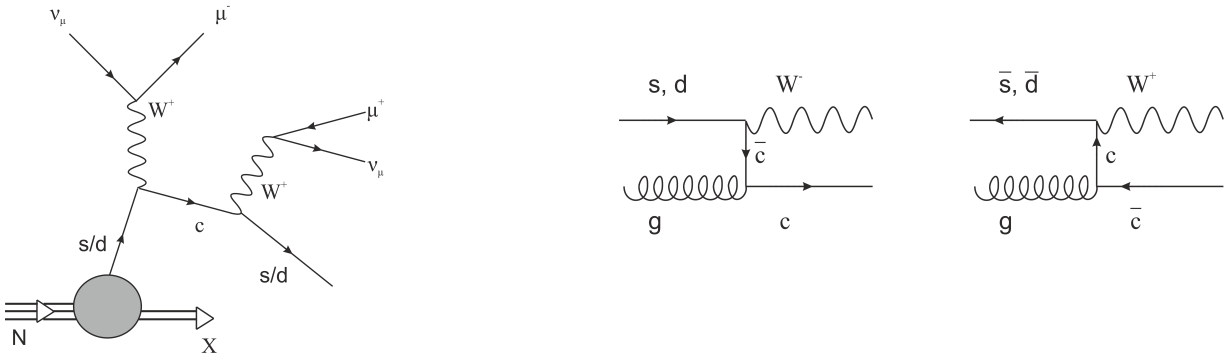

(a) (b)

Figure 2.20: Neutrino scattering DIS and $W + c$ production process from which s-quark PDFs can be constrained.

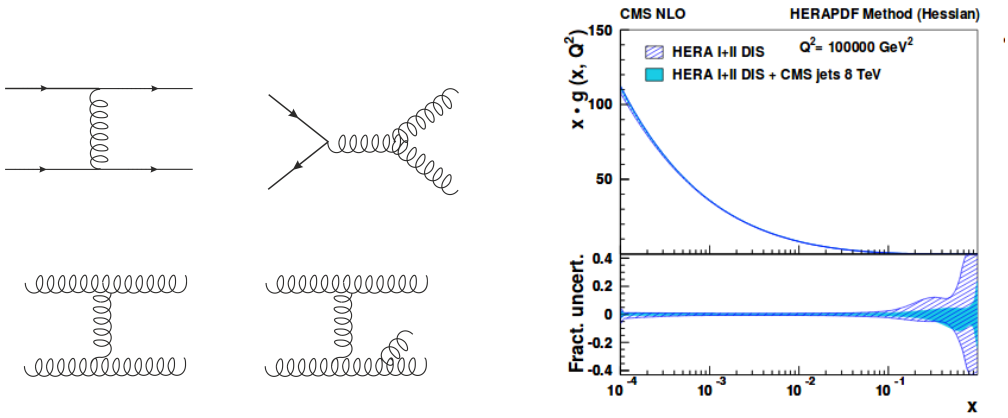

(a) (b)

Figure 2.21: Processes in which quark and gluon PDF can be determined and the improvement of the gluon PDF constraint with CMS inclusive jets data is visible [82].

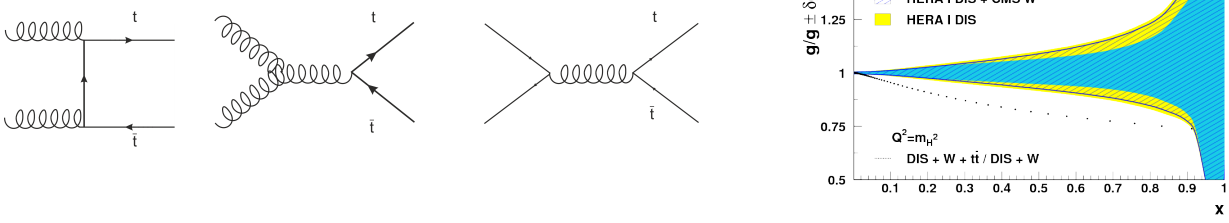

(a) (b)

Figure 2.22: The diagrams for the top pair production from which gluon PDF can be constrained and the improvement of the gluon PDF constraint with top quark production data [83].

Inclusive jet production in pp collisions at the LHC is directly sensitive to gluon and quark PDFs [82]. A simultaneous extraction of PDFs and α_s measurement is possible in these processes. The diagrams contributing to the PDFs studies are shown in fig. 2.21a. The improvement of the PDF constraint including CMS measurements is shown in fig. 2.21b.

A significant improvement in the uncertainty of the gluon distribution, as shown in fig. 2.22b, is obtained from top pair quark production [83]. The diagrams contributing to this process are shown in fig. 2.22a.

Forward c and b production, shown in fig. 2.23a, analysed by LHCb [84] can be used to constrain the gluon PDF, both at low and high x. The impact of these data on the gluon PDF is shown in fig. 2.23b.

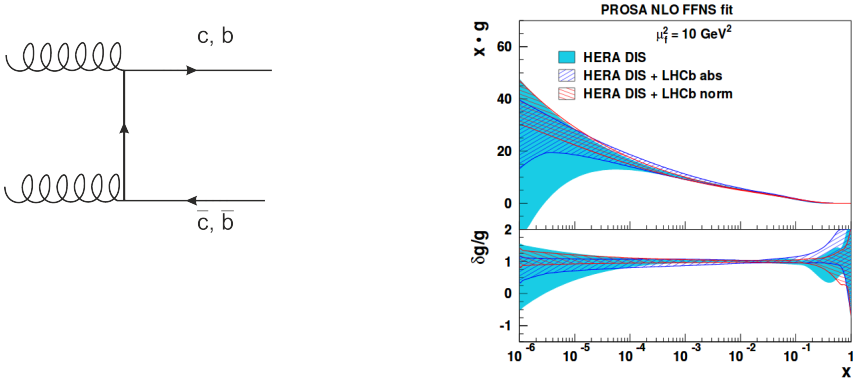

(a) (b)

Figure 2.23: The diagram contributing to forward c and b production and the impact of the forward heavy flavour production on the gluon PDF [84].

There are many groups extracting PDFs from the experimental data, among them are MSTW [85], CTEQ [86], NNPDF [87] and HERAPDF [88]. In general, the results obtained by these groups are in agreement but there are some differences for example in the choice of the data sets, heavy flavour treatment, initial parametrizations, treatment of uncertainties or the order in the perturbation theory.

3 | Interpretation of DGLAP evolution equation

DGLAP evolution scale μ does not have a priori any physical meaning but it can get one by associating the evolution scale with a given kinematic variable. In this section we discuss possible associations and ordering conditions which arise as the consequences of these choices. We also investigate further the issue of the z_M parameter defining the resolvable and non-resolvable branchings. In the second part of this chapter we rewrite the evolution equation using a Sudakov form factor which provides the appealing interpretation of the evolution equation in terms of parton branching picture.

3.1 | Interpretation of the evolution scale

3.1.1 | Virtuality and $p_\perp$-ordering

In this section we discuss the physical interpretation of the evolution scale in the DGLAP evolution equation. The kinematics of the splitting process together with the notation is shown in fig. 3.1 where μ' is the scale of the branching. For a given four vector with coordinates $k = (k^0, k^1, k^2, k^3) = (E_k, \overrightarrow{k}) =$

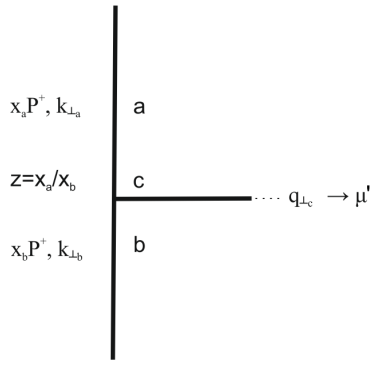

Figure 3.1: The kinematics of the splitting process.

$(E_k, k_\perp, k^3)$, where $k_\perp = (k^1, k^2)$, one can define the light cone variables $k = (k^+, k^-, k_\perp)$, where $k^\pm = \frac{1}{\sqrt{2}}(k^0 \pm k^3)$. Using the light cone variables the following relation holds

$$k^2 = 2k^+k^- - k_\perp^2 \ . \tag{3.1}$$

From that we obtain

$$k^- = \frac{k^2 + k_\perp^2}{2k^+} \ . \tag{3.2}$$

From the kinematics indicated in fig. 3.1 one can write a momentum conservation condition

$$k_b = k_a + q_c \tag{3.3}$$

which can be rewritten in terms of the minus component conservation as

$$\frac{k_b^2 + k_{\perp,b}^2}{2k_b^+} = \frac{k_a^2 + k_{\perp,a}^2}{2k_a^+} + \frac{q_c^2 + q_{\perp,c}^2}{2q_c^+} \,. \tag{3.4}$$

Assuming that $k_a^+ = zk_b^+$, $q_c^+ = (1-z)k_b^+$, eq. (3.4) can be rewritten

$$k_b^2 + k_{\perp,b}^2 = \frac{k_a^2 + k_{\perp,a}^2}{z} + \frac{q_c^2 + q_{\perp,c}^2}{1-z} \,. \tag{3.5}$$

Particle b and c can be put on mass shell $k_b^2 = 0$, $q_c^2 = 0$. In the collinear approximation the strong ordering in the transverse momenta holds $k_{\perp,b}^2 \ll k_{\perp,a}^2$ and one can neglect $k_{\perp,b} = 0$ giving us $k_{\perp,a} = -q_{\perp,c}$. We thus obtain

$$k_a^2(1-z) = -q_{\perp,c}^2 \,. \tag{3.6}$$

One can associate the virtuality of a parton a with the DGLAP scale of the branching μ'^2. Defining the virtuality as $\mu'^2 = -k_a^2$ one gets

$$\mu'^2(1-z) = q_{\perp,c}^2 \,. \tag{3.7}$$

With this association the partons in the cascade are ordered in virtuality. The condition from eq. (3.7) is called *virtuality ordering* condition.

In the limit of $z \to 0$, important for the high energy regime, eq. (3.6) becomes

$$k_a^2 = -q_{\perp,c}^2 \,. \tag{3.8}$$

From that one can associate the DGLAP branching scale with the transverse momentum

$$\mu'^2 = q_{\perp,c}^2 \,. \tag{3.9}$$

With this association the partons in the cascade are ordered in $p_\perp$ and eq. (3.9) is known as $p_\perp$*-ordering* condition.

3.1.2 | Angular ordering

In this subsection we introduce colour coherence phenomena of QCD and the ordering condition arising out of that. Coherence effects are common to all gauge theories. An example of the coherence is the *Chudakov effect* in QED [89], the suppression of soft photons bremsstrahlung from e^+e^- pairs.

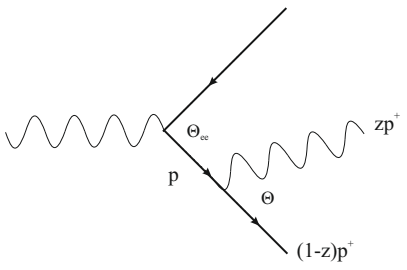

Figure 3.2: Emission of the soft photon from the e^+e^- pair.

The Chudakov effect is shown in fig. 3.2 [1]. Let us assume that the angles are small $\Theta_{ee}, \Theta \ll 1$. The time during which a photon can be emitted from the electron, can be estimated from the uncertainty principle as the inverse of the energy imbalance in the vertex $e^- \to \gamma e^-$, $\Delta t = 1/\Delta E$ where $\Delta E = p - \sqrt{z^2p^2 + k_\perp^2} - \sqrt{(1-z)^2p^2 + k_\perp^2} \approx \frac{k_\perp^2}{2z(1-z)p}$, which is equal to $\frac{k_\perp^2}{2zp}$ for $z \to 0$. The transverse momentum of the emitted photon in the small angle approximation is $k_\perp \approx zp\Theta$. From that $\Delta t \approx 2/zp\Theta^2 \sim 1/z\Theta^2 p$. During this time the electron-positron pair separates by the distance $\Delta b \sim \Theta_{ee}\Delta t$. Only photons which can resolve the electron-positron pair, can be emitted. Otherwise they would see only the total charge of the e^+e^- pair, which is zero so there cannot be any emission and the interaction cross section is zero. In order to be able to resolve the e^+e^- pair, the photon wavelength λ has to fulfil the condition $\Delta b > \lambda/\Theta$. From that $\Theta_{ee} > \Theta$ for photon to be able to resolve the e^+e^- pair.
A similar effect occurs in QCD where the coherence effect reveals itself as an *angular ordering* of the soft

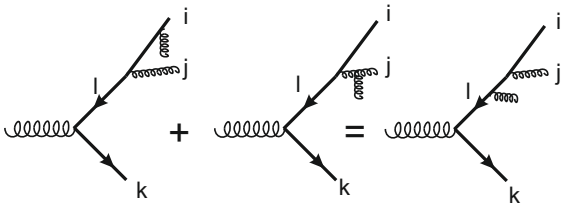

Figure 3.3: Example for $e^+e^- \to q\bar{q}g$ forming a colour singlet. The emission from lines i and j at angles larger then $\Theta_{ij}/2$ can be computed as an emission from the parent line l.

gluons emissions studied in [90–92]. The difference between QCD and QED is that the electric charge of the photon is replaced by the colour charge of the gluon. When the radiation comes from two external lines which form a colour singlet, the effect of angular ordering is the same as in the QED case. An example can be the $e^+e^- \to q\bar{q}$ system, where the radiation from the $q\bar{q}$ pair outside the cone between $q\bar{q}$ is suppressed. The interesting case is $e^+e^- \to q\bar{q}g$ when the soft gluon is radiated from a system of three partons i, j, k which form a colour singlet (for an educational description see e.g. [1]). The soft gluon can be radiated from each of the partons i, j, k proportionally to the colour charge squared of the emitter. The incoherent radiation from parton i and j can occur only in the cone of angle $\Theta_{ij}/2$. If the angle is larger in the direction of parton k, the contribution from line i and j occurs as a coherent radiation which is proportional to the squared sum of their charges and can be calculated as a radiation from the internal line l. This feature is shown in fig. 3.3.

The coherent branching phenomena appears in the cascades of soft gluons emissions as shown in fig. 3.4. From this diagram we have

$$|q_{\perp,i}| = |\overrightarrow{q}_i| \sin\Theta_i = (1-z_i)|\overrightarrow{k}_{i-1}| \sin\Theta_i \ . \tag{3.10}$$

Similarly, for the next emission

$$|q_{\perp,i+1}| = |\overrightarrow{q}_{i+1}| \sin\Theta_{i+1} = (1-z_i)(1-z_{i+1})|\overrightarrow{k}_{i-1}| \sin\Theta_{i+1} \ . \tag{3.11}$$

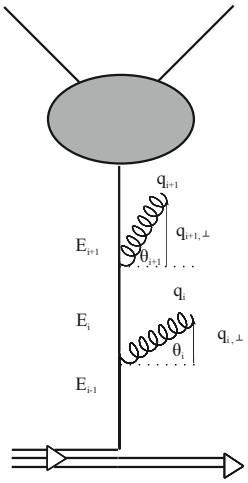

Figure 3.4: Coherent branching in the cascade of soft gluons emissions.

When one calculates $q_{\perp,i}$, it is assumed that $k_{\perp,i-1} = 0$ and the angle Θ_i is with respect to the beam line. Similarly, to compute $q_{\perp,i+1}$, $k_{\perp,i}$ is neglected so the angle Θ_{i+1} is with respect to the beam axis.

Defining the rescaled transverse momentum [93]

$$\frac{|q_{\perp,i}|}{1-z_i} \equiv \overline{q}_{\perp,i} \tag{3.12}$$

one obtains

$$\frac{\overline{q}_{\perp,i+1}}{\overline{q}_{\perp,i}} = z_i \frac{\Theta_{i+1}}{\Theta_i} \tag{3.13}$$

and from that using the angular ordering condition $\Theta_{i+1} > \Theta_i$ one obtains ordering condition for rescaled transverse momenta

$$\overline{q}_{\perp,i+1} > z_i \overline{q}_{\perp,i} \, . \tag{3.14}$$

This condition reduces to ordering in rescaled transverse momenta for large z. For $z \to 0$ the transverse momenta are free to perform a *random walk* [94].

One can associate the rescaled transverse momenta with the DGLAP scale at which the branching happens, $\overline{q}_{\perp,i} = \mu'$, and write

$$q^2_{\perp,i} = (1-z_i)^2 \mu'^2 \, . \tag{3.15}$$

Eq. (3.15) is known as the angular ordering condition.

3.1.3 | z_M definition

As explained in Sec. (2.3.2), partons emitted with a transverse momentum smaller than a certain value given by a resolution scale cannot be resolved. This can be expressed in terms of a condition on z_M: branchings with $z > z_M$ are non-resolvable. In this sense the z_M parameter defines the resolution scale. It can be fixed to some given value close to 1

$$z_M = \text{fixed} \, . \tag{3.16}$$

It can also change dynamically with the evolution scale since the resolution depends on the evolution scale. Two possible prescriptions are given by the *virtuality* and *angular* ordering conditions.

If one replace $q_{\perp,c}$ with some minimum $|q_{\perp,0}| \equiv q_0$ in the eq.(3.7) and eq.(3.15), one obtains conditions for the z_M value. For virtuality ordering

$$q_0^2 = (1-z)\mu'^2 \rightarrow z_M = 1 - \left(\frac{q_0}{\mu'}\right)^2 \tag{3.17}$$

and for the angular ordering

$$q_0^2 = (1-z)^2\mu'^2 \rightarrow z_M = 1 - \left(\frac{q_0}{\mu'}\right) \ . \tag{3.18}$$

3.1.4 | Renormalization scale choice

It has been shown [95] that together with the virtuality ordering condition the renormalization scale in α_s should be chosen to be $q_\perp^2$, rather than the branching scale μ'^2 what in the case described in Sec. (3.1.1) gives

$$\alpha_s \equiv \alpha_s((1-z)\mu'^2) \ . \tag{3.19}$$

With this scale choice some extra large logarithms compared to the basic DGLAP eq. (2.38) with $\alpha_s(\mu'^2)$ are resummed.

In [91] it was quoted that with the angular ordering condition the argument of α_s should be

$$\alpha_s \equiv \alpha_s\left((1-z)^2\mu'^2\right) \tag{3.20}$$

which again corresponds to the transverse momentum squared of the emitted parton. With such a choice the DGLAP equation is improved compared to the one with virtuality ordering - by taking the angular ordering condition and rescaling the renormalization scale in α_s, the phase space available for the successive emissions is reduced and the large infrared corrections are resummed [91, 95].

3.2 | Sudakov form factor

3.2.1 | DGLAP with Sudakov form factor

Eq. (2.85) may be rewritten in terms of the *Sudakov form factor*, defined as

$$\begin{aligned} \Delta_a(\mu^2, \mu_0^2) \ &\equiv \ \Delta_a(\mu^2) = \exp\left(-\sum_b \int_{\mu_0^2}^{\mu^2} \frac{d\mu'^2}{\mu'^2} \int_0^{z_M} dz \ z \ P_{ba}^R(\mu'^2, z)\right) \\ &= \ \exp\left(-\sum_b \int_{\ln\mu_0^2}^{\ln\mu^2} d\ln\mu'^2 \ \int_0^{z_M} dz \ z \ P_{ba}^R(\mu'^2, z)\right) . \end{aligned} \tag{3.21}$$

Using the following relation

$$\frac{d\ \Delta_a(\mu^2)}{d\ln\mu^2} = -\Delta_a(\mu^2) \sum_b \int_0^{z_M} dz \ z \ P_{ba}^R(\mu^2, z) \ , \tag{3.22}$$

one obtains from eq. (2.85)

$$\frac{d\ \widetilde{f}_a(x,\mu^2)}{d\ln\mu^2} = \sum_b \int_x^{z_M} dz \ P_{ab}^R(\mu^2, z) \ \widetilde{f}_b(x/z, \mu^2) + \frac{1}{\Delta_a(\mu^2)} \frac{d\ \Delta_a(\mu^2)}{d\ln\mu^2} \widetilde{f}_a(x, \mu^2) \ . \tag{3.23}$$

Comparing eq. (2.85) and eq. (3.23) one can notice that the virtual piece of the evolution equation is now rewritten with the Sudakov form factor. The Sudakov form factor and eq. (3.23) *resum* the virtual and non-resolvable contributions to all orders [1].

Eq. (3.23) can be rewritten as

$$\Delta_a(\mu^2)\ \frac{d}{d\ln\mu^2}\left(\frac{\widetilde{f}_a(x,\mu^2)}{\Delta_a(\mu^2)}\right)=\sum_b\int_x^{z_M}dz\ P^R_{ab}(\mu^2,z)\ \widetilde{f}_b(x/z,\mu^2)\ . \tag{3.24}$$

Let us rewrite eq. (3.24) changing the names of the variables: $\mu\to\mu_1$ and $z\to z_1$ and dividing both sides by $\Delta_a(\mu_1^2)$

$$\frac{d}{d\ln\mu_1^2}\left(\frac{\widetilde{f}_a(x,\mu_1^2)}{\Delta_a(\mu_1^2)}\right)=\frac{1}{\Delta_a(\mu_1^2)}\sum_b\int_x^{z_M}dz_1\ P^R_{ab}(\mu_1^2,z_1)\ \widetilde{f}_b(x/z_1,\mu_1^2)\ . \tag{3.25}$$

Integrating over $d\ln\mu_1^2$ we obtain

$$\widetilde{f}_a(x,\mu^2)=\Delta_a(\mu^2)\ \widetilde{f}_a(x,\mu_0^2)+\sum_b\int_{\ln\mu_0^2}^{\ln\mu^2}d\ln\mu_1^2\frac{\Delta_a(\mu^2)}{\Delta_a(\mu_1^2)}\int_x^{z_M}dz_1P^R_{ab}(\mu_1^2,z_1)\ \widetilde{f}_b(x/z_1,\mu_1^2) \tag{3.26}$$

where we have used $\Delta_a(\mu_0^2)=1$. Now, let us write the same kind of solution also for $\widetilde{f}_b\left(\frac{x}{z_1},\mu_1^2\right)$:

$$\widetilde{f}_b\left(\frac{x}{z_1},\mu_1^2\right)\ =\ \Delta_b(\mu_1^2)\widetilde{f}_b\left(\frac{x}{z_1},\mu_0^2\right)+\sum_c\int_{\ln\mu_0^2}^{\ln\mu_1^2}d\ln\mu_2^2\frac{\Delta_b(\mu_1^2)}{\Delta_b(\mu_2^2)}\int_{\frac{x}{z_1}}^{z_M}dz_2P^R_{bc}(\mu_2^2,z_2)\ \widetilde{f}_c\left(\frac{x}{z_1z_2},\mu_2^2\right)\ , \tag{3.27}$$

which can be inserted into eq. (3.26). Of course, the solution for $\widetilde{f}_c\left(\frac{x}{z_1z_2},\mu_2^2\right)$ can be written in the same way and inserted into eq. (3.27).

By using the Sudakov form factor one obtains an equation, which has the probabilistic interpretation in the parton branching picture. This will be described in Sec. (3.2.2) and in Sec. (6).

3.2.2 | Probabilistic interpretation of the Sudakov form factor

The Sudakov form factor defined in eq. (3.21) has an intuitive interpretation of being the probability of an evolution without any resolvable branching. One can notice that the expression in the exponent of eq. (3.21) gives the probability that there is a branching of a parton a into a parton b at a given scale μ'^2 and z, integrated over all z valueas between 0 and z_M, all μ'^2 values between μ_0^2 and μ^2 and summed over all partons species.

Under some simplified assumptions, using the *unitarity* and the *Markov property* (the process has *no memory*: the probability that a splitting happens depends only on the scale of the previous splitting, all the splittings that had happened before do not play any role) one can easily prove that the Sudakov form factor is the probability of an evolution without any resolvable branching.

The sum of the emission probability P_E between the scale μ_0 and μ and the probability of no emission P_{NE} between the same scales must be equal 1 (this is the so-called *unitarity condition*)

$$P_{\mathrm{NE}}(\mu^2,\mu_0^2)+P_{\mathrm{E}}(\mu^2,\mu_0^2)=1 \tag{3.28}$$

so

$$P_{\mathrm{NE}}(\mu^2,\mu_0^2)=1-P_{\mathrm{E}}(\mu^2,\mu_0^2)\ . \tag{3.29}$$

Now, dividing the interval between μ_0^2 and μ^2 into n intervals (and assuming that $\mu_0^2<\mu_1^2<\mu_2^2<...<\mu_{n-1}^2<\mu_n^2\equiv\mu^2$) one can notice, that the probability of no emission between scale μ_0 and μ means

that there was no emission between μ_0 and μ_1, μ_1 and μ_2 etc. up to μ_{n-1} and μ so one can use the multiplication law

$$P_{\mathrm{NE}}(\mu^2,\mu_0^2) = P_{\mathrm{NE}}(\mu_1^2,\mu_0^2)P_{\mathrm{NE}}(\mu_2^2,\mu_1^2)...P_{\mathrm{NE}}(\mu^2,\mu_{n-1}^2)\ . \tag{3.30}$$

Under the assumption that the intervals in μ are equally distributed we obtain

$$\mu_i^2 = \mu_0^2 + i\frac{\mu^2-\mu_0^2}{n} \tag{3.31}$$

where $i = 0,1,2,...,n$. Then from eq. (3.30) and eq. (3.31) one obtains

$$P_{\mathrm{NE}}(\mu^2,\mu_0^2) \;=\; \lim_{n\to\infty}\prod_{i=0}^{n-1} P_{\mathrm{NE}}(\mu_{i+1}^2,\mu_i^2) = \lim_{n\to\infty}\prod_{i=0}^{n-1}\left(1-P_{\mathrm{E}}(\mu_{i+1}^2,\mu_i^2)\right)\ . \tag{3.32}$$

Now, let us assume that all $P_{\mathrm{E}}(\mu_{i+1}^2,\mu_i^2)$ are equal so $P_{\mathrm{E}}(\mu_{i+1}^2,\mu_i^2) = \frac{P_{\mathrm{E}}(\mu^2,\mu_0^2)}{n}$. Then, the above equation can be continued in the following way

$$\begin{aligned}
\lim_{n\to\infty}\prod_{i=0}^{n-1}\left(1-P_{\mathrm{E}}(\mu_{i+1}^2,\mu_i^2)\right) &= \lim_{n\to\infty}\left(1-\frac{P_{\mathrm{E}}(\mu^2,\mu_0^2)}{n}\right)^n = \exp\left(-P_{\mathrm{E}}(\mu^2,\mu_0^2)\right)\\
&= \exp\left(-\sum_{i=1}^{n-1}P_{\mathrm{E}}(\mu_{i+1}^2,\mu_i^2)\right)\\
&= \exp\left(-\int_{\mu_1^2}^{\mu^2}\mathrm{d}\mu'^2\frac{\mathrm{d}P_{\mathrm{E}}(\mu'^2)}{\mathrm{d}\mu'^2}\right)
\end{aligned} \tag{3.33}$$

where the definition of the exponential function was used $\mathrm{e}^{-x} = \lim_{n\to\infty}\left(1-\frac{x}{n}\right)^n$. Now one just needs to express the probability of a real emission between μ'^2 and $\mu'^2+\mathrm{d}\mu'^2$ as

$$\frac{\mathrm{d}P_{\mathrm{E}}(\mu'^2)}{\mathrm{d}\mu'^2} = \frac{1}{\mu'^2}\int_0^{z_M} dz\ z\sum_b\ P_{ba}^R(\mu'^2,z) \tag{3.34}$$

and from that one obtains

$$P_{\mathrm{NE}}(\mu^2,\mu_0^2) = \exp\left(-\int_{\mu_0^2}^{\mu^2}\frac{d\mu'^2}{\mu'^2}\int_0^{z_M} dz\ z\sum_b\ P_{ba}^R(\mu'^2,z)\right) \equiv \Delta_a(\mu^2,\mu_0^2) \tag{3.35}$$

which proves that the Sudakov form factor is the probability of an evolution without any resolvable branching.

3.2.3 | Idea of Resummation

In this section the problem of a soft gluon emissions is approached in a different way than before. In Sec. (2.2.2) in eq. (2.19) we have obtained the result for the cross section for the process from fig. 2.5a, where a quark splits into a quark and a gluon and continues the evolution as a gluon which enters the hard interaction. The same equation can be also written for fig. 2.5d where a quark emits a gluon before entering the hard interaction

$$\sigma = \int\frac{\mathrm{d}p_\perp^2}{p_\perp^2}\mathrm{d}z\hat{\sigma}P_{qq}^R(z,\mu^2) \tag{3.36}$$

where $\hat{\sigma}$ is the hard process cross section. Differentiating eq. (3.36) with respect to $p_\perp^2$ we obtain

$$\frac{\mathrm{d}\sigma}{\mathrm{d}p_\perp^2} = \hat{\sigma}\frac{1}{p_\perp^2}\int\mathrm{d}zP_{qq}^R(z,\mu^2)\ . \tag{3.37}$$

From the angular ordering, discussed in Sec. (3.1.3), one obtains the limit on z integral $z_M = 1 - \frac{q_0}{\mu'}$. Let us consider a simplified form of the splitting function $P^R_{qq}(z) \approx \frac{\alpha_s}{2\pi}\frac{2C_F}{1-z}$ [92]. After performing the integral $\int \mathrm{d}z P^R_{qq}(z,\mu^2)$, assuming that $\mu'^2 = s$ and $q_0^2 = p_\perp^2$ is some minimal $p_\perp^2$, the following formula can be written for the case of 1 gluon emission

$$\frac{\mathrm{d}\sigma}{\mathrm{d}p_\perp^2} = \hat{\sigma} C_F \frac{\alpha_s}{\pi}\frac{1}{p_\perp^2}\ln\left(\frac{s}{p_\perp^2}\right) . \tag{3.38}$$

This result was originally obtained by studying the Drell-Yan cross section [96]. This differential cross section diverges for soft gluon emission, when $p_\perp^2 \to 0$. The idea, on how to solve this problem was proposed in [96] and for soft photon emissions in $e^+e^- \to \mu^+\mu^-$ in [97].

For the total cross section the following relation holds

$$\int_0^s \frac{\mathrm{d}\sigma}{\mathrm{d}p_\perp^2}\mathrm{d}p_\perp^2 = \hat{\sigma}(1 + \mathcal{O}(\alpha_s)) . \tag{3.39}$$

This integral can be divided into two integrals

$$\int_0^s \frac{\mathrm{d}\sigma}{\mathrm{d}p_\perp^2}\mathrm{d}p_\perp^2 = \int_0^{k_\perp^2} \frac{\mathrm{d}\sigma}{\mathrm{d}p_\perp^2}\mathrm{d}p_\perp^2 + \int_{k_\perp^2}^s \frac{\mathrm{d}\sigma}{\mathrm{d}p_\perp^2}\mathrm{d}p_\perp^2 \tag{3.40}$$

and used to define the *partially integrated* cross section

$$\Sigma(k_\perp^2) = \frac{1}{\hat{\sigma}}\int_0^{k_\perp^2} \frac{\mathrm{d}\sigma}{\mathrm{d}p_\perp^2}\mathrm{d}p_\perp^2 . \tag{3.41}$$

Taking the derivative from the partially integrated cross section one obtains a formula for the differential cross section $\frac{\mathrm{d}\sigma}{\mathrm{d}k_\perp}$

$$\frac{\mathrm{d}\Sigma(k_\perp^2)}{\mathrm{d}k_\perp^2} = \frac{1}{\hat{\sigma}}\frac{\mathrm{d}\sigma}{\mathrm{d}k_\perp^2} . \tag{3.42}$$

From that

$$\Sigma(k_\perp^2) \approx 1 - \frac{1}{\hat{\sigma}}\int_{k_\perp^2}^s \mathrm{d}p_\perp^2 \hat{\sigma} C_F \frac{\alpha_s}{\pi}\frac{1}{p_\perp^2}\ln\left(\frac{s}{p_\perp^2}\right) = 1 - \frac{\alpha_s}{2\pi}C_F \ln^2\frac{s}{k_\perp^2} . \tag{3.43}$$

This result is called *double-leading-log approximation* because the logarithm is squared.

This formalism can be extended to the emission of more soft gluons, because for soft gluons the matrix element factorizes. Summing up all the contributions from $n \to \infty$ gluon emissions one obtains

$$\Sigma(k_\perp^2) = \exp\left(-\frac{\alpha_s}{2\pi}C_F \ln^2\left(\frac{s}{k_\perp^2}\right)\right) = \exp\left(-\int_{k_\perp^2}^s \frac{\mathrm{d}p_\perp^2}{p_\perp^2}\int_0^{z_M} \mathrm{d}z\; P^R_{qq}(z)\right) . \tag{3.44}$$

The factor $\Sigma(k_\perp^2)$ is referred to as *Sudakov form factor*. Eq. (3.44) has a similar structure as eq. (3.21). One can notice that there is an extra z factor in eq. (3.21). The origin of this factor comes from using momentum weighed parton densities $\widetilde{f}(x,\mu^2)$. Using eq. (3.42) one gets

$$\frac{\mathrm{d}\sigma}{\mathrm{d}k_\perp^2} \approx \hat{\sigma}\frac{\alpha_s}{\pi}C_F\frac{1}{k_\perp^2}\ln\left(\frac{s}{k_\perp^2}\right)\exp\left(-\frac{\alpha_s}{2\pi}C_F\ln^2\left(\frac{s}{k_\perp^2}\right)\right) . \tag{3.45}$$

All the soft gluons giving the contribution $\alpha_s^n\left(\ln^2\left(\frac{s}{k_\perp^2}\right)\right)^n$ are now *resummed* via the exponent, up to all orders in n. The expression from eq. (3.45) does not diverge when $k_\perp^2 \to 0$ but instead it goes to zero.

4 | Other QCD evolution equations

4.1 | BFKL evolution equation

The DGLAP evolution equation sums the contributions proportional to $\alpha_s^n \left(\ln^n \left(\frac{\mu^2}{\mu_0^2}\right) + \ln^{n-1} \left(\frac{\mu^2}{\mu_0^2}\right) + ...\right)$. These contributions are based on collinear factorization so they come from the small angle emissions. However, in the high energy limit, i.e. small x, it becomes important to sum the contributions proportional to $\alpha_s^n \ln^n \frac{1}{x}$. In Sec. 2.2.2 it was discussed that the splitting functions P_{gg}^R and P_{gq}^R are divergent for $z \to 0$ when the gluon, entering the hard interaction, carries only a very small energy. Moreover, when one looks at fig. 2.16, one can see that at small x the gluon parton distribution function dominates. This is why the approach presented in this section concentrates on gluon evolution.

The evolution equation, which sums terms coming from the $1/z$ singularity, $\alpha_s^n \ln^n \frac{1}{x}$, is the *Balitsky-Fadin-Kuraev-Lipatov* (BFKL) evolution equation [31–34]. It evolves the parton density in x: if the parton distribution is known at some scale x_0 it can be evolved with BFKL towards $x < x_0$ as shown in fig. 4.1 [15].

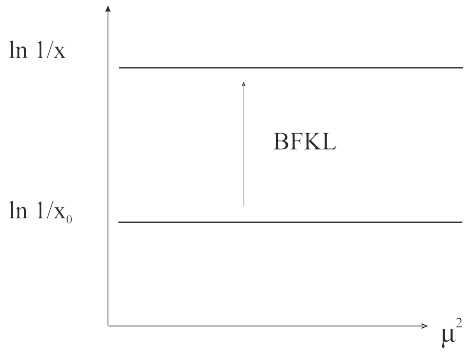

Figure 4.1: The BFKL evolution equation evolves the parton distribution functions in x.

The BFKL equation originates from consideration of a collision of two quark-antiquark bound states called *quarkonia* for which perturbative QCD can be used. The dominant LO process comes from a t-channel gluon exchange shown in fig. 4.2. The ME for this process is proportional to the gluon propagator

$$\mathrm{ME}_{LO} \sim \frac{i g_{\mu\nu}}{l_\perp^2} \,. \tag{4.1}$$

The cross section for this LO process is calculated by taking into account all possible gluon connections to quarks and antiquarks. After the integration over the transverse separations, $x_{1\perp}$, $x_{2\perp}$, between quarks and antiquarks in the quarkonia pairs and their longitudinal momentum fractions and after proper summation and averaging over the quantum numbers, one obtains a cross section independent of s [15]. In [98, 99] the rule was obtained that the contribution of each t-channel exchange particle with spin j to

the total scattering cross section is

$$s^{j-1} \tag{4.2}$$

where s is the center of mass energy squared. When the exchanged particle is a gluon, the cross section should be constant with energy

$$\sigma \sim s^0 \ . \tag{4.3}$$

However, the analyses of the total cross section measurements in pp and $p\overline{p}$ collisions showed that the cross sections grow approximately as [100]

$$\sigma \sim s^{0.08} \ . \tag{4.4}$$

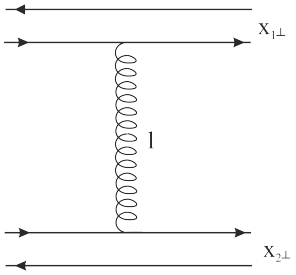

Figure 4.2: LO quarkonium-quarkonium scattering amplitude at high energy.

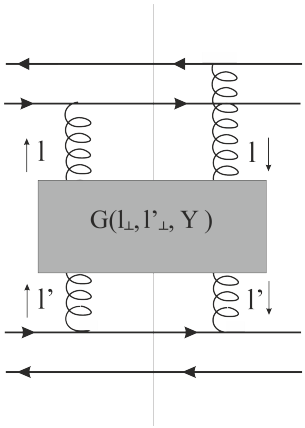

Figure 4.3: Quarkonium-quarkonium scattering amplitude together with its complex conjugate at high energy. The shaded rectangle G denotes all leading $\ln s$ corrections to the LO process.

As a side remark, it is interesting to mention, that before QCD was developed, the cross section of the collision of two hadrons was described in terms of t-channel exchange of some hypothetical particle called *pomeron*. A single pomeron exchange cross section within this description is given by

$$\sigma \sim s^{\epsilon(0)-1} \tag{4.5}$$

where $\epsilon(0)$ is called *pomeron intercept*. The pomeron with $\epsilon(0) - 1 = 0.08$ is called *soft pomeron*.

The increase of the scattering cross section with the energy given by eq. (4.4) is caused by higher order corrections to the process from fig. 4.2. BFKL sums all leading $\ln s$ corrections, which are denoted in fig. 4.3 with a shaded rectangle called Green function G of the BFKL equation.

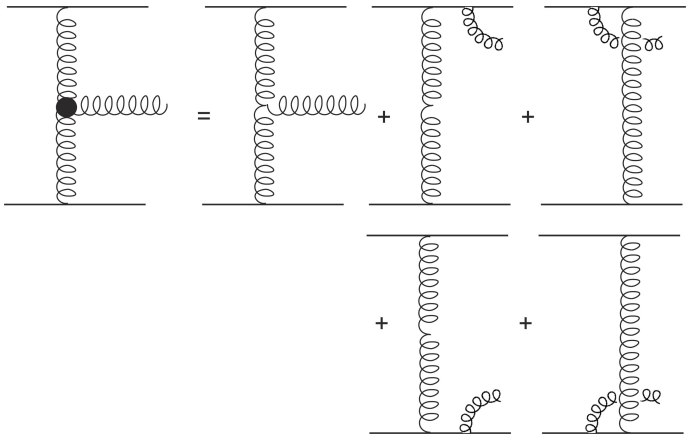

Figure 4.4: Diagrams contributing to the effective Lipatov vertex [15].

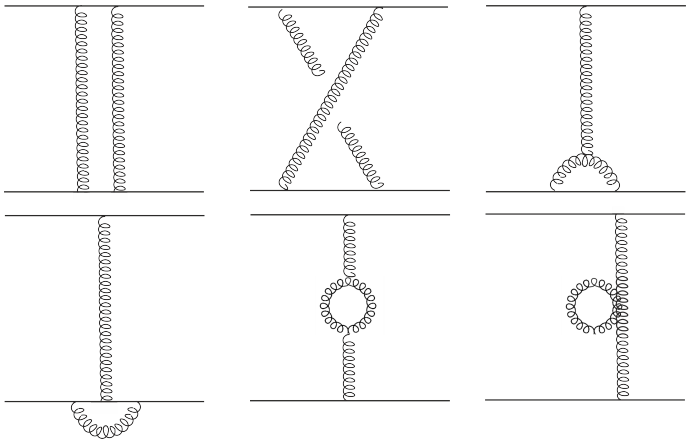

Figure 4.5: LO virtual contributions to the quarkonia scattering amplitude.

All real gluon emission corrections to the scattering from fig. 4.2 are shown in fig. 4.4 on the right hand side of the equality sign. The leading $\ln s$ contributions from all of them sum to the so-called *effective Lipatov vertex* represented by the black dot in the vertex on the left hand side of the equality sign of the fig. 4.4.

Diagrams in fig. 4.5 together with their mirror reflections are all the LO virtual contributions to the quarkonia scattering amplitude.

The total contribution to the amplitude from the virtual corrections from fig. 4.5 can be written as [15]

$$\mathrm{ME}_{virt} = \mathrm{ME}_{LO}(l_\perp)\omega(l_\perp)Y \tag{4.6}$$

where $Y \sim \ln s$, ME_{LO} is the matrix element for the process from fig. (4.2) and $\omega(l_\perp)$ is so called *Regge trajectory*.

It turned out that the higher order virtual corrections in α_s to the amplitude from fig. 4.2 proportional to $\ln s$ can be accounted for by writting the gluon propagator from eq. (4.1) as

$$\frac{ig_{\mu\nu}}{l_\perp^2} s^{\omega(l_\perp)} \,. \tag{4.7}$$

It can be understood as an exchange of a hypothetical particle called *reggeized gluon* with spin $j = 1-\omega$. Such gluons are denoted with the bold gluon line on the Feynman diagrams.

The BFKL equation has the following form [15]

$$\frac{\partial G(l_\perp, l'_\perp, Y)}{\partial Y} = \frac{\alpha_s N_c}{\pi^2} \int \frac{\mathrm{d}^2 q_\perp}{(l_\perp - q_\perp)^2} \left(G(q_\perp, l'_\perp, Y) - \frac{l_\perp^2}{2q_\perp^2} G(l_\perp, l'_\perp, Y) \right) . \tag{4.8}$$

This equation takes into account all the gluon emissions represented by the ladder diagram from fig. 4.6 where the Lipatov vertices and regeized gluons are shown. It is proven [33, 101] that the BFKL equation sums all the leading $\ln s$ corrections up to all orders in α_s, i.e. all the contributions

$$\sim \alpha_s^n \ln^n s \, . \tag{4.9}$$

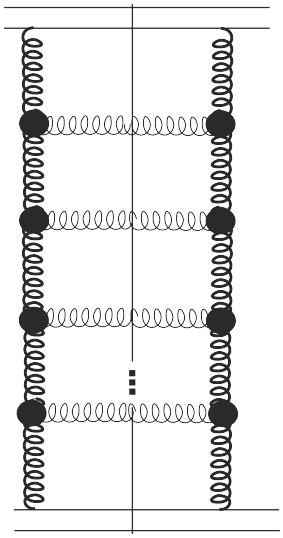

Figure 4.6: BFKL evolution ladder.

The BFKL evolution can be also written in terms of an evolution of *unintegrated gluon distribution* . The quarkonium-quarkonium cross section in light cone variables can be written in the following way [15]

$$\begin{aligned} \sigma \quad \sim \quad & \int \mathrm{d}^2 x_{1\perp} \mathrm{d}^2 x_{2\perp} \int_0^1 \mathrm{d}z_1 \mathrm{d}z_2 |\Psi(x_{1\perp}, z_1)|^2 |\Psi(x_{2\perp}, z_2)|^2 \\ & \int \frac{\mathrm{d}^2 l_\perp \mathrm{d}^2 l'_\perp}{l_\perp^2 l_\perp'^2} \left(2 - e^{-il_\perp x_{1\perp}} - e^{il_\perp x_{1\perp}}\right) \left(2 - e^{-il'_\perp x_{2\perp}} - e^{il'_\perp x_{2\perp}}\right) G(l, l', Y) \end{aligned} \tag{4.10}$$

where $x_{1\perp}, x_{2\perp}$ are the transverse sizes of the quarkonia systems and z_1, z_2 are the light cone momenta fraction carried by the quarks exchanging gluon, Ψ are the quarkonia light cone wave functions. From there one can introduce a concept of *unintegrated gluon distribution* $\mathcal{F}(x, l_\perp)$ by defining

$$\mathcal{F}(x, l_\perp) = \frac{\alpha_s C_F}{\pi} \int \mathrm{d}^2 x_{2\perp} \int_0^1 \mathrm{d}z_2 |\Psi(x_{2\perp}, z_2)|^2 \int \frac{\mathrm{d}^2 l'_\perp}{l_\perp'^2} \left(2 - e^{-il'_\perp x_{2\perp}} - e^{il'_\perp x_{2\perp}}\right) G(l, l', Y) \, . \tag{4.11}$$

The unintegrated distribution function obeys the same equation as the Green function

$$\frac{\partial \mathcal{F}(x, l_\perp)}{\partial \ln\left(\frac{1}{x}\right)} = \frac{\alpha_s N_c}{\pi^2} \int \frac{\mathrm{d}^2 q_\perp}{(l_\perp - q_\perp)^2} \left(\mathcal{F}(x, q_\perp) - \frac{l_\perp^2}{2q_\perp^2} \mathcal{F}(x, l_\perp) \right) \tag{4.12}$$

and it counts the number of gluons inside the hadron with a longitudinal momentum fraction x and the transverse momentum $l_\perp$.

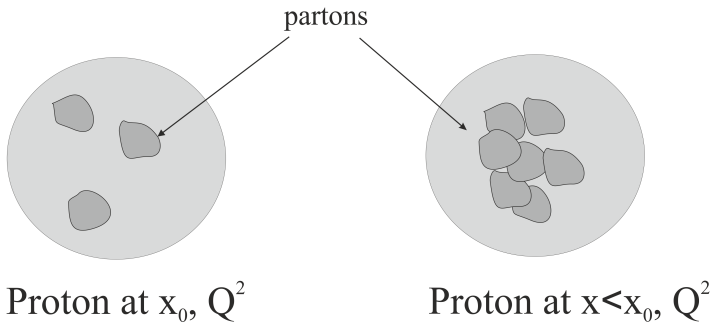

Figure 4.7: Proton in the plane transverse to the beam axis. At small x many new partons are created.

The BFKL equation predicts a cross section which rises as a power of energy $\sigma_{\rm tot} \approx s^{4N_C \frac{\alpha_s}{\pi} \ln 2}$ [102]. This violates the Froissart- Martin bound [103]. The Froissart-Martin bound is a consequence of the *black disc limit* which in nonrelativistic quantum mechanics says that the total cross section for the scattering of the point-like particle on an infinite spherical potential of a radius R (the "black disc") is limited $\sigma_{tot} \leq 2\pi R^2$. Froissart and Martin obtained the QCD version of the black disc limit by considering hadron-hadron collision with impact parameter b. From eq. (4.4) it is known that the cross section has to grow with energy as some positive power Δ. It also has to decrease with the increase of the impact parameter b. Froissart and Martin assumed the slowest physically possible fall e^{-2mb} where m is the mass of the lightest QCD bound state pion. The probability of the interaction is then [15]

$$p \sim s^{\Delta} e^{-2mb} \, . \tag{4.13}$$

The black disc upper limit can be obtained by requiring that $p \approx 1$

$$s^{\Delta} e^{-2mb} = 1 \, . \tag{4.14}$$

From that one obtains

$$b = \frac{\Delta \ln s}{2m} \, . \tag{4.15}$$

By putting $R = b$ and $\sigma_{tot} \leq 2\pi R^2$ one obtains the bound

$$\sigma_{\rm tot} \leq \frac{\Delta^2 \pi \ln^2 s}{2m^2} \tag{4.16}$$

which says that the total cross section can not be greater than the logarithm squared of center of mass energy squared multiplied by some constant.

In BFKL, the transverse sizes of the emitted partons are similar $x_\perp \approx \frac{1}{k_\perp}$ because their typical transverse momenta are of the same order [15]. As a consequence, at some point during the evolution process partons start to overlap and a *dense* system is produced. The picture arising from BFKL can be illustrated by fig. 4.7 [15]. At smaller x there are many more partons inside the proton than at higher x and they create the so-called Colour Glass Condensate (CGC) [104].

Some mechanism has to be introduced to the BFKL equation to slow down the small x evolution in order to make the cross section obey the Froissart - Martin bound. A solution is a concept of *saturation* which says that at very high energies partons can *recombine*: two partons can merge into one. This effect is proportional to the number of pairs of partons which scales as N^2. It can be introduced to BFKL by adding a non-linear term [105, 106]. The exact form of the equation in the limit of large number of colours N_c was given by Balitsky and Kovchegov (BK) [107, 108] and generalised beyond large N_c by Jalilian-Marian-Iancu-McLerran-Weigert-Leonidov-Kovner (JIMWLK) equation [104, 109–112].

4.2 | CCFM evolution equation

The *Catani-Ciafaloni-Fiorani-Marchesini* (CCFM) equation [93, 113–115] combines the formalism of the BFKL evolution equation and DGLAP. It resums not only the singularities coming from $1/z$ terms in the splitting function but also $1/(1-z)$ terms. In the high energy limit CCFM is equivalent to BFKL equation, for large x and high Q^2 it is similar to DGLAP evolution. It includes the angular ordering condition to treat properly gluon coherence effects.

In DGLAP evolution, the Sudakov form factor contains the $1/(1-z)$ terms which cancel the divergences coming from the soft gluons. The idea incorporated in the CCFM equation is to treat the singularities at $1/z$ in a similar way as the $1/(1-z)$ terms are treated in DGLAP. This is done by introducing so-called *non-Sudakov form factor*.

In the CCFM formalism the DGLAP equation is rewritten for an *unintegrated PDF* which depends now on one extra variable - transverse momentum $k_\perp$ [93, 94]

$$\overline{q}^2 \frac{\mathrm{d}}{\mathrm{d}\overline{q}^2} \frac{xA(x,k_\perp^2,\overline{q}^2)}{\Delta_s(\overline{q}^2,Q_0^2)} = \int \mathrm{d}z \frac{\mathrm{d}\Phi}{2\pi} \frac{\widetilde{P}\left(z,\left(\frac{\overline{q}}{z}\right)^2,k_\perp^2\right)}{\Delta_s(\overline{q},Q_0^2)} x'A\left(x',k_\perp'^2,\left(\frac{\overline{q}}{z}\right)^2\right) \tag{4.17}$$

where $\overrightarrow{k}'_\perp = |\overrightarrow{k}_\perp + (1-z)/(z\overrightarrow{q})|$, $\overrightarrow{q}$ is at the azimuthal angle Φ, $z = \frac{x}{x'}$ and $\overline{q}$ is defined in eq. (3.12) together with ordering condition in eq. (3.14).

The Sudakov form factor is defined as

$$\Delta_s\left(\overline{q}^2,Q_0^2\right) = \exp\left(-\int_{Q_0^2}^{\overline{q}^2} \frac{\mathrm{d}\overline{q}'^2}{\overline{q}'^2} \int_0^{1-\frac{Q_0}{\overline{q}'}} \mathrm{d}z \frac{\overline{\alpha}_s\left(\overline{q}'^2(1-z)^2\right)}{1-z}\right) \tag{4.18}$$

where $\overline{\alpha}_s = C_A\alpha_s/\pi$. The splitting function is given by

$$\widetilde{P}\left(z_i,\overline{q}_i^2,k_{\perp,i}^2\right) = \frac{\overline{\alpha}_s\left(\overline{q}_i^2(1-z_i)^2\right)}{1-z_i} + \frac{\overline{\alpha}_s\left(k_{\perp,i}^2\right)}{z_i} \Delta_{NS}\left(z_i,\overline{q}_i^2,k_{\perp,i}^2\right) \tag{4.19}$$

where the *non-Sudakov form factor* Δ_{NS} is

$$\Delta_{NS}\left(z_i,\overline{q}_i^2,k_{\perp,i}^2\right) = \exp\left(-\overline{\alpha}_s\left(k_{\perp,i}^2\right) \int_{z_0 z_i \overline{q}_i^2}^{k_{\perp,i}^2} \frac{\mathrm{d}\overline{q}'^2}{\overline{q}'^2} \int_{z_i}^{z_0} \ln\frac{\mathrm{d}z}{z}\right) \tag{4.20}$$

and

$$z_0 = \begin{cases} 1 \;\text{ if }\; k_{\perp,i}/\overline{q}_i > 1\,, \\ k_{\perp,i}/q_{\perp,i} \;\text{ if }\; z_i < k_{\perp,i}/\overline{q}_i \le 1\,, \\ z_i \;\text{ if }\; k_{\perp,i}/\overline{q}_i \le z_i\,. \end{cases} \tag{4.21}$$

The Sudakov form factor resums contribution from large z region, non-Sudakov from small z.

Both of the evolution equations discussed in this chapter introduce the concept of PDF which depends on the new variable - the transverse momentum. In the next chapter we discuss this topic further.

5 | Transverse momentum dependent PDFs

5.1 | TMD factorization theorem

Collinear PDFs describe the structure of hadrons in the longitudinal direction only. But one can think also about a 3-dimensional imagining of hadrons with some "extended" parton distribution. Such a distribution is the Transverse Momentum Dependent (TMD) PDF which is a generalization of the concept of the PDF. TMD PDFs depend not only on x and μ^2 but also on $k_\perp$. The TMD PDFs will be referred to as TMDs throughout this thesis.

Collinear factorization gives predictions for a wide range of sufficiently inclusive observables in which only one hard scale is relevant (for example the virtuality of the exchanged photon in DIS) and the transverse momenta are integrated over. However, it is known that there are some observables, for example with the transverse momenta measured in the final states, which cannot be predicted with standard collinear factorization (e.g. [116]). In this case TMD PDFs are introduced and a new *TMD factorization theorem* is obtained to factorise perturbative and non-perturbative dynamics. There are many areas where the TMDs play an important role, such as resummation of all orders in the QCD coupling in high-energy hadronic collisions, a proper and consistent simulation of parton showers, multi-scale problems in hadronic collisions etc. TMD factorization theorems can be divided into two groups.

Collins-Soper-Sterman factorization *Collins-Soper-Sterman (CSS)* style of the TMD factorization has been formulated for processes like semi-inclusive DIS(SIDIS), DY and e^+e^- annihilation [117–130]. The formalism is valid for for $q_\perp \ll Q$.

High energy ($k_\perp$-) factorization Another type of TMD factorization theorem was obtained for heavy flavours and heavy boson production in the high energy limit $s \to \infty$ and for arbitrarily large momentum transfer [131–136].

These two approaches differ in many aspects, such as the formalism used, the TMDs concept or the physical application and this makes the comparison of them very complicated.

Historically, the CSS TMD factorization formula was obtained for the DY cross section [123]. When one looks at the eq. (3.45)

$$\frac{\mathrm{d}\sigma}{\mathrm{d}k_\perp^2} \approx \hat{\sigma}\frac{\alpha_s}{\pi}C_F\frac{1}{k_\perp^2}\ln\left(\frac{s}{k_\perp^2}\right)\exp\left(-\frac{\alpha_s}{2\pi}C_F\ln^2\left(\frac{s}{k_\perp^2}\right)\right) \tag{5.1}$$

it can be interpreted as a resummation of the contributions proportional to $\alpha_s^n \ln^{2n}\left(\frac{s}{k_\perp^2}\right)$ by exponentiation of the soft gluon emissions. The formula for the cross section vanishes when $k_\perp^2$ goes to zero. The suppression is too strong since the measured cross section does not vanish at small $k_\perp$. The idea how to deal with this problem was to introduce transverse momentum conservation for the n gluons emission $\delta(p_\perp^2 - k_{\perp 1}^2 - ... - k_{\perp n}^2)$, where $p_\perp^2$ is the sum of the transverse momenta of all emitted gluons. The next issue was how to include in the cross section formula not only terms proportional to $\alpha_s^n \ln^{2n}\left(\frac{s}{k_\perp^2}\right)$ but also sub-leading contributions. These were incorporated within CSS formalism. The delta function and the exponentiation was performed within CSS in b space, where b is a variable Fourier conjugated to the transverse momentum. The following cross section formula was obtained

$$\begin{aligned}\frac{\mathrm{d}\sigma}{\mathrm{d}Q^2\mathrm{d}y\mathrm{d}Q_T^2} \sim \frac{4\pi^2\alpha^2}{9Q^2 s}\frac{1}{(2\pi)^2}\int \mathrm{d}^2 b \exp(iQ_T\cdot b)\sum_j e_j^2 \\ \cdot\sum_a \int_{x_A}^1 \frac{\mathrm{d}\xi_A}{\xi_A} f_{a/A}(\xi_A, 1/b)\sum_b \int_{x_B}^1 \frac{\mathrm{d}\xi_B}{\xi_B} f_{b/B}(\xi_B, 1/b) \\ \exp\left(-\int_{1/b^2}^{Q^2}\frac{\mathrm{d}\overline{\mu}^2}{\overline{\mu}^2}\left[\ln\left(\frac{Q^2}{\overline{\mu}^2}\right)A(g(\overline{\mu})) + B(g(\overline{\mu}))\right]\right) \\ \cdot C_{ja}\left(\frac{x_A}{\xi_A}, g(1/b)\right) C_{jb}\left(\frac{x_B}{\xi_B}, g(1/b)\right) \\ + \frac{4\pi^2\alpha^2}{9Q^2 s} Y(Q_T, Q, x_A, x_B)\end{aligned} \tag{5.2}$$

where $f_{a/A}$ are the parton distribution functions of a parton of species a (gluon and quark and antiquark flavours) in hadron A at the renormalization scale $1/b$, ξ_A is the momentum fraction of a hadron A carried by the parton a, $x_A = \mathrm{e}^y Q/s^{1/2}$, $x_B = \mathrm{e}^{-y} Q/s^{1/2}$, $y = \frac{1}{2}\ln(Q^+/Q^-)$, Q is the mass of the produced boson, Q_T is its transverse momentum, e_j is a charge of a quark of flavour j in the units of e. The functions A, B and C have a perturbative series expansion, term A sums the leading logarithms, term B the next-to-leading ones. The coherent branching formula with a simplified form of the P_{qq}^R splitting function, discussed in Sec. (3.2.3), reproduces the first coefficient in the A expansion, $A^{(1)} = \frac{\alpha_s}{\pi} C_F$ [92]. The first term of the equation is dominant at small transverse momenta $Q_T \ll Q$. The term Y is introduced to match the solution for the region $Q_T \sim Q$.

More details about CSS formalism can be found in [122, 137].

The high energy TMD factorization was obtained to give a prescription for a cross section calculation with BFKL evolution. In BFKL, the virtuality and transverse momentum of the propagating gluon are not ordered and the matrix elements have to be taken off-shell together with a convolution with unintegrated parton distributions. The factorization was obtained for the heavy flavour hadroproduction cross section [131, 132]

$$4M^2\sigma(\rho, M^2) = \int \mathrm{d}^2 k_{\perp 1}\mathrm{d}^2 k_{\perp 2}\int_0^1 \frac{\mathrm{d}z_1}{z_1}\frac{\mathrm{d}z_2}{z_2}\hat{\sigma}\left(\frac{\rho}{z_1 z_2}, k_{\perp 1}, k_{\perp 2}, M^2\right)\mathcal{F}(z_1, k_{\perp 1})\mathcal{F}(z_2, k_{\perp 2}) \tag{5.3}$$

where $\rho = 4M^2/s$, M is the invariant mass of the heavy flavour system, s is the centre of mass energy, $k_{\perp 1,2}$ are the transverse momenta of the incoming gluons, $\mathcal{F}$ are the unintegrated gluon structure functions obeying the BFKL equation, $\hat{\sigma}$ is the off-shell Born cross section for $g^*(k_1) + g^*(k_2) \to Q + \overline{Q}$, $z_{1,2}$ are the fractions of the longitudinal momenta of the colliding hadrons carried by the incoming gluons. Similar factorization formulas were also obtained for lepto- and photo-production.

The eq. (5.2) and eq. (5.3) were obtained for different processes. To compare these two formalism one should consider a process, which can be calculated in both of them, for example Higgs production

through gluon - gluon fusion.
In ref. [138, 139] the total cross section and transverse momentum distributions for $g^*g^* \to H$ was calculated within high energy ($k_\perp$-) factorization with unintegrated gluon distributions obtained from the full CCFM evolution equation [140]. The predictions describe well the LHC 8 and 13 TeV data.
In ref. [141] CSS and small x factorization results were compared for the transverse momentum distributions of Higgs boson in the dilute region and they were found to be consistent.
The detailed comparison of different TMD approaches is still one of the challenges of the TMDs community and there is an ongoing effort. A library TMDlib [142] to collect the different parametrizations in one place and a plotting tool TMDplotter [143] were created to make the comparison easier.
An overview of the field can be found in [144].

In the next sections some of the methods to obtain TMDs and some of the analyses involving TMDs are briefly discussed.

5.2 | Methods to obtain TMDs

The methods to obtain TMDs are based on semi-analytic or approximate solutions of TMD evolution equations, perturbative expansions of the TMDs in terms of collinear pdfs, or some combinations of both. The parameters of the models must be fitted to experimental data to get the TMD sets which can be later used in other experiments.

5.2.1 | TMDs parametrizations

In this subsection several TMD parametrizations included in the TMDlib and TMDplotter [142, 143] are introduced and compared.

TMDs from BFKL A parametrization of an unintegrated gluon distribution satisfying the BFKL equation was proposed by Blumlein [145]. The gluon TMD was obtained as a convolution of an integrated gluon distribution with some function $\mathcal{B}$ [146]

$$\mathcal{F}\left(x, k_\perp^2, \mu^2\right) = \int_x^1 \mathrm{d}z \mathcal{B}\left(z, k_\perp^2, \mu^2\right) \frac{x}{z} g\left(\frac{x}{z}, \mu^2\right) \tag{5.4}$$

where $\mathcal{B}$ can be expanded in terms of series, in which the first term incorporates BFKL dynamics in the double-logarithmic approximation

$$\mathcal{B}\left(z, k_\perp^2, \mu^2\right) = \begin{cases} \frac{\overline{\alpha_s}}{z k_\perp^2} J_0\left(2\sqrt{\overline{\alpha_s} \ln\left(\frac{1}{z}\right) \ln\left(\frac{\mu^2}{k_\perp^2}\right)}\right) & \text{if} \quad k_\perp^2 < \mu^2 \,, \\ \frac{\overline{\alpha_s}}{z k_\perp^2} J_0\left(2\sqrt{\overline{\alpha_s} \ln\left(\frac{1}{z}\right) \ln\left(\frac{k_\perp^2}{\mu^2}\right)}\right) & \text{if} \quad k_\perp^2 > \mu^2 \end{cases} . \tag{5.5}$$

J_0 is the Bessel function and $\overline{\alpha_s} = 2\alpha_s/\pi$.
The method was studied for $x \in (10^{-4}, 1)$. For $x \geq 10^{-3}$ it approaches BFKL double logarithmic approximation [145].

TMDs from the PB method with CCFM and DGLAP One way to obtain TMDs, which incorporates small and large x behaviour, is to solve the CCFM evolution equation.

TMDs from CCFM were obtained in [147, 148] by solving the CCFM evolution equation with a parton branching Monte Carlo method [149]. The light quark evolution was also included according to a method described in [150, 151]. The fits to HERA measurements of the F_2 structure function to obtain TMDs with experimental and theoretical uncertainties were performed using the `herafitter` platform (the mother of `xFitter` [152]). This method was restricted to $x < 0.005$ and $Q^2 > 5$ GeV^2.

The subject of this thesis, which will be discussed in the following chapters, is the determination of TMDs from the PB solution of DGLAP equation [65, 66]. The approach extends the method developed in [147, 148]. The solution with DGLAP is not limited to small x but is applicable in a wide range of x. This method allows also to perform the fits to HERA measurements of the F_2 structure function.

TMDs from GBW dipole model In the method of Golec-Biernat-Wusthoff [153, 154], the parametrization of the dipole-nucleon cross section was used to obtain an unintegrated proton gluon distribution. In the dipole model of DIS, the virtual photon splits into a quark- antiquark pair (dipole), which scatters on the proton [153]. The quark-antiquark cross section and unintegrated distribution are related in the following way within this model [154]

$$\hat{\sigma}(x,r) = \frac{4\pi^2}{3} \int \frac{\mathrm{d}k_\perp^2}{k_\perp^2} \left(1 - J_0(k_\perp r)\right) \alpha_s \mathcal{F}\left(x, k_\perp^2\right) \tag{5.6}$$

and from that

$$\alpha_s \mathcal{F}\left(x, k_\perp^2\right) = \frac{3}{4\pi^2} \sigma_0 R_0^2(x) k_\perp^2 \mathrm{e}^{-R_0^2(x) k_\perp^2} \tag{5.7}$$

where $R_0(x) = \frac{1}{\mathrm{GeV}} \left(\frac{x}{x_0}\right)^{\lambda/2}$. The free parameters of GBW σ_0, x_0 and λ, were fitted to HERA data. This approach is valid for $x < 0.01$ and small Q^2.

TMDs from MRW Kimber, Martin and Ryskin (KMR) developed an easy idea of how to obtain unintegrated parton distribution functions (uPDF) using the DGLAP equation and *last step* evolution to generate $k_\perp$ [155], and later extended it into the Martin-Ryskin-Watt (MRW) version of KMR [156, 157].

This approach is based on the assumption of strong $k_\perp$ ordering in the DGLAP evolution and on the approximation that the $k_\perp$ of the parton entering the hard interaction comes mainly from the last branching in the evolution (up to the leading order accuracy [156]).

At LO, the standard collinear DGLAP evolution is performed up to a scale $k_\perp$. The $k_\perp$ dependent parton distribution is obtained from the collinear one by taking into account only the last real emission and summing all the virtual contributions between $k_\perp^2$ and μ^2 via Sudakov form factor. The LO MRW evolution equation can be written in the following way, for quark and gluon separately

$$\begin{aligned} \widetilde{f}_q\left(x, k_\perp^2, \mu^2\right) =& \Delta_q\left(\mu^2, k_\perp^2\right) \int_x^1 \mathrm{d}z \left(P_{qq}^R\left(z, \alpha_s\left(k_\perp^2\right)\right) \widetilde{f}_q\left(\frac{x}{z}, k_\perp^2\right) \Theta(1 - z_M(k_\perp^2) - z) \right. \\ & \left. + 2 n_f P_{qg}^R\left(z, \alpha_s\left(k_\perp^2\right)\right) \widetilde{f}_g\left(\frac{x}{z}, k_\perp^2\right) \right) , \end{aligned} \tag{5.8}$$

$$\begin{aligned} \widetilde{f}_g\left(x, k_\perp^2, \mu^2\right) =& \Delta_g\left(\mu^2, k_\perp^2\right) \int_x^1 \mathrm{d}z \left(P_{gg}^R\left(z, \alpha_s\left(k_\perp^2\right)\right) \widetilde{f}_g\left(\frac{x}{z}, k_\perp^2\right) \Theta(1 - z_M(k_\perp^2) - z) \right. \\ & \left. + P_{gq}^R\left(z, \alpha_s\left(k_\perp^2\right)\right) \widetilde{f}_q\left(\frac{x}{z}, k_\perp^2\right) \right) , \end{aligned} \tag{5.9}$$

where the z_M parameter expresses an angular ordering condition

$$z_M(k_\perp) = \frac{k_\perp}{k_\perp + \mu} . \tag{5.10}$$

The Sudakov form factors are defined

$$\begin{aligned}\Delta_q\left(\mu^2,k_\perp^2\right) = &\quad \exp\left[-\int_{k_{\perp 2}}^{\mu^2}\frac{\mathrm{d}\kappa_\perp^2}{\kappa^2}\int_0^1 \mathrm{d}z\; z\left(P_{qq}^R\left(z,\alpha_s(\kappa_\perp^2)\right)\Theta\left(1-z_M\left(\kappa_\perp^2\right)-z\right)+P_{gq}^R\left(z,\alpha_s(\kappa_\perp^2)\right)\right)\right]\\ \Delta_g\left(\mu^2,k_\perp^2\right) = &\quad \exp\left[-\int_{k_\perp^2}^{\mu^2}\frac{\mathrm{d}\kappa_\perp^2}{\kappa_\perp^2}\int_0^1 \mathrm{d}z\; z\left(P_{gg}^R\left(z,\alpha_s(\kappa_\perp^2)\right)\Theta\left(1-z_M\left(\kappa_\perp^2\right)-z\right)+2n_f P_{qg}^R\left(z,\alpha_s(\kappa_\perp^2)\right)\right)\right]\end{aligned} \tag{5.11}$$

where the splitting functions are at LO. The unintegrated distributions satisfy the normalization condition

$$\widetilde{f}_a(x,\mu^2) = \int_0^{\mu^2}\frac{\mathrm{d}k_\perp^2}{k_\perp^2}\widetilde{f}_a(x,k_\perp^2\mu^2) \tag{5.12}$$

with the assumption that the parton density for $k_\perp < \mu_0$ for a given x and μ is

$$\left.\frac{1}{k_\perp^2}\widetilde{f}_a(x,k_\perp^2,\mu^2)\right|_{k_\perp<\mu_0} = \frac{1}{\mu_0^2}\widetilde{f}_a(x,\mu^2)\Delta_a(\mu^2,\mu_0^2) \tag{5.13}$$

where $\mu_0 \approx 1$ GeV. From that one can write a differential definition of the unintegrated distribution

$$\frac{1}{k_\perp^2}\widetilde{f}_a(x,k_\perp^2\mu^2) = \frac{\partial\left(\widetilde{f}_a(x,k_\perp^2)\Delta_a(\mu^2,k_\perp^2)\right)}{\partial k_\perp^2}\,. \tag{5.14}$$

At NLO, a new scale is used within MRW

$$k^2 = \frac{k_\perp^2}{1-z}\,. \tag{5.15}$$

The difference between TMDs evolved using k^2 or $k_\perp^2$ is very small at LO or very small z, which is why it was not introduced at LO [156]. With this change the unintegrated parton density is defined as

$$\widetilde{f}_a(x,k_\perp^2,\mu^2) = \int_x^1 \mathrm{d}z\Delta_a\left(\mu^2,k^2\right)\sum_b\frac{\alpha_s\left(k^2\right)}{2\pi}\widetilde{P}_{ab}^{(0+1)}\left(z,k^2\right)\widetilde{f}_b\left(\frac{x}{z},k^2\right)\Theta\left(1-z-\frac{k_\perp^2}{\mu^2}\right) \tag{5.16}$$

where

$$\widetilde{P}_{ab}^{(0+1)}\left(z,k^2\right) = \widetilde{P}_{ab}^{(0)}\left(z,k^2\right) + \frac{\alpha_s\left(k^2\right)}{2\pi}\widetilde{P}_{ab}^{(1)}\left(z,k^2\right) \tag{5.17}$$

and

$$\widetilde{P}_{ab}^{(i)}\left(z,k^2\right) = P_{ab}^{(i)}\left(z,k^2\right) - \Theta(z-1+z_M(k_\perp))F_{ab}^{(i)}\left(k^2\right)\delta_{ab}p_{ab}(z) \tag{5.18}$$

with

$$\begin{aligned}F_{qq}^{(0)} &= C_F\,,\\ F_{gg}^{(0)} &= 2C_A\,,\\ F_{qq}^{(1)}\left(k^2\right) &= -C_F\left(\frac{10}{9}T_R n_f\left(k^2\right)+C_A\left(\frac{\pi^2}{6}-\frac{67}{18}\right)\right)\,,\\ F_{gg}^{(1)}\left(k^2\right) &= -2C_A\left(\frac{10}{9}T_R n_f\left(k^2\right)+C_A\left(\frac{\pi^2}{6}-\frac{67}{18}\right)\right)\,,\\ p_{qq}(z) &= (1+z^2)/(1-z)\,,\\ p_{gg}(z) &= z/(1-z)+(1-z)/z+z(1-z)\,.\end{aligned} \tag{5.19}$$

In [158] TMD sets are obtained with this approach.

The equivalence of the integral (eq. (5.8) - (5.9)) and differential (eq. (5.14)) definition of the KMR unintegrated PDFs is discussed in [159].

Comparison To conclude this section we compare the gluon TMDs obtained from Blumlein, GBW, MRW and PB with CCFM and DGLAP methods listed above. For the PB method with DGLAP evolution we show the set which is the result of this thesis, obtained with angular ordering and with $\alpha_s((1-z)^2\mu'^2)$ (details are given in Sec. (9.1)). We plot the distributions using TMDplotter. Fig. 5.1 shows the comparison of the gluon TMD with a logarithmic scale on the y axis, fig. 5.2 with the linear one. One can clearly see that the differences between these parametrizations are huge.

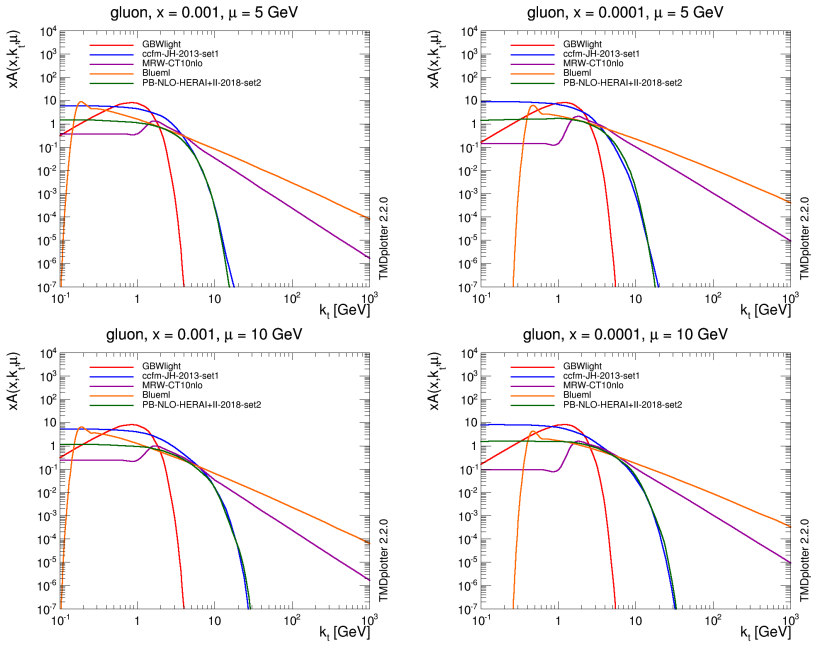

Figure 5.1: TMDs obtained from different parametrizations included in the TMDlib with a logarithmic scale on the y axis.

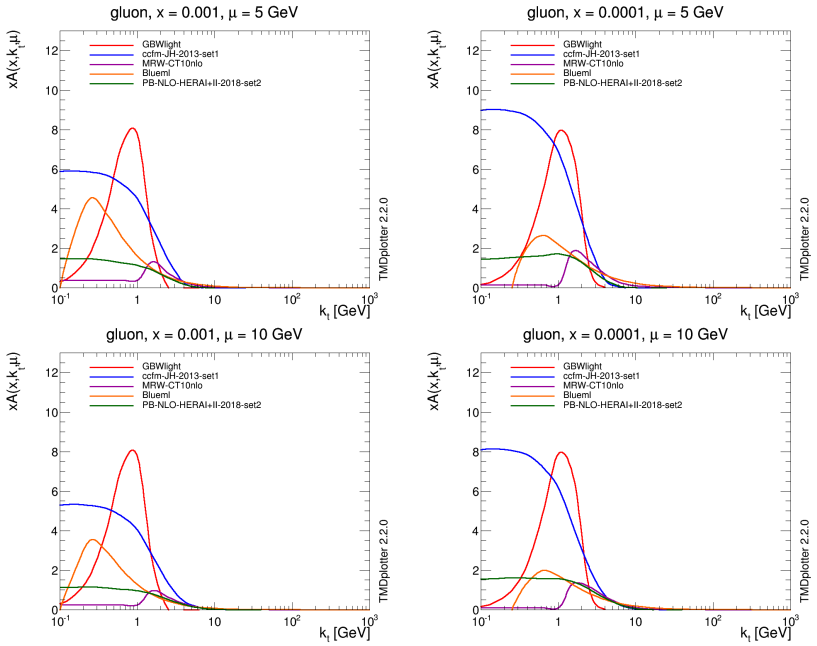

Figure 5.2: TMDs obtained from different parametrizations included in the TMDlib with a linear scale on the y axis.

CCFM and DGLAP TMDs are similar at large $k_\perp$ while GBW, Blumlein and MRW are very different. Only the MRW and PB with DGLAP approach include also the evolution of quarks and antiquarks of all flavours. CCFM approach includes the evolution of the light quarks. CCFM and DGLAP take into account the coherent branching effects. GBW and Blumlein methods parametrize only gluon distribution. An important difference compared to the other parametrizations is that the GBW includes no evolution in μ. To make a conclusion which of the given parametrizations are better than others it is necessary to compare them with measurements.

5.2.2 | Fits of TMDs to experimental data

In addition to the TMD fits described in Sec. (5.2.1) based on PB solution of CCFM [147, 148] and DGLAP equation, which is the major topic of this thesis, there is a huge experimental attempt to extract low $q_\perp$ TMDs based on CSS evolution equations. New analysis extracting unpolarized TMDs simultaneously from SIDIS, DY and Z boson q_T measurements are presented in [160]. The fit is valid only for low $q_\perp$ and it does not contain any matching to fixed-order calculations at high transverse momentum. References to previous TMD extractions can be found therein. Some of the important issues connected with such TMDs are the parametrization of the nonperturbative component and including flavour dependence of the intrinsic transverse momenta [161].

5.3 | Applicability of TMDs

One example of an observable, which cannot be described with standard collinear PDFs and perturbation theory, is the turnover and the low $q_\perp$ region of the Z boson differential cross section, as shown in fig. 5.3 [162]. This region is dominated by soft gluon emissions which cannot be explained by fixed order expansion in perturbative QCD. Instead, a method to sum all the soft gluon contributions is needed. In an approach used in [162] soft gluon emissions and nonperturbative effects at low $q_\perp$ are simulated by Monte Carlo generators (PYTHIA [163] with different tunes and POWHEG [164, 165] + PYTHIA with different tunes). The predictions and CMS data are presented in fig. 5.3 showing that the agreement for PYTHIA with Z2 tune ($\chi^2/ndof = 9.4/8$) and ProQ20 tune ($\chi^2/ndof = 13.3/8$) is good [162]. Another solution could be the usage of TMDs, which solve this issue by summing the enhanced contributions in $\ln M/q_\perp$ up to all orders in α_s [121–123].

The next famous problem of the collinear approach which can be solved by TMD factorization is the raise of the proton PDFs at small x. This region is crucial for many cross sections measured at the LHC but the parton distributions have big uncertainties there and the higher order corrections in perturbation theory can make a huge change. This region is dominated by the radiation over long intervals in rapidity of the gluons unordered in transverse momenta, present up to all orders in perturbation theory [105,166–168]. Here the TMD factorization theorem allows one to sum up enhanced contributions coming from these unordered gluons, proportional to $\ln \sqrt{s}/Q$, where Q is the evolution mass scale and $\sqrt{s}$ is the center of mass energy [131, 132, 134, 135].

Another example of an LHC process, where TMD factorization can be applied, is the measurement of the Higgs differential cross section as a function of $q_\perp$. The main chain of the Higgs boson production is gluon fusion dominated by single eikonal gluon polarization which depends on gluon transverse

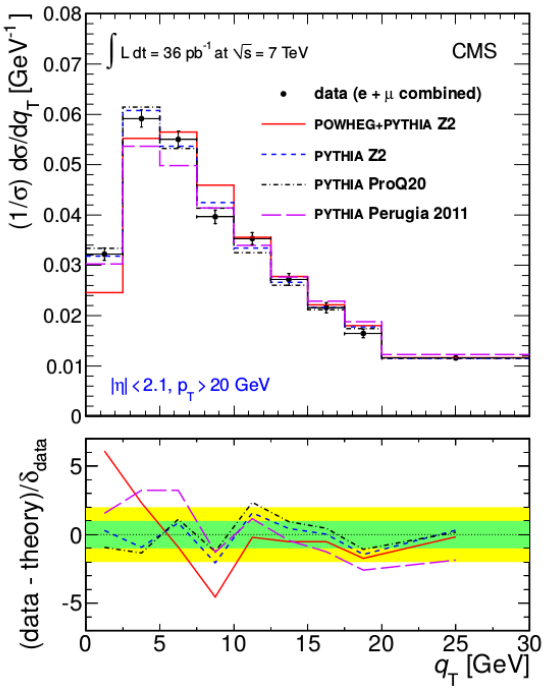

Figure 5.3: Upper part: differential cross section for Z-boson production in pp collision at the LHC as a function of the Z-boson transverse momentum q_T in the lepton pair's invariant mass range $60 < M < 120$ GeV compared with different predictions. Lower part: the difference between the data and the simulation predictions divided by the uncertainty δ on the data. The green (inner) and yellow (outer) bands are the $\pm\delta$ and $\pm 2\delta$ experimental uncertainties [162].

momentum [169]. The contribution of the polarized gluons in the low $q_\perp$ region for Higgs production was studied perturbatively [170–174] and nonperturbatively [141, 175–178]. As mentioned in Sec. (5.1), TMDs can be also used to study Higgs boson production at high momenta (e.g. [138, 139]).

High energy TMD factorization plays an important role in the scenarios with heavy boson production together with high jet multiplicity where high transverse momenta are involved. At higher energies, when the finite order matrix elements for multi-jets are merged with a collinear parton shower, the jet multiplicity distributions and angular correlations are affected due to soft but finite-angle multi-gluon radiation [113, 149, 179]. Moreover, the collinear approximation combined with energy-momentum conservation leads to longitudinal momentum shifts and shower corrections when multi-jet final states are simulated [180–182]. A TMD treatment of QCD shower evolution takes into account such effects correctly. An example can be found in ref. [183] where the azimuthal correlations in $W + n$ jets production predicted by high energy TMD factorization was studied with an unintegrated gluon distribution obtained using CCFM evolution equation in [148]. The azimuthal separation $\Delta\Phi$ between the two hardest jets is shown in fig. 5.4.

An interesting field to study TMDs at low mass scales are the processes of quarkonium production. An example of such an analysis is the production of J/Ψ and $\Psi(2S)$ from the decays of b-flavoured hadrons at LHC which was studied in $k_\perp$ factorization [185]. The authors used off-shell matrix elements [186–188] together with unintegrated gluon distribution obtained from CCFM evolution equation in [189]. They

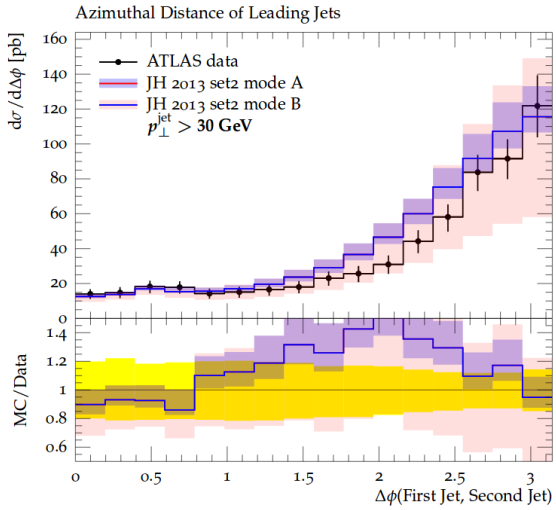

Figure 5.4: Azimuthal separation $\Delta\Phi$ between the two hardest jets associated with W-bosons. The purple and pink bands correspond to different methods of obtaining TMDs from CCFM equation [183]. The experimental data come from [184] with the experimental uncertainty represented by the yellow band [183].

based their investigations on the dominant off-shell gluon-gluon fusion where the transverse momenta of initial gluons are important. They obtained predictions for the double differential cross sections of inclusive non-prompt J/Ψ, $\Psi(2S)$ and associated production of J/Ψ and Z boson as a function of their transverse momenta and rapidities which agree very well with the measurements from CMS, ATLAS and LHCb. An example can be found in fig. 5.5. Other quarkonia studies can be found for example in [190–197].

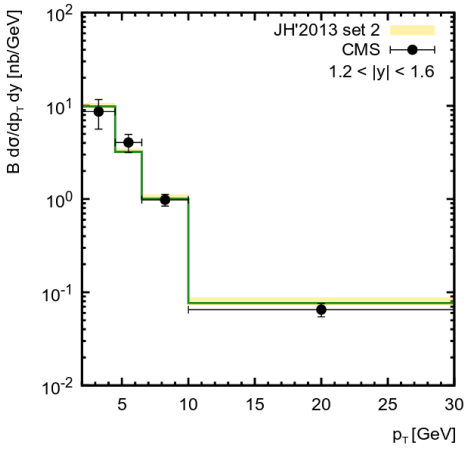

Figure 5.5: The double differential cross sections of inclusive non-prompt J/Ψ meson production at $\sqrt{s} = 7$ TeV as a function of J/Ψ transverse momentum compared with CMS data [198]. Figure from [185].

There is a huge progress in studying TMDs in Double Parton Scattering (DPS). DPS happens when two partons inside one hadron collide with two partons in another hadron. In DPS particles with high invariant mass or high transverse momenta can be generated. The contribution from such processes

becomes important at the LHC energies. DPS is usually described in the framework of collinear factorization with the double parton distribution functions (DPDFs); there is extensive work ongoing to describe DPS also in terms of TMDs (for an overview see eg. [199, 200]). The extension of the KMR formalism to obtain unintegrated double gluon distribution was proposed in [201, 202].

TMDs are applied also in studying the non-linear evolution and saturation phenomena [203–205]. Different fields of application are single spin asymmetries and azimuthal asymmetries in polarized collisions, especially Sivers asymmetry [206–208].

The list of fields, where TMDs are or can potentially be important, given in this section is not complete but it should show how large the interest in TMDs is and how wide is the area of application of TMDs.

6 | The Parton Branching Method

In this chapter the Parton Branching (PB) method to solve the DGLAP evolution equation is introduced. The necessity of the new method and a description of the formalism are discussed. We also present how the transverse momentum dependence can be included in the DGLAP solution.

6.1 | Motivation

As explained in Sec. (5.1), the collinear approach gives a very good description of sufficiently inclusive processes with one hard scale involved. However, whenever a second scale emerges, like e.g. the transverse momentum in the final state, one encounters difficulties, which cannot be solved by the collinear approach.

To obtain predictions for cross sections in the collisions at high energy, the hard scattering cross sections are calculated within perturbation theory, nowadays at NLO or NNLO. Higher order radiation is included (using MC@NLO [209–212] or POWHEG [164, 165]) in the calculations via parton showers performed by Monte Carlo event generators (like PYTHIA [163], Herwig [213, 214], Sherpa [215–217]). Parton showers are supposed to simulate soft gluons emissions and perform their resummation. An example of an observable, where the fixed order perturbation theory breaks, is the Z boson $q_\perp$ spectrum shown in fig. 5.3. Here, the very low $q_\perp$ region is dominated by non-perturbative physics which is modelled by Monte Carlo event generators, the low $q_\perp$ region is dominated by the soft gluons emission, the high $q_\perp$ region is described by perturbation theory. The intermediate $q_\perp$ range must be treated carefully to match these different prescriptions and to avoid double counting. At the end a good description of the spectrum is obtained but it relies on many different inputs. Moreover such problems have to be treated process by process. Another examples of observables with transverse momenta involved, where parton showers play an important role in obtaining predictions, are jet-pair or heavy-quark pair production.

The general procedure of a Monte Carlo event generator for hadronic collisions within collinear approximation is the following: first, the hard scattering process is generated with the initial momenta distributed according to the collinear parton distributions. Then, on top of that, a parton shower is applied by going *backwards* (for efficiency reasons [1]) from the hard scattering process towards the beam particles.

In [180–182] the effects of parton shower on inclusive quantities were studied. It was reported that the parton shower affects not only the transverse momenta, but also the x variable if it is defined in the light cone coordinates. The reason for that is energy-momentum conservation: to keep the same energy when transverse momenta are generated, the longitudinal components have to be shifted. In most of the Monte Carlo event generators a rotation and boost is applied on the hard process to conserve energy-momentum after showering. The simulations of QCD processes, like jets, the Higgs boson, heavy flavours or new particle production are affected by these effects.

In fig. 6.1 the x distribution for inclusive jet events is shown [180]. One can see that including the intrinsic transverse momentum, initial-state and final-state parton showers (POWHEG + PS) one changes the original x distribution (POWHEG) significantly. This is very important for PDFs fits, when the inclusive jet data are used for their determination.

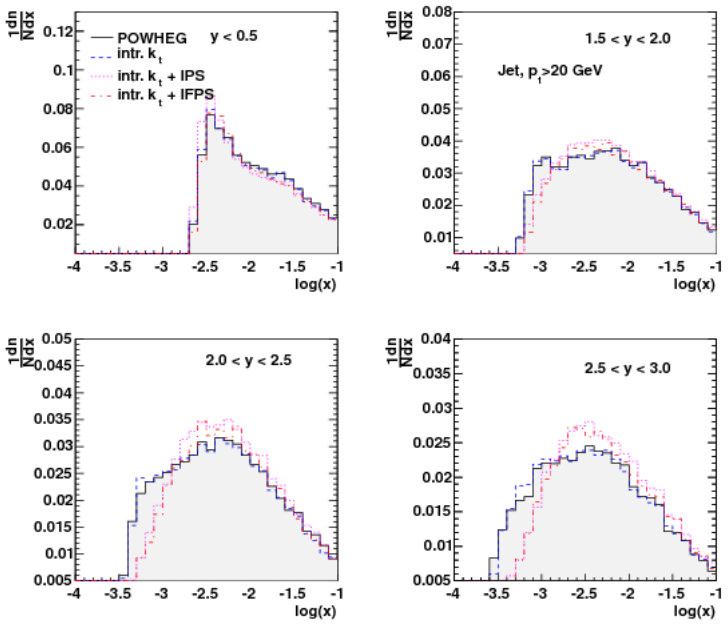

Figure 6.1: The shift in longitudinal momentum fraction after including intrinsic $k_\perp$, initial and final state parton shower for inclusive jet events [180].

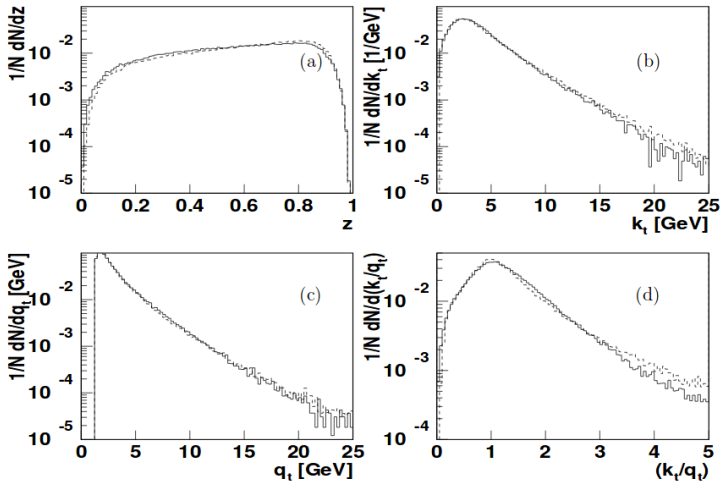

Figure 6.2: Comparison of the splitting variable z, transverse momentum of the propagating (k_t) and emitted (q_t) parton and the ratio of k_t/q_t obtained with backward evolution according to the TMD from CASCADE (solid line) and the SMALLX CCFM evolution (dashed line) [218].

From these considerations an alternative idea arose [218]: if one could generate x, and $k_\perp$ of the matrix element at the given μ^2 according to a TMD, no reshuffling of the momenta would be required.

The TMD fixes the values of x, $k_\perp$ and μ^2. Moreover, one could construct a shower, which evolves exactly according to the kinematics contained in the TMD. From that a consistent picture could be obtained, where parton shower and matrix element follow the same TMD.

However, this project requires several steps to be fulfilled. First of all, the TMD PDF sets have to be obtained. Then, the program to generate the matrix elements must be available. At the end the parton shower, which follows the kinematics according to TMDs, has to be obtained. All these steps have to be properly combined.

The first steps in this direction were performed using the CCFM equation. The forward solution of CCFM gluon evolution equation was obtained in [219] with the Monte Carlo program SMALLX [149,220].

In [218,221] the CASCADE Monte Carlo generator was constructed, which generates a parton shower according to a backward TMD evolution obtained with CCFM equation. The program contains also the generation of the off-shell matrix element for $\gamma^* g^* \to q\bar{q}$ [132]. An important result of these studies is shown in fig. 6.2 in which the kinematic variables obtained with the SMALLX solution of the evolution equation and from the backward parton shower from CASCADE are compared [218].

As discussed already in Sec. (5.2.1), in [147, 148, 222] the CCFM equation was solved with the PB method and the fits to HERA measurements of the F_2 structure function were performed. This method was however restricted to $x < 0.005$ and $Q^2 > 5\text{GeV}^2$.

A new solution, which should be valid over the wide range of x and Q^2, was proposed: to use DGLAP equation instead of CCFM equation to obtain TMD PDF sets for all flavours. This idea was developed in [65, 66] and the rest of this chapter is devoted to describe this method.

6.2 | DGLAP evolution as the Markov Process

It was recognized long time ago that the cascade structure of the DGLAP equation can be seen as *Markov process* [91, 223, 224]: the branching depends only on the last step in the evolution, the previous branchings do not matter, the process has *no memory*. The underlying reason for that is that in the collinear limit the matrix elements factorize (see Sec. (2.2.1)) and there is no interference between Feynman diagrams. The detailed description of the solution of the DGLAP equation in terms of Markovian process can be found in [63].

6.3 | Iterative solution in terms of parton branching

Let us start from the integral form of the evolution equation equation (eq. (3.26) in Sec. (3.2.1)):

$$\widetilde{f}_a(x,\mu^2) = \Delta_a(\mu^2)\ \widetilde{f}_a(x,\mu_0^2) + \sum_b \int_{\ln\mu_0^2}^{\ln\mu^2} d\ln\mu_1^2 \frac{\Delta_a(\mu^2)}{\Delta_a(\mu_1^2)} \int_x^{z_M} dz_1 P_{ab}^R(\mu_1^2, z_1)\ \widetilde{f}_b(x/z_1,\mu_1^2) \tag{6.1}$$

where

$$\widetilde{f}_b\left(\frac{x}{z_1},\mu_1^2\right) = \Delta_b(\mu_1^2)\widetilde{f}_b\left(\frac{x}{z_1},\mu_0^2\right) + \sum_c \int_{\ln\mu_0^2}^{\ln\mu_1^2} d\ln\mu_2^2 \frac{\Delta_b(\mu_1^2)}{\Delta_b(\mu_2^2)} \int_{\frac{x}{z_1}}^{z_M} dz_2 P_{bc}^R(\mu_2^2, z_2)\ \widetilde{f}_c\left(\frac{x}{z_1 z_2},\mu_2^2\right)\ . \tag{6.2}$$

Eq. (6.1) has a vary clear intuitive interpretation.

Let us assume that the parton a is a gluon at the scale μ^2 carrying the proton's momentum fraction x and let us ask where it comes from.

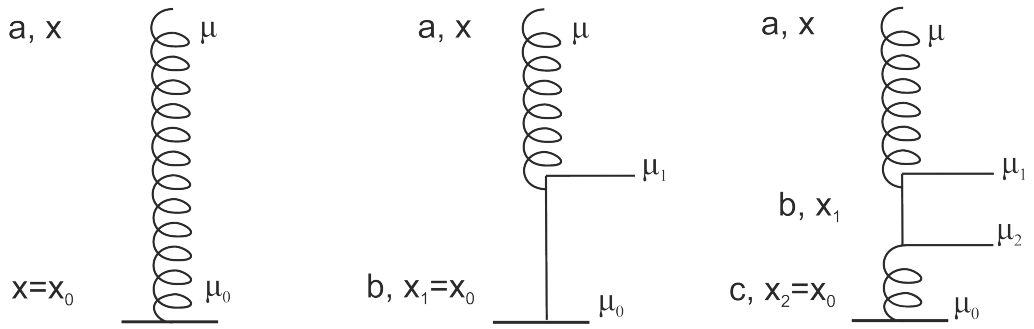

Figure 6.3: Evolution by iteration.

The first possibility is that there was no splitting between some initial scale μ_0^2 and μ^2 which is shown on the left hand side of fig. 6.3 and described by the first term after the equality sign in eq. (6.1). The probability of evolving between μ_0^2 and μ^2 without any resolvable branching is given by the Sudakov form factor $\Delta_a(\mu^2)$. There was no branching so $x_0 = x$.

Another possibility, described by second piece after the equality sign in eq. (6.1), is that the parton a was born during the splitting of a parton b at some scale μ_1^2. Parton b could be a quark splitting into a quark-gluon pair (as visualised in the middle diagram of fig. 6.3) or gluon splitting into a gluon-gluon pair. If we assume that the final parton a carries the fraction x of the longitudinal momentum of the proton then the parton b carried fraction $x_1 = x/z_1$. If parton b was the initial parton (as in the first piece after the equality sign in eq. (6.2)) then $x_0 = x_1 = x/z_1$.

But parton b does not need to be the initial parton, it could come from splitting of another parton c what is described by second piece after the equality sign in eq. (6.2). Parton c carried a momentum fraction $x_2 = x/(z_1 z_2)$ and splitted into parton b at scale μ_2^2. Of course again parton c could be a quark or a gluon (what corresponds to the diagram on the right hand side of fig. 6.3). If it was the initial parton, then $x_0 = x_2$.

A single evolution chain from μ_0 up to μ is called an *event*. In every event following one of the scenarios described above x_0 is different, not only because the number of splittings is different, but also because z_1, z_2 etc. can be different in every event. To obtain the solution of the DGLAP equation one needs to take into account all the possible options, i.e. integrate over all possible x_0 or speaking more generally for bigger amount of splittings, over all possible x from the previous step of course satisfying energy-momentum conservation.
It can be explained by writing the eq. (6.1) in a different way:

$$\widetilde{f}_a(x,\mu^2) = \Delta_a(\mu^2)\ \widetilde{f}_a(x,\mu_0^2) + \sum_b \int_{\ln\mu_0^2}^{\ln\mu^2} d\ln\mu_1^2 \frac{\Delta_a(\mu^2)}{\Delta_a(\mu_1^2)} \int \mathrm{d}x_1 \int_x^{z_M} \mathrm{d}z_1 P_{ab}^R(\mu_1^2, z_1) x f_b(x_1, \mu_1^2) \delta(z_1 x_1 - x) \tag{6.3}$$

and for eq. (6.2)

$$\begin{aligned}\widetilde{f}_b\left(x_1,\mu_1^2\right) &= \Delta_b(\mu_1^2)\widetilde{f}_b\left(x_1,\mu_0^2\right)\\ &+ \sum_c \int_{\ln\mu_0^2}^{\ln\mu_1^2} d\ln\mu_2^2 \frac{\Delta_b(\mu_1^2)}{\Delta_b(\mu_2^2)} \int \mathrm{d}x_2 \int_{x_1}^{z_M} dz_2 P_{bc}^R(\mu_2^2,z_2)\; x_1 f_c\left(x_2,\mu_2^2\right)\delta\left(z_2x_2-x_1\right). \quad (6.4)\end{aligned}$$

The delta function is present in the formula eq. (6.3) to express the relation between x, z_1 and x_1, i.e. the energy-momentum conservation. Analogously in eq. (6.4).

From mathematical point of view the eq. (6.1) is the *Fredholm* type of equation

$$f(t) = f_0(t) + \lambda \int_a^b K(t,y) f(y) \mathrm{d}y \quad (6.5)$$

which is solved by iteration [225] in terms of Neumann series

$$f(t) = \lim_{n\to\infty} \sum_{i=0}^{n} \lambda^i u_i(t) \quad (6.6)$$

with

$$\begin{aligned} u_0(t) &= f_0(t)\,,\\ u_1(t) &= \int_a^b K(t,y) f_0(y) \mathrm{d}y\,,\\ u_2(t) &= \int_a^b \int_a^b K(t,y_1) K(y_1,y_2) f_0(y_2) \mathrm{d}y_2 \mathrm{d}y_1\,,\\ &\ldots\,. \end{aligned} \quad (6.7)$$

6.4 | Parton branching method with Monte Carlo techniques

The goal is to solve the eq. (6.3)

$$\widetilde{f}_a(x,\mu^2) = \Delta_a(\mu^2)\;\widetilde{f}_a(x,\mu_0^2) + \sum_b \int_{\ln\mu_0^2}^{\ln\mu^2} d\ln\mu_1^2 \frac{\Delta_a(\mu^2)}{\Delta_a(\mu_1^2)} \int \mathrm{d}x_1 \int_x^{z_M} \mathrm{d}z_1 P_{ab}^R(\mu_1^2,z_1) x f_b(x_1,\mu_1^2)\delta(z_1x_1-x) \quad (6.8)$$

with a parton branching method using Monte Carlo techniques described in Appendix (A.3).
The parton branching method to be discussed here is a realization of a forward evolution, one starts the evolution from a known parton at a given scale μ_0^2 and evolves up to a maximum scale μ^2. It is not known how many branchings will appear and what will be the final parton at scale μ^2. The scales μ_0^2 and μ^2 stay the same for all the discussed events.
Before we move to the discussion about the parton branching method in detail, we notice that by using the following relation

$$\frac{\mathrm{d}\Delta_b(\mu_1^2)}{\mathrm{d}\ln(\mu_1^2)} = \Delta_b(\mu_1^2)\left(-\sum_c \int_0^{z_M} \mathrm{d}z\; zP_{cb}^R\left(\mu_1^2,z\right)\right) \quad (6.9)$$

the evolution equation eq. (6.3) can be rewritten in a form

$$\begin{aligned}\widetilde{f}_a(x,\mu^2) &= \Delta_a(\mu^2)\;\widetilde{f}_a(x,\mu_0^2)\\ &+ \sum_b \int_{\ln\mu_0^2}^{\ln\mu^2} \mathrm{d}\left(-\Delta_b(\mu_1^2)\right) \frac{\Delta_a(\mu^2)}{\Delta_a(\mu_1^2)} \int \mathrm{d}x_1 \frac{\int_x^{z_M} \mathrm{d}z_1 P_{ab}^R(\mu_1^2,z_1)}{\sum_c \int_0^{z_M} \mathrm{d}z z P_{cb}^R(\mu_1^2,z)} x f_b(x_1,\mu_0^2)\delta(z_1x_1-x)\\ &+ \ldots\,. \end{aligned} \quad (6.10)$$

After this operation the structure of the solution becomes clear: the scale μ_1^2, at which the branching of parton b into another parton happens, can be generated according to

$$R_1 = \int_{\ln \mu_0^2}^{\ln \mu_1^2} \mathrm{d}\left(-\Delta_b(\mu'^2)\right) \tag{6.11}$$

using a uniformly distributed random number $R_1 \in [0,1]$.
At LO, to take a decision about the splitting we use the probabilistic interpretation of the splitting functions. We do it with the method described in eq. (A.84)-(A.88) where the p.d.f. is a sum of two p.d.fs. A new uniformly distributed random number $R_2 \in [0,1]$ is generated and compared with P_1, where

$$\begin{aligned} P_1 &= \frac{\int_0^{z_M} \mathrm{d}z z P_{bb}^R(z,\mu_1^2)}{\sum_{c=a,b}\int_0^{z_M} \mathrm{d}z z P_{cb}^R(z,\mu_1^2)}\,, \\ P_2 &= \frac{\int_0^{z_M} \mathrm{d}z z P_{ab}^R(z,\mu_1^2)}{\sum_{c=a,b}\int_0^{z_M} \mathrm{d}z z P_{cb}^R(z,\mu_1^2)}\,, \\ P &= P_1 + P_2 = 1\,. \end{aligned} \tag{6.12}$$

If $R_2 > P_1$, the parton b splits into a parton a, otherwise it splits into a parton b. After the decision is taken, the z_1 variable can be generated according to chosen splitting function P_{xb}^R

$$R_3 = \frac{\int_0^{z_1} \mathrm{d}z z P_{xb}^R(z,\mu_1^2)}{\int_0^{z_M} \mathrm{d}z z P_{xb}^R(z,\mu_1^2)} \tag{6.13}$$

where $x = a$ or $x = b$, using another uniformly distributed random number $R_3 \in [0,1]$. In practise, it is not possible to find the inverse of the splitting functions analytically. Instead, one has to use *importance sampling* method connected with *weighted events* method, both described in Appendix (A.3.5).

At NLO we decide to keep the same structure of decision taking even if the splitting function do not have a probabilistic interpretation anymore because they can become negative. For the gluon we follow exactly the same recipe as at LO, for the quark splitting the decision is taken according to a generalised method from eq. (A.84)-(A.88), described in Appendix (A.4.5). Since the NLO splitting functions can become negative we have sometimes negative weights. It is however not a problem. It is important to notice is that there is a condition which must be fulfilled to use this method: all the z integrals from the splitting functions have to be positive, otherwise one cannot use a random number $R_2 \in [0,1]$ to make a decision about which branching to take using ratios from eq. (6.12). Also, the positivity of the integrals in the Sudakov form factor is essential for the PB method. The integrals from the splitting functions are positive, both at LO and NLO that is why this method can be used. In Sec. (6.6) the properties of the splitting functions are discussed.

After generating the splitting variable z_1, the scale of the next splitting can be generated. The procedure is repeated until the maximum evolution scale μ^2 one is interested in is reached.

6.5 | The transverse momentum during the evolution

The DGLAP equation is obtained in the collinear limit. The concept of transverse momenta is introduced into the parton distribution functions with the assumption that the emission of a particle is

possible with a $p_\perp$ smaller than some factorization scale μ^2 (see eq. (2.19) in Sec. (2.2)) [16].

In the PB method, we generate the splitting variable z and the branching scale μ' for every branching. The kinematics of a branching is visualised in fig. 6.4.

The transverse momenta of the emitted and propagating partons can be obtained from $p_\perp$-, virtuality or angular ordering conditions, discussed in Sec. (3.1.1) - (3.1.2), where the connection between the transverse momenta and the branching scale was discussed.

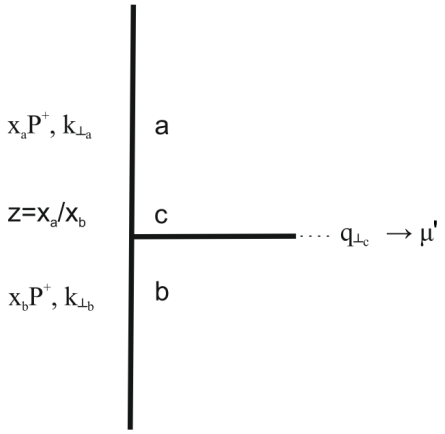

Figure 6.4: The kinematics of the splitting process.

Once the relation of $q_\perp$, and μ' is chosen, one can calculate $k_\perp$ of the propagating parton using the following formula

$$\overrightarrow{k}_{\perp,a} = \overrightarrow{k}_{\perp,b} - \overrightarrow{q}_{\perp,c} \; . \tag{6.14}$$

This formula indicates that the $k_\perp$ is accumulated during the evolution process. This is one of the differences to the MRW approach discussed in Sec. (5.2). In this sense, the transverse momentum in the PB method contains the whole history of the evolution.

Having $k_\perp$ calculated at every branching, one can construct the TMD parton density for every parton species $\widetilde{A}_a\left(x, k_\perp, \mu^2\right)$ which fulfils the condition

$$\int \mathrm{d}k_\perp^2 \widetilde{A}_a\left(x, k_\perp, \mu^2\right) = \widetilde{f}_a\left(x, \mu^2\right) \; . \tag{6.15}$$

Using eq. (6.1) one can write an equation for TMD evolution

$$\begin{aligned} \widetilde{A}_a\left(x, k_\perp, \mu^2\right) &= \Delta_a\left(\mu^2\right) \widetilde{A}_a\left(x, k_\perp, \mu_0^2\right) + \\ &\sum_b \int_{\mu_0^2}^{\mu^2} \frac{\mathrm{d}^2\mu'_\perp}{\pi\mu'^2} \frac{\Delta_a\left(\mu^2\right)}{\Delta_a\left(\mu'^2\right)} \\ &\times \int_x^{z_M} \mathrm{d}z P_{ab}^R\left(z, \mu'^2, \alpha_s(a(z)^2\mu'^2)\right) \widetilde{A}_b\left(\frac{x}{z}, k_\perp + a(z)\mu_\perp, \mu'^2\right) \; . \end{aligned} \tag{6.16}$$

Above the notation was introduced

$$\begin{aligned} \mu'_\perp &= \left(\mu'_x, \mu'_y\right) \; , \\ \mu'^2_\perp &= \mu'^2 \; . \end{aligned} \tag{6.17}$$

It means that the branching scale μ' is generated according to the Sudakov form factor and later, the components of a two dimensional vector of the length μ' are generated. From them the transverse

momentum is calculated according to one of the formulas in eq. (3.7), eq. (3.9), or eq. (3.15). The variable $a(z)$ indicates the possible choices of the argument of α_s discussed in Sec. (3.1.4) and the association of the transverse momenta and the evolution scale. For the $p_\perp$-ordering $a(z) = 1$, for the virtuality ordering $a(z) = \sqrt{1-z}$, for angular ordering $a(z) = 1-z$. The PB method allows one to define the z_M parameter, factorization and renormalization scale independently - one can for example introduce the function $a(z)$ in the definition of $k_\perp$ but not in the argument of α_s. Thanks to that the effect of every individual part of the ordering definition can be studied.

The way of calculating $k_\perp$ does not affect the collinear evolution. The variable μ' is generated according to the Sudakov form factor and the splitting variable z is generated according to collinear splitting functions, in both of these steps no dependence on $k_\perp$ or $q_\perp$ is included.

6.6 | Properties of the DGLAP splitting functions

The knowledge of how the real parts of the splitting functions behave is crucial for the solution of the DGLAP evolution equation by the parton branching method applying Monte Carlo techniques.

The splitting functions depend on z and μ^2 (through α_s and n_f). In this section the real parts of the splitting functions multiplied by z, $zP(z)^R$, as a function of z and the integrals over z of the real part of the splitting functions multiplied by z, $\int^{z_M} \mathrm{d}z\, zP(z)^R$, as a function of $\log(1-z_M)$ are investigated, first at LO, and later at NLO in the $\overline{\mathrm{MS}}$ scheme. The calculations are obtained using a value of $\alpha_s = 0.118$ and $n_f = 5$. The LO contributions to the NLO splitting functions are already multiplied by $\frac{\alpha_s}{2\pi}$ and NLO contributions are multiplied by $\left(\frac{\alpha_s}{2\pi}\right)^2$. For the integrals studies the calculations are performed for $z_{min} = 10^{-8}$.

In fig. 6.5 the LO splitting functions $zP(z)^R$ are shown in the range $z \in (10^{-5}, 1)$. Fig. 6.6 presents a zoom of the plots from fig. 6.5 in a region of large z.

One can also construct the sums of the splitting functions $zP(z)^R$ and their ratios to study their properties from a different perspective. Such sums are used in the parton branching method (see Sec. (6.4)). In fig. 6.7 the sums of the splitting functions $zP(z)^R$ and in fig. 6.8 the ratios of the sums are presented at LO.

From fig. 6.5-6.8 one can see that for small and medium z, $zP^R_{gq_j} \gg zP^R_{q_jq_j}$. For the gluon sector in the whole z region, $zP^R_{gg} \gg 2n_f zP^R_{q_ig}$. Using the probabilistic interpretation of the splitting functions one can say that the region of small and medium z corresponds to having more likely the gluon entering the hard interaction than a quark. At large z, the $zP^R_{q_jq_j}$ and zP^R_{gg} are quickly growing which reflects the soft gluons emissions. In the large z region, after the $q \to qg$ splitting, it is much more probable that it is a quark, which enters the hard interaction, not a gluon. Last but not least, at the LO all the splitting functions are positively defined.

Now, one can study also the real parts of the NLO splitting functions. In fig. 6.9 the NLO splitting functions $zP(z)^R$ are shown in the range $z \in (10^{-5}, 1)$.

The interesting region is the region of large z, in fig. 6.10 the zoom in this region is shown. The splitting functions at NLO contain pieces proportional to $\ln(1-z)$ thus they are divergent (towards $+\infty$ or $-\infty$) when $z \to 1$. Additionally, functions P^R_{gg} and $P^R_{q_jq_j}$ contain pieces $1/(1-z)$.

In fig. 6.11 the sums of the splitting functions $zP(z)^R$ at NLO and in fig. 6.13 the ratios of the sums are

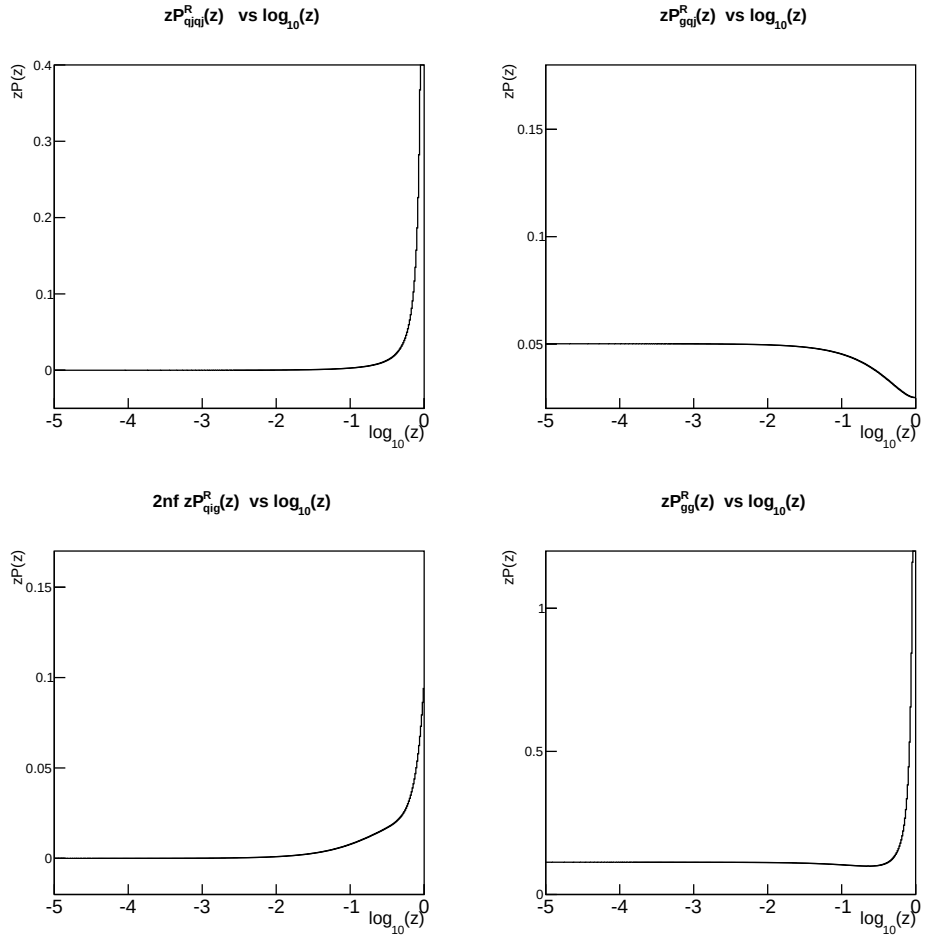

Figure 6.5: Real parts of the LO splitting functions vs $\log_{10}(z)$.

presented. As one can notice in fig. 6.11, the sum of functions $z\left[P^R_{q_jq_j}(z) + P^R_{\overline{q}_jq_j}(z) + 2(n_f-1)P^R_{q_iq_j}(z)\right]$ is close to $z\left[P^R_{q_jq_j}(z) + P^R_{\overline{q}_jq_j}(z)\right]$ and $zP^R_{q_jq_j}(z)$, a zoom of them is shown in fig. 6.12.
It is important to note that the sums in fig. 6.11 and fig. 6.12 are always positive.

Similarly, as at LO, at NLO in the medium and small z region, $zP^R_{gq_j} \gg z(P^R_{q_jq_j} + P^R_{\overline{q}_jq_j} + 2(n_f - 1)P^R_{q_{i\neq j}q_j})$. For the gluon sector in the whole z region, $zP^R_{gg} \gg 2n_f zP^R_{q_ig}$. Even though the probabilistic nature of the NLO splitting functions is lost since they can become negative, their integrals over z are positive (see later in this section) and we take the decisions according to them. In the weighted events method we are using, some of the weights can be negative because of the structure of NLO splitting functions. From fig. 6.9 - 6.13 one can conclude that gluon radiates more than quark. One can also see what are the proportions of the different splitting possibilities.

Having analysed the splitting functions themselves, we can concentrate on the integrals of splitting functions $\int^{z_M} \mathrm{d}zzP(z)^R$. Here, the studies on the dependence of the integral value on the z_M parameter are performed. The choice of the z_M parameter must be a compromise between the accuracy we want to achieve and CPU time consumption. In principle one could think that taking higher z_M should lead to a better accuracy. The result becomes indeed more precise with higher z_M however also the fluctuations become bigger. Moreover, with increasing the z_M parameter, the CPU time needed for the calculation

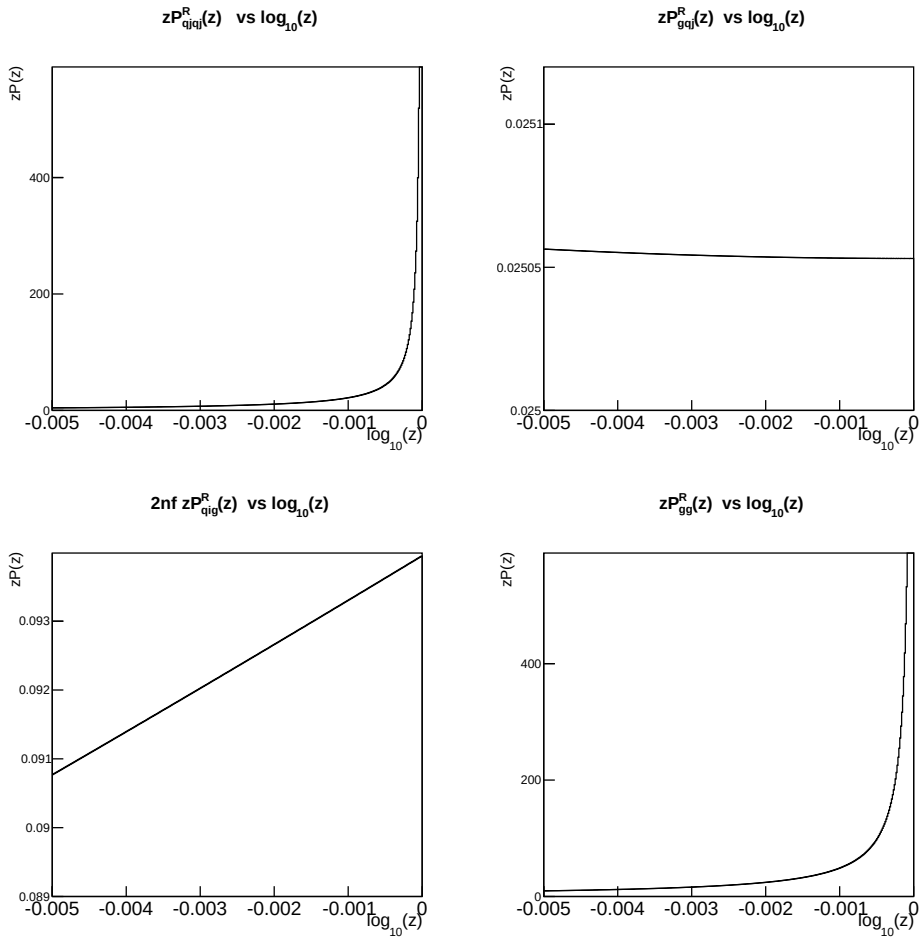

Figure 6.6: Zoom at the real parts of the LO splitting functions vs $\log_{10}(z)$ in the large z region.

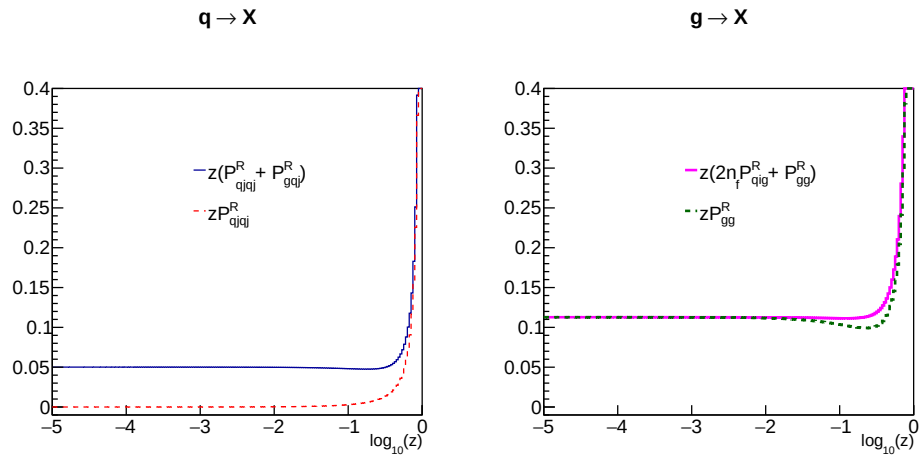

Figure 6.7: Combinations of the LO splitting functions.

increases. For these practical purposes we are studying 6 different values of $z_M = 1 - 10^{-1}$, $1 - 10^{-2}$, $1 - 10^{-3}$, $1 - 10^{-4}$, $1 - 10^{-5}$, $1 - 10^{-6}$ with which one should achieve good compromise.

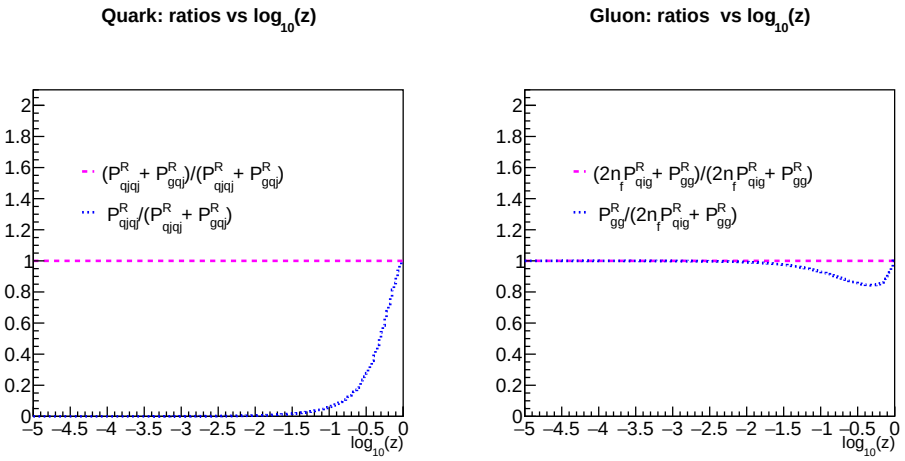

Figure 6.8: Ratios of the sums of the LO splitting functions.

In fig. 6.14 the integrals $\int^{z_M} \mathrm{d}z z P(z)^R$ as a function of $\log_{10}(1-z_M)$ are shown at LO. In fig. 6.15 the sums of the z integrals from the splitting functions and in fig. 6.16 the ratios of the sums are presented.

In fig. 6.17 the integrals of the NLO splitting functions $\int^{z_M} \mathrm{d}z z P^R(z)$, as a functions of $\log_{10}(1-z_M)$ are presented. In fig. 6.18 the sums of the integrals and in fig. 6.19 the ratios of the sums used in the parton branching are presented as a functions of $\log_{10}(1-z_M)$ at NLO.

Both at LO and NLO, the splitting functions which contain the piece $1/(1-z)$ ($zP^R_{q_j q_j}$ and zP^R_{gg}), are very sensitive to the change of the z_M parameter. For $zP^R_{q_i g}$, $zP^R_{\bar{q}_j q_j}$, $zP^R_{\bar{q}_i q_j}$ and $zP^R_{g q_j}$, the dependence on z_M is very weak. At NLO we can see that the pieces proportional to $\ln(1-z)$ can be integrated over up to 1 to give finite result.

All the sums and ratio plots presented here show a dependence on z_M parameter because of $zP^R_{q_j q_j}$ and zP^R_{gg}.

The integrals $\int^{z_M} \mathrm{d}z\, zP(z)$ are positive in the whole range of z, from 0 up to a z_M close to 1, both for the LO and the NLO case. This is understandable from the momentum sum rule. We know that by taking into account real and virtual contributions, the divergences should cancel. Since the virtual corrections give negative contribution, the real splittings should give a positive one.

Thanks to multiplying the splitting functions by z the divergency at $z = 0$ is gone. This is one of the reasons to use the DGLAP evolution equation for the momentum weighted parton densities defined in eq. (2.40).

All of the plots in this section were done for $\alpha_s = 0.118$ and $n_f = 5$, no dependence on α_s and n_f was included. Even though the main conclusions from this section stay valid for other scales μ^2 when the values of n_f and α_s are different, the proportions of different splitting functions and integrals change not only with z or z_M but also with the scale μ^2. Example is depicted in fig. 6.20 where the integrals of the real parts of the splitting functions multiplied by z over z vs $\log_{10}(1-z_M)$ at NLO for different values of α_s and n_f are shown.

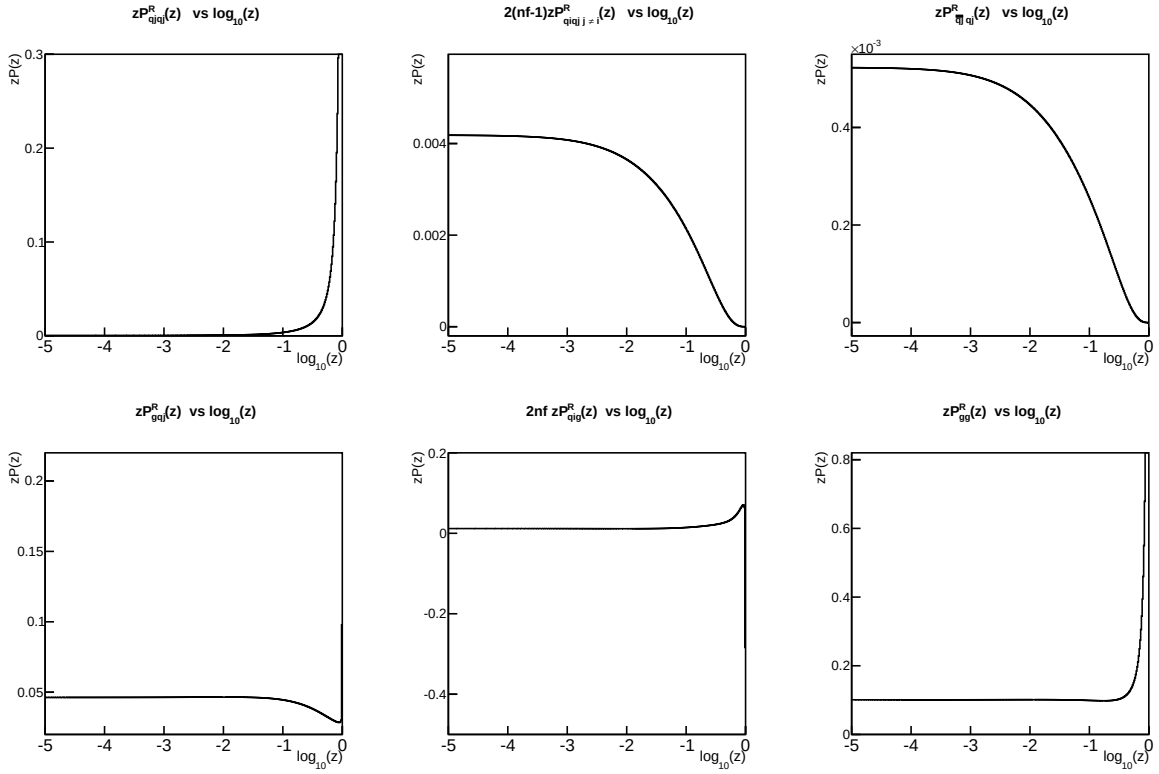

Figure 6.9: Real parts of the NLO splitting functions vs $\log_{10}(z)$.

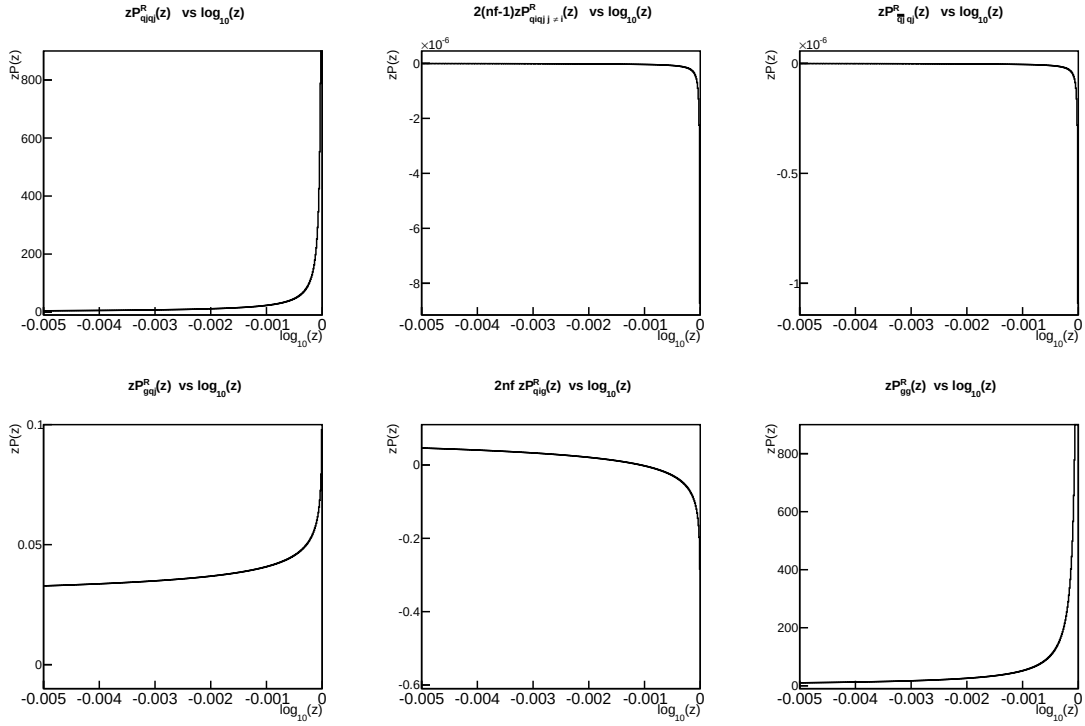

Figure 6.10: Zoom at the real parts of the NLO splitting functions vs $\log_{10}(z)$ in the large z region.

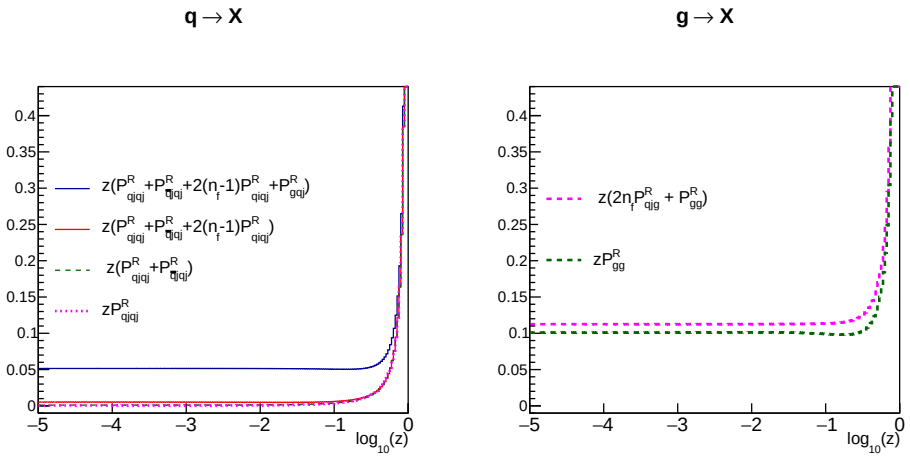

Figure 6.11: The combinations of the NLO splitting functions.

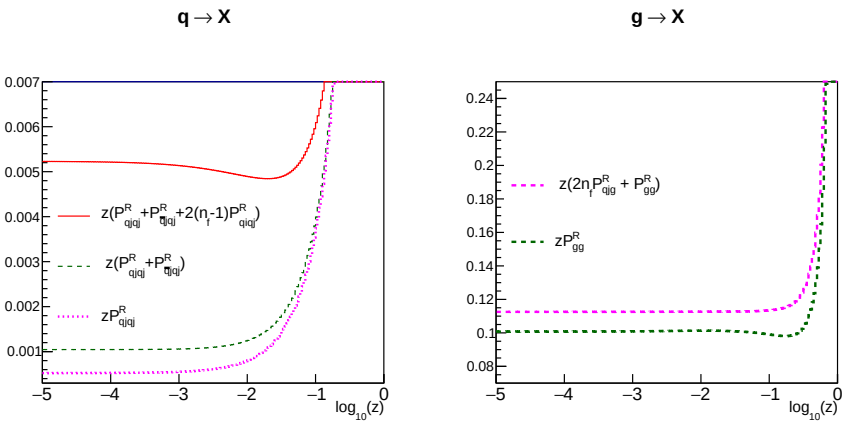

Figure 6.12: Zoom at the combinations of the quark and gluon NLO splitting functions.

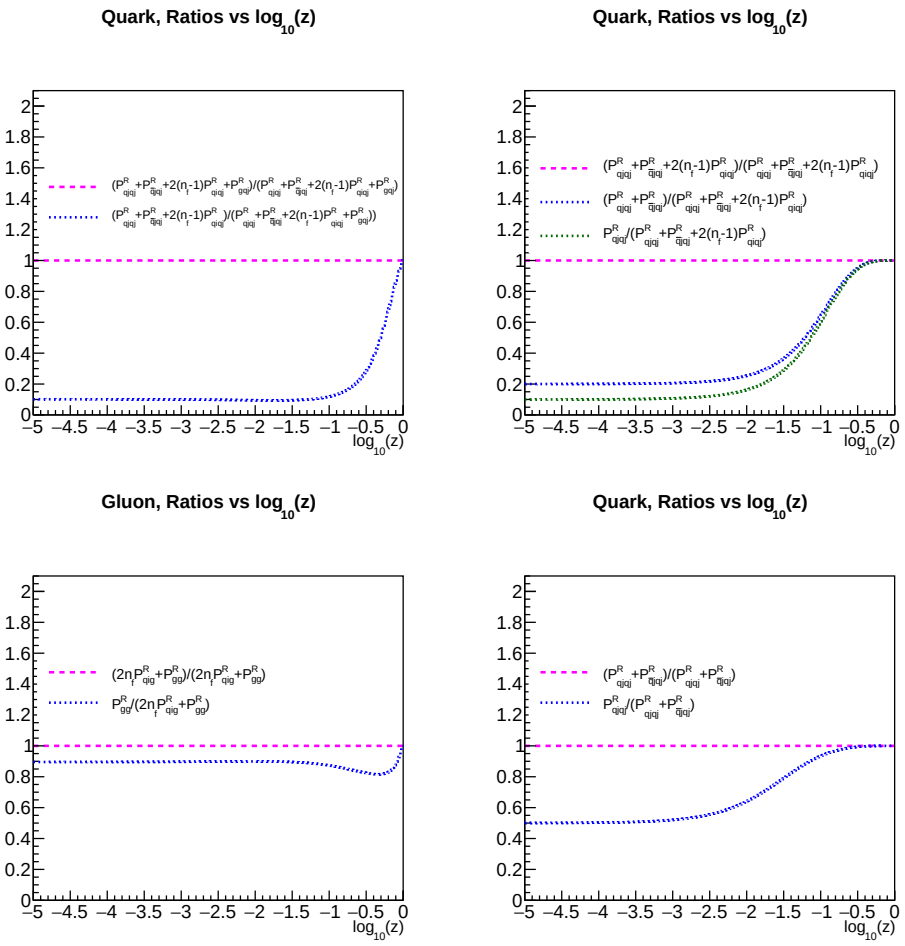

Figure 6.13: Ratios of the sums of the NLO splitting functions.

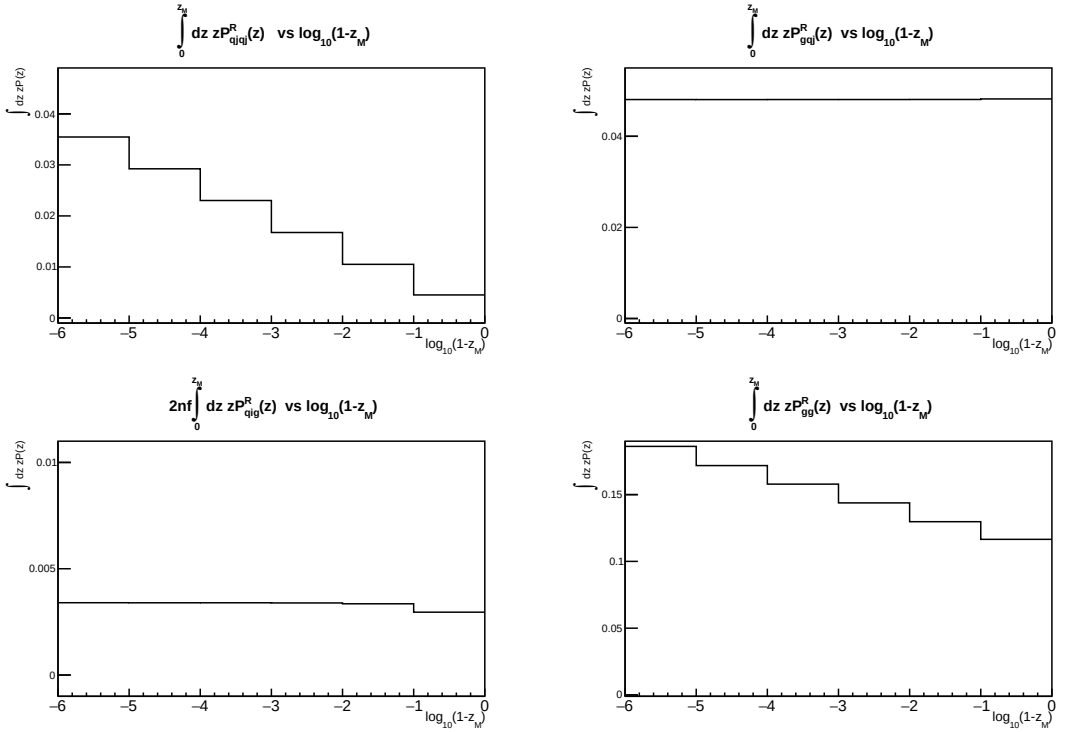

Figure 6.14: The integrals of the real parts of the splitting functions multiplied by z over z vs $\log_{10}(1-z_M)$ at LO.

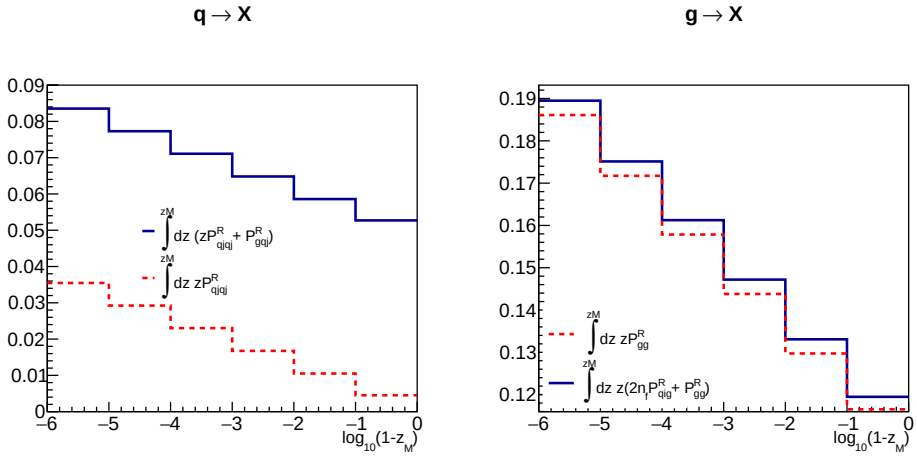

Figure 6.15: Sums of the integrals of the LO real parts of the splitting functions multiplied by z over z vs $\log_{10}(1-z_M)$.

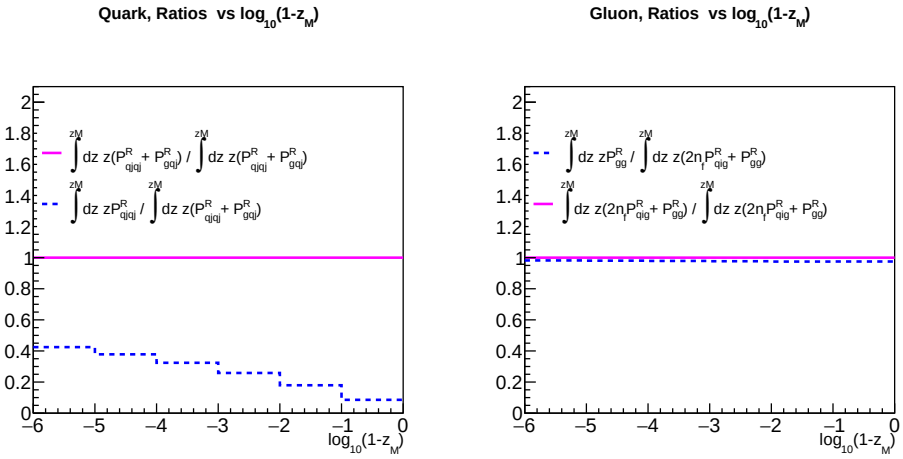

Figure 6.16: Ratios of the sums of the integrals of the LO real parts of the splitting functions multiplied by z over z vs $\log_{10}(1 - z_M)$.

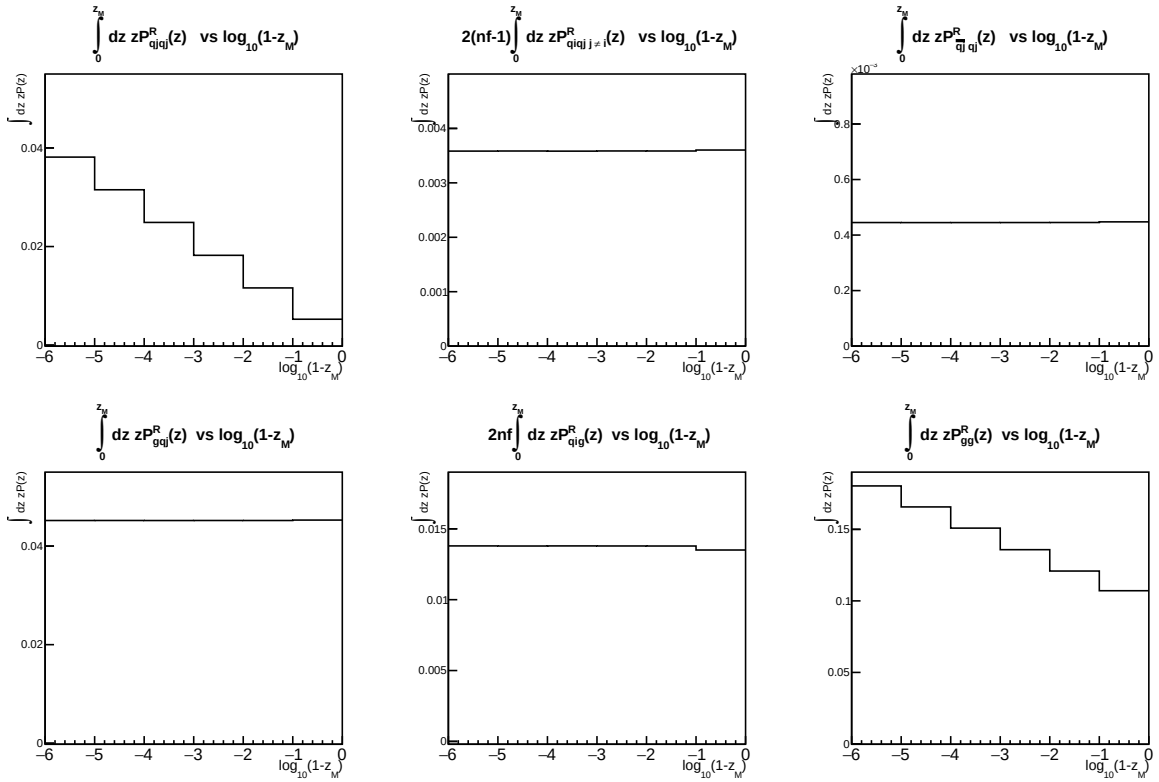

Figure 6.17: The integrals of the real parts of the splitting functions multiplied by z over z vs $\log_{10}(1-z_M)$ at NLO.

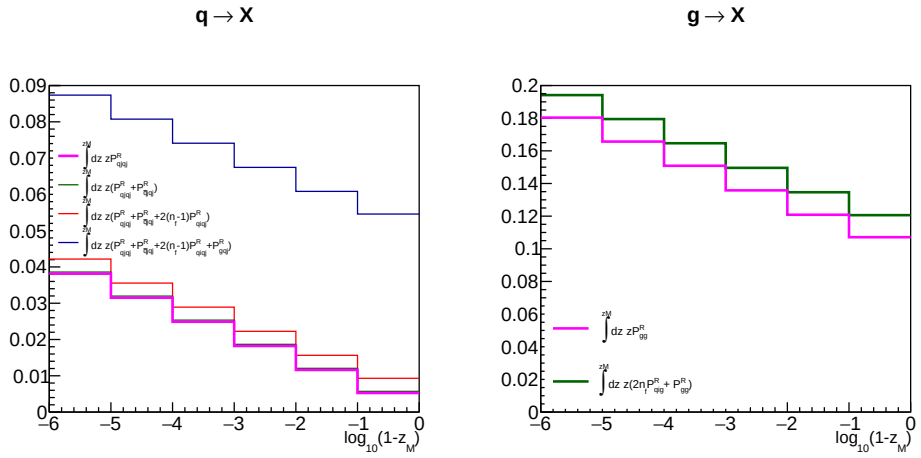

Figure 6.18: Sums of the integrals of the real parts of the splitting functions multiplied by z over z vs $\log_{10}(1 - z_M)$ at NLO.

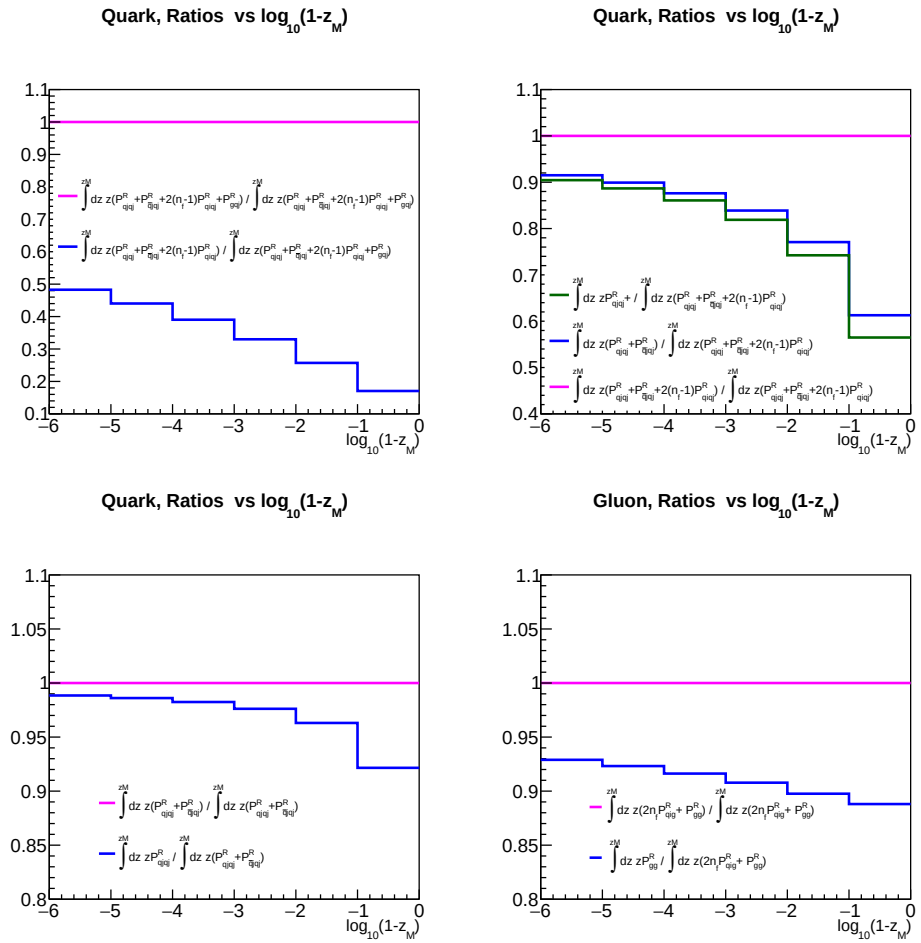

Figure 6.19: Ratios of the sums of the integrals of the real parts of the splitting functions multiplied by z over z vs $\log_{10}(1 - z_M)$ at NLO.

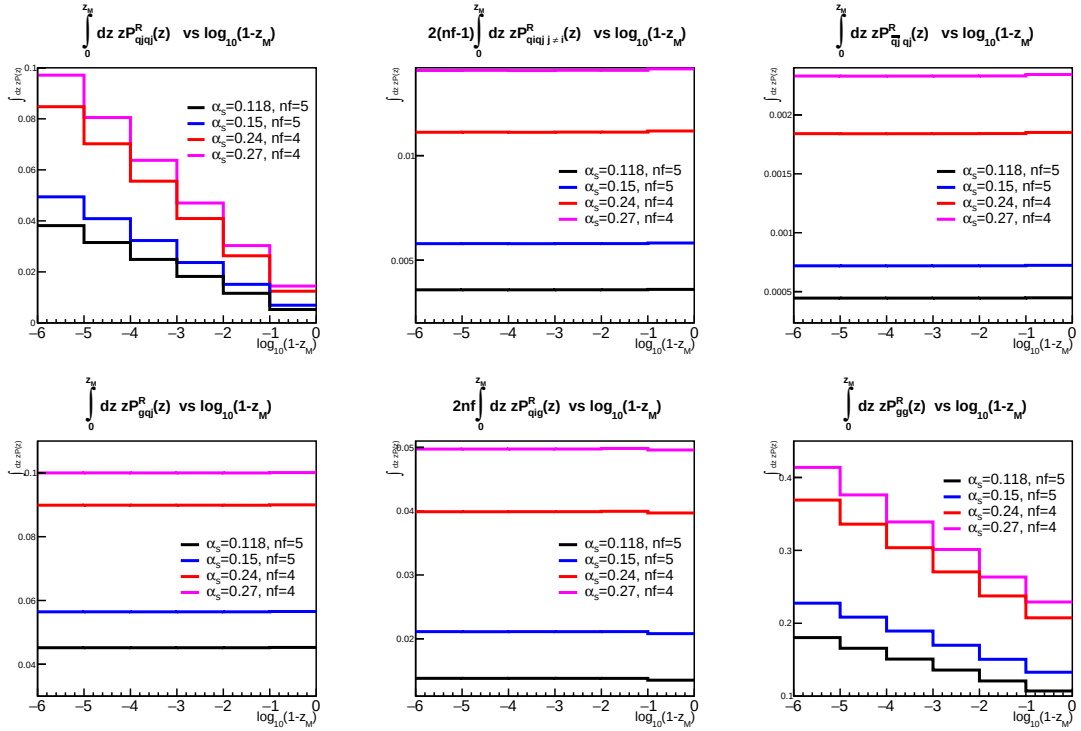

Figure 6.20: Integrals of the real parts of the splitting functions multiplied by z over z vs $\log_{10}(1-z_M)$ at NLO for different values of α_s and n_f.

7 | Validation of the PB method with QCDNUM

The PB method described in Sec. (6.4) was implemented into a computer program called uPDFevolv [222] which was initially used to solve the CCFM equation. In this section we show the consistency and agreement of the PB method for collinear PDFs with QCDNUM.

As mentioned before, to solve the DGLAP evolution equation, one needs to know the parton distribution functions at the initial scale. One of the possible input used in this thesis is a parametrization from QCDNUM [62]. With this choice of initial distribution only three active flavours are assumed at the starting scale, charm quarks are produced during the evolution for scales $\mu > m_c = 1.73$ GeV and bottom quarks are produced for $\mu > m_b = 5.0$ GeV. The strong coupling α_s with a value $\alpha_s(m_Z^2) = 0.118$ at 1- or 2-loop is used.

In Sec. (2.3.2) it was discussed that by introducing the parameter z_M in the integrals, some contributions to the parton density of $\mathcal{O}(1 - z_M)$ are skipped (see eq. (2.82)). Here we want to study how the collinear distributions are affected by the z_M parameter. In this section z_M is kept fixed (eq. (3.16)) and five values of z_M ($z_M = 1 - 10^{-1}$, $1 - 10^{-2}$, $1 - 10^{-3}$, $1 - 10^{-5}$ and $1 - 10^{-7}$) are examined. The argument of α_s is the branching scale μ'^2 (eq. (2.41)). The LO splitting functions and 1-loop α_s are used for the validation at LO and the NLO splitting functions and 2-loop α_s are used to obtain the results at NLO. The calculations are done in the $\overline{\text{MS}}$ scheme. The distributions presented here were obtained for 10^{10} events.

We present the collinear PDFs $xf(x, \mu^2)$ from the PB method as a function of x for a given scale μ^2. The procedure to obtain the results is the following. The initial distribution is evolved with the PB method up to a given evolution scale μ^2 at which the evolution is stopped. The figures with the results are divided into two parts. In the upper part the distributions obtained from PB method are presented. In the lower part the ratios of the results from PB and QCDNUM with the same initial conditions are shown.

Validation of the method at NLO Fig. 7.1 shows the results for the gluon and down quark densities obtained from the PB method with fixed value of z_M compared to the calculation from QCDNUM. One can see a very good agreement between these two methods for $z_M = 1 - 10^{-3}$, $1 - 10^{-5}$ and $1 - 10^{-7}$. However, the values $z_M = 0.9$ and $z_M = 0.99$ are too small and the results from the PB method starts to deviate significantly from the one obtained with QCDNUM. For higher values of z_M both methods agree within the statistical fluctuations.

In fig. 7.2 we show the collinear PDFs from the PB method with fixed value of $z_M = 1 - 10^{-5}$ evolved up to different evolution scales $10, 100, 1000, 10000$ GeV^2 for down-, strange-, charm- quark and gluon densities compared to the calculation from QCDNUM. We illustrate a very good agreement between these two methods for all flavours and different evolution scales.

Validation of the method at LO We validate the PB method also at LO. On the left hand side of fig. 7.3 we present the plot for gluon for five fixed values of $z_M = 1 - 10^{-1}$, $1 - 10^{-2}$, $1 - 10^{-3}$, $1 - 10^{-5}$ and $1 - 10^{-7}$. Additionally we show the NLO QCDNUM result to visualise the effect of going from LO to NLO. Similarly as at NLO, we obtain the same collinear PDFs with large values of z_M. One can also see that the effect of going from LO to NLO is significant. On the right hand side of fig. 7.3 we show the results for gluon PDF at different evolution scales obtained with fixed value of $z_M = 1 - 10^{-5}$. A very good agreement with QCDNUM is obtained.

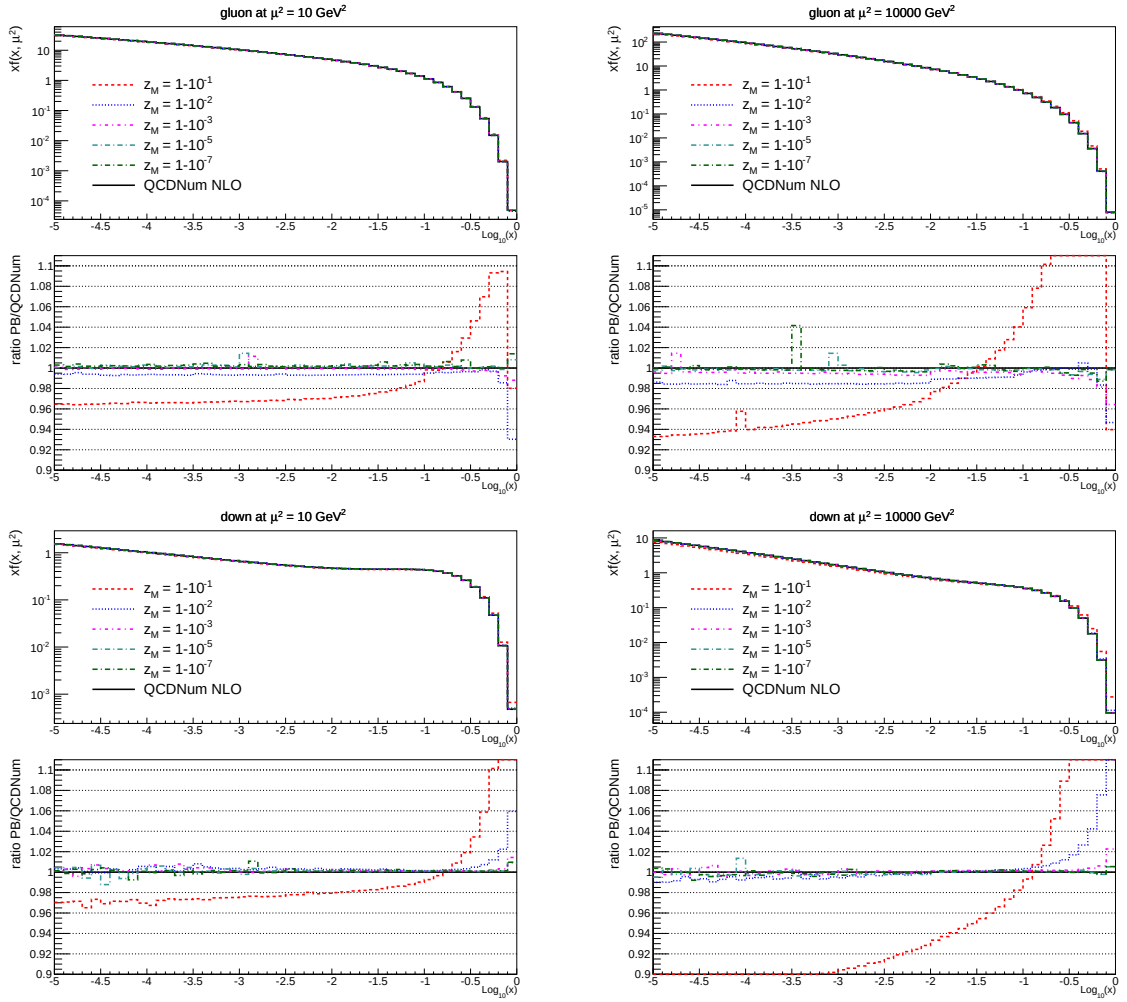

Figure 7.1: Collinear PDFs from the PB method compared with QCDNUM. The results obtained with different values of z_M at NLO.

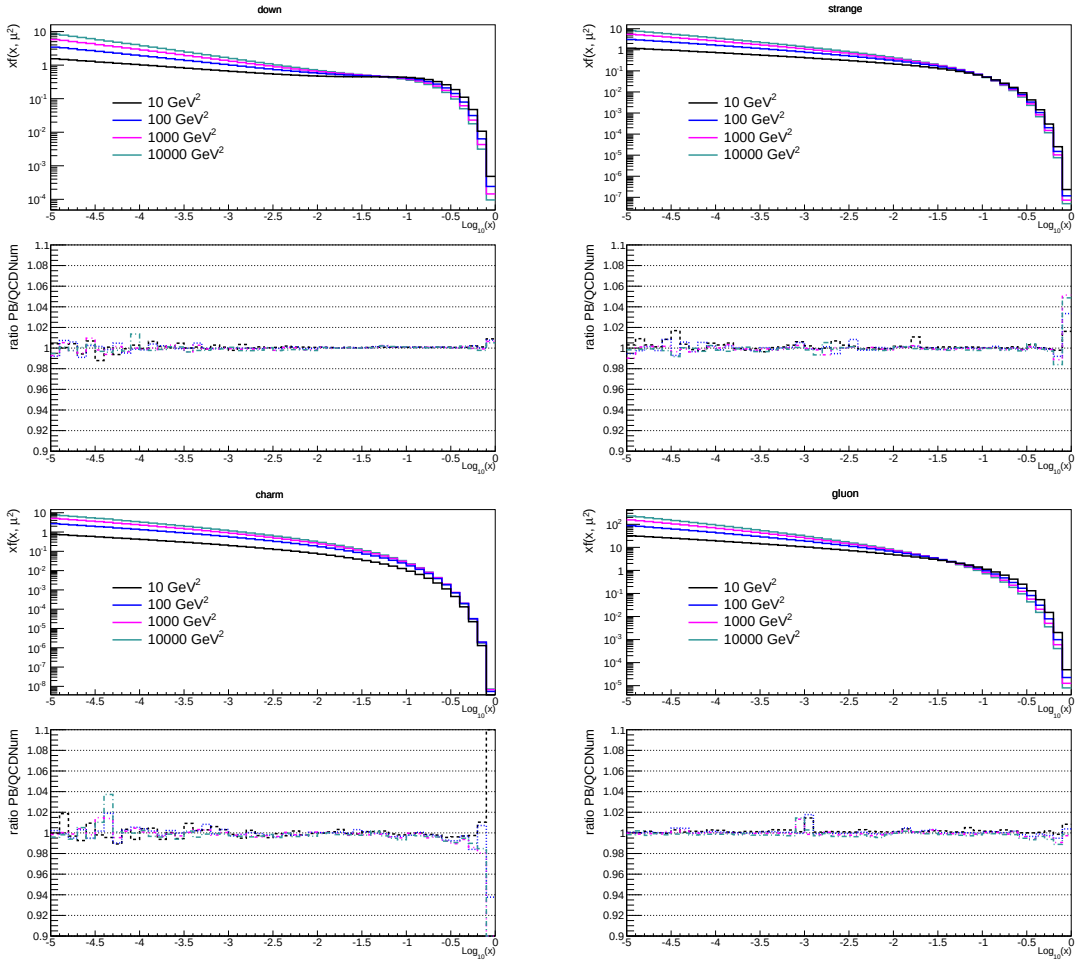

Figure 7.2: Results for the NLO collinear PDFs from the PB method with fixed value of $z_M = 1 - 10^{-5}$ evolved up to different evolution scales $10, 100, 1000, 10000$ GeV^2 compared to the calculation from QCDNUM.

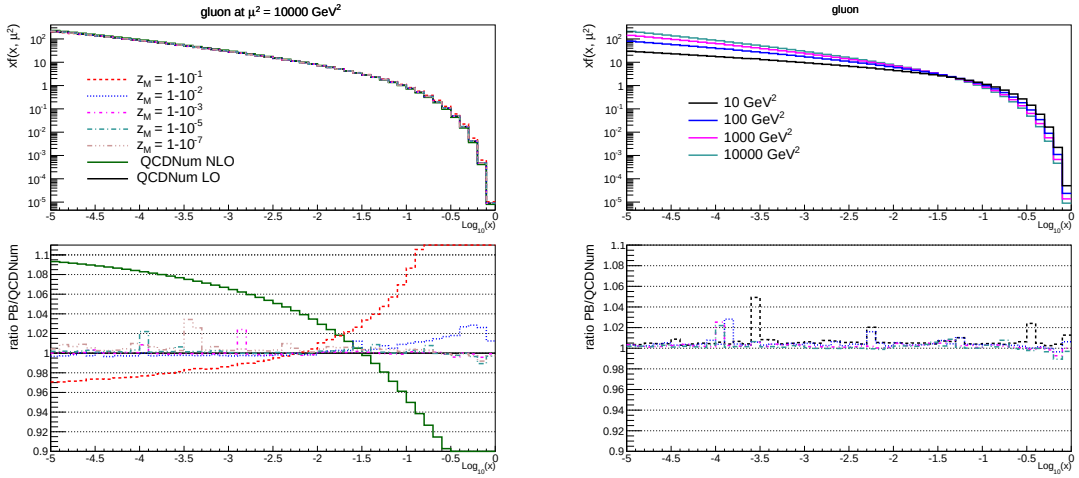

Figure 7.3: Results for the LO gluon collinear PDF from the PB method. The ratio taken with respect to LO QCDNUM. Left: comparison with different fixed values of z_M, LO and NLO QCDNUM shown for comparison. Right: comparison at different evolution scales for fixed value of $z_M = 1 - 10^{-5}$.

8 Collinear and TMD PDFs from PB method

In the previous chapter we performed a validation of the PB method by comparing our results to the QCDNUM package. We showed a very good agreement between these two methods. In this chapter we explore other advantages of the PB method, i.e. we discuss the issues of the ordering variables, the choice of the parameter z_M defining resolvable branching and the renormalization scale choice in α_s. We study the effects both for collinear and TMD distributions. The main results presented in this chapter were published in [65, 66] and in the following proceedings [226–228].

Additionally to the QCDNUM initial parametrization, we use also the HERAPDF2.0 [42] parametrization, again assuming only three active flavours at the initial scale, with charm quarks produced during the evolution for scales $\mu > m_c = 1.47$ GeV and bottom quarks produced for $\mu > m_b = 4.5$ GeV. The strong coupling α_s value $\alpha_s(m_Z^2) = 0.118$ at 2-loop and $\alpha_s(m_Z^2) = 0.13$ at 1-loop is used. The reason for using HERAPDF2.0 is to apply the obtained TMDs to the Z boson $p_\perp$ measurements (see Sec. (9.2)).

definition of $q_\perp$	$p_\perp$ − ordering $q_\perp^2 = \mu'^2$ eq. (3.9)	virtuality ordering $q_\perp^2 = (1-z)\mu'^2$ eq. (3.7)	angular ordering $q_\perp^2 = (1-z)^2\mu'^2$ eq. (3.15)
z_M definition	fixed z_M eq. (3.16)	$z_M = 1 - \left(\frac{q_0}{\mu'}\right)^2$ eq. (3.17)	$z_M = 1 - \frac{q_0}{\mu'}$ eq. (3.18)
renormalization scale	$\alpha_s\left(\mu'^2\right) = \alpha_s\left(q_\perp^2\right)$ eq. (2.41)	$\alpha_s\left((1-z)\mu'^2\right) = \alpha_s\left(q_\perp^2\right)$ eq. (3.19)	$\alpha_s\left((1-z)^2\mu'^2\right) = \alpha_s\left(q_\perp^2\right)$ eq. (3.20)

Table 8.1: The ordering definitions together with the definitions of z_M parameters and renormalization scale choices in α_s.

In this chapter the TMD distributions obtained with the PB method are presented. The prescription to determine $k_\perp$ dependence in the PB method was introduced in Sec. (6.5).

The TMDs are determined in a grid of $50 \otimes 50 \otimes 50$ bins in $\log x$, $\log k_\perp$ and $\log \mu$. A polinomial and linear interpolation is used to obtain the values of the TMDs between the grid points. The intrinsic $k_\perp$ distribution is assumed to be a Gaussian $\exp(-k_\perp^2/\sigma^2)$ with $\sigma^2 = k_0^2/2$ where $k_0 = 0.5$ GeV. The same form is used for all partons. In the figures the TMDs, $xA(x, k_\perp, \mu)$, as a function of $k_\perp$ for a given x and

scale μ or the TMDs as a function of x for a given $k_\perp$ and scale μ are shown. The figures are obtained with TMDplotter plotting tool [143].

In Sec. (3.1.1)- (3.1.2) we introduced $p_\perp$-, virtuality and angular ordering conditions. We showed that from the association of the branching scale μ'^2 with a given kinematic variable, the z_M definition and renormalization scale choice in α_s follows. In Tab. 8.1 we summarize the formulas given in Sec. (3.1.1)-(3.1.2). However, as discussed in Sec. (6.5), the PB method allows one to change the ordering, z_M and renormalization scale independently to examine the individual effects and we performed the studies systematically for different scenarios. In Tab. 8.2 we illustrate the different settings which we study in this chapter additionally to Tab. 8.1. Throughout this thesis we will refer to the expression *ordering* as the association of the branching scale with kinematic variable (eq. (3.7), (3.9) or (3.15)) and we will say explicitly which definition of z_M and α_s we are using.

virtuality ordering $q_\perp^2 = (1-z)\mu'^2$		angular ordering $q_\perp^2 = (1-z)^2\mu'^2$	
fixed z_M	$z_M = 1 - \left(\frac{q_0}{\mu'}\right)^2$	fixed z_M	$z_M = 1 - \frac{q_0}{\mu'}$
$\alpha_s\left(\mu'^2\right)$	$\alpha_s\left(\mu'^2\right)$	$\alpha_s\left(\mu'^2\right)$	$\alpha_s\left(\mu'^2\right)$

Table 8.2: The summary of the settings tested additionally to the prescriptions listed in Tab. 8.1.

8.1 | Collinear PDFs and TMDs with fixed value of z_M

In this section we use NLO splitting functions and 2-loop $\alpha_s\left(\mu'^2\right)$ except the last subsection where the LO splitting functions and 1-loop $\alpha_s\left(\mu'^2\right)$ are used. The initial parametrization comes from QCDNUM.

8.1.1 | Collinear PDFs with virtuality and angular ordering condition with fixed z_M

The results in the previous chapter were calculated using the settings from the first column of Tab. 8.1. In fig. 8.1 we present the results for virtuality and angular ordering condition, with four different fixed z_M values. As explained in Sec. (6.5), the prescription of calculating $k_\perp$ does not affect the collinear evolution. The results presented in fig. 8.1 confirm these predictions. [1]

[1]The evolution variable is always the evolution scale μ^2, which is generated according to the Sudakov form factor and the splitting variable z is generated according to the collinear splitting functions. In both of these steps no dependence on $k_\perp$ or $q_\perp$ is included. An interesting detail can be noticed in fig. 8.1: the way the $k_\perp$ calculations are performed should not affect the collinear distributions, however, the fluctuations on the plot with virtuality ordering looks a bit different than the plot with $p_\perp$- and angular ordering. The reason for that is that the results with virtuality ordering were obtained with different seed for a random number generation than the results for $p_\perp$- and angular ordering.

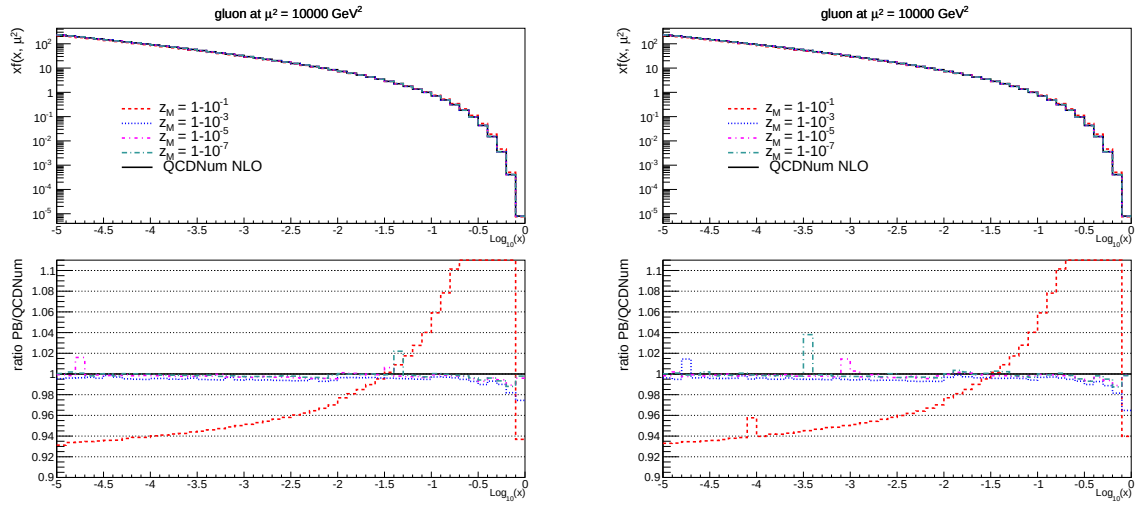

Figure 8.1: Collinear PDFs from the PB method compared with QCDNUM. The results obtained with virtuality (left) and angular (right) ordering condition for four different values of z_M.

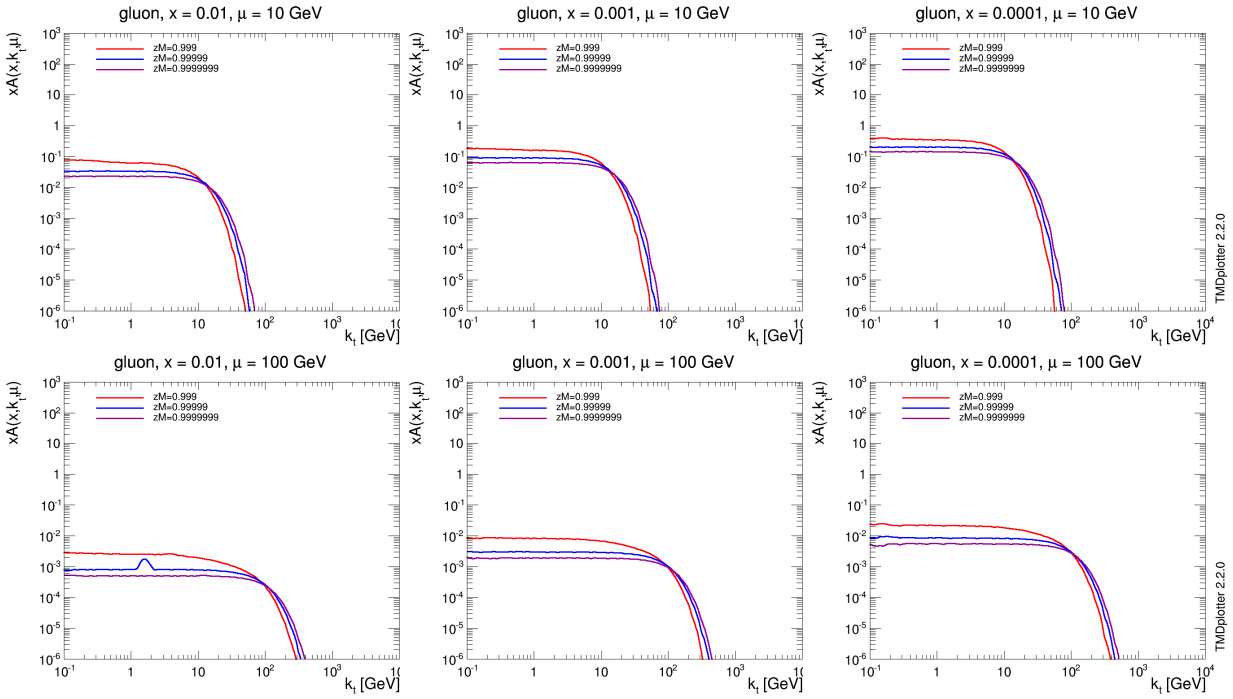

Figure 8.2: Gluon TMD parton densities as a function of $k_\perp$ from the PB method with $p_\perp$-ordering and fixed values of z_M.

8.1.2 | TMDs with fixed z_M and $p_\perp$- ordering condition

In fig. 8.2 the transverse momentum dependence of the gluon TMD with $p_\perp$-ordering is shown for three fixed values of $z_M = 1-10^{-3}$, $1-10^{-5}$ and $1-10^{-7}$ (for which no dependence on z_M was observed for collinear PDFs, see Sec. (7)).

From fig. 8.2 one can see, that for TMDs the situation is different: with each of these values of z_M

one obtains different TMDs. The reason for that is that $p_\perp$- ordering is valid only for the $z \to 0$ region, otherwise it violates the energy-momentum conservation whereas here we observe an effect coming from $z \to 1$. Thus one can conclude that $p_\perp$- ordering does not allow one to define TMD in a consistent way.

Nevertheless, let us still analyse the plots for TMDs with $p_\perp$- ordering. With larger z_M value one obtains larger $k_\perp$ tails. Large z_M means that the Sudakov form factor becomes smaller and the probability to evolve without any resolvable branching is smaller. As a consequence, there are more branchings and higher $k_\perp$ is accumulated in the evolution process (eq. (6.14)).

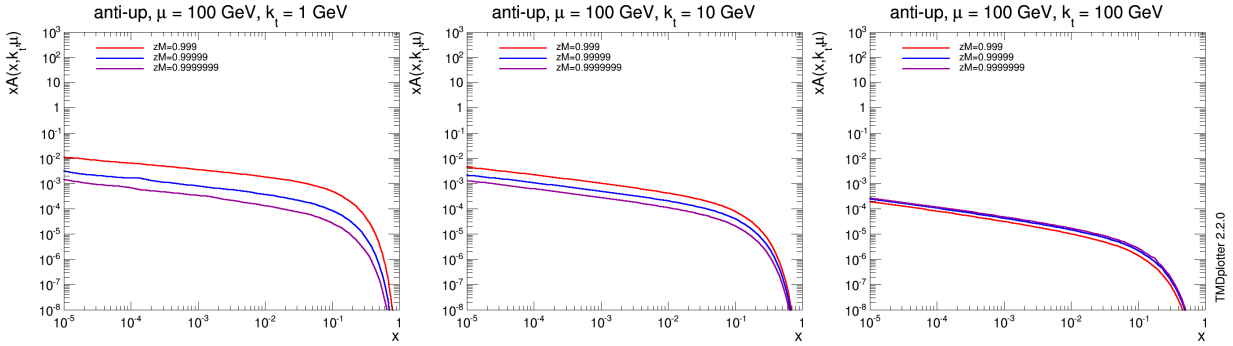

Figure 8.3: Anti-up quark TMD densities as a function of x from the PB method with $p_\perp$-ordering and fixed values of z_M.

In fig. 8.3 distributions for anti-up quark density as a function of x with $p_\perp$-ordering for three fixed values of $z_M = 1 - 10^{-3}$, $1 - 10^{-5}$ and $1 - 10^{-7}$ are shown. In the region of small $k_\perp$, higher densities are obtained with smaller value of the z_M parameter for which the probability of an evolution without any resolvable emission is larger. In the region of large $k_\perp$ the Sudakov form factor with higher z_M gives larger contribution.

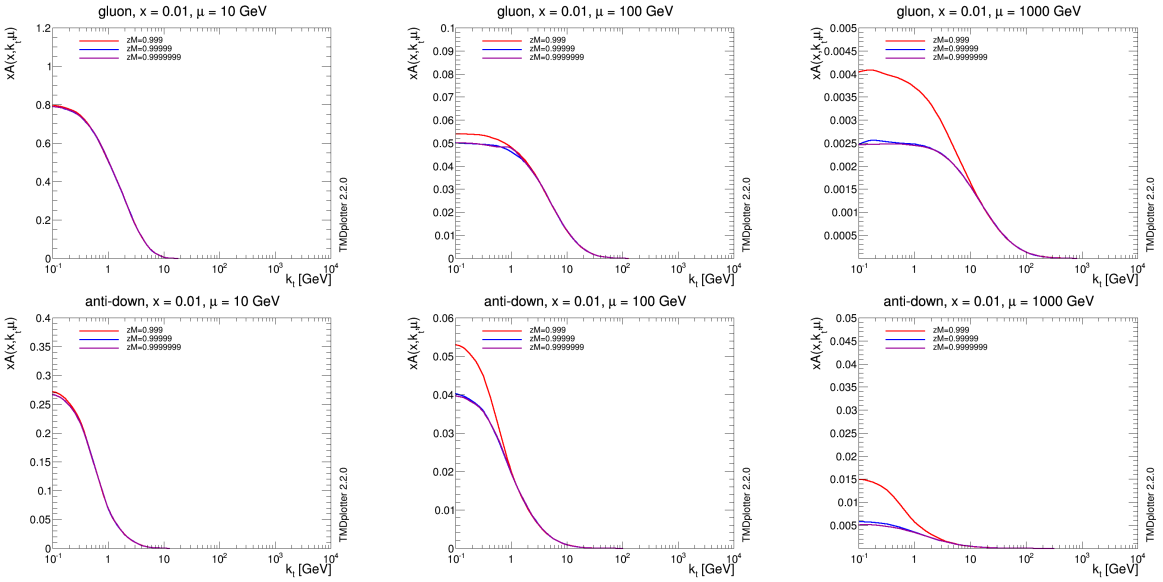

Figure 8.4: Gluon and anti-down quark TMD densities as a function of $k_\perp$ from the PB method with virtuality ordering and fixed values of z_M.

8.1.3 | TMDs with fixed z_M and virtuality and angular ordering condition

In this subsection we study the z_M dependence in TMD distributions with virtuality and angular ordering condition.

In fig. 8.4 the transverse momentum dependence of the gluon and anti-down quark TMD densities with virtuality ordering and in fig. 8.5 with angular ordering for three different values of $z_M = 1 - 10^{-3}$, $1 - 10^{-5}$ and $1 - 10^{-7}$ are shown.

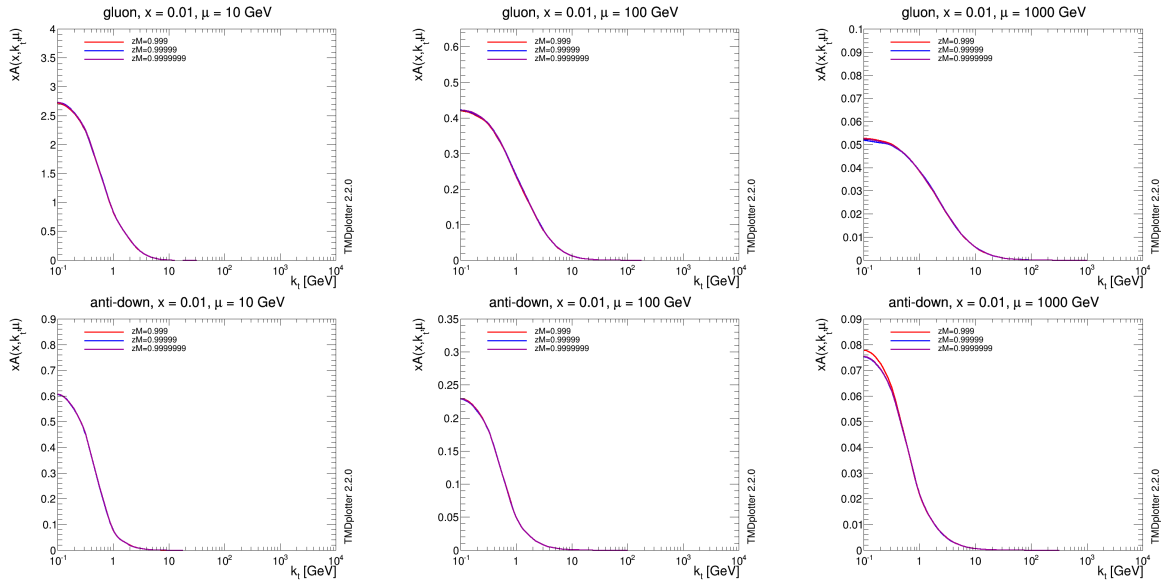

Figure 8.5: Gluon and anti-down quark TMD densities as a function of $k_\perp$ from the PB method with angular ordering and fixed values of z_M.

From fig. 8.4 - 8.5 one can see, that all these values of z_M lead to almost the same TMDs. The difference is visible in the very small $k_\perp$ region at higher scales. The difference between different z_M values starts to be visible at lower scales for quark density than for gluon density and it is bigger for virtuality ordering than for the angular ordering. In the case of TMD distributions with virtuality or angular ordering, there are three effects that influence the distributions at very low $k_\perp$. The first one is the intrinsic $k_\perp$ distribution, the same for both orderings. The second one is the Sudakov form factor, also the same for virtuality and angular ordering, which gives the probability of an evolution without any resolvable branching. Thus with higher z_M we have more emissions in which $k_\perp$ is accumulated. The third effect regards the *diffusion* in the low $k_\perp$ coming from the branchings at higher evolution scales. When a soft gluon is emitted, a parton which continues the evolution has a very large z and a very small $k_\perp$ because of eq. (3.7) and eq. (3.15). These formulas express the energy- momentum conservation. The formula for angular ordering gives $k_\perp$ smaller than the formula for virtuality ordering for a given branching scale μ'^2 and z.

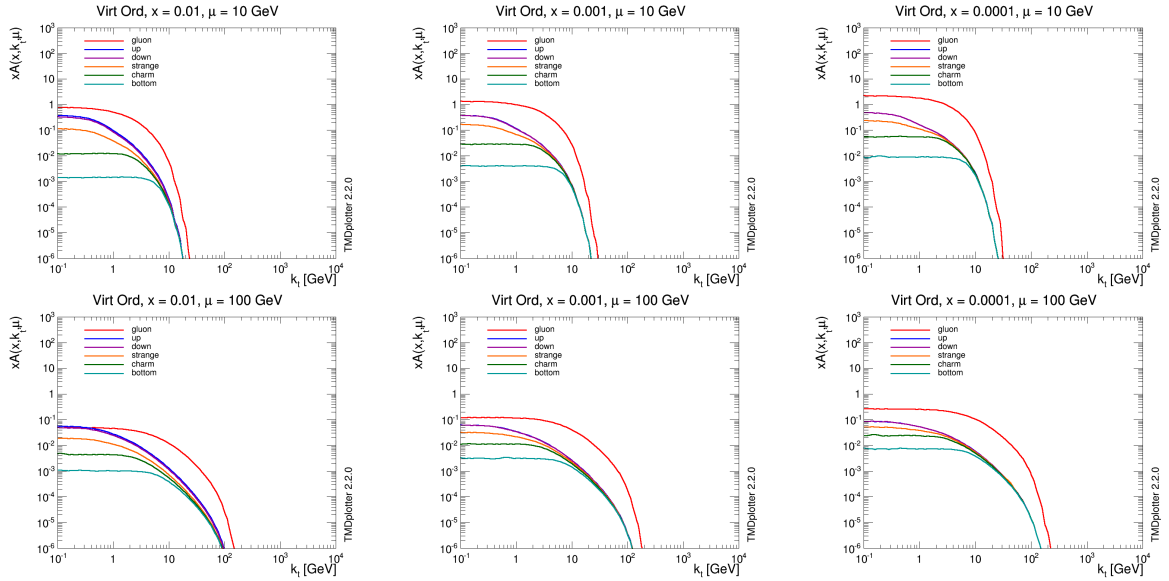

Figure 8.6: TMDs as a function of $k_\perp$ for gluon and all quark flavours from the PB method with virtuality ordering and fixed value of $z_M = 1 - 10^{-5}$.

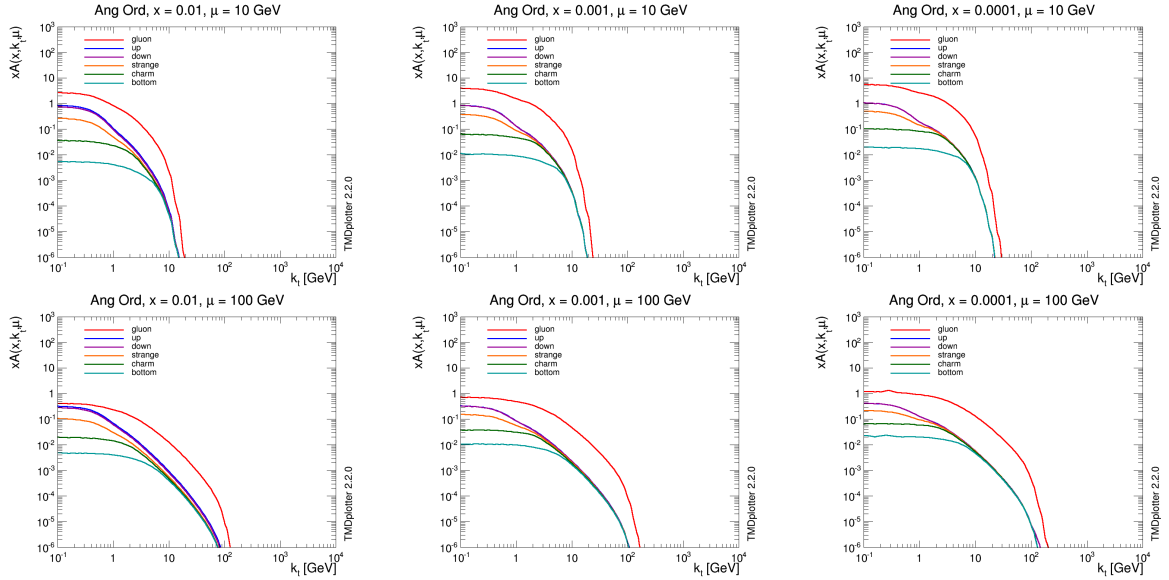

Figure 8.7: TMDs as a function of $k_\perp$ for gluon and all quark flavours from the PB method with angular ordering and fixed value of $z_M = 1 - 10^{-5}$.

PB method can be used to obtain TMD densities for all parton species. In fig. 8.6 TMDs as a function of $k_\perp$ for all quark flavours and gluon densities with virtuality ordering and in fig. 8.7 with angular ordering are shown for $z_M = 1 - 10^{-5}$. An interesting feature can be noticed there: in the low $k_\perp$ region, the quark densities are different for different flavours. The difference comes from the initial distributions and beginning of the evolution. In the high $k_\perp$ region where many emissions contribute, the initial difference between quark flavours is smeared away because the splitting functions do not distinguish between quark flavours if only the mass threshold for a given quark production was reached.

8.1.4 | Comparison between virtuality and angular ordered TMDs with fixed z_M

We have shown above that the $p_\perp$- ordering condition does not lead to stable results for the TMD whereas both virtuality and angular ordering produce results which do not depend on z_M (except very small $k_\perp$ at higher scales), as long as it is close to 1.

The comparison of TMDs as a function of $k_\perp$ with virtuality and angular ordering is shown for $z_M = 1 - 10^{-5}$ in fig. 8.8. The TMDs obtained with angular ordering are larger at small values of $k_\perp$ than the one obtained with virtuality ordering. In addition, TMDs with virtuality ordering have a bit larger $k_\perp$ tail than TMDs with angular ordering. This is expected because of $(1-z)^2$ and $(1-z)$ terms in the angular and virtuality ordering conditions, respectively.

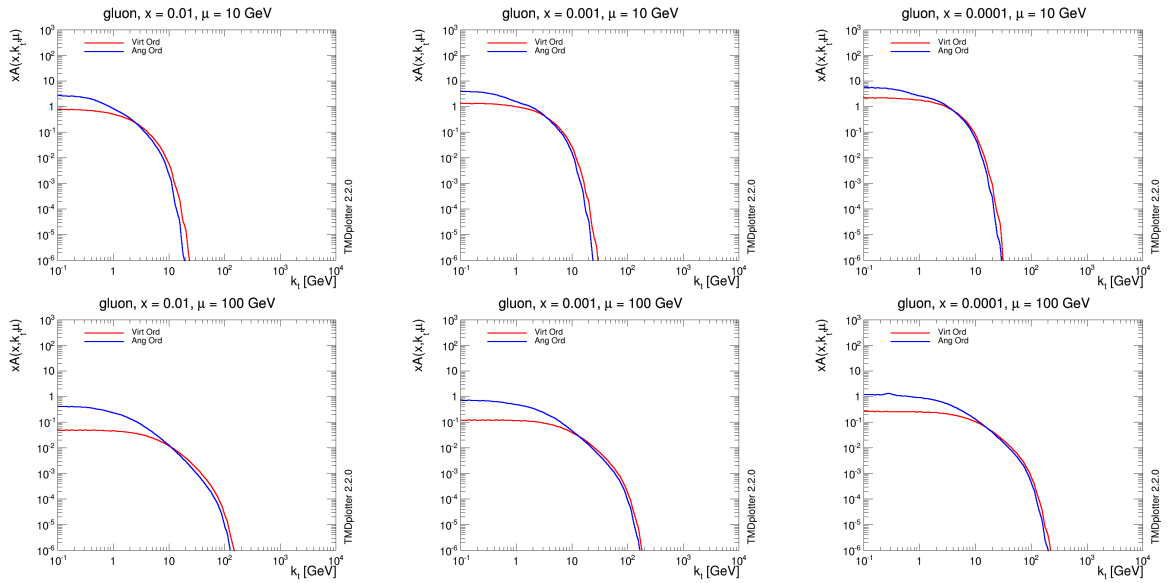

Figure 8.8: Comparison of gluon TMD densities as a function of $k_\perp$ from the PB method with virtuality and angular ordering and fixed value of $z_M = 1 - 10^{-5}$.

Both ordering conditions give $k_\perp$ tails which can be even larger than the evolution scale μ, however this contribution is very small. This is a consequence of eq. (6.14) where $k_\perp$ is calculated by summing all the transverse momenta from the previous emissions.

8.1.5 | Comparison of virtuality and angular ordered TMDs with fixed z_M at LO and NLO

At the end of this section we investigate the difference between LO and NLO TMDs.

In fig. 8.9 a comparison of the gluon TMDs from the PB method at LO and NLO with angular ordering and in fig. 8.10 with virtuality ordering, for fixed value of $z_M = 1 - 10^{-5}$ is shown[2].

[2]The fluctuations on the plots are due to limited statistics.

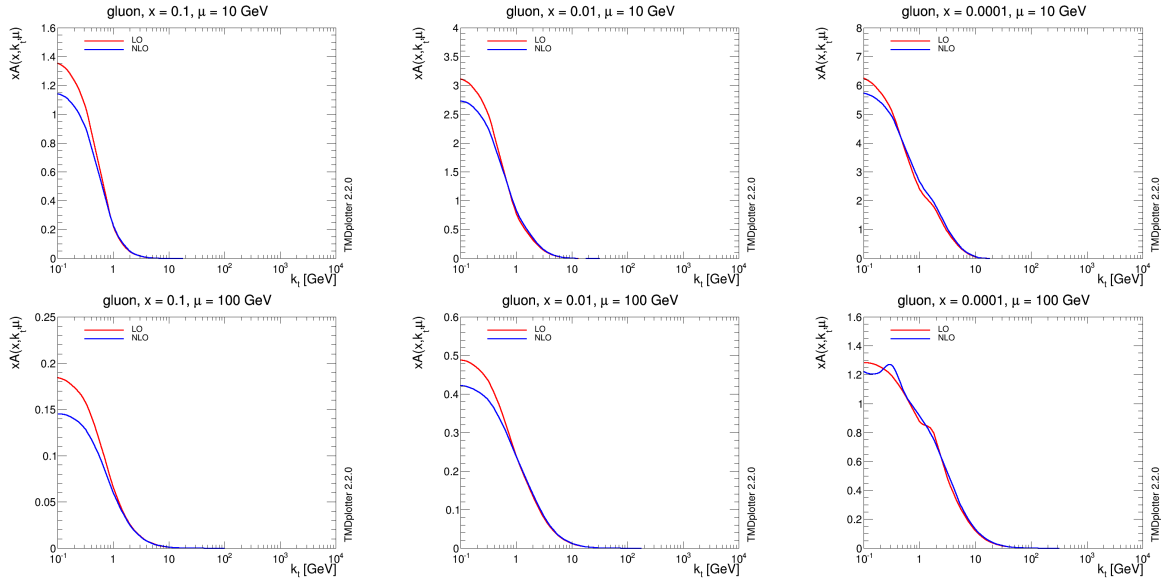

Figure 8.9: Comparison of gluon TMD densities as a function of $k_\perp$ from the PB method with angular ordering at LO and NLO.

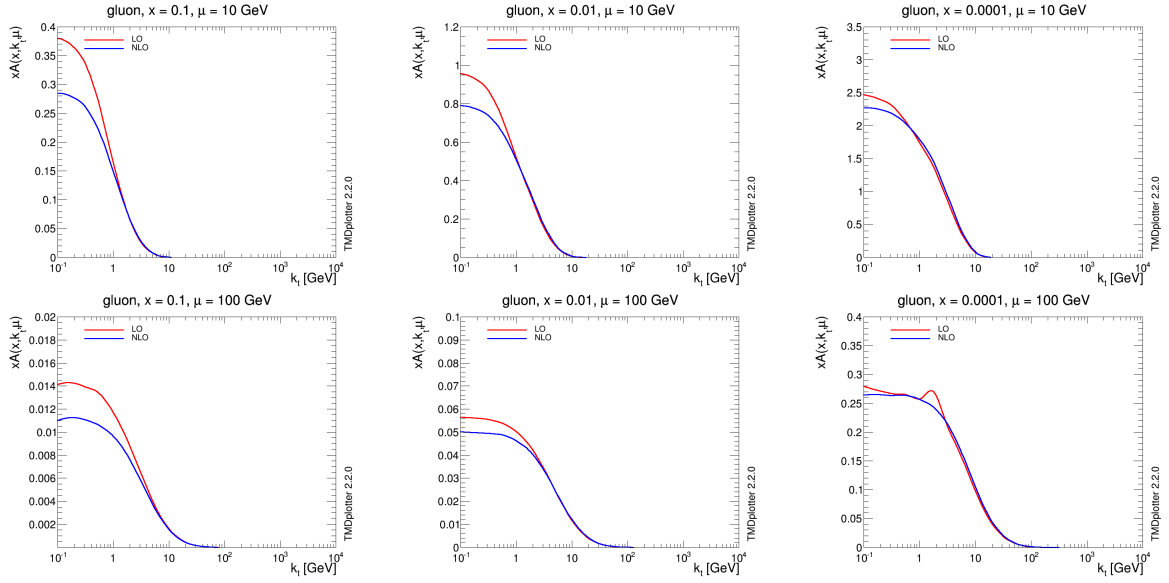

Figure 8.10: Comparison of gluon TMD densities as a function of $k_\perp$ from the PB method with virtuality ordering at LO and NLO.

The TMDs densities obtained from the PB method are similar at LO and NLO. This is understandable, because we use the same initial distribution from QCDNUM for LO and NLO case and we use splitting functions which do not depend on $k_\perp$. The only thing which can influence the distributions, is α_s, which differs between 1-loop and 2-loop mainly at small scales.

In fig. 8.11 TMDs as a function of $k_\perp$ for gluon at LO are shown for $p_\perp$-, virtuality and angular ordering condition for different values of z_M parameter. Similarly, as at NLO, $p_\perp$- ordering does not give stable results for the TMD.

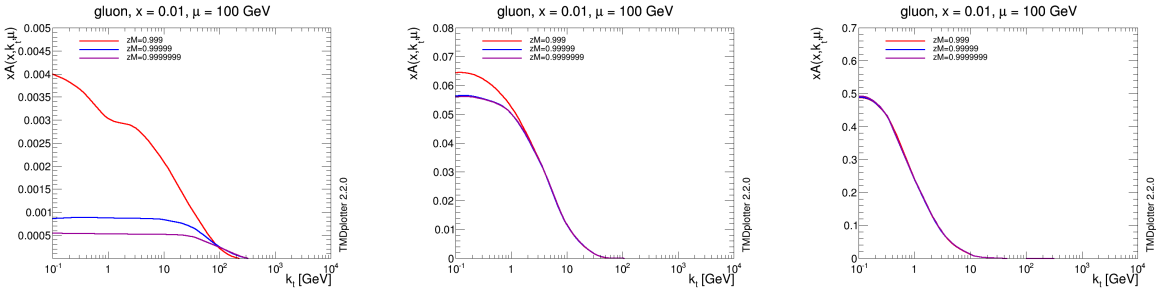

Figure 8.11: Comparison of gluon TMD densities as a function of $k_\perp$ from the PB method with $p_\perp$- (left), virtuality (middle) and angular (right) ordering at LO.

8.2 | Collinear PDFs and TMDs with dynamic z_M

In this section we investigate the effect of using the definitions of z_M which follow from the virtuality and angular ordering conditions. The parameter z_M is calculated for every branching and depends on the scale of the branching μ'^2 and some parameter q_0. We call such z_M *dynamic*.

In Sec. (8.1) we showed that virtuality and angular ordering condition give consistent and stable results for the TMDs for different fixed z_M values except the very low $k_\perp$ region at higher scales. Here we study the usage of the dynamic z_M.

The first issue is what should be the value of the q_0 parameter. One can estimate the required value by assuming that even at the smallest scales the z_M value should reproduce the standard collinear PDFs (e.g. QCDNUM or HERAPDF). We know from eq. (2.82) that when z_M is too small, the approximation in eq. (2.83) is not good anymore. In Sec. (7) we have shown that $z_M \approx 0.999$ gives the results which agree with QCDNUM. Using z_M definitions from Tab. (8.1) with the initial scale $\mu = 1.41$ GeV we obtain $q_0 \approx 0.04$ GeV for virtuality ordering and $q_0 \approx 10^{-3}$ GeV for angular ordering. In Sec. (3.1.3) we introduced q_0 as some minimum $q_\perp$ allowed for an emission to be resolvable. This physical interpretation of values $q_0 \approx 0.04$ GeV or $q_0 \approx 10^{-3}$ GeV is not accurate. Nevertheless, we test such a small values treating them just as some parameters.

In this section we use NLO splitting functions and 2-loop $\alpha_s\left(\mu'^2\right)$. The initial conditions for the PB method come from HERAPDF2.0.

8.2.1 | Collinear PDFs with dynamic z_M

In fig. 8.12 the results for collinear PDFs with angular ordering and dynamic $z_M = 1 - \frac{q_0}{\mu'}$ as a function of x for different values of the parameter $q_0 = 0.001$ GeV, $q_0 = 0.01$ GeV, $q_0 = 0.1$ GeV, $q_0 = 0.2$ GeV, $q_0 = 0.5$ GeV and 1.0 GeV are presented. One can see that the choice of the resolution scale has an effect on collinear distributions. The distribution obtained with the value $q_0 = 0.001$ GeV turns out to be consistent with HERAPDF2.0 while for bigger q_0 values the deviation from HERAPDF2.0 starts to be visible because the parameter z_M is too small (see Sec. (2.3.2)).

Similarly, in fig. 8.13 the results for collinear PDFs with virtuality ordering and dynamic $z_M = 1 - \left(\frac{q_0}{\mu'}\right)^2$ as a function of x for different values of the parameter $q_0 = 0.04$ GeV, $q_0 = 0.1$ GeV, $q_0 = 0.2$ GeV, $q_0 = 0.5$ GeV and 1.0 GeV are presented. With higher q_0 the results start to deviate from HERAPDF2.0.

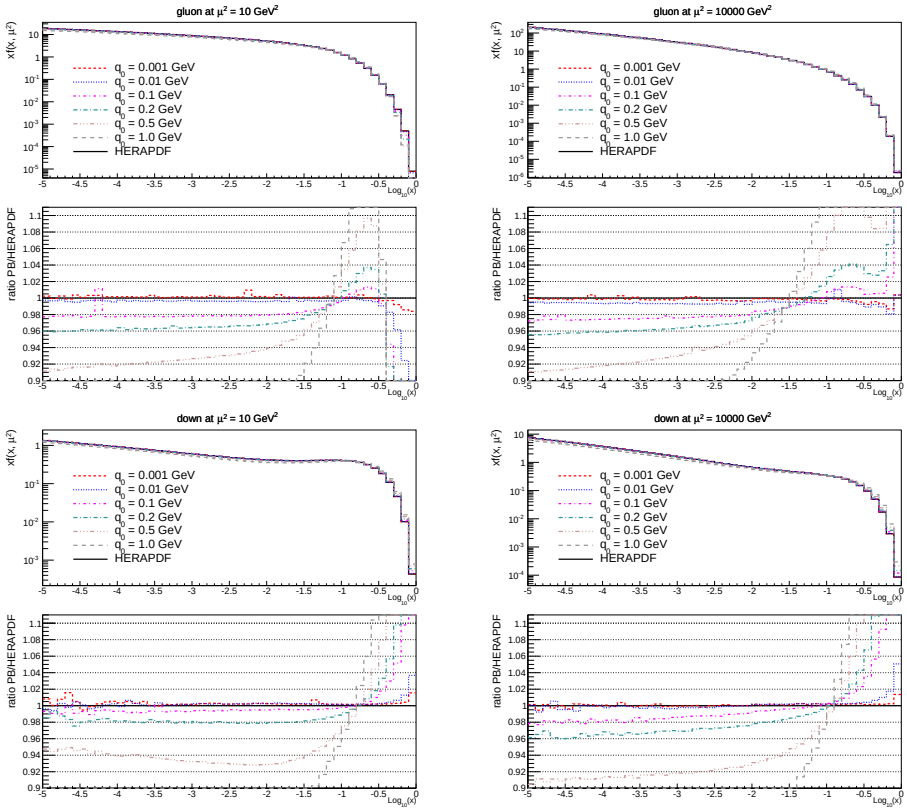

Figure 8.12: Collinear PDFs from the PB method compared with HERAPDF2.0. The results obtained with angular ordering condition for different values of q_0 parameter in z_M definition.

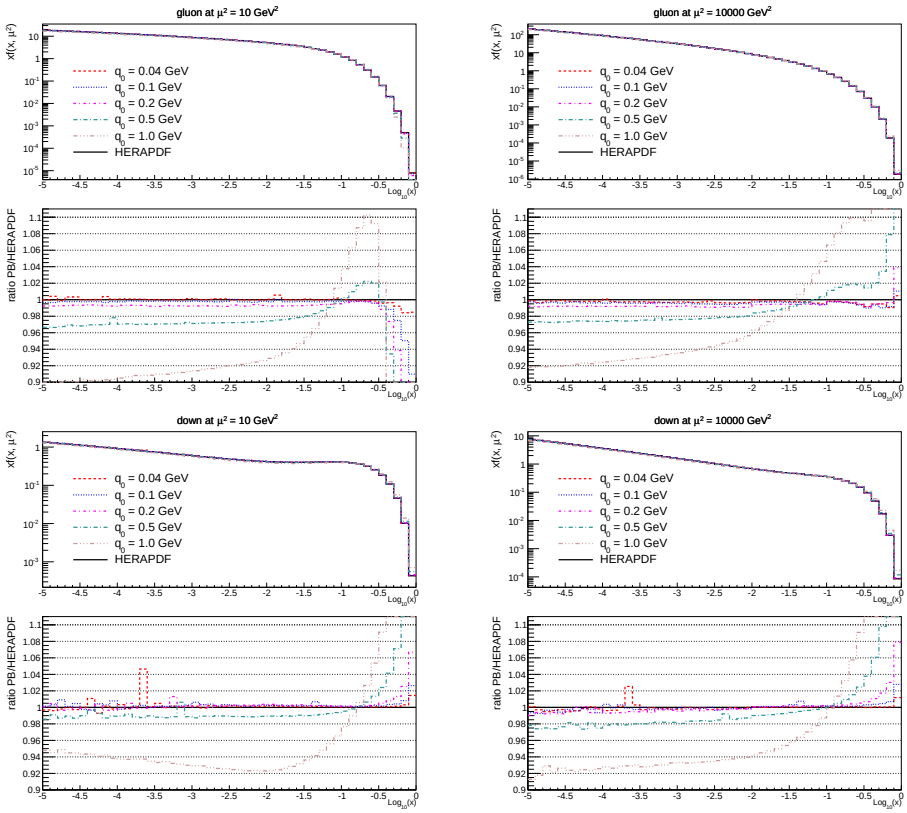

Figure 8.13: Collinear PDFs from the PB method compared with HERAPDF2.0. The results obtained with virtuality ordering condition for different values of q_0 parameter in z_M definition.

8.2.2 | TMDs with dynamic z_M

In the previous subsection the collinear PDFs with dynamic z_M were discussed and it was shown that only small values of the resolution scale parameter q_0 give results in agreement with standard collinear evolution. Here we want to study how the choice of q_0 influences the TMD distributions [3]. We test small values of q_0 and we expect a similar behaviour as in the case if fixed z_M value, however with the dynamic z_M definition we have continuous variation of the resolution scale.

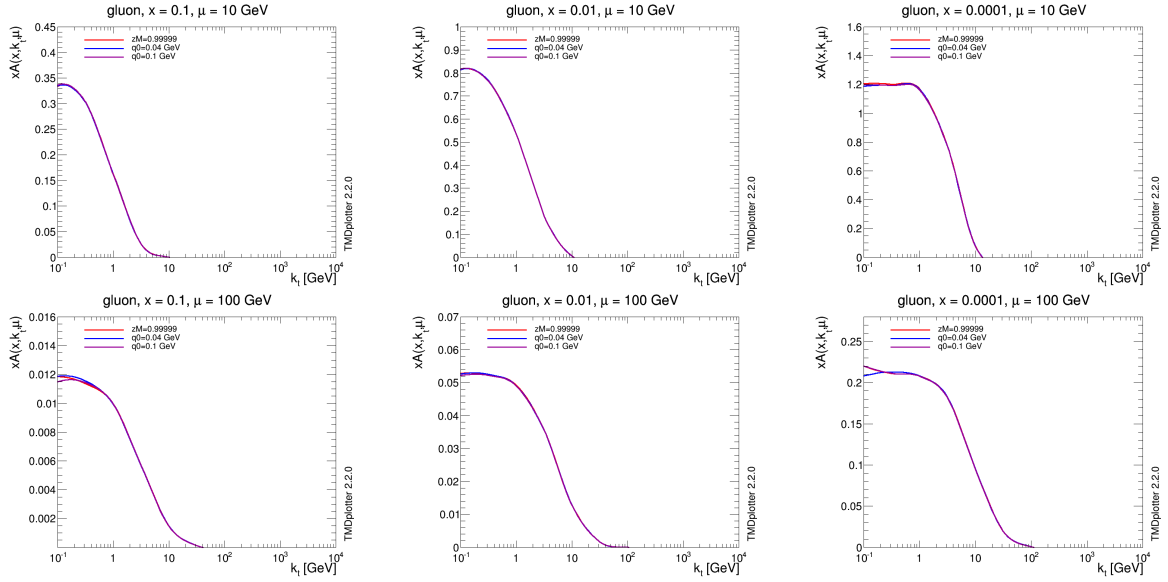

Figure 8.14: Comparison of gluon TMD densities as a function of $k_\perp$ from the PB method with virtuality ordering and different choices of z_M parameter.

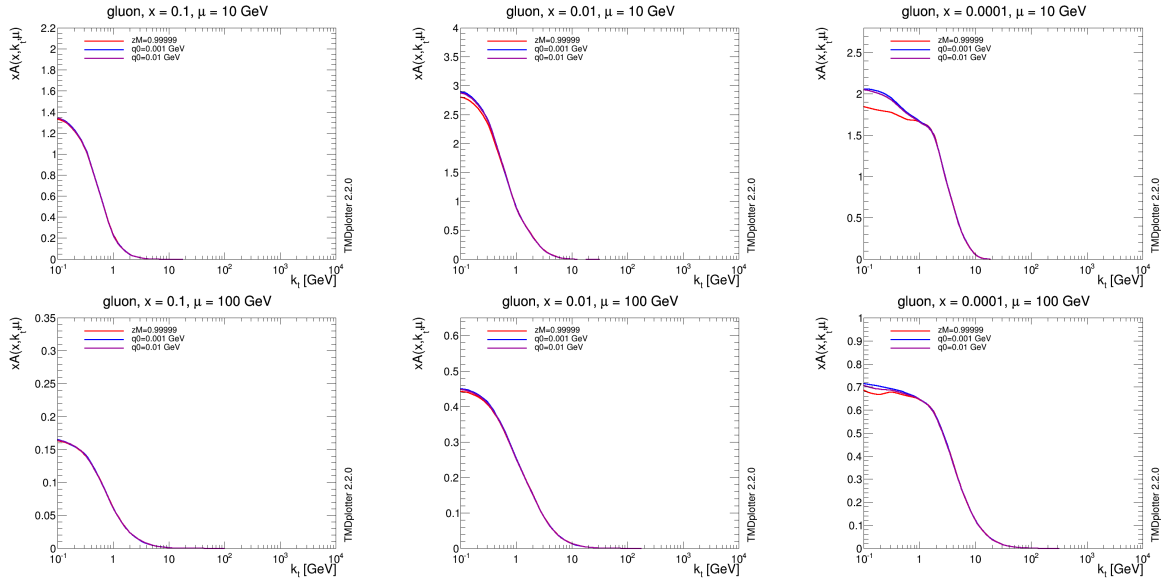

Figure 8.15: Comparison of gluon TMD densities as a function of $k_\perp$ from the PB method with angular ordering and different choices of z_M parameter.

[3]The distributions shown in this section are obtained with different initial parametrization than the distributions in Sec. (8.1).

In fig. 8.14 TMD distributions as a function of $k_\perp$ for gluon density from the PB method with virtuality ordering are shown. Additionally to the dynamic z_M with $q_0 = 0.04$ GeV and 0.1 GeV, the curve for the fixed value $z_M = 1 - 10^{-5}$ is drawn (obtained with the same initial conditions from HERAPDF2.0). In fig. 8.15 TMD distributions as a function of $k_\perp$ for gluon density from the PB method with angular ordering obtained with the dynamic z_M parameters with $q_0 = 0.001$ GeV, $q_0 = 0.01$ GeV and with the fixed value of $z_M = 1 - 10^{-5}$ are shown.

In both figures the difference between the different z_M is visible in the very small $k_\perp$ region, for higher $k_\perp$ values all the z_M options give consistent results.

The effects from fig. 8.14 - 8.15 can be explained in a similar way as for the fixed z_M values in Sec. (8.2.2).

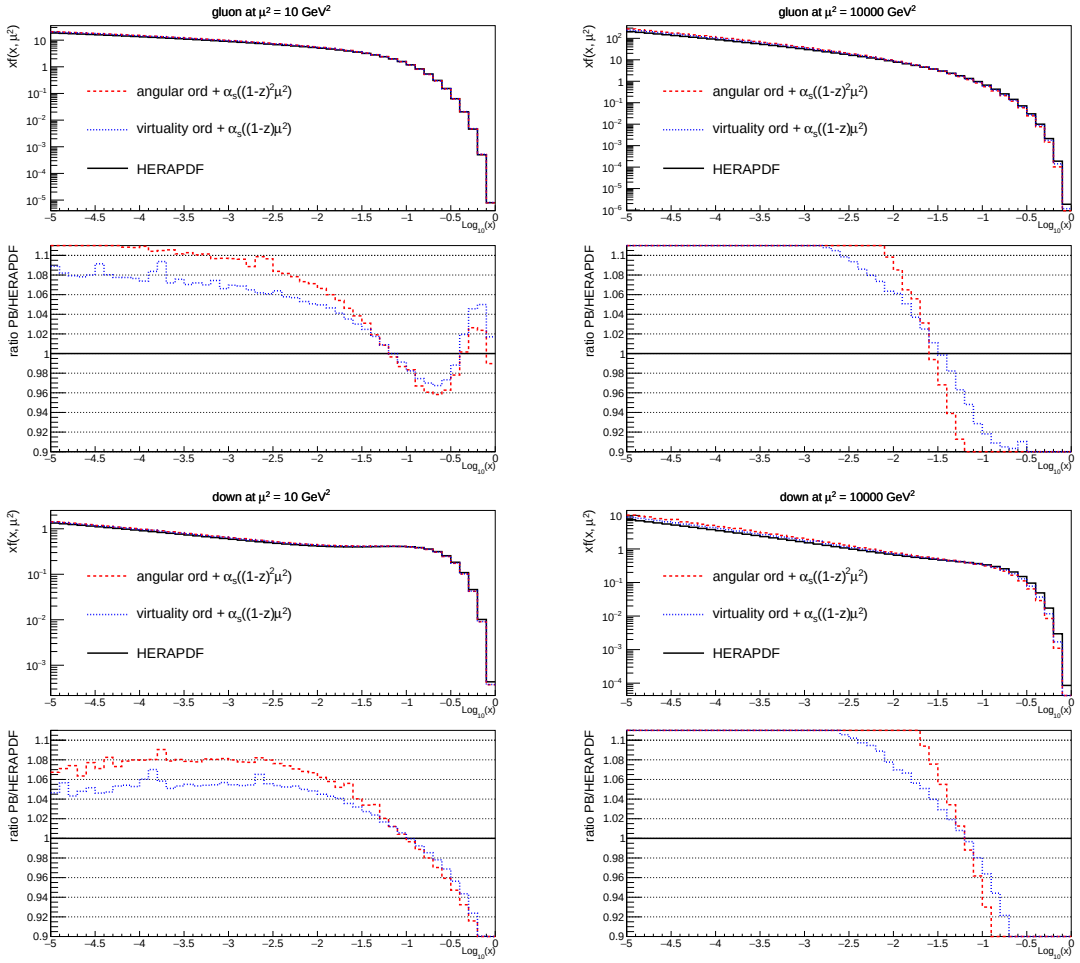

Figure 8.16: Collinear PDFs from the PB method compared with QCDNUM. The PB results obtained with virtuality and angular ordering condition with $\alpha_s(q_\perp^2)$.

8.3 | Influence of the renormalization scale choice on collinear and TMD PDFs

As discussed in Sec. (3.1.4), the virtuality and angular ordering not only give the prescriptions how to associate the $k_\perp$, $q_\perp$ and μ'^2 and how to calculate the z_M parameter, but also on the renormalization scale choice in the α_s argument. Up to now, in Sec. (8.1)- (8.2), the argument of α_s was always the

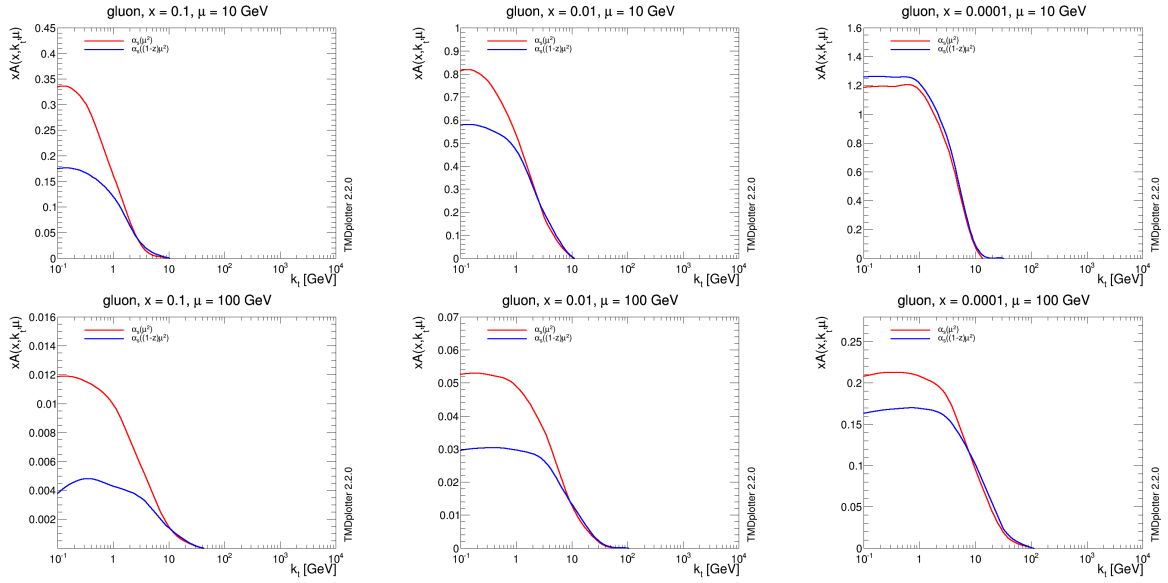

Figure 8.17: Comparison of gluon TMD densities as a function of $k_\perp$ from the PB method with virtuality ordering and different arguments of α_s.

branching scale μ'^2 (eq. (2.41)). In this section we study the renormalization scale given by the virtuality and angular ordering condition (Sec. (3.1.4)).

In this section the virtuality and angular ordering condition is introduced together with the dynamic z_M definition and with $q_\perp$ in the argument of α_s (see Tab. 8.1). We introduce a cut off on the argument of α_s to ensure that the renormalization scale is above the initial evolution scale. The NLO splitting functions and 2-loop α_s are used to obtain the results. The results are compared to HERAPDF2.0 which the initial conditions for PB method come from.

The parameter q_0 is chosen to be $q_0 = 0.04$ GeV for virtuality ordering and to $q_0 = 0.001$ GeV for angular ordering so in the case of $\alpha_s(\mu'^2)$ one obtains the results consistent HERAPDF2.0 (see Sec. (8.2)) for collinear distributions. The results shown in fig. 8.16 show that the influence of changing the argument of α_s parameter on the collinear distributions is significant.

The fact that we do not obtain anymore the collinear PDFs which agree with standard methods, is not surprising. By introducing full virtuality or angular ordering we resum extra large logarithms compared to $\alpha_s\left(\mu'^2\right)$ [91, 95].

The results shown in fig. 8.17-8.18 show that the influence of the argument of α_s parameter on the TMD distributions is significant, especially in the low $k_\perp$ region.

8.4 | Conclusions from the studies on collinear and TMD PDFs from the PB method

In Sec. (7)-(8) we have shown that the PB method can be used to solve DGLAP evolution equation and to obtain collinear PDFs which agree well with other methods (QCDNUM). We demonstrated how we can include in the solution also different orderings, the dynamic resolution scale parameter z_M and different renormalization scale choices in the argument of α_s. We studied different scenarios given in Tab. 8.1 and Tab. 8.2. For $\alpha_s(\mu'^2)$ we have found that as long as the z_M parameter is close enough

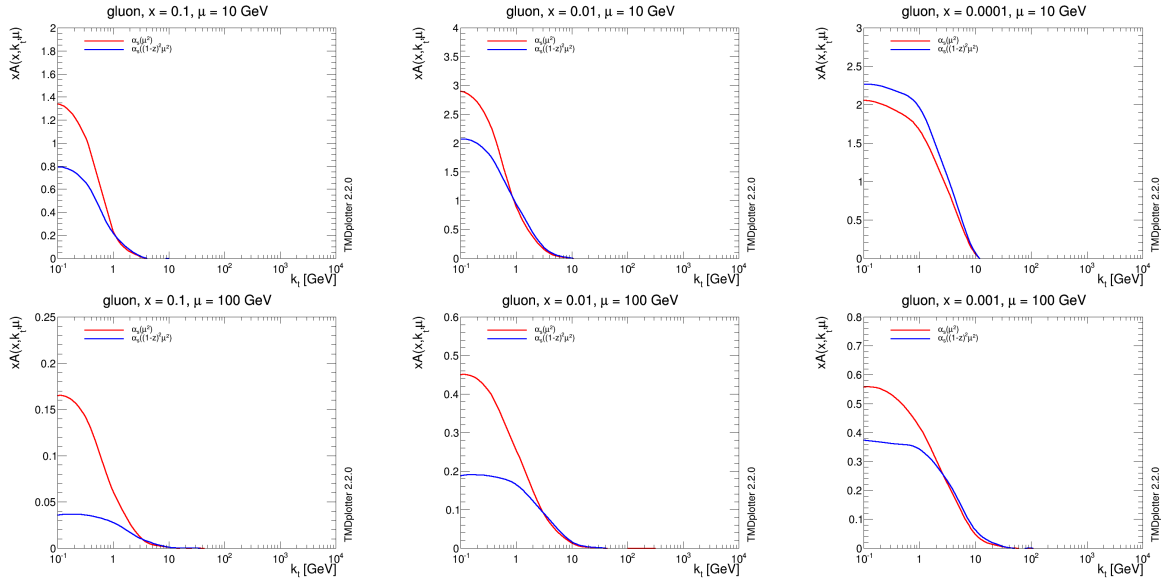

Figure 8.18: Comparison of gluon TMD densities as a function of $k_\perp$ from the PB method with angular ordering and different arguments of α_s.

to 1, the results for collinear PDFs are not affected and we reproduce the standard collinear PDFs from QCDNUM or HERAPDF, both for fixed and dynamic values of z_M, regardless of the ordering we are using. However, $p_\perp$-ordering does not produce stable results for the TMDs since we observe a dependence on z_M parameter in the whole $k_\perp$ range. The reason for that is that $p_\perp$- ordering violates the energy-momentum conservation. TMDs with virtuality and angular ordering do not depend on z_M definition except a very small $k_\perp$ region (compared to the evolution scale μ^2 we are looking at). This residual z_M dependence is unavoidable. By changing z_M we reorganize the pieces which go into resolvable and non-resolvable branchings which must affect the small $k_\perp$ region. Moreover, we observe a diffusion into the small $k_\perp$ region from the evolution which is a consequence of the expressions we use to calculate $k_\perp$ to conserve energy-momentum. The small $k_\perp$ behaviour should be understood better. This would require some special treatment, for example introduction of a scale dependent intrinsic $k_\perp$. This is out of the scope of this thesis where we concentrate on the perturbative region.

We performed also studies on the effect of changing the renormalization scale in α_s to the scale given by virtuality and angular ordering. We found out that both collinear and TMD PDFs are affected significantly.

At this stage both virtuality and angular ordering are considered in this thesis as two equivalent descriptions without giving a statement which one is more appropriate. In the next chapter we will apply obtained TMDs to the measurements to further explore the ordering and renormalization scale dependence.

9 | Outlook: determination of TMDs and application to measurements

In the previous chapter we obtained the TMD distributions with the PB method using the initial parametrization of QCDNUM or HERAPDF2.0. In this chapter we describe the procedure to obtain the parameters of the initial distributions from a fit to HERA F_2 data. Having obtained the TMD PDFs, we can test the idea introduced in Sec. (6.1) to obtain the predictions for high energy collision observables by using TMDs instead of collinear PDFs. In the second part of this chapter we apply the TMDs obtained from the fit to a measurement of the Z boson $p_\perp$ spectrum at 8 TeV.

9.1 | Fits of integrated TMDs to HERA F_2 data

The parameters of the initial parton density distributions have to be obtained from the fits to the experimental data. For the fits presented in this chapter [229] this is done within `xFitter` package [230] - a standard tool to obtain PDF fits. The method to obtain the fits was developed in [148]. The procedure is the following: first, an evolution kernel $K_a^b(x'', \mu^2)$ is obtained from the PB method for every initial parton of flavour b and final parton a. The initial parametrization at the scale μ_0^2 is given by $x_0 = 1 - 10^{-6}$ (the term -10^{-6} is added because of the technical reasons) and the kernel is produced during the evolution process. The convolution of the kernel with the starting distribution $A_{0,b}$ is performed in the following way

$$\begin{aligned} \widetilde{f}_a(x,\mu^2) &= x\int \mathrm{d}x' \int \mathrm{d}x'' A_{0,b}(x') K_a^b(x'',\mu^2)\delta(x'x''-x) \\ &= \int \mathrm{d}x' A_{0,b}(x')\frac{x}{x'}K_a^b\left(\frac{x}{x'},\mu^2\right) . \end{aligned} \tag{9.1}$$

The parametrization of the initial distribution has the form of HERAPDF2.0

$$\begin{aligned} xg(x) &= A_g x^{B_g}(1-x)^{C_g} - A'_g x^{B'_g}(1-x)^{C'_g} , \\ xu_v(x) &= A_{u_v} x^{B_{u_v}}(1-x)^{C_{u_v}}(1+E_{u_v}x^2) , \\ xd_v(x) &= A_{d_v} x^{B_{d_v}}(1-x)^{C_{d_v}} , \\ x\overline{U}(x) &= A_{\overline{U}} x^{B_{\overline{U}}}(1-x)^{C_{\overline{U}}}(1+D_{\overline{U}}x) , \\ x\overline{D}(x) &= A_{\overline{D}} x^{B_{\overline{D}}}(1-x)^{C_{\overline{D}}} . \end{aligned} \tag{9.2}$$

The obtained distribution $\widetilde{f}_a(x,\mu^2)$ is convoluted with the matrix element to obtain the structure function at NLO, which can be fitted to experimental data. Then, the procedure is repeated with different values of the initial parameters until the minimal χ^2 is found. It turned out in [222] that in practice it is enough to determine the evolution kernel only for one initial state light quark and gluon.

The method described above can be also extended to the TMDs case. A new kernel, depending now also on $k_\perp$, can be obtained from the PB method and convoluted with the initial distribution

$$\begin{aligned} xA_a(x,k_\perp,\mu^2) &= x\int \mathrm{d}x' \int \mathrm{d}x'' A_{0,b}(x')B(k_{\perp,0})K_a^b(x'',k_{\perp,0},k_\perp,\mu^2)\delta(x'x''-x) \\ &= \int \mathrm{d}x' A_{0,b}(x')\frac{x}{x'}B(k_{\perp,0})K_a^b\left(\frac{x}{x'},k_{\perp,0},k_\perp,\mu^2\right) . \end{aligned} \tag{9.3}$$

For all flavours the intrinsic $k_{\perp,0}$ distribution $B(k_{\perp,0})$ is assumed to be a Gaussian $\exp(-k_{\perp,0}^2/\sigma^2)$ with $\sigma^2 = k_0^2/2$ where $k_0 = 0.5$ GeV. The obtained distribution $xA_a(x,k_\perp,\mu^2)$ can be then integrated numerically over $k_\perp^2$ using eq. (6.15) and used to fit the experimental data. This is however time consuming and it is enough to use the collinear kernel to fit the starting distribution. The parameters of the initial distribution from the collinear fit are then used to obtain the TMDs using TMD kernel $K_a^b(x'',k_{\perp,0},k_\perp,\mu^2)$ according to eq. (9.3).

The evolution kernel, $K_a^b(x'',\mu^2)$, is stored in a grid of size 50×50 in $\log x$ and $\log\mu$ and the TMD evolution kernel, $K_a^b(x'',k_{\perp,0},k_\perp,\mu^2)$, in a grid of size $50\times 50\times 50$ in $\log x$, $\log k_\perp$ and $\log\mu$. A proper grid spacing has to be used since the distributions are quickly falling at large x and the grid spacing is made more dense in this region. To obtain the results shown in this section the range in x was divided into 5 intervals with the edges at $10^{-6}, 0.01, 0.1, 0.4, 0.9, 1$. In every of these intervals there are 10 grid points distributed logarithmically.

The fit presented in this chapter was obtained with the data from HERA H1 and ZEUS combined measurement [42] - the most precise measurement of the DIS cross section in a wide range of x and Q^2. In [42] the fit to these data was done and the HERAPDF2.0 parton distributions were obtained using QCDNUM and `xFitter`. In our work we use the same analytic form of the parametrization for the initial distributions (eq. (9.2)). At the initial scale μ_0^2 we assume that $x\overline{U} = x\overline{u}$ and $x\overline{D} = x\overline{d}+x\overline{s}$. For the initial strange quark distribution we use $x\overline{s} = f_s x\overline{D}$ with $f_s = 0.4$. We set $B_{\overline{U}} = B_{\overline{D}}$ and $A_{\overline{U}} = A_{\overline{D}}(1-f_s)$. The normalization parameters A_{u_v}, A_{d_v}, A_g and $A_{g'}$ are constrained by the quark number and momentum sum rules. We use the same hard scattering coefficient functions and we treat heavy flavours in the same way as was done in [42].

The fits were performed in the range of $3.5 < Q^2 < 50000$ GeV^2, $4\cdot 10^{-5} < x < 0.65$ (the same as for HERAPDF2.0) using the kernels obtained with the PB method for the angular ordering condition (eq. (3.15)). The fit was performed twice, for two different values of argument of α_s, with $\alpha_s\left(\mu'^2\right)$ (eq. (2.41)) and with $\alpha_s\left((1-z)^2\mu'^2\right)$ (eq. (3.20)) for $z_M = 1-10^{-5}$ (to concentrate on the effect of changing the renormalization scale). The χ^2 was calculated within the `xFitter` package in the same way as was done in [42]. The systematic shifts and treatment of correlated and uncorrelated systematic uncertainties are included in the χ^2 definition. 162 systematic uncertainties and uncertainties from combining H1 and ZEUS data were treated as correlated. The experimental uncertainties were obtained using the Hessian method [231] with $\Delta\chi^2 = 1$. The model uncertainties were obtained by varying the charm ($m_c = 1.41, 1.47, 1.53$ GeV) and the bottom mass ($m_b = 4.25, 4.5, 4.75$ GeV), and the starting evolution scale ($\mu_0^2 = 1.6, 1.9, 2.2$ GeV^2 for the fit with $\alpha_s\left(\mu'^2\right)$ and $\mu_0^2 = 1.1, 1.4, 1.7$ GeV^2 for the fit with $\alpha_s\left((1-z)^2\mu'^2\right)$) where the numbers in brackets are the lower, central and upper values respectively. For $\alpha_s\left((1-z)^2\mu'^2\right)$ we also varied the cut off q_{cut} (0.9, 1.0, 1.1 GeV) in α_s which ensures that the renormalization scale is not too small. The best χ^2 was obtained for the initial scale value $\mu_0^2 = 1.9$ GeV^2 with $\alpha_s\left(\mu'^2\right)$ ($\chi^2/(\mathrm{d.o.f}) = 1.21$) and for the initial scale value $\mu_0^2 = 1.4$ GeV^2 with $\alpha_s\left((1-z)^2\mu'^2\right)$ ($\chi^2/(\mathrm{d.o.f}) = 1.21$). The number of degrees of freedom was d.o.f = 1131. The fit parameters obtained for $\alpha_s\left(\mu'^2\right)$ reproduce the parameters of HERAPDF2.0, for $\alpha_s\left((1-z)^2\mu'^2\right)$, especially for gluon, they are different [229].

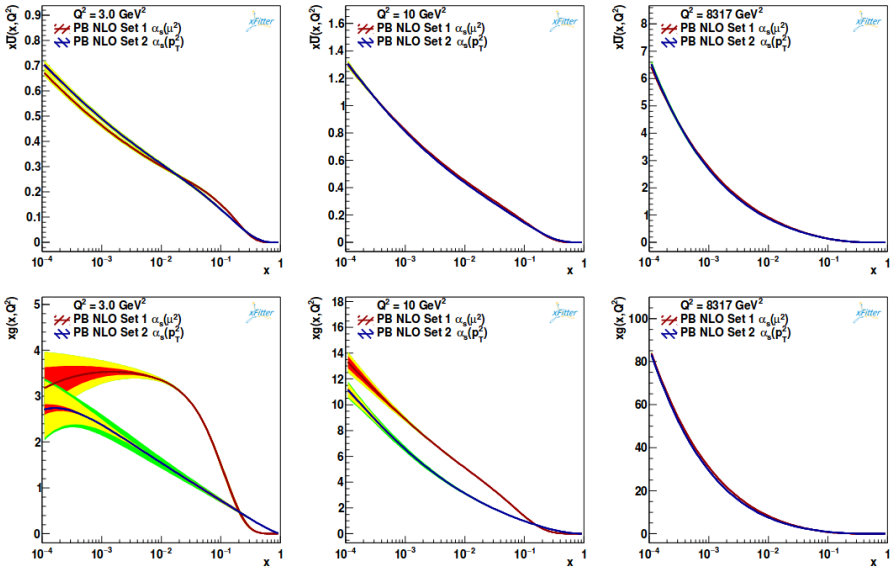

Figure 9.1: Collinear PDFs obtained from the fit with $\alpha_s\left(\mu'^2\right)$ (Set1) and $\alpha_s\left((1-z)^2\mu'^2\right)$ (Set2). Experimental uncertainty is shown in red, model dependence in yellow, additional dependence on q_{cut} in green.

In fig. 9.1 the collinear pdfs with uncertainties coming from fits with $\alpha_s\left(\mu'^2\right)$ (Set1) and $\alpha_s\left((1-z)^2\mu'^2\right)$ (Set2) are shown. One can clearly see the difference between them, especially for gluon. This agrees with our observations from Sec. (8.2.1) where the collinear PDFs obtained from the PB method with $\alpha_s\left((1-z)^2\mu'^2\right)$ were very different from the HERAPDF2.0 results. In fig. 9.2 the ratios of the upper and lower uncertainty bound to the central value result are presented. At the large x the uncertainties with $\alpha_s\left((1-z)^2\mu'^2\right)$ and $\alpha_s\left(\mu'^2\right)$ behave differently.

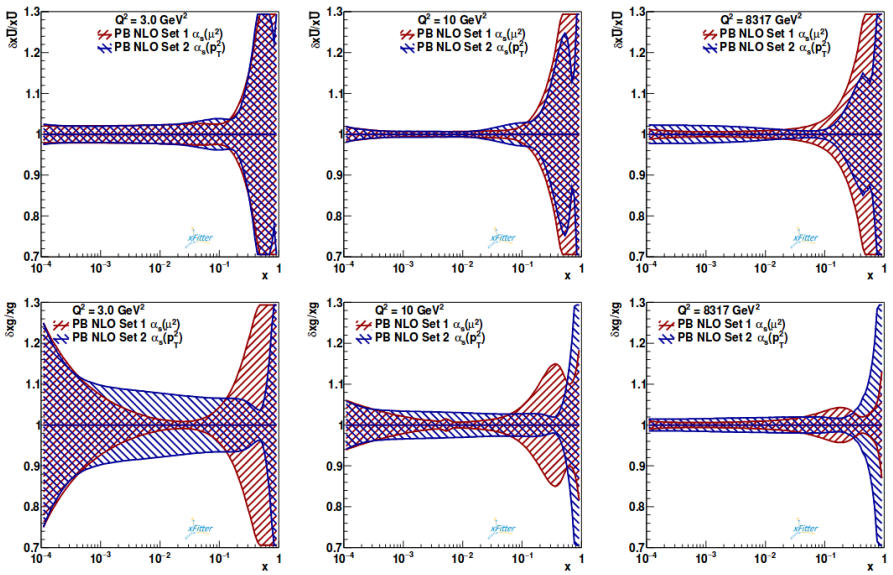

Figure 9.2: Uncertainties of the collinear PDFs from the fit for $\alpha_s\left(\mu'^2\right)$ (Set1) and $\alpha_s\left((1-z)^2\mu'^2\right)$ (Set2).

In fig. 9.3 the comparison of the TMDs for $\alpha_s\left(\mu'^2\right)$ and $\alpha_s\left((1-z)^2\mu'^2\right)$ obtained from the fit is

shown. The same conclusions hold as discussed in Sec. (8.3). The TMDs obtained with $\alpha_s\left((1-z)^2\mu'^2\right)$ are smaller in the small $k_\perp$ region than the TMDs with $\alpha_s\left(\mu'^2\right)$.

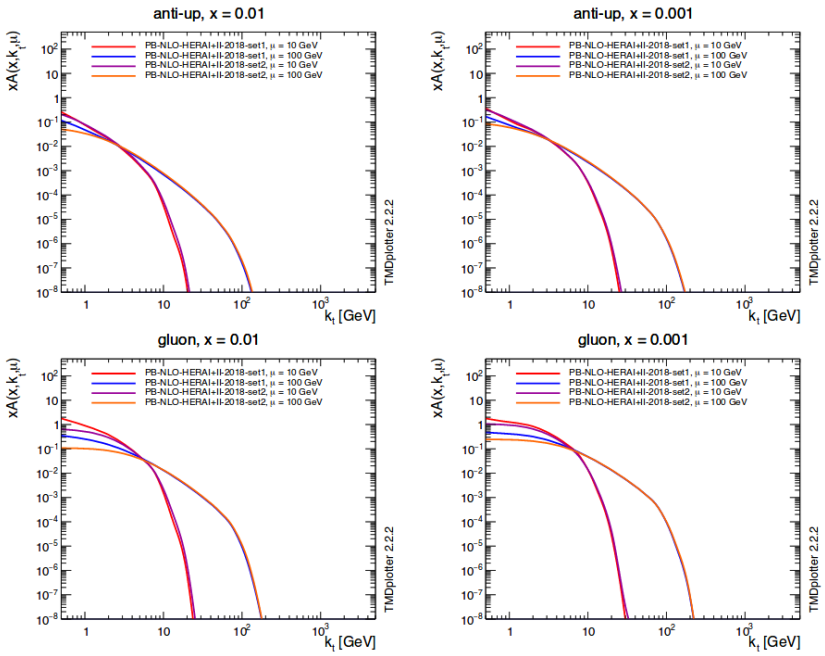

Figure 9.3: Comparison of the TMD distributions obtained from the fit for $\alpha_s\left(\mu'^2\right)$ (Set1) and $\alpha_s\left((1-z)^2\mu'^2\right)$ (Set2).

9.2 | Application of the TMDs from the PB method to the LHC measurements

In this section we test the idea introduced in Sec. (6.1) to obtain the predictions for high energy collision observables by using TMDs instead of collinear PDFs. One of the observables, which is very problematic for the collinear approach, is the Z boson $p_\perp$ spectrum.

In the standard approach, the Z-boson $p_\perp$ spectrum is described by Monte Carlo event generators, which model the non-perturbative effects, simulate the soft gluon emissions via parton showers and combine the radiation effects with the perturbative calculations for the hard process. In [232] the implementation of the NLO DGLAP evolution in the PS was discussed. In fig. 9.4 the prediction obtained in [232] with DIRE [233] + PYTHIA compared with ATLAS measurement at 7 TeV [234] is presented. The distribution is limited to $p_\perp < 30$ GeV since there is no fixed order calculation of the hard process included. The prediction was obtained with the default PYTHIA8 tune, no additional tuning of DIRE + PYTHIA was performed. An overall agreement within 15% with the data was obtained at NLO.

We now calculate the same observable with the PB method. The procedure is the following: we take the LO matrix element for the DY Z boson production generated by PYTHIA8. The matrix element does not contain any transverse momentum. The next steps are performed by the CASCADE (version 2.4.X) Monte Carlo event generator [218,221,235]. From the kinematics of the event x and μ^2 are known and the transverse momenta of the incoming quark-antiquark pair can be generated according to the TMDs we obtained from the PB method. With that the virtualities Q_1^2, Q_2^2 of the incoming partons 1,

2 are calculated. In the next step the initial partons are boosted into their CM frame. The energies $E_{1,2}$ and z components $p_{z,1,2}$ of the partons' momenta are changed according to [236]

$$\begin{aligned} E_{1,2} &= \frac{\hat{s} \pm \left(Q_2^2 - Q_1^2\right)}{2\hat{s}^{1/2}}\,, \\ p_{z,1} &= -p_{z,2} = \left(\frac{\left(\hat{s}^2 + Q_1^2 + Q_2^2\right)^2 - 4Q_1^2 Q_2^2}{4\hat{s}} \right)^{1/2} \end{aligned} \tag{9.4}$$

to take the virtualities into account and to keep the $\hat{s} = (p_1 + p_2)^2$ fixed. Then, also the final state is boosted into its CM frame. Afterwords, the whole system is boosted and rotated back to the laboratory frame. Due to this operation, the $k_\perp$ added to the initial state is compensated by the final state, the longitudinal fractions x_1 and x_2 of the incoming quark and antiquark are changed and the mass m_{DY} of the quark-antiquark pair is kept fixed. The events are then analysed by Rivet [237, 238] and compared with the 8 TeV measurement [239]. We are interested only in the inclusive Z boson spectrum so we do not need any parton shower.

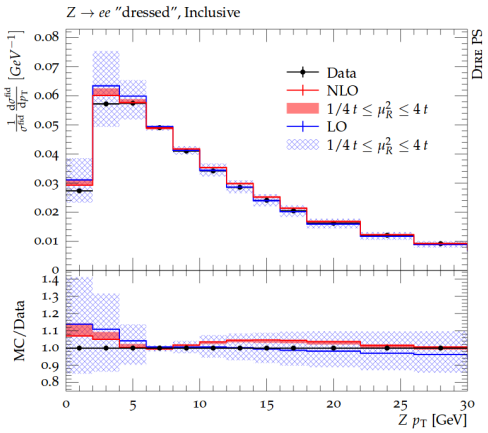

Figure 9.4: Comparison of the predictions of the Z boson $p_\perp$ spectrum obtained with the DIRE+PYTHIA PS with ATLAS data [232].

On the left hand side of fig. 9.5 we present the results obtained with the TMDs from the PB method, for virtuality and angular ordering condition, fixed value of the z_M parameter being $z_M = 1 - 10^{-5}$ and $\alpha_s\left(\mu'^2\right)$. The outcome with angular ordering is very encouraging, however with virtuality ordering it looks a bit worse. With the TMDs obtained from the PB method we can predict the correct shape of the Z boson $p_\perp$ spectrum. All the $p_\perp$ dependence comes directly from the PB method. There is no tuning of free parameters. The prediction for the whole spectrum comes from one method, there is no mixture of different approaches in the different $p_\perp$ ranges. It is also interesting to see the difference between virtuality and angular ordering in the physical observable spectrum.

In the next step we test different options for the argument of α_s. On the right hand side of fig. 9.5 we show the comparison of predictions obtained with the TMDs from the PB method with virtuality and angular ordering condition with dynamic z_M and $q_\perp$ in the argument of α_s (see Tab. (8.1)). The parameter q_0 is chosen to 0.2 GeV for both virtuality and angular ordering condition, to be not too far away from the approximation from eq. (2.82) and at the same time keep $q_0 = \mathcal{O}(\Lambda)$. The result obtained with angular ordering with $\alpha_s\left((1-z)^2\mu'^2\right)$ agrees within 20 % with the data in the whole range in $p_\perp$. Virtuality ordering underestimates the data in the small $p_\perp$ region and overestimates them in the large

$p_\perp$ region.

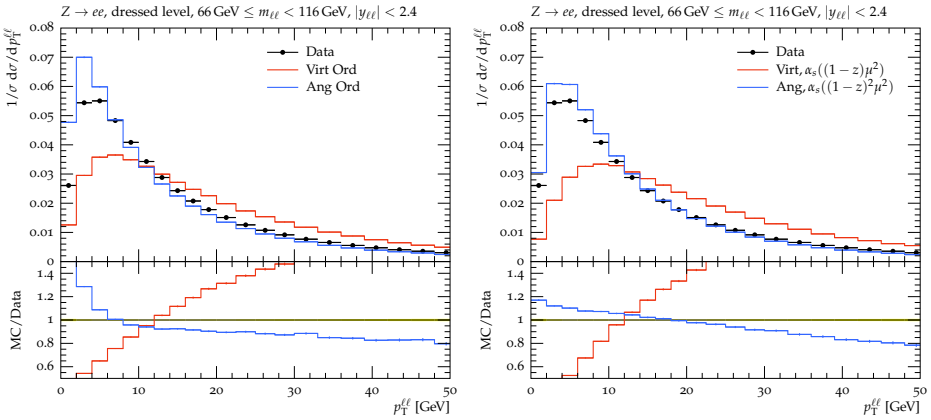

Figure 9.5: Comparison of the predictions of the Z boson $p_\perp$ spectrum obtained with the TMDs from the PB method with virtuality and angular ordering condition and the ATLAS data. Left: results obtained with with $\alpha_s(\mu'^2)$. Right: results obtained with $q_\perp$ being the argument of α_s.

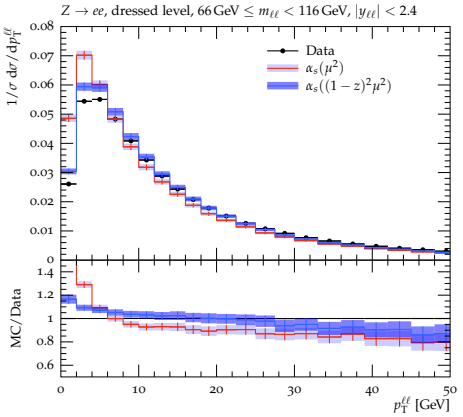

Figure 9.6: Comparison of the predictions of the Z boson $p_\perp$ spectrum obtained with the TMDs from the fit with angular ordering condition with $\alpha_s\left(\mu'^2\right)$ and $\alpha_s\left((1-z)^2\mu'^2\right)$ and the ATLAS data.

In the next step we repeat the analysis for Z boson $p_\perp$ spectrum, but instead of using TMDs directly from the PB method, we use the TMDs from the fits. Based on the results from fig. 9.5 we decided to perform the fits for the angular ordering since it looks more promising than virtuality ordering.

In fig. 9.6 we show the prediction for the Z boson $p_\perp$ spectrum obtained with the TMDs with angular ordering condition to calculate $k_\perp$ from the fits with properly defined uncertainty bands for two different renormalization scales in α_s. The result confirms the previous observation. With both sets one can predict the correct shape of the Z boson $p_\perp$ spectrum, the TMD with $\alpha_s\left((1-z)^2\mu'^2\right)$ describes the data better. The level of agreement is of the same level as what is done in the standard MC approach presented above. With that we can conclude that our method is successful and competitive with other methods.

10 | Conclusions and closing remarks

In this thesis a new approach to solve the DGLAP evolution equation was proposed. We presented a solution with the Parton Branching method from which we can obtain, in addition to the standard collinear PDFs, also the TMDs. We have validated the PB method by comparing the results for collinear PDFs with predictions from semi-analytical calculation and we found a very good agreement.

One of the advantages of the PB method is the possibility to study independently different elements of ordering condition: the connection between the evolution scale and a kinematic variable, the soft gluons resolution scale parameter z_M and renormalization scale in α_s. Using the PB method, we could systematically analyse every individual part of the ordering definitions.

For renormalization scale being the scale of a branching we have confirmed that as long as the z_M parameter is close enough to 1, the results for collinear PDFs are not affected, both for fixed and dynamic definitions of z_M, regardless of the ordering we are using. However, we concluded that $p_\perp$- ordering does not give the stable results for the TMDs (since they depend on z_M parameter), whereas virtuality and angular ordering do. We compared the angular and virtuality ordered TMDs. We also explored the consequence of changing the scale in α_s in the case of collinear and TMD distributions and we observed a significant effect.

The initial parameters of the parton distributions have to be obtained from the fit to the experimental data. The structure of our evolution code enables one to perform such a fit within the `xFitter` package. By fitting the integrated TMDs to HERA H1 and ZEUS combined F_2 data we obtained two TMD sets (with uncertainties) with angular ordering for two different renormalization scales.

Our approach allows us to test the TMDs directly in the measurements. We tested our method by applying the TMDs to the Z boson $p_\perp$ spectrum and we obtained a very good description of the 8 TeV data. The method can be, nonetheless, applied to any QCD process, like jet production, $\Delta\Phi$ decorrelation in dijets events, Higgs production etc., especially one could study the low energy DY data which might be sensitive to the intrinsic momenta.

The approach presented here is a part of a broader program which aims in precision predictions for observables at high energy collisions. The general procedure within collinear approximation to obtain predictions for hadronic collisions is the following. A Monte Carlo event generator generates the hard scattering process with the initial momenta distributed according to the collinear parton distributions. Then a parton shower is applied and, in most of the Monte Carlo event generators, the hard process is rotated and boosted to conserve energy-momentum after showering. Such a procedure leads to a shift, not only in transverse momenta, but also in the x variable if it is defined in the light cone coordinates.

This affects the simulations of many QCD processes.

In Sec. (6.1) an alternative approach to obtain the predictions for observables using TMDs instead of collinear PDFs was discussed. Using TMDs to generate the ME and to perform PS has enormous advantages, since the transverse momentum is included from the beginning and no adjustment of the kinematics has to be performed at the end.

In this thesis the TMDs- the first link in a chain needed for this alternative approach- were constructed in a wide range of x, $k_\perp$ and μ^2. This opens new perspectives for a better precision for the calculations of higher order corrections to the physical observables, not only for LHC measurements, but also in the context of the new colliders. For example, multi-dimensional mapping of the nucleon structure is one of the main goals of the Electron-Ion Collider [240].

Acknowledgements I would like to thank Hannes Jung, Francesco Hautmann and Radek Žlebčík for many hours of useful discussions and explanations. I am especially grateful to Hannes for his patient supervision and big heart.
I would also like to thank my family, most of all my husband, sister and parents, as well as my friends for their support.

A | Appendix

A.1 | NLO splitting functions

At NLO, the coefficients for d_a and k_a are given by [47]:

$$\begin{aligned} d_q^{(1)}\left(\mu^2\right) &= C_F^2\left(\frac{3}{8}-\frac{\pi^2}{2}+6\,\zeta(3)\right)+C_F C_A\left(\frac{17}{24}+\frac{11\pi^2}{18}-3\,\zeta(3)\right)-C_F T_R n_f\left(\frac{1}{6}+\frac{2\pi^2}{9}\right)\,, \\ d_g^{(1)}\left(\mu^2\right) &= C_A^2\left(\frac{8}{3}+3\,\zeta(3)\right)-\frac{4}{3}\,C_A T_R n_f - C_F T_R n_f\,, \end{aligned} \tag{A.1}$$

where ζ is the Riemann zeta function, and

$$\begin{aligned} k_q^{(1)}\left(\mu^2\right) &= 2\,C_F\,\Gamma\left(\mu^2\right)\,,\;\; k_g^{(1)}\left(\mu^2\right)=2\,C_A\,\Gamma\left(\mu^2\right)\,, \\ \text{where }\;\Gamma\left(\mu^2\right) &= C_A\left(\frac{67}{18}-\frac{\pi^2}{6}\right)-T_R n_f\frac{10}{9}\,. \end{aligned} \tag{A.2}$$

The NLO contributions to the functions R_{ab} are:

$$\begin{aligned} R_{gq}^{(1)}\left(z,\mu^2\right) &= C_F^2\left[-\frac{5}{2}-\frac{7}{2}z+\left(2+\frac{7}{2}z\right)\ln z+\left(\frac{1}{2}z-1\right)\ln^2 z-2z\ln(1-z)\right. \\ &- \left.\left(3\ln(1-z)+\ln^2(1-z)\right)p_{gq}(z)\right] \\ &+ C_F C_A\left[\frac{28}{9}+\frac{65}{18}z+\frac{44}{9}z^2+\left(-12-5z-\frac{8}{3}z^2\right)\ln z+(4+z)\ln^2 z+2z\ln(1-z)\right. \\ &+ \left(-2\ln z\ln(1-z)+\frac{1}{2}\ln^2 z+\frac{11}{3}\ln(1-z)+\ln^2(1-z)-\frac{\pi^2}{6}+\frac{1}{2}\right)p_{gq}(z) \\ &+ \left.p_{gq}(-z)S_2(z)\right]+C_F T_R n_f\left[-\frac{4}{3}z-\left(\frac{20}{9}+\frac{4}{3}\ln(1-z)\right)p_{gq}(z)\right]\,, \end{aligned} \tag{A.3}$$

$$\begin{aligned} R_{qg}^{(1)}\left(z,\mu^2\right) &= \frac{1}{2}C_F T_R\left[4-9z+(-1+4z)\ln z+(-1+2z)\ln^2 z+4\ln(1-z)\right. \\ &+ \left.\left(-4\ln z\ln(1-z)+4\ln z+2\ln^2 z-4\ln(1-z)+2\ln^2(1-z)-\frac{2}{3}\pi^2+10\right)p_{qg}(z)\right] \\ &+ \frac{1}{2}C_A T_R\left[\frac{182}{9}+\frac{14}{9}z+\frac{40}{9z}+\left(\frac{136}{3}z-\frac{38}{3}\right)\ln z-4\ln(1-z)-(2+8z)\ln^2 z\right. \\ &+ \left(-\ln^2 z+\frac{44}{3}\ln z-2\ln^2(1-z)+4\ln(1-z)+\frac{\pi^2}{3}-\frac{218}{9}\right)p_{qg}(z) \\ &+ \left.2p_{qg}(-z)S_2(z)\right]\,, \end{aligned} \tag{A.4}$$

$$R_{gg}^{(1)}\left(z,\mu^2\right) = C_F T_R n_f\left[-16+8z+\frac{20}{3}z^2+\frac{4}{3z}+(-6-10z)\ln z+(-2-2z)\ln^2 z\right]$$

$$
\begin{aligned}
&+ \quad C_A T_R n_f \left[2 - 2z + \frac{26}{9}z^2 - \frac{26}{9z} - \frac{4}{3}(1+z)\ln z - \frac{20}{9}\left(\frac{1}{z} - 2 + z - z^2\right)\right] \\
&+ \quad C_A^2 \left[\frac{27}{2}(1-z) + \frac{67}{9}(z^2 - \frac{1}{z}) + \left(-\frac{25}{3} + \frac{11}{3}z - \frac{44}{3}z^2\right)\ln z \right. \\
&+ \quad 4(1+z)\ln^2 z + 2p_{gg}(-z)S_2(z) + \left(-4\ln z \ln(1-z) + \ln^2 z\right) p_{gg}(z) \\
&+ \quad \left.\left(\frac{67}{9} - \frac{\pi^2}{3}\right)\left(\frac{1}{z} - 2 + z - z^2\right)\right] , \qquad \text{(A.5)}
\end{aligned}
$$

$$
R^{(1)}_{q_{i\neq j}q_j} = R^{(1)}_{\overline{q}_{i\neq j}q_j} = \frac{1}{2}C_F T_R \left(\left(10z + \frac{16}{3}z^2 + 2\right)\ln z - \frac{112}{9}z^2 + \frac{40}{9z} - 2(1+z)\ln^2 z - 4 + 12z\right) , \qquad \text{(A.6)}
$$

$$
\begin{aligned}
R^{(1)}_{q_j q_j} &= C_F^2 \left[-\left(2\ln z \ln(1-z) + \frac{3}{2}\ln z\right) p_{qq}(z) - \left(\frac{3}{2} + \frac{7}{2}z\right)\ln z - \frac{1}{2}(1+z)\ln^2 z \right. \\
&- \left. 5(1-z)\right] + C_F C_A \left[\left(\frac{1}{2}\ln^2 z + \frac{11}{6}\ln z\right) p_{qq}(z) - (1+z)\left(\frac{67}{18} - \frac{\pi^2}{6}\right) \right. \\
&+ \left. (1+z)\ln z + \frac{20}{3}(1-z)\right] + C_F T_R n_f \left[-\frac{2}{3}\ln z p_{qq}(z) + \frac{10}{9}(1+z) - \frac{4}{3}(1-z)\right] \\
&+ \frac{1}{2}C_F T_R \left(\left(10z + \frac{16}{3}z^2 + 2\right)\ln z - \frac{112}{9}z^2 + \frac{40}{9z} - 2(1+z)\ln^2 z - 4 + 12z\right) \qquad \text{(A.7)}
\end{aligned}
$$

and

$$
\begin{aligned}
R^{(1)}_{\overline{q}_j q_j} &= C_F \left(C_F - \frac{C_A}{2}\right)\left[2p_{qq}(-z)S_2(z) + 2(1+z)\ln z + 4(1-z)\right] \\
&+ \frac{1}{2}C_F T_R \left(\left(10z + \frac{16}{3}z^2 + 2\right)\ln z - \frac{112}{9}z^2 + \frac{40}{9z} - 2(1+z)\ln^2 z - 4 + 12z\right) . \qquad \text{(A.8)}
\end{aligned}
$$

In the above expressions

$$
p_{qq}(z) = \frac{2}{1-z} - 1 - z , \qquad \text{(A.9)}
$$

$$
p_{qg}(z) = z^2 + (1-z)^2 , \qquad \text{(A.10)}
$$

$$
p_{gq}(z) = \frac{1 + (1-z)^2}{z} , \qquad \text{(A.11)}
$$

$$
p_{gg}(z) = \frac{1}{1-z} + \frac{1}{z} - 2 + z(1-z) , \qquad \text{(A.12)}
$$

and

$$
S_2(z) = -2\mathrm{Li}_2(-z) + \frac{1}{2}\ln^2 z - 2\ln z \ln(1+z) - \frac{\pi^2}{6} . \qquad \text{(A.13)}
$$

A.2 | Computation of the LO ME for quark → quark + gluon*

In this section the amplitude for the process of quark splitting into quark and gluon at leading order, represented by the diagram shown in fig. A.1, is calculated from the Feynman rules. The conventions for the Feynman rules follow [16].

The 4-momentum convention is $p^\mu = (p^0, \overrightarrow{p}) = (p^0, p^1, p^2, p^3) = (p^0, p_\perp, p^3)$, $p_\mu = (p^0, -\overrightarrow{p})$ and the metric tensor is

$$
g_{\mu\nu} = g^{\mu\nu} = \begin{pmatrix} 1 & 0 & 0 & 0 \\ 0 & -1 & 0 & 0 \\ 0 & 0 & -1 & 0 \\ 0 & 0 & 0 & -1 \end{pmatrix} . \qquad \text{(A.14)}
$$

The full list of Feynman rules is given in [16], here only the relations and conventions used in the computations in this section are listed.

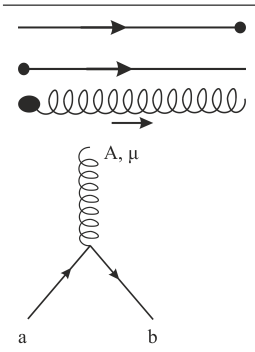

$u_a(p_1, s_1)$ - spinor of the incoming quark

$\overline{u}_a(p_1, s_1)$ - spinor of the outgoing quark

$\varepsilon_\mu(p_1, \lambda)^*$ - polarization vector of the outgoing gluon

$-igT^A_{ba}\gamma^\mu$ - vertex for quark-quark-gluon

In the notation above a, b are colours of the quarks, A is a colour of the gluon, p_1 is the 4-momentum, s_1 is the spin, λ is the polarization index, T^A_{ba} is the Gell-Mann matrix and γ^μ is the gamma matrix. Gell-Mann matrices are hermitian. The following relations and conventions are used

$$\overline{u} = u^\dagger\gamma^0 , \tag{A.15}$$

$$\gamma^\mu\gamma^\nu\gamma_\mu = -2\gamma^\nu , \tag{A.16}$$

$$\mathrm{Tr}(\gamma^\mu\gamma^\nu\gamma^\rho\gamma^\sigma) = 4(g^{\mu\nu}g^{\rho\sigma} - g^{\mu\rho}g^{\nu\sigma} + g^{\mu\sigma}g^{\nu\rho}) , \tag{A.17}$$

$$\sum_s u(p,s)\overline{u}(p,s) = \not{p} + m , \tag{A.18}$$

$$\sum_\lambda \varepsilon_{\mu\perp}(p,\lambda)\varepsilon_{\nu\perp}(p,\lambda)^* = -g_{\mu\nu} + \varepsilon_{\mu+}\varepsilon^*_{\nu-} + \varepsilon_{\mu-}\varepsilon^*_{\nu+} . \tag{A.19}$$

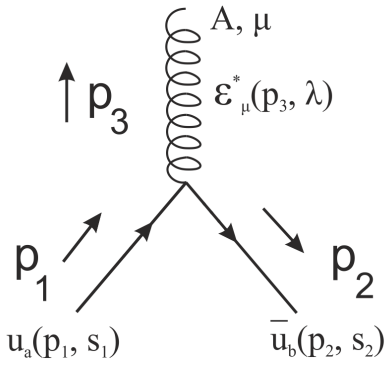

Figure A.1: The diagram of the $q \to q + g$ splitting.

In the computation we assume that incoming quark (with 4-momentum p_1) and emitted quark (with 4-momentum p_2) are on shell and the gluon (with 4-momentum p_3) is slightly off-shell. It means that $p_1^2 = 0$ and $p_2^2 = 0$.

We start from writing the expression for the ME and the conjugate of the ME from the diagram in fig. A.1 using the Feynamn rules

$$\begin{aligned} \mathrm{ME} &= -ig\overline{u}_b(p_2, s_2)T^A_{ba}\gamma^\mu u_a(p_1, s_1)\varepsilon_\mu(p_3, \lambda)^* , \\ |\mathrm{ME}|^\dagger &= ig\varepsilon_\nu(p_3, \lambda)\overline{u}_a(p_1, s_1)\gamma^\nu(T^A_{ab})u_b(p_2, s_2) . \end{aligned} \tag{A.20}$$

The square of the ME, summed over the spins, colors and polarizations of final particles and averaged

over the spin and color of the initial quark is

$$|\overline{\mathrm{ME}}|^2 = \frac{C_F}{2}\mathrm{Tr}\left[g^2 \sum_{s_1,s_2,\lambda} \varepsilon^*_\mu(p_3,\lambda)\varepsilon_\nu(p_3,\lambda)u_b(p_2,s_2)\overline{u}_b(p_2,s_2)\gamma^\mu u_a(p_1,s_1)\overline{u}_a(p_1,s_1)\gamma^\nu\right] . \quad (A.21)$$

The trace invariance under cyclic permutations was used to move $u_b(p_2,s_2)$ to the current position, the factor $\frac{1}{2}$ comes from averaging over the initial quark spin and the colour factor is $\frac{1}{3}\sum_{A,a,b} T^A_{ba}T^A_{ab} = C_F = \frac{4}{3}$ with $C_F = T_F\frac{N^2-1}{N}$, $T_F = \frac{1}{2}$ and N being the number of SU(N) generators equal to 3 in SU(3). Now, the spin sum rules eq. (A.18) and eq. (A.19), with the masses of the quarks set to zero, are used to obtain

$$|\overline{\mathrm{ME}}|^2 = \frac{C_F}{2}g^2\mathrm{Tr}\left[(-g_{\mu\nu} + \varepsilon_{\mu+}\varepsilon_{\nu-} + \varepsilon_{\mu-}\varepsilon_{\nu+})\not{p}_2\gamma^\mu\not{p}_1\gamma^\nu\right] \quad (A.22)$$

and from that

$$|\overline{\mathrm{ME}}|^2 = 4C_F g^2\left[p_1\cdot p_2 + (p_2\cdot\varepsilon_+)(p_1\cdot\varepsilon_-) - p_1\cdot p_2\varepsilon_+\varepsilon_- + (p_2\cdot\varepsilon_-)(p_1\cdot\varepsilon_+)\right] . \quad (A.23)$$

The choice of the 4-momenta is such that $p_1^2 = p_2^2 = 0$ (neglecting the pieces $\mathcal{O}(p_\perp^4)$) and the gluon is slightly off-shell

$$\begin{aligned} p_1 &= (p,0,0,p) , \\ p_2 &= ((1-z)p, -p_\perp, (1-z)p - \frac{p_\perp^2}{2(1-z)p}) , \\ p_3 &= (zp, p_\perp, zp + \frac{p_\perp^2}{2(1-z)p}) . \end{aligned} \quad (A.24)$$

The polarization vectors are defined in the following way: $\varepsilon_+ = (\varepsilon_0+\varepsilon_3)/\sqrt{2}$ and $\varepsilon_- = (\varepsilon_0-\varepsilon_3)/\sqrt{2}$ where $\varepsilon_0 = (1,0,0,0)$, $\varepsilon_1,\varepsilon_2$ are the polarization vectors perpendicular to the direction of gluon's 3-momentum vector, ε_3 is a vector pointing in the direction of the gluon's 3-momentum. So

$$\begin{aligned} \varepsilon_+ &= \frac{1}{\sqrt{2}}\left(1, \frac{p_\perp}{A}, \frac{1}{A}\left(zp + \frac{p_\perp^2}{2(1-z)p}\right)\right) , \\ \varepsilon_- &= \frac{1}{\sqrt{2}}\left(1, -\frac{p_\perp}{A}, -\frac{1}{A}\left(zp + \frac{p_\perp^2}{2(1-z)p}\right)\right) . \end{aligned} \quad (A.25)$$

$A = zp\sqrt{1+\frac{p_\perp^2}{(1-z)z^2p^2}}$ is a normalization, such that $\varepsilon_+\cdot\varepsilon_- = 1$ so $1/A = \frac{1}{zp}\left(1 - \frac{p_\perp^2}{2(1-z)z^2p^2}\right)$. Moreover $\varepsilon_1\cdot\varepsilon_2 = 0$ and $\varepsilon_i\cdot\varepsilon_j = g_{ij}$.

From that one obtains

$$|\overline{\mathrm{ME}}|^2 = 8\pi\alpha_s C_F\frac{p_\perp^2}{z^2}\left(\frac{1+(1-z)^2}{1-z}\right) \quad (A.26)$$

where the definition of a strong coupling $\alpha_s = g^2/(4\pi)$ was used.

A.3 | Introduction to probability theory and Monte Carlo techniques

This chapter summarizes the elements of the probability theory which are needed for this thesis. Further details can be found in statistics text books, especially [241–243] on which this chapter is based on.

A.3.1 | Short summary of probability theory

The basic concept of probability theory is an *event*. The meaning of an event is intuitively clear from everyday life. Events are facts or processes which are characterized by a specific property. It can be, for example, the fact that someone won in a lottery or that someone is ill. An event can be a throwing of "3" with a dice or throwing a number "less than 3".

An event is often defined as an outcome of an experiment. The experiment has a set of possible outcomes, to every outcome a probability can be assigned. The outcome of the experiment is random if any of the outcome from the outcomes' set can appear and we can only say what is the probability of the given outcome to appear.

Probability was a subject of study since at least 17th century and over the years a few different definitions of *probability* were formulated. The one obtained by Kolmogorov [244] is commonly used and it defines probability in terms of *set theory*.

Fig. A.2 shows so called *Venn diagram* which represents logical relations between events. In the diagram we can see set A containing some events characterized by a given property and set B which is characterized by another property. Events not belonging to set A are called *complement* of A and belong

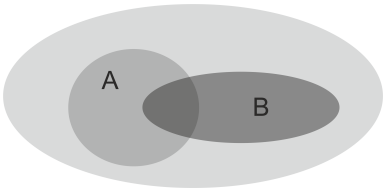

Figure A.2: Venn diagram.

to set $\overline{A}$. They exclude each other. An event can belong to A *or* to $\overline{A}$, not both at the same time but it must belong to one of those. If an event can belong to set A *or* B it is denoted as $A \cup B$ and it means that an event belongs to one of those sets or it has features of both what is shown in the diagram in fig. A.2 by the common area of set A and B. Events belonging to both sets at the same time are denoted as $A \cap B$. If there is an empty set containing no events it is denoted as $\emptyset$ so $A \cap \overline{A} = \emptyset$, if there is a set containing all possible events it is denoted by Ω, it is *certain* to have an event belonging to this set, so $A \cup \overline{A} = \Omega$. As mentioned already, to every event a probability is assigned. The axioms *defining the probability* in terms of set theory are listed here

1. the probability of a certain event is $P(\Omega) = 1$,
2. the probability is a real positive number $P(A) \geq 0$,
3. $P(A \cup B) = P(A) + P(B)$ if the events are mutually exclusive (so when $A \cap B = \emptyset$).

Further, the following relations hold

$$\begin{aligned} P(\emptyset) &= 0 \\ P(\overline{A}) &= 1 - P(A) \\ P(A \cup B) &= P(A) + P(B) - P(A \cap B). \end{aligned} \tag{A.27}$$

One can ask what is the *conditional* probability, the probability of A knowing B. The conditional probability is defined in the following way:

$$P(A|B) = \frac{P(A \cap B)}{P(B)} \tag{A.28}$$

assuming that $P(B) \neq 0$ and analogously, for probability of B given A, $P(B|A)$. From that one can write the equality

$$P(A|B)P(B) = P(B|A)P(A) \tag{A.29}$$

which can be reformulated into *Bayes' theorem*

$$P(A|B) = \frac{P(B|A)P(A)}{P(B)}. \tag{A.30}$$

From the last few relations one can see that if events are *independent* (so $P(A|B) = P(A)$ for every B) one obtains

$$P(A \cap B) = P(A)P(B) \tag{A.31}$$

and at the same time $P(B|A) = P(B)$.

A.3.2 | Events, random variables and probability distributions

If we perform an experiment once, and we measure a given quantity, the number, which characterizes it, is a *random number*.

Some of the experiments, like throwing a dice, have discrete outcomes, other can take values from continuous set. Let us concentrate for a moment on the continuous case. If we perform the experiment n times, we obtain a set of x_1,...,x_n results which can be displayed in a *histogram*. The range of all the possible x is displayed on a horizontal axis of the histogram and is divided into m bins of the width Δ_i, where $i = 1, 2, ..., m$. The bin width does not need to be the same for every bin. On the vertical axis the number of entries n_i in each bin i is displayed. One can calculate the area A under the histogram using

$$A = \sum_{i=1}^{m} \Delta_i n_i \tag{A.32}$$

and normalize it to the unity by dividing each n_i by the bin width and the total number of entries $\sum_{i=1}^{n} n_i$. In the limit of zero bin width and infinite number of entries the histogram corresponds to *probability density function* (p.d.f.) $f(x)$ [242]. The probability of observing a value in the interval $[x, x+\mathrm{d}x]$ is equal to $f(x)\mathrm{d}x$ and the probability to find x in the interval $[x_1, x_2]$ is given by

$$P(x_1 \leq x \leq x_2) = \int_{x_1}^{x_2} \mathrm{d}x f(x) \ . \tag{A.33}$$

The p.d.f. is normalised in the following way

$$\int_{-\infty}^{\infty} \mathrm{d}x f(x) = 1 \tag{A.34}$$

what means that the probability of obtaining any value of x from the range of all the possible outcomes is equal to 1. It must satisfy

$$f(-\infty) = f(\infty) = 0 \ . \tag{A.35}$$

In the case of discrete outcomes, instead of p.d.f., one speaks about the *probability distribution*. This distribution assigns probabilities $p(x_i)$ to every possible outcome x_i from the set of all available outcomes $i = 1, 2, ..., N$, where N can be infinite. The normalization condition in the discrete case is analogous to the condition for continuous outcomes

$$\sum_{i=1}^{N} p(x_i) = 1 \ . \tag{A.36}$$

Knowing a p.d.f., one can calculate the probability to obtain x smaller or equal than $t \in [-\infty, \infty]$

$$P(x \leq t) = F(t) = \int_{-\infty}^{t} \mathrm{d}x f(x) \; . \tag{A.37}$$

$F(t)$ is called a *cumulative or integral distribution* or just distribution function. If eq. (A.37) is taken as a definition of the cumulative distribution, it can be used to define the p.d.f.

$$f(x) = \frac{\mathrm{d}F(x)}{\mathrm{d}x} \; . \tag{A.38}$$

For discrete distributions the probability to observe values x less or equal to t is given by cumulative distribution defined as

$$F(t) = \sum_{x_i \leq t} p(x_i) \; . \tag{A.39}$$

One of the very widely used quantities is the *average value* defined as

$$\overline{x} = \frac{1}{N} \sum_{i=1}^{N} x_i \; . \tag{A.40}$$

Now, let us assume we have a quantity $u(x)$ which depends on a random variable x, we know the probability density $f(x)$ and we want to calculate the expected value of the quantity u. The *expected* or *expectation value* $E(u(x))$ is defined in the following way

$$E(u(x)) = \int_{-\infty}^{\infty} \mathrm{d}x f(x) u(x) \tag{A.41}$$

for a continuous distribution and

$$E(u(x)) = \sum_{i=1}^{\infty} p(x_i) u(x_i) \tag{A.42}$$

for a discrete case.

The expected value of a certain variable x is called *mean value* and is defined

$$E(x) = \int_{-\infty}^{\infty} \mathrm{d}x f(x) x = \langle x \rangle = \mu \tag{A.43}$$

for a continuous distribution and

$$E(x) = \sum_{i=1}^{\infty} p(x_i) x_i = \langle x \rangle = \mu \tag{A.44}$$

for a discrete case.

It is important to notice that in general

$$\langle u(x) \rangle \neq u(\langle x \rangle) \; . \tag{A.45}$$

The spread of the distribution is measured by the *variance* defined in the following way

$$var(x) = \sigma^2 = E((x - \mu)^2) \tag{A.46}$$

which is the mean quadratic deviation of the random variable from its mean value. The quantity σ is called *standard deviation*.

From eq. (A.41) we can calculate the expected value of a quantity $u(x)$ knowing the distribution $f(x)$. Sometimes one wants not only to calculate the expected value but also the distribution of u: $g(u)$. This can be done using *variable transformation*.

If $u(x)$ is a growing function (it can be uniquely inverted) then using the relation that the probability of finding x in the interval $x_1 \leq x \leq x_2$ is equal to the probability to find u in the range $u(x_1) \leq u \leq u(x_2)$ we obtain

$$P(x_1 \leq x \leq x_2) = P\left(u(x_1) \leq u \leq u(x_2)\right) = \int_{x_1}^{x_2} \mathrm{d}x' f(x') = \int_{u_1}^{u_2} \mathrm{d}u' g(u') \tag{A.47}$$

which can be rewritten in the following way

$$g(u) = f(x)\left|\frac{\mathrm{d}x}{\mathrm{d}u}\right| , \tag{A.48}$$

where the absolute value was taken to obtain positive $g(u)$.

In case of functions which are not monotonic (e.g. $u(x) = x^2$) one has to sum contributions from different branches.

Another frequently encountered problem is, how to obtain random numbers distributed according to a given distribution $g(u)$ when random numbers x are distributed according to another distribution $f(x)$. Very often one has uniformly distributed numbers and from that one wants to obtain random numbers distributed according to another distribution. To solve the problem, a transformation $u(x)$ connecting distributions $f(x)$ and $g(u)$ has to be found. Using the relation that the probability to find $x' \leq x$ is equal to the probability to find $u' \leq u(x)$

$$\int_{-\infty}^{x} \mathrm{d}x' f(x') = \int_{-\infty}^{u(x)} \mathrm{d}u' g(u') , \tag{A.49}$$

which reads

$$F(x) = G(u(x)) , \tag{A.50}$$

one obtains a formula to calculate u distributed according to $g(u)$

$$u(x) = G^{-1}(F(x)) \tag{A.51}$$

where G^{-1} is the inverse of G. Of course, to solve the problem analytically, G^{-1} must exist and be analytically calculable and f and g must be integrable analytically. Very often it is not the case, but the problem can be solved using a Monte Carlo method, which is described in Sec. (A.3.5).

At the end of this section let us discuss the generalization of the issues mentioned above to the case of probability density of two variables. If a measurement is characterized by two quantities, the result of it are two random numbers x, y. After performing the measurements n times, one obtains a set of n pairs of outcomes $(x_1, y_1), ..., (x_n, y_n)$ which can be then shown on a two dimensional histogram. Similarly, as in the case of one variable, in the limit of infinitely many measurements and infinitely small bin width, the (normalized) histogram corresponds to the *joint p.d.f.* $f(x, y)$. The *joint probability* to obtain x in the range $[x, x + \mathrm{d}x]$ and y in the range $[y, y + \mathrm{d}y]$ is given by $f(x, y)\mathrm{d}x\mathrm{d}y$ and the probability to find x in the range $x_1 \leq x \leq x_2$ and y in the range $y_1 \leq y \leq y_2$ is given by

$$P\left((x_1 \leq x \leq x_2) \cap (y_1 \leq y \leq y_2)\right) = \int_{x_1}^{x_2} \mathrm{d}x \int_{y_1}^{y_2} \mathrm{d}y f(x, y) . \tag{A.52}$$

The normalization condition is

$$\int_{-\infty}^{\infty} \mathrm{d}x \int_{-\infty}^{\infty} \mathrm{d}y f(x, y) = 1 \tag{A.53}$$

which means that the probability to find x and y having any of the possible values is equal to 1. Sometimes one knows $f(x, y)$ and one would like to know the probability density of x, regardless of the value of

y. This is done by projecting the normalized two-dimensional histogram onto an x axis. In the limit of infinitely many entries and infinitely small bin width it corresponds to the *marginal p.d.f.*

$$f_x(x) = \int_{-\infty}^{\infty} \mathrm{d}y f(x,y) \ . \tag{A.54}$$

Analogously, $f_y(y)$ is defined as an integral over x, a projection onto y axis.

Also a cumulative distribution can be defined in the two-dimensional case as a probability to find x' smaller or equal then x and y' smaller or equal than y

$$P\left((x' \leq x) \cap (y' \leq y)\right) = F(x,y) = \int_{-\infty}^{x} \mathrm{d}x' \int_{-\infty}^{y} \mathrm{d}y' f(x',y') \tag{A.55}$$

and it can be used to define the p.d.f.

$$f(x,y) = \frac{\partial^2 F}{\partial x \partial y} \ . \tag{A.56}$$

The *conditional probability density* which gives the probability density of obtaining x knowing the value of y, is given by

$$f_x(x|y) = \frac{f(x,y)}{\int_{-\infty}^{\infty} \mathrm{d}x f(x,y)} = \frac{f(x,y)}{f_y(y)} \ . \tag{A.57}$$

An analogous relation can be written for $f_y(y|x)$. From that a relation

$$f(x,y) = f_x(x|y) f_y(y) = f_y(y|x) f_x(x) \tag{A.58}$$

is obtained which is another formulation of Bayes' theorem.

For the two dimensional p.d.f., one can calculate the expected value of x

$$E(x) = \mu_x = \int_{-\infty}^{\infty} \int_{-\infty}^{\infty} \mathrm{d}x\mathrm{d}y \ x f(x,y) \ , \tag{A.59}$$

the variance

$$\sigma_x^2 = E((x-\mu_x)^2) = \int_{-\infty}^{\infty} \int_{-\infty}^{\infty} \mathrm{d}x\mathrm{d}y (x-\mu_x)^2 f(x,y) \tag{A.60}$$

and

$$\sigma_{xy}^2 = E((x-\mu_x)(y-\mu_y))) = \int_{-\infty}^{\infty} \int_{-\infty}^{\infty} \mathrm{d}x\mathrm{d}y (x-\mu_x)(y-\mu_y) f(x,y) \ . \tag{A.61}$$

The factor σ_{xy}^2 is the *covariance* and is used to expressed the correlation between variables through a *correlation coefficient*

$$\rho_{xy} = \frac{\sigma_{xy}^2}{\sigma_x \sigma_y} \ . \tag{A.62}$$

If the correlation coefficient is different from zero, the variables x, y are correlated. However, a correlation factor equal to zero does not mean that the variables x, y are independent.

Variables x and y are *independent* if the joint probability density factorizes into

$$f(x,y) = f_x(x) f_y(y) \ . \tag{A.63}$$

It means that the probability density of x does not depend on the value of y and vice versa so the conditional probability densities are equal to the marginal probability densities $f_x(x|y) = f_x(x)$ and $f_y(y|x) = f_y(y)$.

All the topics discussed in this section can be easily generalised to the case of many variables. Details can be found in literature.

A.3.3 | Summary of the properties of the most common distributions

In this section some of the most common distributions are listed and their properties are given.

Uniform distribution A uniform distribution is the simplest distribution, which often serves as a base for generating random variables following another distribution. The probability density for a continuous uniform random number $x \in [x_{min}, x_{max}]$ is given by

$$f(x) = \begin{cases} \frac{1}{x_{max}-x_{min}}, & x \in [x_{min}, x_{max}] \ , \\ 0 \ \text{ otherwise} \ . \end{cases} \tag{A.64}$$

It means that obtaining any value of x in the range $[x_{min}, x_{max}]$ is equally probable. The mean value of x is given by

$$E(x) = \frac{x_{min} + x_{max}}{2} \tag{A.65}$$

and the variance is

$$\sigma^2 = \frac{(x_{max} - x_{min})^2}{12} \ . \tag{A.66}$$

An important feature of uniform distribution is that from a random number u following any distribution $g(u)$ a random number x following uniform distribution $f(x) = 1$ (where for simplicity $x_{min} = 0, x_{max} = 1$) can be easily obtained. It can be shown using the relation eq. (A.49) that in this case

$$x = G(u) \ . \tag{A.67}$$

The problem can be also reversed. Having a uniformly distributed random number x in the range $(0, 1)$, one can easily obtain a random number u following another distribution $g(u)$ using again eq. (A.49)

$$u(x) = G^{-1}(x) \tag{A.68}$$

if only G^{-1} can be found.

$1/x$ distribution A $1/x$ distribution is defined in the following way

$$f(x) = \frac{1}{\ln \frac{x_{max}}{x_{min}}} \frac{1}{x}, \quad x \in [x_{min}, x_{max}] \ . \tag{A.69}$$

If one has a random number u generated according to uniform distribution $g(u) = 1$, $u \in (0, 1)$, one can obtain random variables following a $1/x$ distribution using eq. (A.49)

$$\frac{1}{\ln \frac{x_{max}}{x_{min}}} \int_{x_{min}}^{x} \mathrm{d}x' \frac{1}{x'} = u \tag{A.70}$$

and from that

$$x = x_{min} \left(\frac{x_{max}}{x_{min}} \right)^u \ . \tag{A.71}$$

Linear distribution A linear distribution is defined in the following way

$$f(x) = 2x, x \in [0, 1] \ . \tag{A.72}$$

If one has a random number u generated according to uniform distribution $g(u) = 1$, one can obtain random variables following linear distribiution using eq. (A.49)

$$\int_0^x \mathrm{d}x' 2x' = x^2 = u \tag{A.73}$$

and from that

$$x = \sqrt{u} \ . \tag{A.74}$$

Exponential distribution An exponential distribution is defined as

$$f(x) = \gamma \exp(-\gamma x), x \in [0, \infty] \; . \tag{A.75}$$

Using eq. (A.49) one obtains a recipe to obtain numbers x following exponential distribution $f(x)$ using random numbers u following uniform distribution $g(u) = 1$

$$x(u) = -\frac{1}{\gamma} \ln(1 - u) \; . \tag{A.76}$$

Power-law distribution A power-law distribution is defined by

$$f(x) = (n + 1)x^n, \quad x \in [0, 1], \;\; n > -1 \; . \tag{A.77}$$

Using eq. (A.49) one obtain numbers x following power-law distribution $f(x)$ using random numbers u following uniform distribution $g(u) = 1$ from the formula

$$x(u) = u^{\frac{1}{n+1}} \; . \tag{A.78}$$

Normal distribution A normal (Gauss) distribution of a variable $x \in [-\infty, \infty]$ is defined in the following way

$$N(x; \mu, \sigma^2) = \frac{1}{\sqrt{2\pi\sigma^2}} \exp\left(-\frac{(x - \mu)^2}{2\sigma^2}\right) \tag{A.79}$$

where μ and σ^2 are at the same time the parameters of the distribution and its mean value and variance respectively.

An important feature (called *stability*) of the normal distribution is the fact that the sum of normally distributed random numbers is again distributed according to normal distribution with $\mu = \sum_i \mu_i$ and $\sigma^2 = \sum_i \sigma_i^2$.

Binomial distribution Let us imagine an experiment which has only two possible outcomes: success or failure. A binomial distribution describes the probability to have n successes in N trials

$$p(n, N, p) = \frac{N!}{n!(N - n)!} p^n (1 - p)^{N-n} \tag{A.80}$$

where p is the probability of success in a single trial. The generalization of the binomial distribution for the case where more than two outcomes is possible, is called *multinomial distribution.*

Poisson distribution In the limit of very large number of trials N and very small probability of a success p, the expected value of the number of successes Np is a fixed value λ. In this limit, the binomial distribution eq. (A.80) leads to a Poisson distribution defined as

$$f(n, \lambda) = \frac{\lambda^n}{n!} \mathrm{e}^{-\lambda} \tag{A.81}$$

where λ is the parameter of this distribution and at the same time its mean value and variance

$$E(n) = \lambda, \quad \sigma^2 = \lambda \; . \tag{A.82}$$

A.3.4 | Law of large numbers and the central limit theorem

There are two very important laws in probability theory, all data analysis and Monte Carlo methods are based on.

Let us generate n randomly distributed numbers x_i following uniform distribution in an interval from a to b. Let us then calculate for each of the generated x_i the value of quantity u which depends on x_i: $u(x_i)$. The average of $u(x_i)$ converge to the expectation value of u when $n \to \infty$

$$\frac{1}{n}\sum_{i=1}^{n} u(x_i) \to \frac{1}{b-a}\int_a^b u(x)\mathrm{d}x \; . \tag{A.83}$$

This is the content of the *law of large numbers* [243], proven by Jakob Bernoulli in 1713. The quantity on the left hand side is called *consistent estimator* of the integral on the right hand side.

Another essential law of statistics is the *central limit theorem* which is closely related to the normal distribution. It tells us how the estimator of the integral from eq. (A.83) is distributed for large but finite n. Let us generate n times radnom variables x_i which follow the same distribution, the exact form of which does not matter. The distributions of these variables have expectation values e_i and variances v_i. The central limit theorem tells us that the sum of these variables $S = \sum_i x_i$ follows a Gauss distribution with the expectation value $E = \sum_i e_i$ and the variance $V = \sum_i v_i$ [243].

A.3.5 | Basics of the Monte Carlo techniques

The Monte Carlo method is the computational algorithm which makes use of a sequence of random numbers to calculate the probabilities, generate variables according to a given distribution, to find the expected values or values of the integrals. Based on the law of large numbers and the central limit theorem it can be used to solve any problem which has a probabilistic nature or which is too difficult and too complex to be solved analytically, especially multidimensional problems. Nowadays, the Monte Carlo method is widely used not only in physics but also in engineering, medical imaging or economy.

The basic idea is the following: one generates a set of random numbers r_i, for example according to a uniform distribution $g(r)$, and uses them to generate random numbers x_i following another distribution $f(x)$ which can be treated as the simulated outcomes of an experiment. Having generated x_i one can estimate for example the expected value of $f(x)$ or calculate the probability that x will have a value in a given range. One can also calculate the integral of $f(x)$ over x. In this section a short summary of the basic methods used in Monte Carlo algorithms are discussed, more details can be found in the literature (e.g. [241–243]).

A commonly encountered problem is how to generate a variable x following a distribution $f(x)$ which can be written as a sum of two (or more) terms

$$f(x) = f_1(x) + f_2(x) \tag{A.84}$$

where $f_1(x), f_2(x) \geq 0 \; \forall x$. Let us assume

$$\begin{aligned} P_1 &= \int_{-\infty}^{\infty} f_1(x)dx \; , \\ P_2 &= \int_{-\infty}^{\infty} f_2(x)dx \; , \end{aligned}$$

$$P_1 + P_2 \quad = \quad 1 \, . \tag{A.85}$$

The probability to obtain x smaller than r generated according to $f_1(x)$ and $f_2(x)$ is given respectively by

$$\begin{aligned} F_1(r) &= \int_{-\infty}^{r} \mathrm{d}x f_1'(x) \, , \\ F_2(r) &= \int_{-\infty}^{r} \mathrm{d}x f_2'(x) \end{aligned} \tag{A.86}$$

where $f_i'(x) = \frac{f_i(x)}{P_i}$. One can imagine a line segment (see fig. A.3) of the length $P = P_1 + P_2$ divided into two pieces with length P_1 and P_2. One can now generate random numbers $r_1, r_2 \in [0, 1]$ from a uniform distribution and check if r_1 is bigger or smaller than P_1. Then one can generate x according to

$$x = F_1^{-1}(r_2) \quad \text{for} \quad r_1 < P_1 \tag{A.87}$$

or

$$x = F_2^{-1}(r_2) \quad \text{for} \quad r_1 > P_1 \, . \tag{A.88}$$

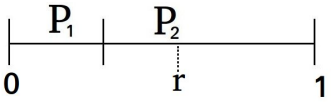

Figure A.3: Line segment of the lenght $P_1 + P_2 = 1$ and a random number $r \in [0, 1]$ compared with the lenght of a segment. Here $r > P_1$ so the random number x should be generated according to f_2 (see eq. (A.84)-(A.88)).

In most of the cases the analytical inverse of the distribution function does not exist and the desired distribution cannot be generated directly. To solve this, so called *rejection sampling* illustrated in fig. A.4 is applied.

Let us imagine a function $f(x)$ in a given range $[x_{min}, x_{max}]$ (in fig. A.4 $x \in [0, 10]$) according to which one wants to generate a random number. This function has values between 0 and f_{max} (zero chosen for simplicity). One can draw this function and a step function $g(x) = f_{max}\Theta(x - x_{min})\Theta(x_{max} - x)$ in the same range of x. Now one can generate pairs of uniformly distributed random numbers (r_1, r_2), $r_1 \in [x_{min}, x_{max}]$ and $r_2 \in [0, f_{max}]$. This pairs of random numbers are compared with $f(x)$. If they lie below the curve $f(x)$ they are kept, otherwise they are rejected. The density of values r_1, which are left, follow the distribution $f(x)$. This method is easy but it can be very ineffective - one generates a lot of pairs of random numbers which are rejected. The efficiency, the ratio of the number of accepted points and all generated points, is given by the ratio of the areas below the curves $f(x)$ and $g(x)$ for $x \in [x_{min}, x_{max}]$. Moreover, for functions which extend to infinity it is not possible to use this method at all.

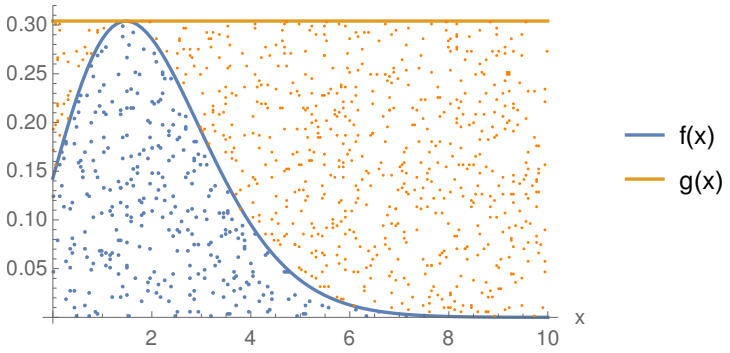

Figure A.4: Illustration of the simple rejection method to generate variables following $f(x)$. All the orange and blue points are generated uniformly in an area $x \in [0, 10]$ and $y \in [0, f_{max}]$. Points lying above the curve $f(x)$ (in orange) are rejected, points lying below the curve $f(x)$ (in blue) are kept and the density of the kept x follows $f(x)$.

An improved version of the rejection sampling is *importance sampling*. One needs to find a function $g(x)$, which approximates $f(x)$ well and fulfils the following requirements: $g(x) \geq f(x)$ for all x and is invertible. One generates x according to the properly normalized $g'(x) = \frac{g(x)}{\int_{-\infty}^{\infty} \mathrm{d}x g(x)}$ using a uniformly distributed random number $r_1 \in [0, 1]$

$$r_1 = \int_{-\infty}^{x(r_1)} \mathrm{d}x g'(x) = G(x(r_1))$$
$$x(r_1) = G^{-1}(r_1) \tag{A.89}$$

and another random number $r_2 \in [0, 1]$ according to uniform distribution. If $r_2 g(x) > f(x)$ this x is rejected, otherwise it is kept and its density follows $f(x)$. When $g(x)$ is not very different from $f(x)$ this method of generation can be very efficient. It can be also used for distributions which extend to infinity.

Another approach to the problem of generating variables according to some distribution is to consider *weighted events*.
To obtain a distribution $f(x)$ in a range $x \in [a, b]$ one needs to generate n uniformly distributed random numbers r_i, $i = 0, ..., n$, in a range $[a, b]$, calculate the quantity one is interested in, using r_i instead of x_i, and multiply every event calculated with r_i with weight $w = f(r_i)$.

One can also combine the importance sampling method with the weighted events method. In the importance sampling method given above, instead of generating the second random number r_2 and comparing $r_2 g(x)$ with $f(x)$ one can compute the quantity of interests with x_i, where x_i was generated according to $g(x)$, and multiply every event with a weight

$$w_i = f(x_i)/(g(x_i)) \; . \tag{A.90}$$

This will give the proper distribution of x_i according to $f(x_i)$. Here $g(x)$ does not need to be larger than $f(x)$, it is enough when it is similar.

Up to now this chapter focused on the problem of generating variables according to a given distribution or on generating the distributions itself. However, the Monte Carlo method can be used also to

solve integrals. These two issues are very similar.

Lets assume one wants to solve an integral

$$\int_{x_1}^{x_2} \mathrm{d}x f(x) \tag{A.91}$$

using the Monte Carlo methods.

One method to solve this integral uses the law of large numbers: if we generate N random numbers $x_i \in [x_{min}, x_{max}]$ from a uniform distribution, calculate $f(x_i)$ for every x_i and average them what we obtain will be the expected value of $f(x)$ so

$$E(f(x)) = \int_{x_{min}}^{x_{max}} \mathrm{d}x g(x) f(x) \approx \frac{1}{N} \sum_{i=1}^{N} f(x_i) = \overline{f} \tag{A.92}$$

where $g(x) = \frac{1}{x_{max} - x_{min}}$ is a uniform distribution of x so

$$\int_{x_{min}}^{x_{max}} \mathrm{d}x f(x) \approx \frac{x_{max} - x_{min}}{N} \sum_{i=1}^{N} f(x_i) = I \ . \tag{A.93}$$

The uncertainty of this estimate of the integral is given by

$$(\delta \overline{f})^2 = \frac{1}{N(N-1)} \sum_{i=1}^{N} (f(x_i) - \overline{f})^2 \ . \tag{A.94}$$

Another option to estimate the integral eq. (A.91) is to use also the definition of the expected value but this time together with importance sampling and a normalized function $g(x)$ which approximates $f(x)$. The integral eq. (A.91) can be rewritten

$$I = \int_{x_{min}}^{x_{max}} \mathrm{d}x f(x) = \int_{x_{min}}^{x_{max}} \mathrm{d}x \frac{f(x)}{g(x)} g(x) = \int_{x_{min}}^{x_{max}} \mathrm{d}x h(x) g(x) = E(h(x)) \tag{A.95}$$

where $h(x) = f(x)/g(x)$ and x is generated according to $g(x)$. Using the law of large numbers one can generate N times x_i according to $g(x)$, for every x_i calculate $h(x_i)$, average them and obtain the approximation of $E(h(x))$

$$I \approx \frac{1}{N} \sum_{i=1}^{N} \frac{f(x_i)}{g(x_i)} \ . \tag{A.96}$$

The uncertainty of this method can be obtained from a variance $\sigma^2 \left(\frac{f(x)}{g(x)} \right)$.

Now, let us have a look at the example with simple rejection method described above, where in fig. A.4 the function $f(x)$ and a step function $g(x)$ were shown. The purpose of the method was to obtain from uniformly distributed pairs of random numbers (from which the points lying below $f(x)$ were accepted and others were rejected) the random variables x with density $f(x)$. These points can be also used to estimate the area below the function $f(x)$ so the integral $\int_{x_{min}}^{x_{max}} \mathrm{d}x f(x)$. To obtain the value of this integral one can multiply the area under the function $g(x)$ by the fraction of accepted (N_a) and generated (N_g) points

$$\int_{x_{min}}^{x_{max}} \mathrm{d}x f(x) \approx I = \frac{N_a}{N_g} \int_{x_{min}}^{x_{max}} \mathrm{d}x g(x) \ . \tag{A.97}$$

The uncertainty is given by

$$\frac{\delta I}{I} = \frac{\delta N_a}{N_a} = \sqrt{\frac{1 - N_a/N_g}{N_a}}, \tag{A.98}$$

the more points are generated the more accurate the estimation is.

The accuracy of the simple rejection method can be improved by using function $g(x)$ which is a better approximation of $f(x)$ than the step function, as described in the importance sampling method. The integral can be then estimated by the same equation as eq.(A.97) but $g(x)$ being a function, which approximates $f(x)$.

One can also notice, that in eq. (A.97) the ratio of accepted and generated events can be rewritten using the ratio of area below $f(x)$ and $g(x)$:

$$\frac{N_a}{N_g} = \frac{\int_{x_{min}}^{x_{max}} \mathrm{d}x f(x)}{\int_{x_{min}}^{x_{max}} \mathrm{d}x g(x)} = \frac{(x_{max} - x_{min})/N \sum_i f(x_i)}{(x_{max} - x_{min})/N \sum_i g(x_i)} = \frac{\sum_i f(x_i)}{\sum_i g(x_i)} \tag{A.99}$$

where x_i were generated according to a uniform random number in range $[x_{min}, x_{max}]$.

A.4 | Parton branching method from scratch

In this section the parton branching method is described step by step. The generation of every variable (μ^2 and z) using the Monte Carlo techniques (all discussed generally in Sec. (A.3)) with the discussion of the weights is presented here.

This section is divided into 5 subsections. The first subsection describes the method of the scale generation used in the evolution program. The next three subsections correspond to the left, middle and right hand side of fig. A.5 where 0- branching, 1- branching and 2- branching cases are shown respectively. We discuss these cases at LO. The notation agrees with the notation on a corresponding piece of fig. A.5. In the last subsection the 1-branching event at NLO is discussed.

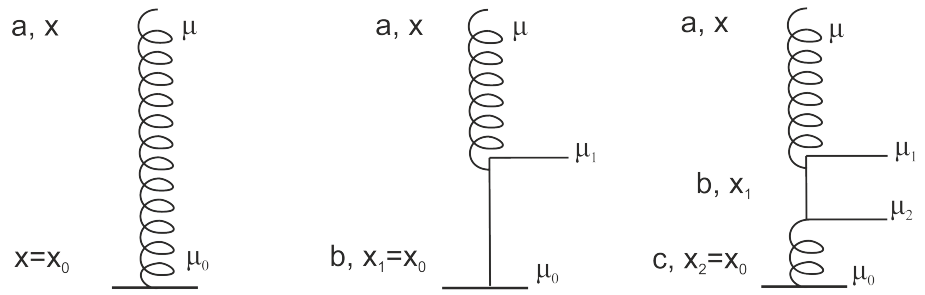

Figure A.5: Evolution by iteration.

A.4.1 | Details on the scale generation

In the practical implementation of the PB method into a numerical program, the integrals over the splitting functions over z and μ, which are the parts of the Sudakov form factors, are calculated once for different scales and partons, at the beginning, and tabulated in the Sudakov tables. The calculation of these integrals is very time consuming therefore it is of advantage to perform the calculation only once and then use the Sudakov tables for all other events.

Let us write an equality

$$\Delta_b(\mu_1^2, \mu_2^2) = \exp\left(- \int_{\mu_2^2}^{\mu_1^2} \frac{\mathrm{d}\mu^2}{\mu^2} \sum_a \int_0^{z_M} \mathrm{d}z \; z P_{ab}^R(\mu^2, z) \right) =$$

$$= \exp\left(- \int_{\mu_2^2}^{\mu_x^2} \frac{\mathrm{d}\mu^2}{\mu^2} \sum_a \int_0^{z_M} \mathrm{d}z \; z P_{ab}^R(\mu^2, z) - \int_{\mu_x^2}^{\mu_1^2} \frac{\mathrm{d}\mu^2}{\mu^2} \sum_a \int_0^{z_M} \mathrm{d}z \; z P_{ab}^R(\mu^2, z) \right) \quad \text{(A.100)}$$

where the notation for μ_1^2, μ_2^2 agrees with fig. A.5 and μ_x^2 is any scale. Without loss of generality we can choose $\mu_x^2 = \mu_0^2$. From eq. (A.100) the following relation holds

$$\begin{aligned} \ln \Delta_b(\mu_1^2, \mu_2^2) &= - \int_{\mu_2^2}^{\mu_0^2} \frac{\mathrm{d}\mu^2}{\mu^2} \sum_a \int_0^{z_M} \mathrm{d}z \; z P_{ab}^R(\mu^2, z) - \int_{\mu_0^2}^{\mu_1^2} \frac{\mathrm{d}\mu^2}{\mu^2} \sum_a \int_0^{z_M} \mathrm{d}z \; z P_{ab}^R(\mu^2, z) = \\ &= \underbrace{\int_{\mu_0^2}^{\mu_2^2} \frac{\mathrm{d}\mu^2}{\mu^2} \sum_a \int_0^{z_M} \mathrm{d}z \; z P_{ab}^R(\mu^2, z)}_{\mathrm{s}_2} - \underbrace{\int_{\mu_0^2}^{\mu_1^2} \frac{\mathrm{d}\mu^2}{\mu^2} \sum_a \int_0^{z_M} \mathrm{d}z \; z P_{ab}^R(\mu^2, z)}_{\mathrm{s}_1} . \end{aligned} \quad \text{(A.101)}$$

The scale at which the branching happens, should be calculated by solving the equation

$$R = \int_{\ln \mu_2^2}^{\ln \mu_1^2} \mathrm{d}\left(-\Delta_b(\mu'^2, \mu_2^2) \right) , \quad \text{(A.102)}$$

what gives

$$\Delta_b(\mu_1^2, \mu_2^2) = 1 - R \quad \text{(A.103)}$$

where the fact that $\Delta_b(\mu_2^2, \mu_2^2) = 1$ was used. $1 - R$ is also a uniformly distributed random number so this equation can be just written as

$$\Delta_b(\mu_1^2, \mu_2^2) = R \, . \quad \text{(A.104)}$$

From eq. (A.104) we obtain

$$\ln R = \ln\left(\Delta_b(\mu_1^2, \mu_2^2) \right) = \mathrm{s}_2 - \mathrm{s}_1 \, . \quad \text{(A.105)}$$

In the evolution program, the scale μ_2^2 is known from the previous branching. The term s_2, corresponding to μ_2^2, is calculated from the Sudakov table using interpolation methods. We generate R and calculate s_1. Using interpolation methods we obtain from the Sudakov tables the value of μ_1^2 which corresponds to s_1. The scale μ_1^2 is generated exactly according to eq. (A.102) so there is no weight associated with this step.

The number of grid points in the Sudakov table has a huge effect on the accuracy of the method. The bigger the size is, the better agreement between the PB method and QCDNUM [62] is found. In fig. A.6 the results for the collinear PDFs for down quark at 10 and 1000 GeV^2 and gluon at 100 and 10000 GeV^2 for 3 different sizes of the Sudakov table are shown for 10^{10} events. For the size 65536 of the Sudakov table for a comparison we show also the result obtained with 2×10^{10} events. With all these sizes of the Sudakov table the obtained results agree well with QCDNUM, however one can see the improvement when the Sudakov table is larger. On the other hand, increasing the size of the grid increases also the CPU time.

A.4.2 | 0-branching event

At the beginning, let us have a look at an example of an event with no branching. The evolution starts from a parton a at a scale μ_0^2 and x.

1. x has to be generated according to some starting distribution

$$\widetilde{f}_a(x, \mu_0^2) \quad \text{(A.106)}$$

where the functional form of a starting distribution is a needed input to this method. Any parametrization can be used.

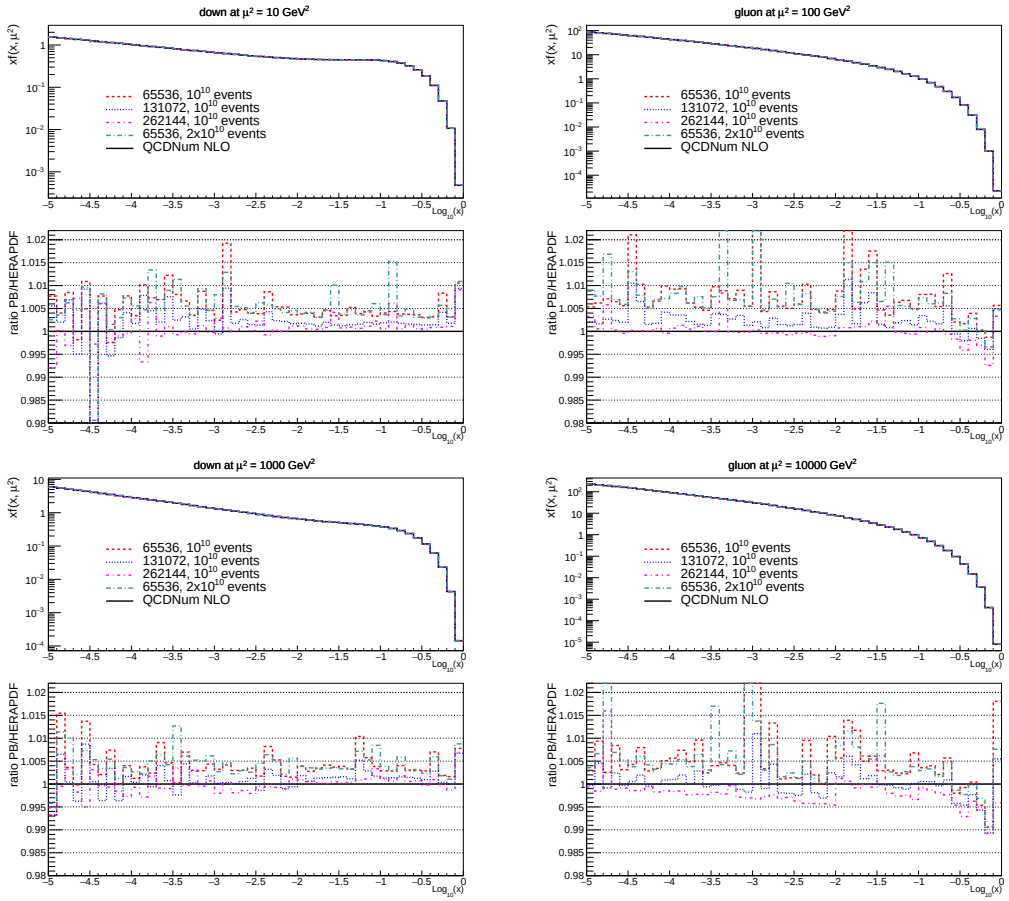

Figure A.6: The comparison of different sizes of Sudakov table.

2. Next, the scale μ_1^2 at which the branching should happen has to be generated using a uniformly distributed random number $R_1 \in [0,1]$

$$R_1 = \int_{\ln \mu_0^2}^{\ln \mu_1^2} \mathrm{d}\left(-\Delta_b(\mu'^2, \mu_0^2)\right) \ . \tag{A.107}$$

Notice, the integral

$$\int_{\ln \mu_0^2}^{\infty} \mathrm{d}\left(-\Delta_b(\mu'^2, \mu_0^2)\right) = 1 \tag{A.108}$$

is properly normalized.

The solution of eq. (A.107) is discussed in Appendix (A.4.1). Let us assume that the generated scale was above μ^2. It means there was no branching between scale μ_0^2 and μ^2 and information about an event with a parton a at a scale μ^2 and x can be put to the histogram for $\widetilde{f}_a(x,\mu^2)$ vs x.

From events of this type we include following piece of the evolution equation:

$$\widetilde{f}_a(x,\mu_0^2)\Delta_a(\mu^2,\mu_0^2). \tag{A.109}$$

A.4.3 | 1-branching event

Now, let us analyse an event, which will be 1-branching event.

1. The evolution starts with a parton b and one needs to generate the initial momentum fraction x_1 from the starting distribution
$$\widetilde{f}_b(x_1, \mu_0^2) \, . \tag{A.110}$$

2. Now one needs to generate the scale μ_1^2 at which the first branching happens. It is done according to the integral
$$R_1 = \int_{\ln \mu_0^2}^{\ln \mu_1^2} \mathrm{d}\left(-\Delta_b(\mu'^2, \mu_0^2)\right) \tag{A.111}$$
using a uniformly distributed random number $R_1 \in [0,1]$. Let's assume that the generated scale $\mu_1^2 < \mu^2$.

3. Now the splitting variable z_1 has to be generated. The splitting functions are complicated and the generation is not performed exactly according to the splitting function but according to some easier function and a special weight w_z must be applied.

   It was discussed in Sec. (2.2.5) that at LO there are always only two possibilities to consider: a quark can split only to the same kind of quark or a gluon and a gluon can split only to a gluon or a quark. The splitting function Pqg is the same for every quark flavour q_i so it is enough first to decide if to continue the evolution as a "gluon" or "quark" using $2n_f Pqg^R$ and later, if quark was chosen, to decide which kind of quark. In other words, the question to answer is if b splits into a parton b (P_{bb}^R) or different a parton a (P_{ab}^R). At NLO the quark sector becomes more complicated, because the quark can split into a quark or antiquark of the same or different flavour.

   At LO, the splitting functions have a probabilistic interpretation. The probability density according to which we want to generate the splitting variable consists of two parts, like discussed in Appendix (A.3.5), in eq. (A.84).

   One can draw a line segment, like in fig. A.3, where
$$\begin{aligned} P_1 &= \frac{\int_0^{z_M} \mathrm{d}z z P_{bb}^R(z, \mu_1^2)}{\sum_{c=a,b} \int_0^{z_M} \mathrm{d}z z P_{cb}^R(z, \mu_1^2)} \, , \\ P_2 &= \frac{\int_0^{z_M} \mathrm{d}z z P_{ab}^R(z, \mu_1^2)}{\sum_{c=a,b} \int_0^{z_M} \mathrm{d}z z P_{cb}^R(z, \mu_1^2)} \, , \\ P &= P_1 + P_2 = 1 \end{aligned} \tag{A.112}$$
   and solve the problem with the method from eq. (A.84) - (A.88). A uniformly distributed random number $R_2 \in [0,1]$ is generated and compared with P_1. If
$$R_2 < P_1 \tag{A.113}$$
   z_1 should be generated according to properly normalized $zP_{bb}^R(z, \mu_1^2)$
$$R_3 = \frac{\int_0^{z_1} \mathrm{d}z z P_{bb}^R(z, \mu_1^2)}{\int_0^{z_M} \mathrm{d}z z P_{bb}^R(z, \mu_1^2)} \, , \tag{A.114}$$
   where $R_3 \in [0,1]$ is a uniformly distributed random number. Otherwise, if
$$R_2 > P_1 \tag{A.115}$$

then z_1 should be generated according to properly normalized $zP^R_{ab}(z,\mu_1^2)$

$$R_3 = \frac{\int_0^{z_1} \mathrm{d}z z P^R_{ab}(z,\mu_1^2)}{\int_0^{z_M} \mathrm{d}z z P^R_{ab}(z,\mu_1^2)} \,. \tag{A.116}$$

There is one more difficulty included at this stage. The splitting functions in eq. (A.114) and eq. (A.116) are complicated and it is not possible to find analytically the inverse of these functions. Instead, the *importance sampling* method connected with *weighted events* method, both described in Appendix (A.3.5), has to be used.

We choose a normalized function $g(z) = \frac{1}{1-z}\frac{1}{\int_0^{z_M} \mathrm{d}z \frac{1}{1-z}}$ and we solve, instead of eq. (A.114) or eq. (A.116), equation

$$R_3 = \int_0^{z_1} g(z)\mathrm{d}z \tag{A.117}$$

for z_1.

A cut off value on the lower limit of the integral is introduced

$$R_3 = \int_{z_{min}}^{z_1} g(z)\mathrm{d}z \tag{A.118}$$

because of the issue described in Sec. (2.2), after eq. (2.28).

From eq.(A.118) we have

$$R_3 \ln\left(\frac{1-z_{min}}{1-z_M}\right) = \ln\left(\frac{1-z_{min}}{1-z_1}\right) \tag{A.119}$$

and from that we calculate z_1

$$z_1 = 1 - (1-z_{min})\left(\frac{1-z_M}{1-z_{min}}\right)^{R_3}. \tag{A.120}$$

Now, the weight to compensate for generating z_1 according to eq. (A.118) instead of eq. (A.114) or eq. (A.116) has to be calculated like in eq. (A.90)

$$w_z = \frac{zP^R_{xb}(z_1,\mu_1^2)}{\int_0^{z_M} \mathrm{d}z z P^R_{xb}(z,\mu_1^2)} \frac{1}{g(z_1)} \tag{A.121}$$

where $x = a$ or $x = b$.

Having generated z_1, x can be calculated applying the momentum conservation condition expressed by the delta function $\delta(z_1 x_1 - x)$

$$x = z_1 x_1. \tag{A.122}$$

4. Now a scale of the next branching can be generated and let us assume it is higher than the maximum evolution scale μ^2 and the evolution is stopped.

A histogram is filled with x and weight w_z for the scale μ^2 and parton a ($\widetilde{f}_a(x,\mu^2)$).

The procedure is repeated many times ($\sim 10^6$ or more) and one has many 1-branching events generated. There are different options possible: the evolution starts from parton a which splits into parton a or b, or the evolution starts from parton b which splits into a parton a or b. Of course x_1, μ_1^2, z_1, x and w_z can have different values in every event. In such procedure, a histogram for every parton species $\widetilde{f}_i(x,\mu^2)$ vs x is built.

The contribution to the histogram $\widetilde{f}_a(x,\mu^2)$ vs x from the 1-branching events come from the following term of evolution equation

$$\int_{\mu_0^2}^{\mu^2} \mathrm{d}\ln\mu_1^2 \frac{\Delta_a(\mu^2,\mu_0^2)}{\Delta_a(\mu_1^2,\mu_0^2)} \int_x^{z_M} \mathrm{d}z_1 \int_0^1 dx_1 \sum_b P_{ab}^R(\mu_1^2,z_1) x f_b(x_1,\mu_0^2)\delta(z_1x_1-x)\Delta_a(\mu_1^2,\mu_0^2)\,. \tag{A.123}$$

A.4.4 | 2-branching event

Now let us have a look at a 2-branching event.

1. The evolution starts from a parton c and one generates the initial momentum fraction x_2 from the starting distribution distribution
$$\widetilde{f}_c(x_2,\mu_0^2)\,. \tag{A.124}$$

2. Now one needs to generate the scale μ_2^2 at which the branching can happen. It is done according to the Sudakov form factor using a uniformly distributed $R_1 \in [0,1]$
$$R_1 = \int_{\mu_0^2}^{\mu_2^2} \mathrm{d}\left(-\Delta_c(\mu'^2,\mu_0^2)\right)\,. \tag{A.125}$$
Let us assume that the generated scale $\mu_2^2 < \mu^2$.

3. Now a decision about the branching has to be taken: if c splits into parton c or different parton b. The decision is taken according to the ratio
$$\begin{aligned} P_1 &= \frac{\int_0^{z_M}\mathrm{d}z z P_{cc}^R(z,\mu_1^2)}{\sum_{d=b,c}\int_0^{z_M}\mathrm{d}z z P_{dc}^R(z,\mu_1^2)}\,, \\ P_2 &= \frac{\int_0^{z_M}\mathrm{d}z z P_{bc}^R(z,\mu_1^2)}{\sum_{d=b,c}\int_0^{z_M}\mathrm{d}z z P_{dc}^R(z,\mu_1^2)}\,, \\ P &= P_1+P_2=1\,. \end{aligned} \tag{A.126}$$
A uniformly distributed random number R_2 in an interval $(0,1)$ is generated and compared with P_1.

Let us assume that $R_2 > P_1$ so the parton c splits into a parton b and splitting variable z_2 should be generated according to
$$R_3 = \frac{\int_0^{z_2}\mathrm{d}z z P_{bc}^R(z,\mu_1^2)}{\int_0^{z_M}\mathrm{d}z z P_{bc}^R(z,\mu_1^2)} \tag{A.127}$$
using the method described in the previous subsection and the weight w_{z2} coming from the z_2 generation has to be calculated.

4. Now the next scale μ_1 of the next branching is generated
$$R_4 = \int_{\mu_2^2}^{\mu_1^2} \mathrm{d}\left(-\Delta_b(\mu'^2,\mu_2^2)\right) \tag{A.128}$$
and let us assume that $\mu_1^2 < \mu^2$.

5. A decision about the next branching has to be taken: if parton b splits into parton a or b according to

$$P_1 = \frac{\int_0^{z_M} \mathrm{d}z z P^R_{bb}(z,\mu_1^2)}{\sum_{d=a,b}\int_0^{z_M} \mathrm{d}z z P^R_{db}(z,\mu_1^2)},$$
$$P_2 = \frac{\int_0^{z_M} \mathrm{d}z z P^R_{ab}(z,\mu_1^2)}{\sum_{d=a,b}\int_0^{z_M} \mathrm{d}z z P^R_{db}(z,\mu_1^2)},$$
$$P = P_1 + P_2 = 1, \tag{A.129}$$

using uniformly distributed $R_5 \in [0,1]$.

Let us assume that $R_5 > P_1$ so parton b splits into parton a. Now z_1 can be generated according to this splitting function

$$R_6 = \frac{\int_0^{z_1} \mathrm{d}z z P^R_{ab}(z,\mu_1^2)}{\int_0^{z_M} \mathrm{d}z z P^R_{ab}(z,\mu_1^2)} \tag{A.130}$$

using the method described above and the weight w_{z1} coming from this generation has to be computed.

6. If now a new scale μ generated is bigger than the evolution scale, the evolution is stopped after two branchings. The information about the parton a at scale μ^2 and $x = z_1 z_2 x_2$ with weights coming from two z generations $w_{z1}w_{z2}$ is put to the histogram $\widetilde{f}_a(x,\mu^2)$ vs x.

There are many possibilities how to obtain at the end of the evolution the parton a in the 2-branching event: the evolution can start from another parton (not c) or it can start from the same parton c but then split into another parton than the parton b. By repeating the procedure many times all the possible options are taken into account with the proper proportions.

The contribution to the histogram $\widetilde{f}_a(x,\mu^2)$ vs x coming from the 2-branching events comes from the following term of the evolution equation

$$\sum_b \int_{\mu_0^2}^{\mu^2} \frac{d\mu_1^2}{\mu_1^2}\frac{\Delta_a(\mu^2)}{\Delta_a(\mu_1^2)} \int \mathrm{d}x_1 \int_x^{z_M} \mathrm{d}z_1 P^R_{ab}(\mu_1^2,z_1)x$$
$$\left(\sum_c \int_{\mu_0^2}^{\mu_1^2} \frac{d\mu_2^2}{\mu_2^2}\frac{\Delta_b(\mu_1^2)}{\Delta_b(\mu_2^2)} \int \mathrm{d}x_2 \int_{x_1}^{z_M} dz_2 P^R_{bc}(\mu_2^2,z_2)\; x_1 f_c\left(x_2,\mu_2^2\right)\delta\left(z_2x_2 - x_1\right)\right)\delta(z_1x_1 - x)\,. \tag{A.131}$$

Now we are ready to combine all the pieces from Appendix (A.4.2)-(A.4.4) together and to answer the question what is the probability of finding a parton a at a scale μ^2 at a given x. In the histogram $\widetilde{f}_a(x,\mu^2)$ vs x for a parton a at scale μ^2 there are events coming from 0-branching events, 1-branching events, 2-branching events etc. They all sum up to give the solution of the evolution eq. (6.3)

$$\begin{aligned}
\widetilde{f}_a(x,\mu^2) &= \widetilde{f}_a(x,\mu_0^2)\Delta_a(\mu^2,\mu_0^2) \\
&+ \int_{\mu_0^2}^{\mu^2} \mathrm{d}\ln\mu_1^2 \frac{\Delta_a(\mu^2,\mu_0^2)}{\Delta_a(\mu_1^2,\mu_0^2)} \int_x^{z_M} \mathrm{d}z_1 \int_0^1 dx_1 \sum_b P^R_{ab}(\mu_1^2,z_1)x f_a(x_1,\mu_0^2)\delta(z_1x_1 - x)\Delta_a(\mu_1^2,\mu_0^2) \\
&+ \sum_b \int_{\mu_0^2}^{\mu^2} \frac{d\mu_1^2}{\mu_1^2}\frac{\Delta_a(\mu^2)}{\Delta_a(\mu_1^2)} \int \mathrm{d}x_1 \int_x^{z_M} \mathrm{d}z_1 P^R_{ab}(\mu_1^2,z_1)x \\
&\times \left(\sum_c \int_{\mu_0^2}^{\mu_1^2} \frac{d\mu_2^2}{\mu_2^2}\frac{\Delta_b(\mu_1^2)}{\Delta_b(\mu_2^2)} \int \mathrm{d}x_2 \int_{x_1}^{z_M} dz_2 P^R_{bc}(\mu_2^2,z_2)\; x_1 f_c\left(x_2,\mu_2^2\right)\delta\left(z_2x_2 - x_1\right)\right)\delta(z_1x_1 - x) \\
&+ \ldots\,.
\end{aligned} \tag{A.132}$$

A.4.5 | 1- branching event for quark at NLO

In Appendix. A.4.3 the parton branching method for the 1-branching event at LO was discussed in detail. Here the structure of the solution at NLO is described. The integrals of the NLO splitting functions over z are positive so despite the fact that the splitting functions can be negative and they do not have a proper probabilistic interpretation, we use the same method to generate the variables, as at LO. The main difference between LO and NLO enters at the moment of z_1 generation (of course in the μ_1^2 generation also the NLO splitting functions are used, but the structure of the solution stays the same).

At NLO, the structure of a decision for gluon splitting stays the same as at LO, but the quark sector becomes more complicated. Quark can split into a quark of the same flavour P^R_{qjqj}, antiquark of the same flavour $P^R_{\overline{q}_j q_j}$, quark or antiquark of different flavour $P^R_{qjq_i}$ ($2(n_f-1)$ options) or into a gluon P^R_{gq}.

The decision about the branching can be taken according to the method from Appendix (A.3.5), eq. (A.84)-(A.88). First the line segment representing all the options is divided into 4 pieces corresponding to quark going to any quark or antiquark and quark going to gluon

$$\begin{aligned}
P_1 &= \frac{\int_0^{z_M} \mathrm{d}z z P^R_{q_j q_j}(\mu_1^2, z)}{\int_0^{z_M} \mathrm{d}z\ z P_{tot}(z,\mu_1^2)}\,, \\
P_2 &= \frac{\int_0^{z_M} \mathrm{d}z z P^R_{\overline{q}_j q_j}(\mu_1^2, z)}{\int_0^{z_M} \mathrm{d}z\ z P_{tot}(z,\mu_1^2)}\,, \\
P_3 &= \frac{\int_0^{z_M} \mathrm{d}z z 2(n_f-1) P^R_{q_i q_j}(\mu_1^2, z)}{\int_0^{z_M} \mathrm{d}z\ z P_{tot}(z,\mu_1^2)}\,, \\
P_4 &= \frac{\int_0^{z_M} \mathrm{d}z P^R_{g q_j}(\mu_1^2, z)}{\int_0^{z_M} \mathrm{d}z\ z P_{tot}(z,\mu_1^2)}\,, \\
P &= P_1 + P_2 + P_3 + P_4 = 1
\end{aligned} \tag{A.133}$$

where $zP_{tot}(z,\mu_1^2) = z\left[P^R_{q_j q_j}(\mu_1^2,z) + P^R_{\overline{q}_j q_j}(\mu_1^2,z) + 2(n_f-1)P^R_{q_i q_j}(\mu_1^2,z) + P^R_{g q_j}(\mu_1^2,z)\right]$.

The decision is made in more steps, using more uniformly distributed random numbers in the interval $(0,1)$.

- If $R_2 < P_1$ then z_1 has to be generated according to $R_3 = \frac{\int_0^{z_1} \mathrm{d}z z P^R_{q_j q_j}(z,\mu_1^2)}{\int_0^{z_M} \mathrm{d}z z P^R_{q_j q_j}(z,\mu_1^2)}$. Otherwise,
- if $R_2 < P_1 + P_2$ then z_1 has to be generated according to $R_3 = \frac{\int_0^{z_1} \mathrm{d}z z P^R_{\overline{q}_j q_j}(z,\mu_1^2)}{\int_0^{z_M} \mathrm{d}z z P^R_{\overline{q}_j q_j}(z,\mu_1^2)}$. Otherwise,
- if $R_2 < P_1 + P_2 + P_3$ then z_1 has to be generated according to $R_3 = \frac{\int_0^{z_1} \mathrm{d}z z P^R_{q_i q_j}(z,\mu_1^2)}{\int_0^{z_M} \mathrm{d}z z P^R_{q_i q_j}(z,\mu_1^2)}$. In the next step the decision if the evolution continues as a quark or antiquark and about the flavour has to taken.
- if $R_2 > P_1 + P_2 + P_3$ then z_1 has to be generated according to $R_3 = \frac{\int_0^{z_1} \mathrm{d}z z P^R_{g q_j}(z,\mu_1^2)}{\int_0^{z_M} \mathrm{d}z z P^R_{g q_j}(z,\mu_1^2)}$.

The NLO splitting functions are even more complicated than at LO so the inverse of them can not be found analytically and, similarly as at LO , z_1 variable is generated according to an easier function $g(z)$ and later the weight is applied to correct for that (as described in eq. (A.118) - (A.121)).

Plots showing the integrals of the NLO splitting functions over z used in the above ratios (and also for gluon) are showed in Sec. (6.6).

Bibliography

[1] R.K.Ellis, W.J.Stirling, and B.R.Webber, *QCD and Collider Physics*. Cambridge University Press, 2003.

[2] D. J. Gross and F. Wilczek, Phys. Rev. Lett. **30**, 1343 (1973).

[3] H. D. Politzer, Phys. Rev. Lett. **30**, 1346 (1973).

[4] G. Hooft (1972).

[5] W. E. Caswell, Phys. Rev. Lett. **33**, 244 (1974).

[6] D. R. T. Jones, Nucl. Phys. **B75**, 531 (1974).

[7] E. Egorian and O. V. Tarasov, Teor. Mat. Fiz. **41**, 26 (1979). [Theor. Math. Phys.41,863(1979)].

[8] O. V. Tarasov, A. A. Vladimirov, and A. Yu. Zharkov, Phys. Lett. **93B**, 429 (1980).

[9] S. A. Larin and J. A. M. Vermaseren, Phys. Lett. **B303**, 334 (1993). `hep-ph/9302208`.

[10] T. van Ritbergen, J. A. M. Vermaseren, and S. A. Larin, Phys. Lett. **B400**, 379 (1997). `hep-ph/9701390`.

[11] G. 't Hooft, Nucl. Phys. **B61**, 455 (1973).

[12] W. A. Bardeen, A. J. Buras, D. W. Duke, and T. Muta, Phys. Rev. **D18**, 3998 (1978).

[13] A. Warburton, *Measurements of α_s in pp Collisions at the LHC*, in *Proceedings, 12th Conference on the Intersections of Particle and Nuclear Physics (CIPANP 2015): Vail, Colorado, USA, May 19-24, 2015*. 2015. Also in preprint 1509.04380.

[14] Particle Data Group Collaboration, K. A. Olive *et al.*, Chin. Phys. **C38**, 090001 (2014).

[15] E. Levin and Y. V. Kovchegov, *Quantum Chromodynamics at High Energy*. Cambridge Monographs on Particle Physics and Cosmology, 2012.

[16] M. Peskin and D. V. Schroeder, *An Introduction to Quantum Field Theory*. Avalon Publishing, 1995.

[17] F. Halzen and A. D. Martin, *Quarks & Leptons: An Introductory Course in Modern Particle Physics*. John Wiley & Sons, 1984.

[18] O. Nachtmann, *Elementary Particle Physics Concepts and Phenomena*. Springer- Verlag Berlin Heidelberg, 1990.

[19] D. E. Soper, *Basics of QCD perturbation theory*, in *The Strong interaction, from hadrons to partons: Proceedings, 24th SLAC Summer Institute on Particle Physics (SSI 96), Stanford, Calif., 19-30 Aug 1996*, pp. 15–42. 1996. Also in preprint hep-ph/9702203.

[20] M. L. Mangano, *Introduction to QCD*, in *Particles and fields. Proceedings, 10th Jorge Andre Swieca Summer School, Sao Paulo, Brazil, February 6-12, 1999*. 1998.

[21] R. P. Feynman, Phys. Rev. Lett. **23**, 1415 (1969).

[22] J. D. Bjorken and E. A. Paschos, Phys. Rev. **185**, 1975 (1969).

[23] S. D. Drell and T.-M. Yan, Annals Phys. **66**, 578 (1971). [Annals Phys.281,450(2000)].

[24] P. V. Landshoff, J. C. Polkinghorne, and R. D. Short, Nucl. Phys. **B28**, 225 (1971).

[25] P. V. Landshoff and J. C. Polkinghorne, Nucl. Phys. **B28**, 240 (1971).

[26] J. D. Bjorken and E. A. Paschos, Physical Review. 185 (5): 1975–1982 (1969).

[27] C. G. Callan, Jr. and D. J. Gross, Phys. Rev. Lett. **22**, 156 (1969).

[28] ZEUS, H1 Collaboration, F. D. Aaron *et al.*, JHEP **01**, 109 (2010). 0911.0884.

[29] E. D. Bloom *et al.*, Phys. Rev. Lett. **23**, 930 (1969).

[30] M. Breidenbach, J. I. Friedman, H. W. Kendall, E. D. Bloom, D. H. Coward, H. C. DeStaebler, J. Drees, L. W. Mo, and R. E. Taylor, Phys. Rev. Lett. **23**, 935 (1969).

[31] V. S. Fadin, E. A. Kuraev, and L. N. Lipatov, Phys. Lett. **60B**, 50 (1975).

[32] E. A. Kuraev, L. N. Lipatov, and V. S. Fadin, Sov. Phys. JETP **44**, 443 (1976). [Zh. Eksp. Teor. Fiz.71,840(1976)].

[33] E. A. Kuraev, L. N. Lipatov, and V. S. Fadin, Sov. Phys. JETP **45**, 199 (1977). [Zh. Eksp. Teor. Fiz.72,377(1977)].

[34] I. I. Balitsky and L. N. Lipatov, Sov. J. Nucl. Phys. **28**, 822 (1978). [Yad. Fiz.28,1597(1978)].

[35] F. Bloch and A. Nordsieck, Phys. Rev. **52**, 54 (1937).

[36] T. Kinoshita, J. Math. Phys. **3**, 650 (1962).

[37] T. D. Lee and M. Nauenberg, Phys. Rev. **133**, B1549 (1964). [,25(1964)].

[38] V. N. Gribov and L. N. Lipatov, Sov. J. Nucl. Phys. **15**, 438 (1972). [Yad. Fiz.15,781(1972)].

[39] L. N. Lipatov, Sov. J. Nucl. Phys. **20**, 94 (1975). [Yad. Fiz.20,181(1974)].

[40] G. Altarelli and G. Parisi, Nucl. Phys. **B126**, 298 (1977).

[41] Y. L. Dokshitzer, Sov. Phys. JETP **46**, 641 (1977). [Zh. Eksp. Teor. Fiz.73,1216(1977)].

[42] ZEUS, H1 Collaboration, H. Abramowicz *et al.*, Eur. Phys. J. **C75**, 580 (2015). 1506.06042.

[43] S. Moch, J. A. M. Vermaseren, and A. Vogt, Nucl. Phys. Proc. Suppl. **135**, 137 (2004). hep-ph/0408075.

[44] J. Chyla, Quarks, partons and Quantum Chromodynamics, A course in the phenomenology of the quark-parton model and Quantum Chromodynamics.

[45] G. Curci, W. Furmanski, and R. Petronzio, Nucl. Phys. **B175**, 27 (1980).

[46] W. Furmanski and R. Petronzio, Z. Phys. **C11**, 293 (1982).

[47] W. Furmanski and R. Petronzio, Phys. Lett. **97B**, 437 (1980).

[48] D. Kotlorz and A. Kotlorz, Acta Phys. Polon. **B36**, 3023 (2005). hep-ph/0510295.

[49] S. Kumano and T. H. Nagai, J. Comput. Phys. **201**, 651 (2004). hep-ph/0405160.

[50] P. Santorelli and E. Scrimieri, PoS **corfu98**, 023 (1998). hep-ph/9909289.

[51] L. Schoeffel, Nucl. Instrum. Meth. **A423**, 439 (1999).

[52] M. Gluck, E. Reya, and A. Vogt, Z. Phys. **C48**, 471 (1990).

[53] M. Gluck, E. Reya, and A. Vogt, Phys. Rev. **D45**, 3986 (1992).

[54] D. A. Kosower, AIP Conf. Proc. **407**, 669 (1997). hep-ph/9706446.

[55] S. Forte and L. Magnea, Phys. Lett. **B448**, 295 (1999). hep-ph/9812479.

[56] S. Forte, L. Magnea, A. Piccione, and G. Ridolfi, Nucl. Phys. **B594**, 46 (2001). hep-ph/0006273.

[57] W. Furmanski and R. Petronzio, Nucl. Phys. **B195**, 237 (1982).

[58] N. Cabibbo and R. Petronzio, Nucl. Phys. **B137**, 395 (1978).

[59] M. Miyama and S. Kumano, Comput. Phys. Commun. **94**, 185 (1996). hep-ph/9508246.

[60] M. Hirai, S. Kumano, and M. Miyama, Comput. Phys. Commun. **108**, 38 (1998). hep-ph/9707220.

[61] M. Hirai, S. Kumano, and M. Miyama, Comput. Phys. Commun. **111**, 150 (1998). hep-ph/9712410.

[62] M. Botje, Comput. Phys. Commun. **182**, 490 (2011). 1005.1481.

[63] S. Jadach and M. Skrzypek, Acta Phys. Polon. **B35**, 745 (2004). hep-ph/0312355.

[64] S. Jadach, W. Placzek, M. Skrzypek, and P. Stoklosa, Comput. Phys. Commun. **181**, 393 (2010). 0812.3299.

[65] F. Hautmann, H. Jung, A. Lelek, V. Radescu, and R. Zlebcik, Phys. Lett. **B772**, 446 (2017). 1704.01757.

[66] F. Hautmann, H. Jung, A. Lelek, V. Radescu, and R. Zlebcik, JHEP **01**, 070 (2018). 1708.03279.

[67] J. C. Collins, D. E. Soper, and G. F. Sterman, Adv. Ser. Direct. High Energy Phys. **5**, 1 (1989). hep-ph/0409313.

[68] CTEQ Collaboration, R. Brock *et al.*, Rev. Mod. Phys. **67**, 157 (1995).

[69] G. Altarelli, R. K. Ellis, and G. Martinelli, Nucl. Phys. **B143**, 521 (1978). [Erratum: Nucl. Phys.B146,544(1978)].

[70] J. Feltesse, *Introduction to deep inelastic scattering: Past and present*, in *Proceedings, 20th International Workshop on Deep-Inelastic Scattering and Related Subjects (DIS 2012): Bonn, Germany, March 26-30, 2012*, pp. 3–12. 2012.

[71] S. Glazov *et al.*, Brazilian Journal of Physics, **37** (2007).

[72] xFitter Developers' Team Collaboration, F. Giuli *et al.*, Eur. Phys. J. **C77**, 400 (2017). 1701.08553.

[73] CMS Collaboration, S. Chatrchyan *et al.*, Phys. Rev. **D90**, 032004 (2014). 1312.6283.

[74] ATLAS Collaboration, G. Aad *et al.*, Phys. Rev. **D85**, 072004 (2012). 1109.5141.

[75] CMS Collaboration, S. Chatrchyan *et al.*, JHEP **04**, 050 (2011). 1103.3470.

[76] LHCb Collaboration, R. Aaij *et al.*, JHEP **06**, 058 (2012). 1204.1620.

[77] CMS Collaboration, V. Khachatryan *et al.*, Eur. Phys. J. **C76**, 469 (2016). 1603.01803.

[78] CDF Collaboration, T. Aaltonen *et al.*, Phys. Rev. Lett. **102**, 181801 (2009). 0901.2169.

[79] D0 Collaboration, V. M. Abazov *et al.*, Phys. Rev. Lett. **101**, 211801 (2008). 0807.3367.

[80] D0 Collaboration, V. M. Abazov *et al.*, Phys. Rev. **D88**, 091102 (2013). 1309.2591.

[81] NOMAD Collaboration, O. Samoylov *et al.*, Nucl. Phys. **B876**, 339 (2013). 1308.4750.

[82] CMS Collaboration, V. Khachatryan *et al.*, JHEP **03**, 156 (2017). 1609.05331.

[83] M. Guzzi, K. Lipka, and S.-O. Moch, JHEP **01**, 082 (2015). 1406.0386.

[84] PROSA Collaboration, O. Zenaiev *et al.*, Eur. Phys. J. **C75**, 396 (2015). 1503.04581.

[85] *MSTW*. https://mstwpdf.hepforge.org/.

[86] *CT14*. http://hep.pa.msu.edu/cteq/public/index.html.

[87] *NNPDF*. http://nnpdf.mi.infn.it/.

[88] *HERAPDF*. http://pprc.qmul.ac.uk/research/herapdf.

[89] A. E. Chudakov, Izvestiya Akademii Nauk SSSR **Seriya Fizicheskaya**, 650 (1955).

[90] G. Marchesini and B. R. Webber, Nucl. Phys. **B238**, 1 (1984).

[91] G. Marchesini and B. R. Webber, Nucl. Phys. **B310**, 461 (1988).

[92] S. Catani, B. R. Webber, and G. Marchesini, Nucl. Phys. **B349**, 635 (1991).

[93] G. Marchesini, Nucl. Phys. **B445**, 49 (1995). hep-ph/9412327.

[94] Small x Collaboration, B. Andersson *et al.*, Eur. Phys. J. **C25**, 77 (2002). hep-ph/0204115.

[95] D. Amati, A. Bassetto, M. Ciafaloni, G. Marchesini, and G. Veneziano, Nucl. Phys. **B173**, 429 (1980).

[96] Y. L. Dokshitzer, D. Diakonov, and S. I. Troian, Phys. Rept. **58**, 269 (1980).

[97] G. Parisi and R. Petronzio, Nucl. Phys. **B154**, 427 (1979).

[98] T. Regge, Nuovo Cim. **14**, 951 (1959).

[99] T. Regge, Nuovo Cim. **18**, 947 (1960).

[100] A. Donnachie and P. V. Landshoff, Phys. Lett. **B296**, 227 (1992). hep-ph/9209205.

[101] Y. Balitskii and L. N. Lipatov, Sov. J. Nucl. Phys. **28**, 6 (1978).

[102] V. S. Fadin, Acta Phys. Polon. **B39**, 2193 (2008).

[103] M. Froissart, Phys. Rev. **123**, 1053 (1961).

[104] E. Iancu, A. Leonidov, and L. D. McLerran, Phys. Lett. **B510**, 133 (2001). hep-ph/0102009.

[105] L. V. Gribov, E. M. Levin, and M. G. Ryskin, Phys. Rept. **100**, 1 (1983).

[106] A. H. Mueller and J.-w. Qiu, Nucl. Phys. **B268**, 427 (1986).

[107] I. Balitsky, Nucl. Phys. **B463**, 99 (1996). hep-ph/9509348.

[108] Y. V. Kovchegov, Phys. Rev. **D60**, 034008 (1999). hep-ph/9901281.

[109] J. Jalilian-Marian, A. Kovner, A. Leonidov, and H. Weigert, Phys. Rev. **D59**, 014014 (1998). hep-ph/9706377.

[110] J. Jalilian-Marian, A. Kovner, and H. Weigert, Phys. Rev. **D59**, 014015 (1998). hep-ph/9709432.

[111] J. Jalilian-Marian, A. Kovner, A. Leonidov, and H. Weigert, Phys. Rev. **D59**, 034007 (1999). [Erratum: Phys. Rev.D59,099903(1999)], hep-ph/9807462.

[112] E. Iancu, A. Leonidov, and L. D. McLerran, Nucl. Phys. **A692**, 583 (2001). hep-ph/0011241.

[113] M. Ciafaloni, Nucl. Phys. **B296**, 49 (1988).

[114] S. Catani, F. Fiorani, and G. Marchesini, Phys. Lett. **B234**, 339 (1990).

[115] S. Catani, F. Fiorani, and G. Marchesini, Nucl. Phys. **B336**, 18 (1990).

[116] J. Collins and H. Jung, *Need for fully unintegrated parton densities*, in *HERA and the LHC: A Workshop on the implications of HERA for LHC physics. Proceedings, Part B.* 2005. Also in preprint hep-ph/0508280.

[117] J.-y. Chiu, A. Jain, D. Neill, and I. Z. Rothstein, Phys. Rev. Lett. **108**, 151601 (2012). 1104.0881.

[118] J. C. Collins and D. E. Soper, Nucl. Phys. **B193**, 381 (1981). [Erratum: Nucl. Phys.B213,545(1983)].

[119] J. C. Collins and D. E. Soper, Nucl. Phys. **B194**, 445 (1982).

[120] J. C. Collins, D. E. Soper, and G. F. Sterman, Phys. Lett. **109B**, 388 (1982).

[121] J. C. Collins, D. E. Soper, and G. F. Sterman, Nucl. Phys. **B223**, 381 (1983).

[122] J. C. Collins, D. E. Soper, and G. F. Sterman, Nucl. Phys. **B250**, 199 (1985).

[123] J. Collins, *Foundations of Perturbative QCD.* Cambridge University Press, 2013.

[124] M. G. Echevarria, A. Idilbi, and I. Scimemi, JHEP **07**, 002 (2012). 1111.4996.

[125] X.-d. Ji, J.-P. Ma, and F. Yuan, Phys. Lett. **B597**, 299 (2004). hep-ph/0405085.

[126] X.-d. Ji, J.-p. Ma, and F. Yuan, Phys. Rev. **D71**, 034005 (2005). hep-ph/0404183.

[127] R. Meng, F. I. Olness, and D. E. Soper, Phys. Rev. **D54**, 1919 (1996). hep-ph/9511311.

[128] P. M. Nadolsky, D. R. Stump, and C. P. Yuan, Phys. Rev. **D61**, 014003 (2000). [Erratum: Phys. Rev.D64,059903(2001)], hep-ph/9906280.

[129] P. M. Nadolsky, D. R. Stump, and C. P. Yuan, Phys. Rev. **D64**, 114011 (2001). hep-ph/0012261.

[130] J. Collins (2012). 1212.5974.

[131] S. Catani, M. Ciafaloni, and F. Hautmann, Phys. Lett. **B242**, 97 (1990).

[132] S. Catani, M. Ciafaloni, and F. Hautmann, Nucl. Phys. **B366**, 135 (1991).

[133] E. M. Levin, M. G. Ryskin, Yu. M. Shabelski, and A. G. Shuvaev, Sov. J. Nucl. Phys. **53**, 657 (1991). [Yad. Fiz.53,1059(1991)].

[134] F. Hautmann, M. Hentschinski, and H. Jung (2012). 1205.6358.

[135] J. C. Collins and R. K. Ellis, Nucl. Phys. **B360**, 3 (1991).

[136] F. Hautmann, Phys. Lett. **B535**, 159 (2002). hep-ph/0203140.

[137] T. C. Rogers, Eur. Phys. J. **A52**, 153 (2016). 1509.04766.

[138] A. V. Lipatov and N. P. Zotov, Eur. Phys. J. **C44**, 559 (2005). hep-ph/0501172.

[139] N. A. Abdulov, A. V. Lipatov, and M. A. Malyshev (2017). 1708.04057.

[140] H. Jung, Mod. Phys. Lett. **A19**, 1 (2004). hep-ph/0311249.

[141] P. Sun, B.-W. Xiao, and F. Yuan, Phys. Rev. **D84**, 094005 (2011). 1109.1354.

[142] P. Connor, F. Hautmann, H. Jung, M. Kramer, P. J. Mulders, E. R. Nocera, T. C. Rogers, and A. Signori, *TMDlib*. https://tmdlib.hepforge.org/doxy/html/index.html.

[143] P. Connor, F. Hautmann, and H. Jung, *TMDplotter Webinterface*. http://tmdplotter.desy.de.

[144] R. Angeles-Martinez *et al.*, Acta Phys. Polon. **B46**, 2501 (2015). 1507.05267.

[145] J. Blumlein, *On the k(T) dependent gluon density of the proton*, in *Deep inelastic scattering and QCD. Proceedings, Workshop, Paris, France, April 24-28, 1995*, pp. 265–268. 1995. Also in preprint hep-ph/9506403.

[146] A. Szczurek, Acta Phys. Polon. **B34**, 3191 (2003). hep-ph/0304129.

[147] H. Jung and F. Hautmann, *Determination of transverse momentum dependent gluon density from HERA structure function measurements*, in *Proceedings, 20th International Workshop on Deep-Inelastic Scattering and Related Subjects (DIS 2012): Bonn, Germany, March 26-30, 2012*, pp. 433–436. 2012. Also in preprint 1206.1796. [,433(2012)].

[148] F. Hautmann and H. Jung, Nucl. Phys. **B883**, 1 (2014). 1312.7875.

[149] G. Marchesini and B. R. Webber, Nucl. Phys. **B386**, 215 (1992).

[150] M. Deak, F. Hautmann, H. Jung, and K. Kutak (2010). 1012.6037.

[151] M. Deak, F. Hautmann, H. Jung, and K. Kutak, Eur. Phys. J. **C72**, 1982 (2012). 1112.6354.

[152] *xFitter*. https://www.xfitter.org/xFitter/.

[153] K. J. Golec-Biernat and M. Wusthoff, Phys. Rev. **D59**, 014017 (1998). hep-ph/9807513.

[154] K. J. Golec-Biernat and M. Wusthoff, Phys. Rev. **D60**, 114023 (1999). hep-ph/9903358.

[155] M. A. Kimber, A. D. Martin, and M. G. Ryskin, Phys. Rev. **D63**, 114027 (2001). hep-ph/0101348.

[156] A. D. Martin, M. G. Ryskin, and G. Watt, Eur. Phys. J. **C66**, 163 (2010). 0909.5529.

[157] G. Watt, A. D. Martin, and M. G. Ryskin, Eur. Phys. J. **C31**, 73 (2003). hep-ph/0306169.

[158] M. Bury, A. van Hameren, H. Jung, K. Kutak, S. Sapeta, and M. Serino (2017). 1712.05932.

[159] K. Golec-Biernat and A. M. Stasto (2018). 1803.06246.

[160] A. Bacchetta, F. Delcarro, C. Pisano, M. Radici, and A. Signori, JHEP **06**, 081 (2017). 1703.10157.

[161] A. Signori, A. Bacchetta, M. Radici, and G. Schnell, JHEP **11**, 194 (2013). 1309.3507.

[162] CMS Collaboration, S. Chatrchyan *et al.*, Phys. Rev. **D85**, 032002 (2012). 1110.4973.

[163] T. Sjostrand, S. Mrenna, and P. Z. Skands, Comput. Phys. Commun. **178**, 852 (2008). 0710.3820.

[164] S. Alioli, K. Hamilton, P. Nason, C. Oleari, and E. Re, JHEP **04**, 081 (2011). 1012.3380.

[165] S. Frixione, P. Nason, and C. Oleari, JHEP **11**, 070 (2007). 0709.2092.

[166] A. H. Mueller, Nucl. Phys. **B415**, 373 (1994).

[167] S. Catani and F. Hautmann, Phys. Lett. **B315**, 157 (1993).

[168] S. Catani and F. Hautmann, Nucl. Phys. **B427**, 475 (1994). hep-ph/9405388.

[169] P. J. Mulders and J. Rodrigues, Phys. Rev. **D63**, 094021 (2001). hep-ph/0009343.

[170] S. Mantry and F. Petriello, Phys. Rev. **D81**, 093007 (2010). 0911.4135.

[171] S. Mantry and F. Petriello, Phys. Rev. **D83**, 053007 (2011). 1007.3773.

[172] S. Catani and M. Grazzini, Nucl. Phys. **B845**, 297 (2011). 1011.3918.

[173] T. Becher, M. Neubert, and D. Wilhelm, JHEP **05**, 110 (2013). 1212.2621.

[174] P. M. Nadolsky, C. Balazs, E. L. Berger, and C. P. Yuan, Phys. Rev. **D76**, 013008 (2007). hep-ph/0702003.

[175] M. G. Echevarria, T. Kasemets, P. J. Mulders, and C. Pisano, JHEP **07**, 158 (2015). [Erratum: JHEP05,073(2017)], 1502.05354.

[176] D. Boer, W. J. den Dunnen, C. Pisano, M. Schlegel, and W. Vogelsang, Phys. Rev. Lett. **108**, 032002 (2012). 1109.1444.

[177] D. Boer, W. J. den Dunnen, C. Pisano, and M. Schlegel, Phys. Rev. Lett. **111**, 032002 (2013). 1304.2654.

[178] D. Boer and W. J. den Dunnen, Nucl. Phys. **B886**, 421 (2014). 1404.6753.

[179] F. Hautmann and H. Jung, JHEP **10**, 113 (2008). 0805.1049.

[180] S. Dooling, P. Gunnellini, F. Hautmann, and H. Jung, Phys. Rev. **D87**, 094009 (2013). 1212.6164.

[181] S. Dooling, P. Gunnellini, F. Hautmann, and H. Jung, *Nonperturbative corrections and showering in NLO-matched event generators*, in *Proceedings, 48th Rencontres de Moriond on QCD and High Energy Interactions: La Thuile, Italy, March 9-16, 2013*, pp. 305–308. 2013. Also in preprint 1304.7180.

[182] F. Hautmann and H. Jung, Eur. Phys. J. **C72**, 2254 (2012). 1209.6549.

[183] S. Dooling, F. Hautmann, and H. Jung, Phys. Lett. **B736**, 293 (2014). 1406.2994.

[184] ATLAS Collaboration, G. Aad *et al.*, Phys. Rev. **D85**, 092002 (2012). 1201.1276.

[185] A. V. Lipatov, S. P. Baranov, H. Jung, and M. A. Malyshev, Eur. Phys. J. **C78**, 2 (2018). 1711.05625.

[186] H. Jung, M. Kraemer, A. V. Lipatov, and N. P. Zotov, JHEP **01**, 085 (2011). 1009.5067.

[187] H. Jung, M. Kraemer, A. V. Lipatov, and N. P. Zotov, Phys. Rev. **D85**, 034035 (2012). 1111.1942.

[188] S. P. Baranov, H. Jung, A. V. Lipatov, and M. A. Malyshev, Eur. Phys. J. **C77**, 772 (2017). 1708.07079.

[189] H. Jung, *Un-integrated PDFs in CCFM*, in *Proceedings, 12th International Workshop on Deep Inelastic Scattering (DIS 2004): Strbske Pleso, Slovakia, April 14-18, 2004*, pp. 299–302. 2004. Also in preprint hep-ph/0411287.

[190] S. P. Baranov, A. V. Lipatov, and N. P. Zotov, Phys. Rev. **D85**, 014034 (2012). 1108.2856.

[191] S. P. Baranov and N. P. Zotov, JETP Lett. **86**, 435 (2007). 0707.0253.

[192] J.-P. Lansberg and H.-S. Shao, Phys. Rev. Lett. **111**, 122001 (2013). 1308.0474.

[193] J. P. Lansberg, J. Phys. **G38**, 124110 (2011). 1107.0292.

[194] C. Pisano, Int. J. Mod. Phys. Conf. Ser. **37**, 1560031 (2015). 1412.1423.

[195] D. Boer and C. Pisano, Phys. Rev. **D86**, 094007 (2012). 1208.3642.

[196] J. P. Ma, J. X. Wang, and S. Zhao, Phys. Rev. **D88**, 014027 (2013). 1211.7144.

[197] J. P. Ma, J. X. Wang, and S. Zhao, Phys. Lett. **B737**, 103 (2014). 1405.3373.

[198] CMS Collaboration, V. Khachatryan *et al.*, Eur. Phys. J. **C71**, 1575 (2011). 1011.4193.

[199] M. Diehl, D. Ostermeier, and A. Schafer, JHEP **03**, 089 (2012). [Erratum: JHEP03,001(2016)], 1111.0910.

[200] M. Diehl and J. R. Gaunt (2017). 1710.04408.

[201] K. Golec-Biernat and A. M. Stasto, Phys. Rev. **D95**, 034033 (2017). 1611.02033.

[202] E. Elias, K. Golec-Biernat, and A. M. Stasto (2017). 1801.00018.

[203] M. Deak and K. Kutak, JHEP **05**, 068 (2015). 1503.00536.

[204] M. Deak, Acta Phys. Polon. Supp. **8**, 295 (2015). 1505.04466.

[205] P. Kotko, K. Kutak, C. Marquet, E. Petreska, S. Sapeta, and A. van Hameren, JHEP **09**, 106 (2015). 1503.03421.

[206] D. W. Sivers, Phys. Rev. **D41**, 83 (1990).

[207] J. C. Collins, Phys. Lett. **B536**, 43 (2002). hep-ph/0204004.

[208] S. J. Brodsky, D. S. Hwang, and I. Schmidt, Phys. Lett. **B530**, 99 (2002). hep-ph/0201296.

[209] S. Frixione and B. R. Webber, JHEP **06**, 029 (2002). hep-ph/0204244.

[210] S. Frixione and B. R. Webber (2002). hep-ph/0207182.

[211] S. Frixione, P. Nason, and B. R. Webber, JHEP **08**, 007 (2003). hep-ph/0305252.

[212] J. Alwall, R. Frederix, S. Frixione, V. Hirschi, F. Maltoni, O. Mattelaer, H. S. Shao, T. Stelzer, P. Torrielli, and M. Zaro, JHEP **07**, 079 (2014). 1405.0301.

[213] S. Gieseke, P. Stephens, and B. Webber, JHEP **12**, 045 (2003). hep-ph/0310083.

[214] S. Platzer and S. Gieseke, JHEP **01**, 024 (2011). 0909.5593.

[215] T. Gleisberg, S. Hoeche, F. Krauss, M. Schonherr, S. Schumann, F. Siegert, and J. Winter, JHEP **02**, 007 (2009). 0811.4622.

[216] S. Schumann and F. Krauss, JHEP **03**, 038 (2008). 0709.1027.

[217] J.-C. Winter and F. Krauss, JHEP **07**, 040 (2008). 0712.3913.

[218] H. Jung and G. P. Salam, Eur. Phys. J. **C19**, 351 (2001). hep-ph/0012143.

[219] H. Jung, Nucl. Phys. Proc. Suppl. **79**, 429 (1999). hep-ph/9905554.

[220] G. Marchesini and B. R. Webber, Nucl. Phys. **B349**, 617 (1991).

[221] H. Jung, Comput. Phys. Commun. **143**, 100 (2002). hep-ph/0109102.

[222] F. Hautmann, H. Jung, and S. T. Monfared, Eur. Phys. J. **C74**, 3082 (2014). 1407.5935.

[223] K. Konishi, A. Ukawa, and G. Veneziano, Nucl. Phys. **B157**, 45 (1979).

[224] A. Bassetto, M. Ciafaloni, and G. Marchesini, Nucl. Phys. **B163**, 477 (1980).

[225] *A Wolfram Web Resource.* https://mathworld.wolfram.com/IntegralEquationNeumannSeries.html/.

[226] A. Lelek, F. Hautmann, and H. Jung, PoS **DIS2016**, 036 (2016).

[227] A. Lelek, H. Jung, and F. Hautmann, PoS **ICHEP2016**, 961 (2017).

[228] A. Lelek (2017). 1710.04114.

[229] A. Bermudez Martinez, P. Connor, F. Hautmann, H. Jung, A. Lelek, V. Radescu, and R. Zlebcik (2018). 1804.11152.

[230] S. Alekhin *et al.*, Eur. Phys. J. **C75**, 304 (2015). 1410.4412.

[231] J. Pumplin, D. Stump, R. Brock, D. Casey, J. Huston, J. Kalk, H. L. Lai, and W. K. Tung, Phys. Rev. **D65**, 014013 (2001). hep-ph/0101032.

[232] S. Höche, F. Krauss, and S. Prestel (2017). 1705.00982.

[233] S. Höche and S. Prestel, Eur. Phys. J. **C75**, 461 (2015). 1506.05057.

[234] ATLAS Collaboration, G. Aad *et al.*, JHEP **09**, 145 (2014). 1406.3660.

[235] H. Jung *et al.*, Eur. Phys. J. **C70**, 1237 (2010). 1008.0152.

[236] M. Bengtsson, T. Sjostrand, and M. van Zijl, Z. Phys. **C32**, 67 (1986).

[237] B. M. Waugh, H. Jung, A. Buckley, L. Lonnblad, J. M. Butterworth, and E. Nurse, *HZTool and Rivet: Toolkit and Framework for the Comparison of Simulated Final States and Data at Colliders*, in *15th International Conference on Computing in High Energy and Nuclear Physics (CHEP 2006) Mumbai, Maharashtra, India, February 13-17, 2006*. 2006. Also in preprint hep-ph/0605034.

[238] A. Buckley, J. Butterworth, L. Lonnblad, D. Grellscheid, H. Hoeth, J. Monk, H. Schulz, and F. Siegert, Comput. Phys. Commun. **184**, 2803 (2013). 1003.0694.

[239] ATLAS Collaboration, G. Aad *et al.*, Eur. Phys. J. **C76**, 291 (2016). 1512.02192.

[240] A. Accardi *et al.*, Eur. Phys. J. **A52**, 268 (2016). 1212.1701.

[241] G. Bohm and G. Zech, *Introduction to Statistics and Data Analysis for Physicists*. Deutsches Elektronen-Synchrotron, 2010.

[242] G. Cowan, *Statistical Data Analysis*. Oxford Science Publications, 1998.

[243] F. James, Rept. Prog. Phys. **43**, 1145 (1980).

[244] A. Kolmogorov, *Grundbegriffe der Wahrscheinlichkeitsrechnung*. Springer, Berlin, 1933.